Experimental Examination of Plasma Formation and

Current Loss in Post-Hole Convolutes

by

Matthew Robert Gomez

A dissertation submitted in partial fulfillment
of the requirements for the degree of
Doctor of Philosophy
(Nuclear Engineering and Radiological Sciences)
in The University of Michigan
2011

Doctoral Committee:

Professor Ronald M. Gilgenbach, Chair
Professor Yue Y. Lau
Professor Brian E. Gilchrist
Assistant Professor John E. Foster
Michael E. Cuneo, Sandia National Laboratories

2011

To my parents, Bob and Sue

ACKNOWLEDGEMENTS

I would like to thank all of the people that made completion of this dissertation possible.

First, I would like to thank Professor Ronald M. Gilgenbach, my advisor and the chair of my doctoral committee, whose guidance has kept me steadily moving towards graduation throughout graduate school. Without his suggestions for projects to work on and advice on framing a question to be answered, diagnosing it, and forming sound conclusions based on the data, I would likely not be finishing as soon as I am.

I would also like to thank Dr. Michael E. Cuneo, my current and future manager at Sandia National Laboratories as well as a member of my doctoral committee. My time working with Mike at Sandia over the last year was so enjoyable that I decided to continue working in his group after graduation.

Additionally, I would like to thank Professors Yue Ying Lau, John E. Foster, and Brian E. Gilchrist both for being on my doctoral committee and for teaching many of the plasma physics courses that I took during my time at the University of Michigan.

Aside from my doctoral committee members, I would also like to thank the other graduate students, past and present, that have helped me move towards graduation. Three of my contemporaries in the Plasma, Pulsed Power, and Microwave lab stand out as having significantly helped to move me along through graduate school. I worked in

the lab with Dr. Jacob C. Zier, Dr. David M. French, and Dr. Brad W. Hoff each for 4 or more years. Not only did Brad, Jacob, and David help considerably with the actual work that was conducted at the PPPM lab, but they also added to the social experience, for which I might be equally grateful. Having Brad go through the PhD process a year ahead helped tremendously in knowing what to expect, and being able to go through the experience of writing and defending concurrently with David and Jacob was similarly helpful.

Earlier in my graduate school experience, I looked up to the senior grad students. I could always count on them for help with setting up and running experiments, but more than anything, they helped me realize that in order to be a successful experimentalist I needed to get my hands dirty. For that I would like to thank Dr. Will White, Dr. Nick Jordan, and Dr. Trevor Strickler.

I would also like to thank the students following me through the PPPM Lab, Matt Franzi, David Simon, Ian Rittersdorf, Ed Cruz, and Sonal Patel, for all of the help that they have given me over the years. I look forward to seeing how their research projects and graduate careers progress over the next few years.

There is one final member of the PPPM lab I would like to say thank you to, Mark Perrault. Mark's help in setting up the LTD support systems was immeasurable. There are a lot of things that need to be done to bring a new experiment online and very few of them are considered scientifically interesting. Mark is the one that typically takes care of

these jobs in the PPPM lab, and for that he deserves a lot more than a brief thank you in the acknowledgements section of a dissertation.

Almost a year of the time I spent in graduate school, I spent in Albuquerque, NM working as an intern at Sandia National Labs. While there I interacted with dozens of people that in some way contributed to my research. Thanks to the research scientists that allowed me to conduct ride-along experiments: Dr. Ryan McBride, Dr. Daniel Sinars, Dr. Gregory Rochau, Dr. James Bailey, Dr. David Ampleford, and Dr. Brent Jones. Thanks to the scientists and technologists that helped set up or field my diagnostic: Dr. Mark D. Johnston, Pat Lake, Linda Weber, Alan Carlson, Dan Nielsen, Steve Ploor, Tom Avila, Terrence Bock, and Don Petmecky. Thanks to the staff members that facilitated conducting experiments on the Z-machine: Dr. Mike Lopez, Dr. Michael Jones, Dr. Aaron Edens, Dr. Ken Struve, Brian Stoltzfus, and Ray Thomas. Thanks to the guys in center section and Lab 101 that installed my probes and fiber optics: Steve Toledo, Leo Molina, Matt Kernaghan, Mike Sullivan, Eric Breden, and Tommy Mulville. Thanks to the members of the drafting/design team that helped with design of my probes: James Cisneros, Marcelino Vigil, T. J. Rogers, Monica Cleveland, Andy Maurer, and Daniel Sandoval. Thanks to the B-dot team who both gave me useful insight about B-dot probe design and helped with installation of the fiber optic probe: Jim Moore and Tim Wagoner. Lastly, I would like to thank the group of scientists and technologists that worked on LTDs at Sandia from whom I learned a lot about the construction and operation of the device: Dr. Michael Mazarakis, Dr. Joseph Woodworth, Bill Fowler, and Rob Sharpe.

Beyond the people that contributed to the completion of my dissertation research from a technical standpoint, there were a number of people whose social support was important to my graduation. In particular, my scheduled event for every Tuesday night for the last three plus years has been the U of M Euchre club. I appreciate the evenings full of distractions provided by the friends I met over the years through the club. Finally, and most importantly, I would like to thank my family for the years of support. The encouragement from my parents, Bob and Sue, and my sisters, Amy, Lisa, and Sandy, have always made my career aspirations seem easily within reach.

This work was funded by the DOE through a Sandia National Laboratories subcontract to the University of Michigan. This work was supported by U. S. DoE through Sandia National Laboratories award document numbers 240985, 768225, 790791 and 805234 to the University of Michigan. Sandia is a multi-program laboratory operated by Sandia Corporation, a Lockheed Martin Company, for the United States Department of Energy's National Nuclear Security Administration under Contract DEAC04-94AL85000. A portion of my time in graduate school was funded by the Stewardship Science Graduate Fellowship awarded by the Krell Institute in conjunction with the United States Department of Energy's National Nuclear Security Administration.

TABLE OF CONTENTS

LIST OF FIGURES

LIST OF TABLES

LIST OF APPENDICES

CHAPTER 1

INTRODUCTION

High current pulsed power drivers (10's of MA) have many applications in the areas of high energy density physics and plasma physics. Primarily, the large amplitude, short duration (100's of ns) current pulses are used to produce x-rays [1-5] or drive dynamic materials experiments [6-8]. The x-rays are used for experiments ranging from indirect drive inertial confinement fusion [1] to material x-ray opacity measurements [9] to photo-ionization of gases for astrophysics applications [10]. The dynamic materials experiments typically fall into one of two categories: shock physics [6],[8] and isentropic compression [7]. In the shock physics experiments, information about the material properties of the sample can be determined based on the propagation of the shock through it. The isentropic compression experiments also provide information about the material properties of a sample, but cover a different region of phase-space. These High Energy Density Physics (HEDP) experiments would not be practical (or in some cases possible) without large scale pulsed power drivers.

Pulsed power devices are an important class of circuits in which energy is stored over a relatively long time and then released in a short burst such that the power has increased by many orders of magnitude. Pulses with peak powers on the order of several hundred TW (approximately ten times the world's power production) have been achieved [11].

While the power output by these devices is large, the energy in a single pulse is relatively small (12 MJ in a Z-Machine pulse which is roughly the equivalent of the energy stored in 0.1 gallons of gasoline) because the duration of the pulse is so short (100's of ns).

One typical form for a pulsed power device is the Marx generator (or bank). In a Marx bank, a voltage is supplied to an array of capacitors, which are resistively coupled in parallel (timescales for charging could be on the order of milliseconds to minutes). Once fully charged, a set of switches are closed which changes the capacitor coupling from parallel to series. This causes the output voltage to increase from the capacitor charge voltage, V_{ch}, to N x V_{ch}, where N is the number of capacitor stages. The output voltage discharges through the load (on timescales that are on the order of microseconds). Marx banks are typically high impedance drivers (10-100 Ohm), so they are useful for providing high voltage (MV), moderate current pulses (10's of kA) with fast risetimes. In cases where a high current with a fast risetime is desired, Marx banks can be used to drive a pulse compression circuit, which is used to reduce the driver impedance, thus allowing a higher current with short risetime. Not only do the pulse compression circuits have less than perfect efficiency, but they add to the cost and complexity of the system, thus, ideally they would be avoided if possible.

A second style of pulsed power device is the Linear Transformer Driver (LTD) [12-24], which has been developed in Tomsk, Russia at the Institute of High Current Electronics with support from Sandia National Labs. In an LTD, two capacitor banks are slowly

charged to opposite polarities. Switches are used to connect the high voltage ends of the capacitors; when the switches close a voltage pulse of twice the charge voltage is sent to the driver output. The LTD is designed such that the risetime of the output pulse will be approximately 100 ns regardless of the number of capacitors connected in parallel. This allows the LTD architecture to be used to supply a high-current, short risetime pulse without the need for any intermediate pulse compression. As a result, the next generation of large scale pulsed power drivers are based on LTD technology [12].

Pulsed power is used to drive many vacuum electron devices and both plasma physics and high energy density experiments. The Michigan Electron Long Beam Accelerator (MELBA) is a 1 MV Marx bank at the University of Michigan [25] that has been used to drive relativistic magnetron, gyrotron, and electron beam diode experiments. Additionally, at the University of Michigan, the Michigan Accelerator for Inductive Z-pinch Experiments (MAIZE) is a 1 MA class, LTD-based pulsed power device [13]. MAIZE has been used to study a device associated with transmitting pulsed power known as a post-hole convolute, as well as magneto-Rayleigh Taylor instability development in plasmas [26].

The largest pulsed power device in the world is the Z-Machine at Sandia National Laboratories (see Fig. 1.1) [1-3],[11],[26-39]. The Z-Machine is based on Marx bank technology, and utilizes several pulse compression techniques to deliver an approximately 100 ns risetime 25 MA, 2MV pulse to the load. Once the pulse is compressed, it is passed through an insulating stack into a vacuum section (nearly all

HEDP and plasma physics experiments take place in a vacuum). Within the vacuum section, the pulse is propagated along four parallel transmission lines (not shown in Fig. 1.1) towards the load (the inductance of the system is reduced by transmitting the pulse along several parallel lines). The load typically requires a single anode-cathode (A-K) gap, so the four transmission line A-K gaps are combined into a single A-K gap with a double post-hole convolute (the subject of this dissertation).

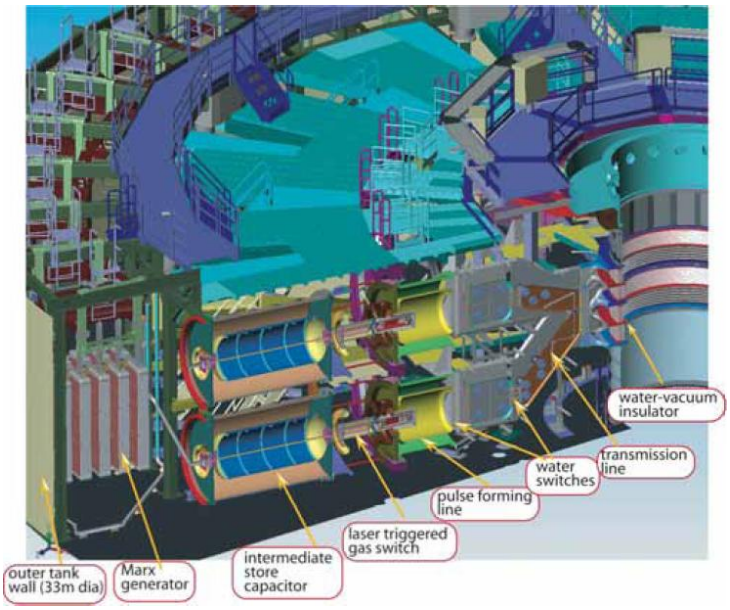

Fig. 1.1 A schematic of the Z-Machine at Sandia National Laboratories. (Figure courtesy of K. R. LeChien et al. [27].)

The Z-Machine is typically used to drive two types of loads: z-pinch loads and dynamic material loads. The z-pinch loads consist of either a cylindrical array of fine wires [1-3] (approximately 10 microns in diameter), a solid cylindrical Z-pinch (liner) [40], or of an annular gas puff. In either case, the current passes through the material, ionizes it, and the current and self-induced magnetic field create a JxB force which collapses the material on axis. There it stagnates and emits x-rays; the Z-Machine is the world's most

powerful pulsed x-ray source with peak powers of up to 330 TW [4]. For the dynamic materials loads, either a flyer plate is accelerated by the current pulse and collides with the sample material [6],[8], driving a shock wave through it (shock physics), or a shaped current pulse is used to compress a material along the isentrope (isentropic compression) [7]. Flyer plates have been accelerated to 34 km/second, and pressures of up to 12 GPa have been produced with the Z-Machine; both of these milestones are not achievable with other dynamic materials techniques presently available.

In this dissertation, the original research by the author that pertains to post-hole convolutes will be described. Chapter 2 contains a background on post-hole convolutes, including previous simulation studies that has been performed. In chapter 3, the experimental facilities at the University of Michigan that were used in this work are described. The results of small-scale post-hole convolute experiments are presented in chapter 4. Additional research pertaining to post-hole convolutes was conducted at Sandia National Labs on the Z-Machine. A brief description of the Z-Machine itself, as well as the diagnostic setup and calibration used for these experiments are included in chapter 5. In chapter 6, the data from the experiments on the Z-Machine are presented. Chapter 7 describes the analysis of the spectra recorded at the Z-Machine. Chapter 8 compares the plasma parameters recorded for different cases and compares the results with simulations. Also included in chapter 8 are estimates of the gap closure velocity of the plasma. Chapter 9 summarizes the results from the previous chapters and makes recommendations for future work.

CHAPTER 2

CONVOLUTE PHYSICS AND PRIOR SIMULATIONS

In this chapter, a background on post-hole convolutes is presented. The purpose, typical geometries, and an explanation of physical mechanisms are included. Additionally, the results from a number of simulations, which were previously conducted to understand the convolute physics, will be discussed.

2.1. Post-Hole Convolutes

Post-Hole Convolutes are used to convert several parallel transmission lines into a single transmission line. This is accomplished by connecting the anodes (or cathodes) of the transmission lines with a post, which passes through a hole in the cathode (or anode), hence the term "post-hole" convolute. A simple version of a post-hole convolute is shown in Fig. 2.1. Typically, the post connects the anodes (as opposed to the cathodes) in order to place the cathode on the outside edge of the coaxial geometry of the post-hole. This imposes a lower electric field at the surface of the cathode, thus the time to electron emission from the cathode is increased.

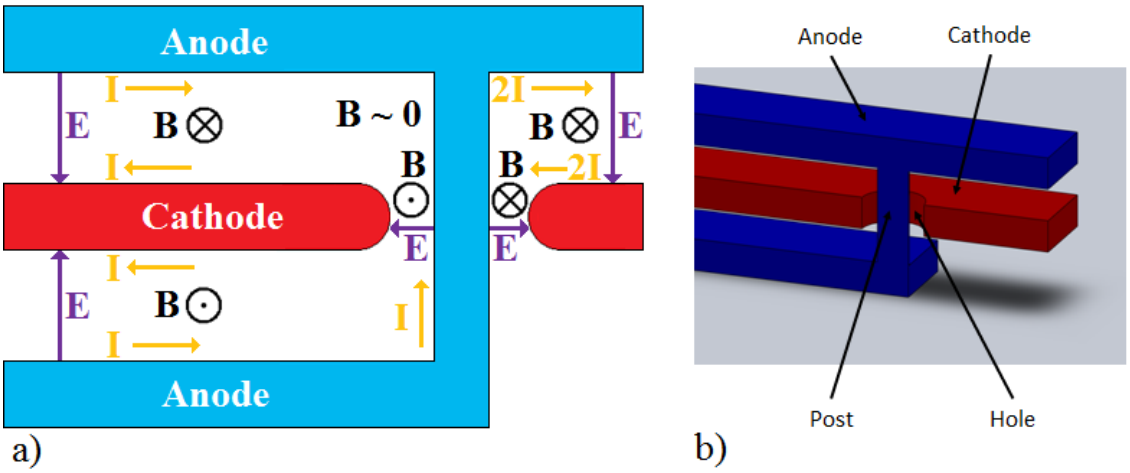

Fig. 2.1 a) 2D cross-section of a generic post-hole convolute. The anodes are represented in blue, and are joined by a post, which passes through a hole in the central cathode (red). Electric and Magnetic field directions and currents are shown in purple, black and orange, respectively. b) A 3D rendering of a generic post-hole convolute. Similarly to the image in (a), there are two anodes (blue) and one shared cathode (red); a post connects the two anodes through a hole in the cathode.

Short pulse, high current pulsed power drivers typically attempt to minimize the inductance of the system. For a given drive voltage and system inductance, parameters of the current pulse (risetime and peak amplitude) are related by

$$V = \frac{dI}{dt}L + I\frac{dL}{dt} + IR \tag{2.1}$$

where V is the drive voltage, L is the system inductance, R is the system resistance, I is the current in the system, and V, L, R, and I are all functions of time. In order to minimize the risetime of the current, the inductance of the system must be small. For this reason, typically several transmission lines are used in parallel to reduce the inductance. Close to the load, the current from each transmission line is combined into a single transmission line using a post-hole convolute. For each additional transmission line added in parallel, the inductance drops as

$$L_{system} = \left(\sum_N \frac{1}{L_{TL}}\right)^{-1} \tag{2.2}$$

where L_{TL} is the inductance of an individual transmission line, N is the number of parallel transmission lines, and L_{system} is the equivalent inductance of the parallel transmission lines. It is clear from this equation that adding more transmission lines in parallel will continue to reduce the inductance, but that there are diminishing returns. Contrary to this effect, the more transmission lines used, the larger and more complicated the convolute must be, which increases the inductance (as well as the cost) of the system. In many cases, the optimal number of parallel transmission lines is four; however, in the designs for the next generation pulsed power driver, a triple post-hole convolute is used (six parallel transmission lines) [12].

On many large pulsed power machines (Saturn, Z-Machine, etc.), the electrical pulse originates at a ring of Marx banks at a large radius (10's of meters) with a long risetime (microseconds). The pulse is concentrated in both space and time until it passes through the load at a ~ 1 cm radius with a 100 ns risetime. The need to spatially concentrate the pulse lends itself to a radial (or conical) transmission line. Fig. 2.2 shows a 12-post, double post-hole convolute (combines 4 parallel conical transmission lines) that was previously used on the Z-Machine.

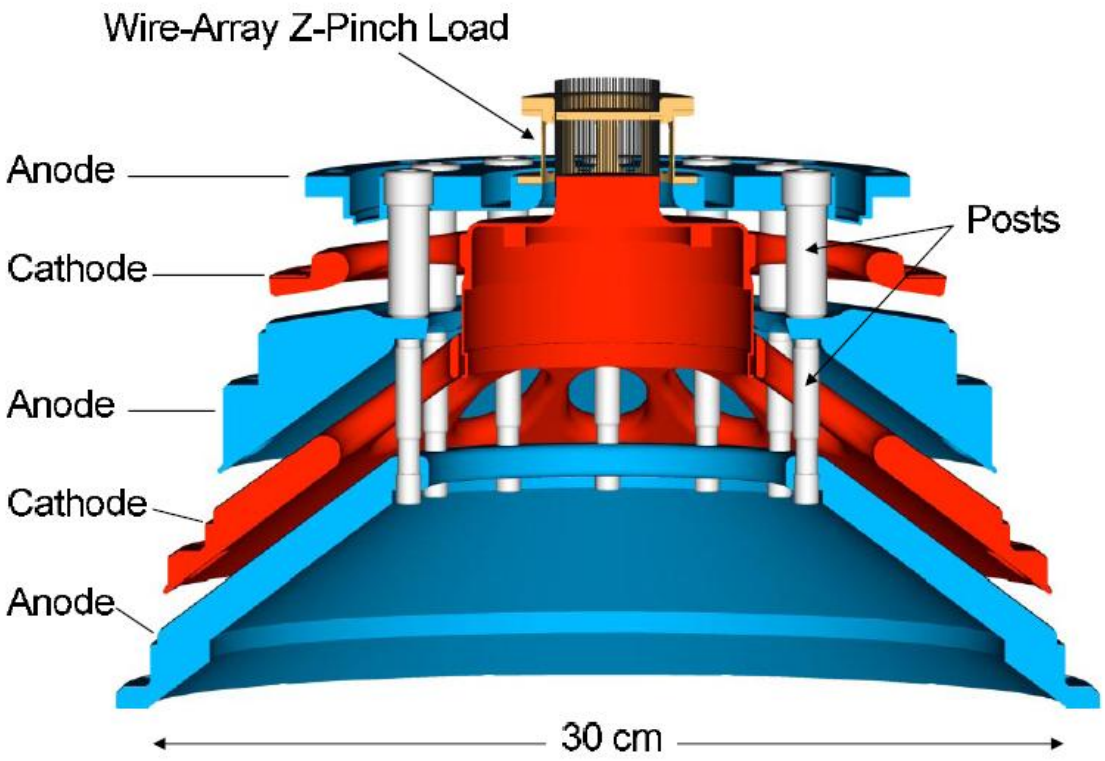

Fig. 2.2 A 3D rendering of the double post-hole convolute used on the Z-Machine prior to the refurbishment designed by W. A. Stygar et al. Four A-K gaps are combined into one using a 12 post, double post-hole convolute. (Figure courtesy of D. V. Rose et al. [28].)

2.2. Field Estimates in a Post-Hole Convolute

The electric and magnetic fields in the post-hole convolute have a significant impact on its performance. Once the electric fields exceed a threshold (typically assumed to be 240 kV/cm [29],[30]) at the surface of the cathode, electrons are explosively emitted into the gap. These "flow" electrons will stream across the anode-cathode gap until the current flowing in the system reaches the threshold for self-magnetic insulation; this value is dependent on the voltage and the transmission line geometry.

The magnetic field around the post can be approximated using the following assumptions: the fields from the surrounding transmission lines do not affect the field if

the measurement is made close enough to the post, the contribution from flow electrons can be ignored (flow electrons are a small fraction of total current), and the post is sufficiently long. In this case, from Ampere's law, the magnetic field is the same as that for a current carrying wire:

$$B = \frac{\mu_0 I}{2\pi r} \tag{2.3}$$

where μ_0 is the permeability of free-space, I is the current carried by the post, and r is the distance from the axis of the post at which the measurement is being made. On the Z-Machine, the total current has peak amplitude of 24 MA. The upper posts conduct roughly 75% of this current (the remaining 25% flows in the top anode, thus does not pass through the top post), and there are 12 posts in parallel, thus an individual post carries approximately 1.5 MA. The radius of the posts is 7.9 mm; therefore at the surface of the post, the peak magnetic field is approximately 38 T. At the surface of the cathode hole (r = 19.2 mm) this drops to 15.6 T.

Similarly, one can estimate the electric field around the post with a few assumptions; the post-hole geometry is coaxial and long compared to the A-K gap, fields from other portions of the convolute can be ignored, and flow electron effects can be ignored. The electric field is then

$$E = \frac{V}{r * ln\left(\frac{b}{a}\right)} \tag{2.4}$$

where V is the gap voltage, r is the radial distance from the axis, b is the outer radius, and a is the inner radius. For the upper convolute posts on the Z-Machine, a = 7.9 mm

and b = 19.2 mm, V peak is approximately 2 MV. At the surface of the post, the peak electric field is roughly 2.9 MV/cm, and at the surface of the hole, the peak electric field is 1.2 MV/cm, well above the threshold for explosive electron emission.

The electric and magnetic fields calculated above are orthogonal to one another (at least under the assumptions used to calculate the values). For E and B fields with components normal to one another, there is an associated drift velocity given by

$$v_{ExB} = \frac{ExB}{B^2} \tag{2.5}$$

where E is the electric field and B is the magnetic field. Assuming the peak current and peak voltage occur at the same time, the ExB drift velocity would be 0.026c (780 cm/μs) at both the cathode and anode surfaces.

2.3. Convolute Issues

Post-hole convolutes have been fielded on several large pulsed power drivers over the last three decades, from Proto-II in 1980 to ZR in 2007 (including Double Eagle, Saturn, and the Z-Machine) [41]. During this span, the power that the convolute is subject to has increased significantly (more than a factor of 10). Until recently, the design of the convolute relied heavily on the assumption that what worked previously will work for the new machine.

The current in each of the four parallel magnetically insulated transmission lines (MITL) [42-44] is determined based on integrated B-dot (dB/dt) measurements upstream of the convolute. Additional B-dot monitors are used to characterize the current downstream

of the convolute in the final feed gap. Dividing the downstream current by the sum of the currents upstream of the convolute gives the efficiency of the convolute. Prior to the refurbishment, the Z-Machine had load currents on the order of 17 MA and MITL currents of 18.5 MA, which gives an efficiency of 92%. This fell within the 5-10% loss range, which was considered to be acceptable. Post-refurbishment, peak load currents of 18 MA, with MITL currents of 22 MA were recorded in this dissertation. This corresponds to an efficiency of 82%, which is not acceptable.

The increased losses in the convolute region have sparked interest in diagnosing the loss mechanism. Simulations of the convolute have been performed, and the results match the experimental data fairly well, but these simulations make some assumptions about the rate at which plasma forms within the convolute, as well as the conditions of the plasma.

2.4. Convolute Simulations

Several teams have worked on simulating post-hole convolutes [28-33]. In particular, two groups have recently worked on simulating the double post-hole convolute used in the Z-Machine; both of which used electromagnetic Particle-In-Cell codes (although each used a different code, with different capabilities). An additional simulation effort at the University of Michigan modeled the simplified post-hole convolute design fielded on MAIZE at U of M.

2.4.1. MAGIC PIC Simulations by French

Particle-In-Cell simulations using MAGIC 3D [45] were conducted by D. M. French at the University of Michigan. These simulations specifically attempted to match the one-post, single post-hole convolute experiments run on MAIZE at the University of Michigan. The simulations allowed explosively emitted electron flow in the A-K gap, but neglected any cathode or anode plasma effects. The results of these simulations are discussed in detail in Section 4.4.

These experiments had a relatively high current to voltage ratio (~ 50x that of the Z-Machine), thus the magnetic insulation conditions were well satisfied and current losses were not significant. Current traces from the simulations are shown in Fig. 2.3. Dividing the total loss current (current lost to the anode plus current lost through the simulation boundaries) by the current through the load, the loss is on the order of 0.1%, thus the efficiency of this convolute was 99.9%.

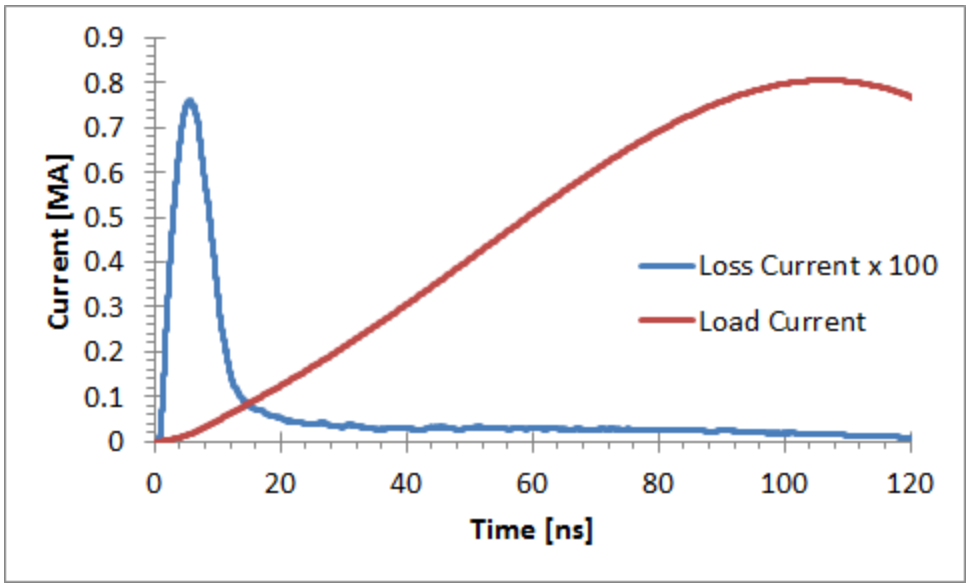

Fig. 2.3 Plot of the loss current and the load current for the MAGIC simulations of the U of M convolute performed by French. The loss current peaks at approximately 7.5 kA prior to self-magnetic insulation. Late in time, the losses are less than 0.5 kA out of ~ 800 kA, which is negligible.

While the significant difference in efficiency indicates that the experimental setups are not directly comparable, there is still some information to be gained from these simulations. Qualitatively, the flow currents should behave similarly in the two cases in regions where the conditions for self-magnetic insulation are satisfied. In these simulations there is evidence that electrons are "born" on the upstream side of the hole, follow magnetic field lines, and collect on the downstream side of the post. Images of simulated electron position are shown in Fig. 2.4.

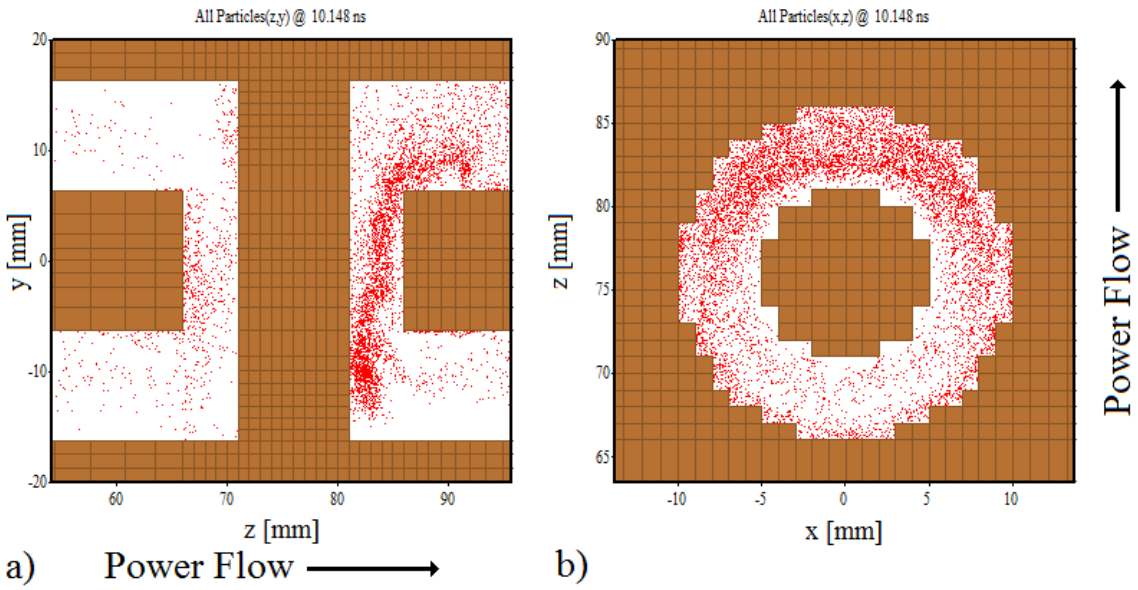

Fig. 2.4 Plots of the electron locations (red dots) from French's MAGIC simulations. The concentration of electrons is significantly greater on the downstream side of the post.

2.4.2. QuickSilver PIC Simulations by Pointon

QuickSilver has been used to simulate the double post-hole convolute on Z [29],[32],[33]. These simulations show 36 discrete magnetic field nulls (3 for each of the 12 post sets) and 1 large, approximately azimuthally symmetric magnetic field null. Initial simulations using QuickSilver did not include electrode plasma effects. Additionally, a number of simplifications were necessary to reduce the runtime of the simulations. These included: a 20 ns risetime (as opposed to 100 ns), emission limited to $r < 14$ cm (emission was expected out to 1.3 m) [29], which reduced the flow current entering the convolute, and the load impedance was assumed static for the duration of the shot, but was adjusted in value until the simulations matched the experimental results.

Despite the unrealistic assumptions used in these simulations, some useful information can be gained from them. Electron impact damage is observed on the experimental

electrodes post shot, and the location of this damage matches the location of magnetic field nulls (the areas of highest electron energy deposition) in the simulations. This shows qualitative agreement between the experiment and simulation.

When using load parameters in the simulation that match those used experimentally, the simulated loss current is less than 5% of the measured value of the current loss. This indicates that another loss mechanism is responsible for the majority of the loss. Electrode plasmas, which may account for the increased losses, are not included in this model.

Using the high impedance load model (which artificially increases the voltage in the convolute), the loss currents in the simulations quantitatively match those observed experimentally. Given these losses, the simulations track the electron energy deposited in the electrodes. The peak surface temperature in the convolute region is ~ 2400°C, which is significantly higher than the melt temperature for 304 SS (1430°C). Throughout the convolute, the temperature rise is 100's of °C (as shown in Fig. 2.5). A temperature increase in excess of 400 °C is sufficient to liberate contaminants from within the electrodes [29],[46].

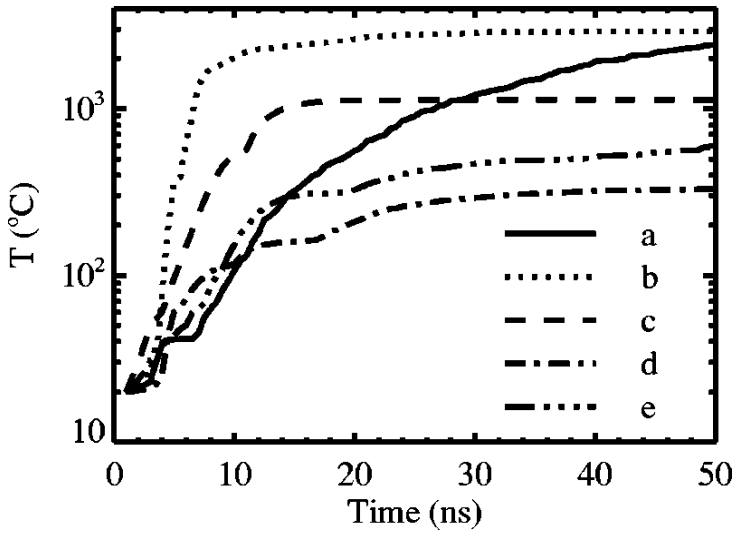

Fig. 2.5 Plot showing the time history of the maximum anode temperature for several regions of the simulation. (a) is the anode in the final feed gap, (b) is the top post, (c) is the bottom post, (d) is the middle anode, and (e) is the bottom anode. (Figure courtesy of T. D. Pointon, et al [29].)

Other important notes from these simulations are that reducing the number of posts from 12 to 6 did not reduce the losses in the simulations. Additionally, the losses scale approximately linearly with convolute voltage.

The QuickSilver model was updated to include a time-dependent loss term associated with the convolute losses. Without this term, simulations that used realistic load and current parameters only matched losses early in time (first 20 ns of the pulse). Attempts were made to include electrode plasma effects, but it was determined that the cell size required to avoid numerical heating was too small to reasonably run the simulation (sub-100 micron cell size).

Simulations of a much simpler geometry were run with the electrode plasma effects included. A planar diode with electric field on the order of 2 MV/cm, plasma

temperature equal to 3 eV, and plasma density ~ 5 x 10^{15} cm^{-3} had plasma expansion velocities in the range of 3 cm/μs.

2.4.3. LSP PIC Simulations by Rose

A parallel effort to simulate the convolute utilized the PIC code LSP [28],[30],[31], which also contains an energy-conserving, cloud-in-cell plasma model to avoid the numerical heating observed in the QuickSilver simulations. The LSP simulations utilize a 1D imploding cylindrical shell model for the load impedance, which is a reasonable approximation to the actual Z-pinch load; the simulated pulse risetime matches that of the experiment as well. Once the electric field in a cathode cell exceeds 240 kV/cm, electrons are explosively emitted from that cathode cell, and neutral hydrogen is desorbed into the first cell in the A-K gap. The rate at which hydrogen is desorbed is assumed to be constant for the duration of the pulse, and the amplitude is chosen such that the simulated currents best match the experimentally measured values. This typically gives a value on the order of 0.1 monolayers/ns [47].

These simulations were conducted for the following cases: a cold test with no electron or hydrogen emission, an electron emission only test, and an electron and hydrogen plasma test. The cold test, which was treated as the lossless case, delivered 18.5 MA to the load. With only electron emission, the loss current was on the order of 100 kA as has been shown in previous simulations. When hydrogen desorption is also enabled, losses on the order of 2 MA are observed, which is in good agreement with the experimental

results. A plot is shown in Fig. 2.6 comparing the load current for the electron only and the electron-hydrogen simulations.

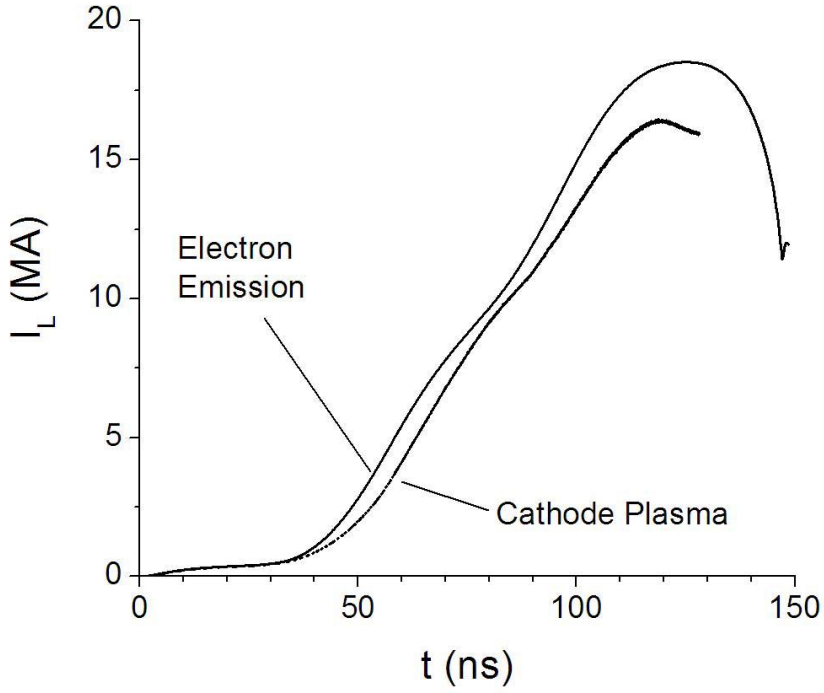

Fig. 2.6 Plot of the load current as a function of time for the electron only and the electron and hydrogen emission cases in Rose's LSP simulations of the Z-Machine post-hole convolute. The difference between the case with only electron emission and the case that includes both electron emission and cathode plasma is ~ 100's of kA for most of the pulse, and reaches 1.5 MA by peak current. (Figure courtesy of D. V. Rose et al. [30].)

The location and intensity of electron energy deposition in the post is shown in Fig. 2.8 for both the electron only and the electron-hydrogen cases. Qualitatively, both cases show energy deposition occurs in the same regions, but quantitatively there is a significant difference between the two. In the electron only case, the energy deposition is more highly concentrated at the magnetic nulls. The energy deposition is considerably more spread out in the case that includes the hydrogen plasma. This

indicates that when there is substantial plasma formation in the convolute, the magnetic nulls (shown in) are not the primary loss mechanism.

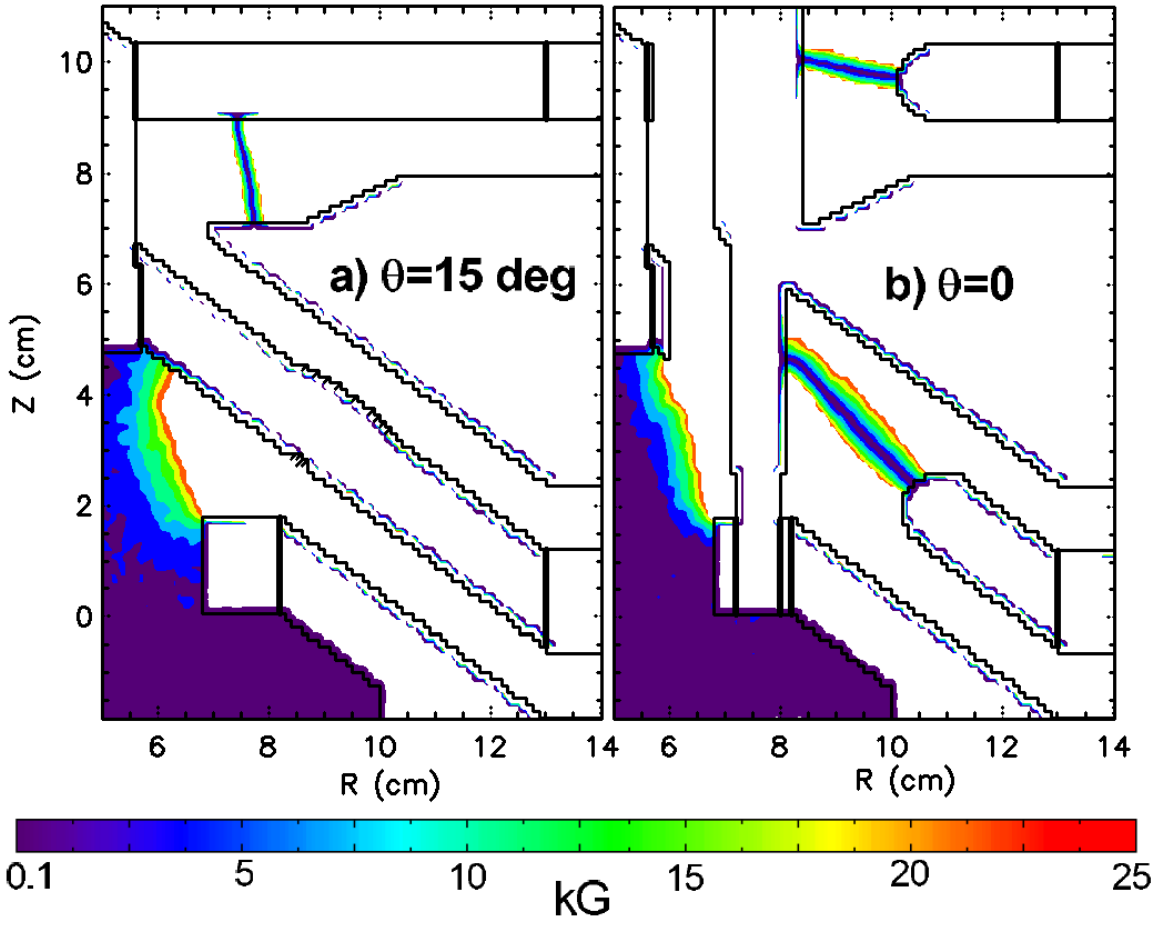

Fig. 2.7 Locations of magnetic nulls in the Z-Machine double post hole convolute. A total of 36 localized nulls and one azimuthally extended null exists. a) shows the null located in between two upper posts and the extended null. b) shows the two nulls located in the plane of the posts and the extended null. (Figure courtesy of D. V. Rose et al. [28].)

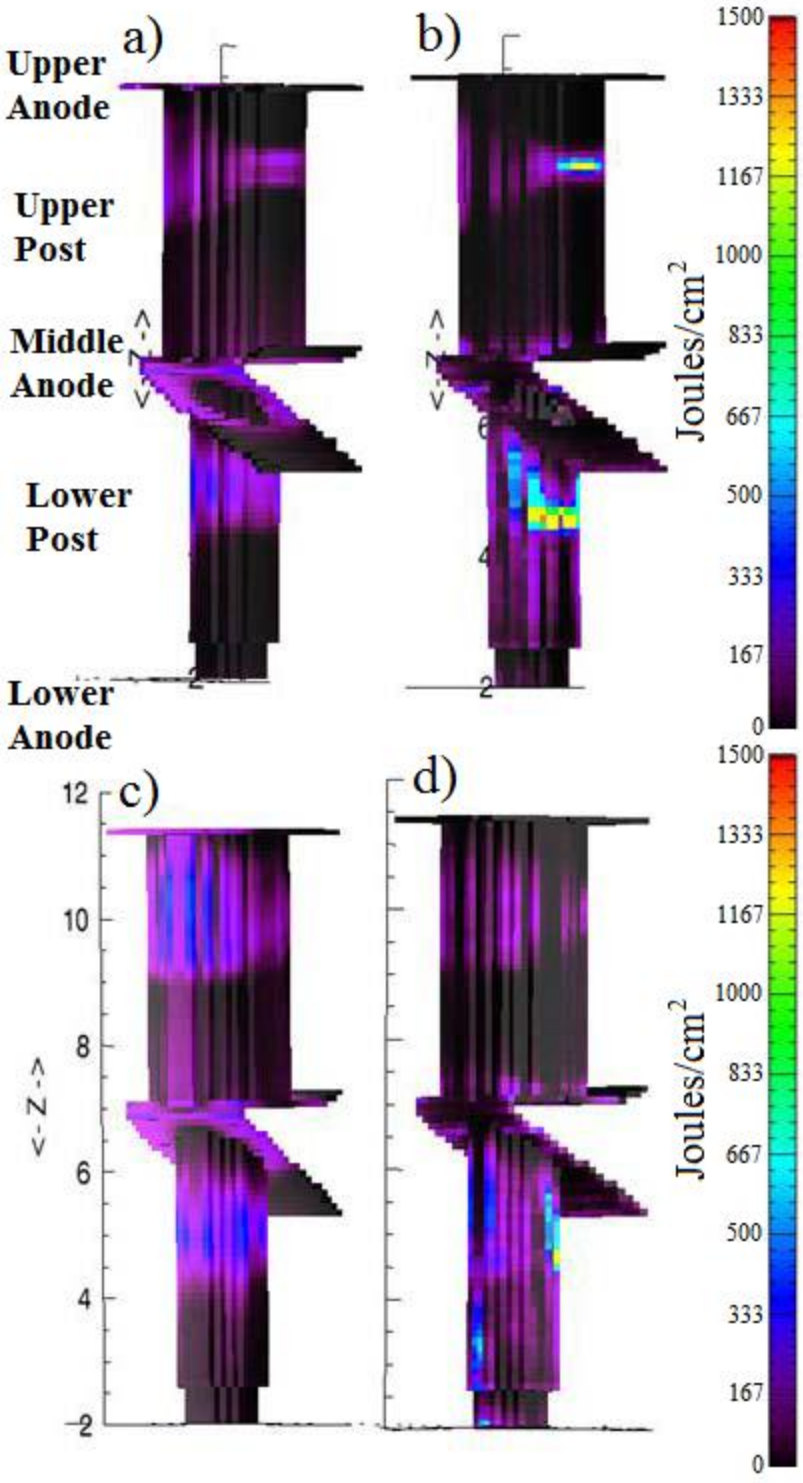

Fig. 2.8 Location of electron energy deposition in the upper and lower post at 100 ns in Rose's LSP simulations. a) and b) are the upstream view and c) and d) are the downstream view. a) and c) are for the electron only emission case, and b) and d) are from the simulation with electron and hydrogen emission. (Figure courtesy of D. V. Rose et al. [30].)

Updates to this model allowed the anode to form a surface plasma as well. When this effect is included and the hydrogen desorption rate is held constant, the loss current increased to 3.5 MA, which is no longer in good agreement with the experimental data, thus the desorption rate was decreased to ~ 0.03 monolayers/ns to resolve the issue. A plot of the loss current as a function of the hydrogen desorption rate is shown in Fig. 2.9 (simulations include electron emission and both anode and cathode plasma formation). Ideally, the desorption rate (or plasma density) would be known as a function of time and space; this would allow another parameter in the simulation to be fixed, thus making it more predictive.

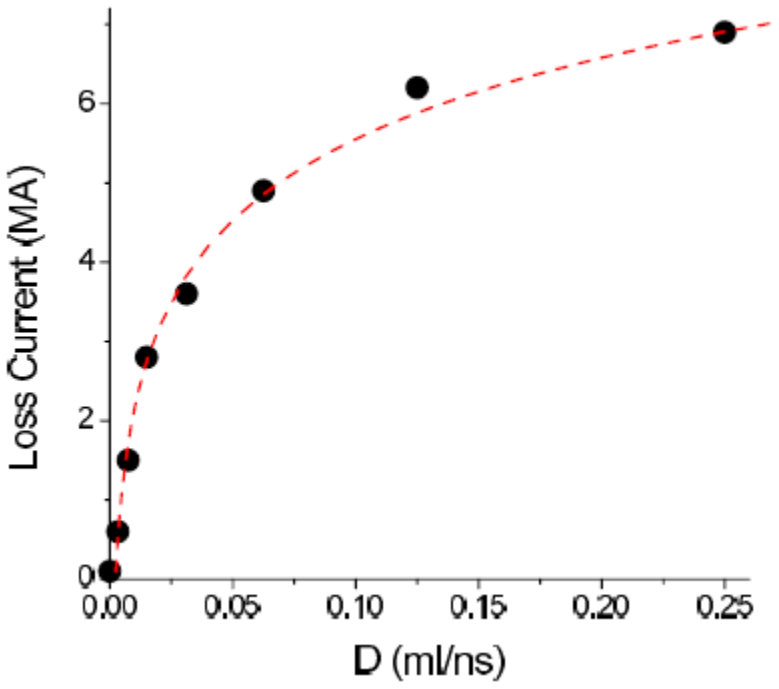

Fig. 2.9 Plot of the loss current as a function of the hydrogen desorption rate for Rose's LSP simulations of the Z-Machine post-hole convolute prior to the refurbishment of the Z-Machine. Dots represent the loss current for the simulations and the dashed line is a fit to the data. (Figure courtesy of Rose et al. [28].)

Using a slightly lower desorption rate (0.0075 monolayers/ns), a plot of the electron density, cathode plasma density, and anode plasma density just prior to peak current is shown in Fig. 2.10. The cathode plasma density is greatest within the convolute holes on the downstream side of the post, which is the location at which particles collect after streaming along the magnetic field lines that wrap around the post according to previous simulations. In these regions, the hydrogen plasma density is as high as 10^{16} cm^{-3}. Lower density plasma (less than 10^{14} cm^{-3}) persists throughout the entire A-K gap.

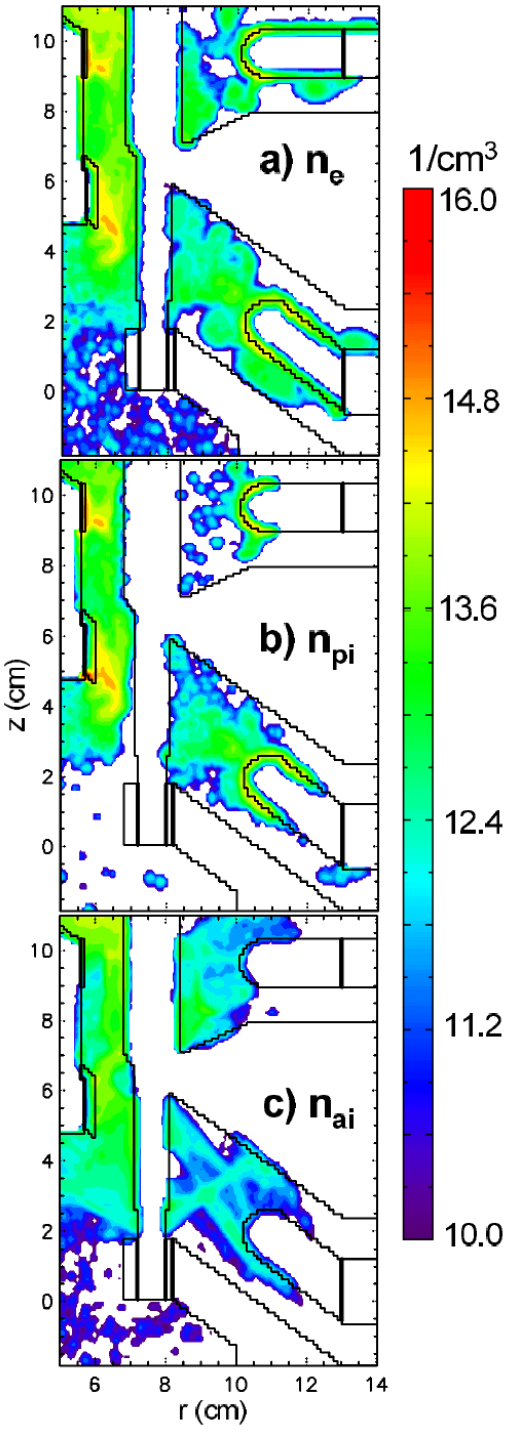

Fig. 2.10 Data from Rose's LSP simulation of the pre-refurbishment Z-Machine convolute at 120 ns with a H desorption rate of 0.0075 monolayers/ns. Data are plotted as Log(Density [cm^{-3}]). a) location of electrons, b) location of cathode ions, c) location of anode ions. (Figure courtesy of Rose et al. [28].)

The plasma that forms in the post-hole region is sufficiently dense to act as an extension of the cathode, thus the effective A-K gap decreases with time. As a result, the impedance of the convolute also decreases, which should cause the loss current to increase. The increase in loss current with time in these simulations matches the experimental results both qualitatively and quantitatively. This indicates that the loss mechanism could be space-charge limited electron emission [48] from the dense cathode plasma, which increases in amplitude as the gap reduces in size due to plasma gap closure. (No publications are available in which the plasma gap closure is extensively detailed, but estimates of the closure velocity based on Rose's simulations are 20-30 of cm/μs.)

Several modifications to the convolute hardware were proposed in order to improve performance. These new designs were tested experimentally on the Z-Machine, but ideally new designs would be validated through simulation prior to being fielded experimentally. Simulations of these geometries were performed post-shot to determine if the LSP model matched the experiment. Three new cases were tested: the "standard" ZR convolute (12 post, double post-hole convolute), "cut-away" ZR convolute (identical to standard, but the middle anode has portions removed to lengthen magnetic nulls), and a "9-post" ZR convolute.

Simulations of these three cases utilized the same model as the one used to simulate the previous Z-Machine convolute. It is interesting to note that the plasma desorption rate used for these cases was consistent with the one used in the previous simulations. This

potentially indicates that the desorption rate is a good match to what occurs experimentally, but it is surprising that the desorption would remain constant, since the power through the convolute was doubled for the ZR simulations/experiments. Regardless, the load current in the simulations matches that in the respective experiments in the Standard and Cut-Away cases; the 9-Post case seems to fail late in time as shown in Fig. 2.11. This is a good indication that the LSP model accurately depicts the behavior of the convolute designs being fielded on the present-day generation of high current pulse power drivers. In order to confidently design convolutes for future machines, it is important to experimentally benchmark the plasma conditions from the simulations.

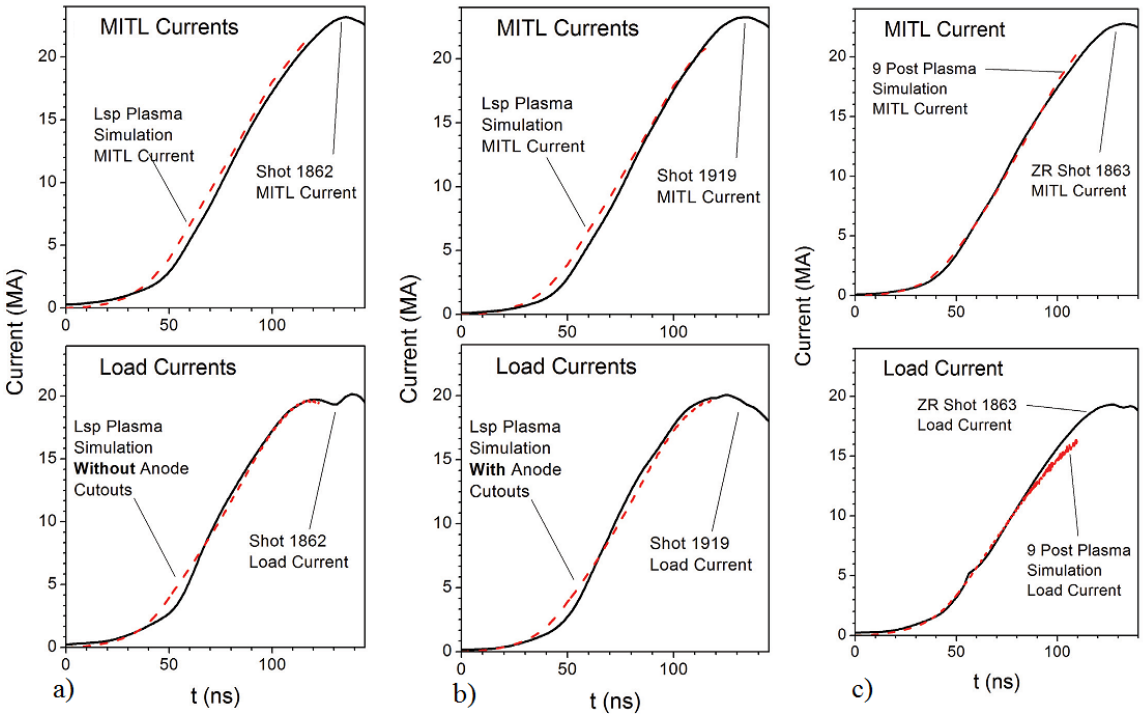

Fig. 2.11 Plots of the MITL and load currents from the a) Standard, b) Cut-Away, and c) 9-Post simulations. (Figure courtesy of Rose, et al. [31].)

CHAPTER 3

MAIZE LINEAR TRANSFORMER DRIVER FACILITY

This chapter describes the major high current facility at U of M, the Michigan Accelerator for Inductive Z-pinch Experiments (MAIZE). The MAIZE facility is based on the Russian fast Linear Transformer Driver Technology (LTD). Construction of the LTD is discussed in Appendix A. The output of the LTD is coupled to a vacuum transmission line, which propagates the pulse to the load. Results of the resistive load and transmission line tests, as well as a description of the design of the pulsed power diagnostics will be presented. Additionally, simulations of the resistive load experiments using a discrete element circuit model, and simulations of the transmission line using a Particle-In-Cell model will be discussed.

3.1 Driver Description

The Michigan Accelerator for Inductive Z-pinch Experiments (MAIZE) [13] utilizes a single 1 mega-ampere, fast Linear Transformer Driver (LTD) cavity [14-16]. This 1 MA LTD was designed and originally constructed at the Institute of High Current Electronics in Tomsk, Russia. The LTD contains 40 bricks, each consisting of two capacitors and a spark gap switch connected in series (see Fig. 3.1a). With a charge voltage of ±100 kV,

each brick is capable of delivering 25 kA into a matched resistive load. The 40 bricks in the LTD are connected in parallel (Fig. 3.1b), thus the LTD itself is capable of driving 1 MA with 100 ns rise-time into a matched resistive load.

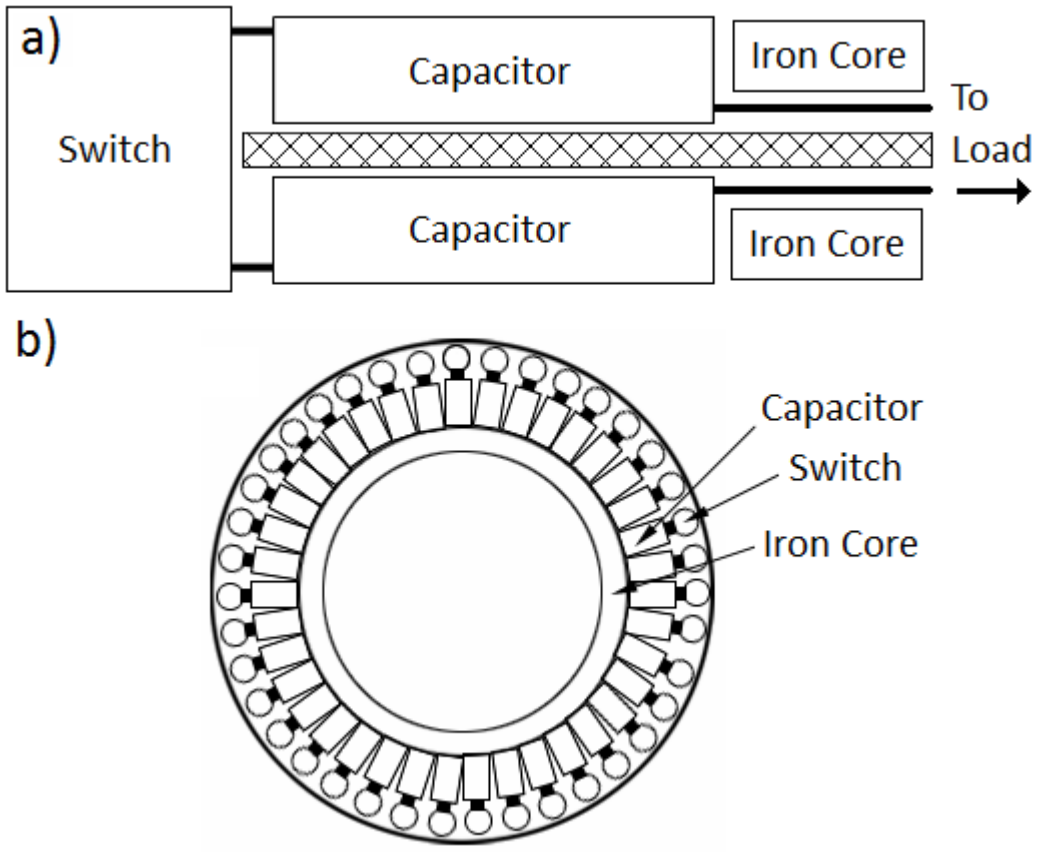

Fig. 3.1. a) R-Z schematic of a single LTD brick. The top capacitor is charged negatively and the bottom positively; when the switch closes, the voltage pulse travels from the other ends of the capacitors towards the load. A pair of iron cores is used to inductively isolate the driver from ground, which forces the pulse to pass through the load. b) R-θ schematic of the full LTD. Forty bricks are connected in parallel to sum their output current.

The LTD output pulse is applied across two stainless steel electrodes that are separated by a 22 mm thick, 45 degree slanted insulator as shown in Fig. 3.2. The electrodes are directly shorted to one another through the LTD case; however, the electrodes are inductively isolated for short pulses due to the iron cores. Prior to each shot, a relatively long (~ microseconds), relatively low (~ kilo-amperes) current is passed around the cores

in the opposite direction of the shot-current to reset the magnetic flux in the cores. During the shot, the cores inductively hold the voltage across the output electrodes until the volt-second product of the cores is reached, at which point, the cores flip, and the electrodes are shorted through the case.

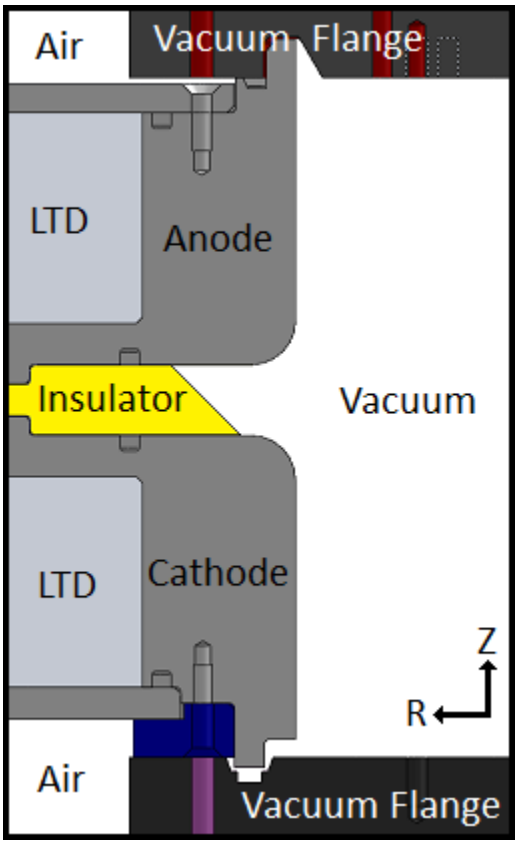

Fig. 3.2 SolidWorks model of the LTD output electrodes/vacuum section. The insulator is slanted to maximize its hold off for a given axial distance between the anode and cathode output electrodes. Vacuum flanges are directly connected to the output electrodes.

Typically, during operation of the accelerator, the insulator separating the high voltage electrodes is exposed to vacuum ($1x10^{-5}$ Torr). The insulator is slanted away from the cathode to avoid electrons cascading along the insulator surface, which would cause flash-over and short out the system. LTDs are designed to stack together by connecting the anode of one stage to the cathode of the next in order to add the output voltage from

each stage. As a result, the output electrodes of the LTD are designed to make a vacuum seal to one another or, in the case of the end cavity, to a vacuum plate. For a single cavity, as is the case with MAIZE, each electrode is capped with a vacuum plate.

A fully integrated, LabVIEW-based, computer control system has been implemented on MAIZE. The control system sets up the oscilloscopes and trigger/delay generators, controls the charging/grounding Ross relays, operates the Glassman high voltage power supplies, triggers the experiment, and performs post-shot data collection. Auxiliary systems also controlled by the labVIEW code include the compressed air system and pre-magnetization of the LTD iron cores. The automated system takes approximately 60 seconds to setup, fire a shot, and return to a safe state. Charge time to 90 kV is approximately 8 seconds. This allows for a very high shot rate into static loads.

3.1.1 Pulsed Power Diagnostics

In a pulsed power driven experiment, the current through the load and the voltage across the load are important parameters. The current through the load can be measured using a B-dot monitor, a Rogowski coil, or a resistive shunt [34]. A B-dot monitor consists of a wire loop which generates a voltage across the terminals that is proportional to the time derivative of the current. B-dot monitors are highly sensitive to position and angle. A Rogowski coil consists of a loop of wire with another wire wound around it. The two wires are attached at one end. The signal generated by a Rogowski coil is also proportional to the time derivative of the current. Rogowski coils are typically more sensitive than B-dot monitors (generate a larger signal) and are less

affected by position, but they do require that the entire measured current pass through the coil. The time response of a Rogowski coil is dependent on the length of wire used to construct it, thus, typically a Rogowski coil risetime is greater than 1 ns, whereas a B-dot can respond to sub-ns signals. A resistive shunt generates a voltage due to the current passing through it. In order to get an accurate measurement, all current must pass through the shunt, or have a well-known distribution. Typically, the shunts are on the order of 1 mOhm, which for a 1 MA pulse generates a 1 kV signal. Thus shunts are more useful in lower current pulsed power experiments.

Pulsed power diagnostics for the resistive load and transmission line tests included two non-concurrent sets of B-dot monitors (BD-01 or BD-01-Mod-A and BD-03), a set of six Rogowski coils (RC-01), and a NorthStar high voltage probe. Additional diagnostics attempted included a variety of resistive dividers and a number of D-dot monitors; however, none of these voltage diagnostics provided useful signals. The following subsections describe the construction of the diagnostics as well as their placement in the experiment.

3.1.1.1 Single Loop B-Dot Monitor

A set of four B-dot monitors (BD-01) were used for the resistive load tests and some of the transmission line tests. The monitors were azimuthally evenly spaced at a radius of 794 mm in the anode vacuum plate. These B-dot monitors consist of a copper rod with a piece of RG-405 semi-rigid coaxial cable on axis. At one end the cable connects to a

hermetically sealed SMA vacuum feed through. At the other end of the cable a 4 mm x 2.5 mm rectangular loop of wire connects the center pin to the ground shield. The wire loop is coated with an insulating varnish to avoid shorting to the 5.75 mm diameter hole in the 31.8 mm thick aluminum vacuum flange in which the monitor is embedded. The diameter of the copper rod is 5.5 mm, which requires that the loop be approximately centered in the hole. The length of the monitors was set so the loop is approximately flush with the surface of the anode. These B-dot monitors were later modified (BD-01-Mod-A) by encasing the wire loop in Torr-Seal vacuum epoxy. This was done in an attempt to reduce the spurious signals generated by electron interactions with the probes.

3.1.1.2 Double-Loop B-Dot Monitor

An opposite-polarity double loop B-dot monitor (BD-02) was fielded on some of the transmission line tests in place of the BD-01-Mod-A B-dot monitor with the worst performance. The base of this monitor consisted of a brass plate with an o-ring groove and two through holes. Two pieces of RG-405 semi-rigid coaxial cable were soldered in the holes with approximately 20 mm on the vacuum side and 50 mm on the air side. On the air side, a female SMA connector was soldered to each coaxial cable. On the vacuum side, one side of a 2 mm x 4 mm rectangular wire loop was soldered to the center pin of the coaxial cable, and on the other side was soldered to the ground shield of the coaxial cable. The loops were connected in such a way that they would generate opposite

polarity signals when detecting a time changing current. This allowed one of the signals to be inverted and added to the other during data analysis, thus cancelling the common mode noise to first order. The wire loops were coated with Torr-Seal to reduce electron interactions with the probe. This monitor did not prove successful due to a weak signal, but was a useful step in developing the BD-03 monitors.

3.1.1.3 Single-Loop Dual-Output B-Dot Monitor

A single loop dual output B-dot monitor (BD-03) was fielded on some transmission line test shots and during the planar thin foil magneto-Rayleigh-Taylor instability measurements being conducted by Zier, et al. on the MAIZE facility. These B-dot monitors were not designed to be vacuum-tight, and as such could not be fielded at the same location as the previously mentioned monitors. These monitors were fielded at the same azimuthal positions as the other monitors, but at a radius of 432 mm.

These monitors consisted of a brass base plate with a single hole, a 5.6 mm diameter copper tube, a copper end cap with two holes, and a single piece of RG-405 coaxial cable. The ground shield was removed from the center 11 mm of the cable. The non-shielded piece of the cable was bent into a 4 mm x 3 mm loop, and the ends of the cable were fed through the two holes in the end cap. The ground shields were soldered in place and the end cap was soldered into the end of the tube. The tube was soldered to the base plate such that 19.5 mm of the tube protruded from the surface of the plate. An extension tube (with a vent hole) was soldered to the other side of the end cap and Torr-

Seal was used to pot the end of the monitor. A 5 micron thick Ni-Chrome foil was attached to the open end of the extension tube. The Ni-Chrome foil was chosen because it is thin and made from a highly resistive material, thus the electro-magnetic fields will still be detected by the probe, but any static charge due to electron strikes on the probe will be conducted away. A solidWorks model of the monitor is shown in Fig. 3.3.

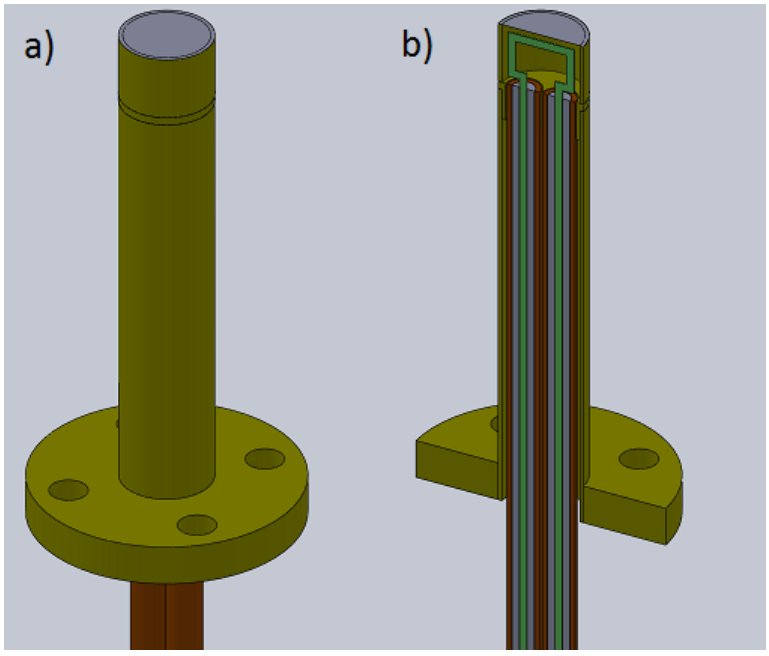

Fig. 3.3 SolidWorks model of the BD-03 B-dot monitor. a) BD-03 B-dot monitor designed to measure the MITL current on MAIZE. The loop is entirely encased in a copper tube, the end of which has a 5 micron thick piece of NiChrome foil epoxied to it. b) A cut away view of the BD-03 B-dot monitor. Two RG-405 semi-rigid coaxial cables run down to the end of the tube; the center conductors of these cables are connected by a loop of wire, which generates the signal of interest.

3.1.1.4 Rogowski Coils

Six Rogowski coils (RC-01) were placed around individual load resistors to monitor the current through the load. The Rogowski coils were made from RG-405 semi-rigid coaxial cable with a length of the outer conductor removed. Magnet wire was wound 5

times around the bare insulator of the coaxial cable and soldered to the center pin at one end and the ground shield at the other end. The end of the cable was wrapped around a 19 mm diameter rod and glued in place. A precision 50 ohm resistor was connected in series with the coil in order to match it to the impedance of the cable. Due to the resistance variation in the transmission line load resistors, a weighting factor was assigned to each coil based on the resistor it was monitoring.

3.1.2 Resistive Load Tests in Atmospheric Pressure SF_6

The MAIZE vacuum plates were both machined with a 40 x ¼-20 bolt circle at a radius of 783 mm. These holes were used to mount the resistive load to the vacuum plates, which acted as the conducting connection to the LTD high voltage electrodes. The resistive load consisted of twelve ~ 1 ohm resistors (63 g/100 mL potassium bromide solution, 50.8 mm diameter, 82.5 mm length) connected in parallel. The resistors were connected as shown in Fig. 3.4. The overall resistance of the load was estimated to be 84 mOhm, and the inductance of the load was estimated to be 5.9 nH using

$$L = 0.002 * l * \left(ln\left(\frac{\rho_1}{a}\right) + \frac{1}{n} * ln\left(\frac{a}{n\rho}\right) + \frac{1}{4n} - 1 \right) \tag{3.1}$$

where a is the radius at which the resistors are located, ρ_1 is the radius of the LTD electrodes, ρ is the radius of the resistors, n is the number of resistors, and l is the length of the geometry [49].

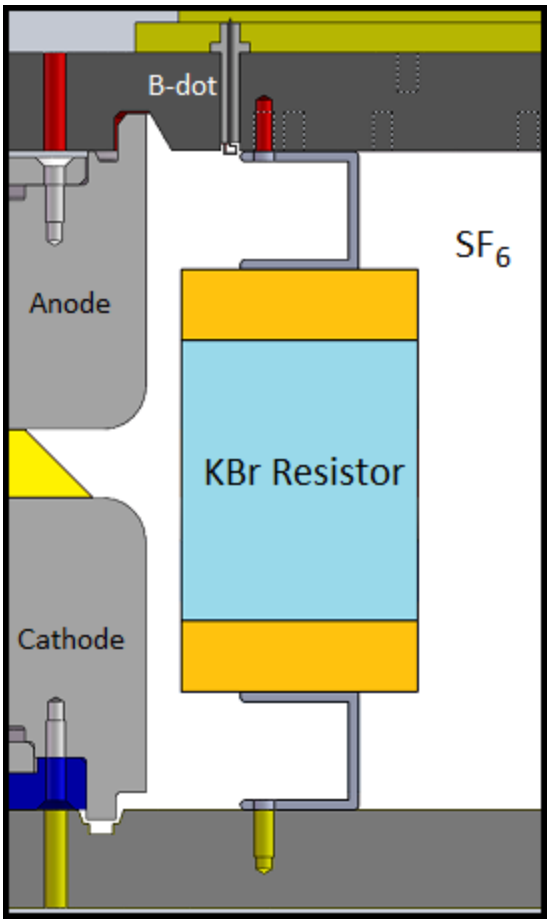

Fig. 3.4 SolidWorks model of an R-Z cut of the resistive load. The KBr resistor connects the top vacuum plate (anode) to the bottom vacuum plate (cathode). A B-dot monitor is inserted in the top vacuum plate to measure the current through the resistor. The vacuum region was filled with atmospheric-pressure SF_6 for these experiments.

Diagnostics for the resistive load tests included 4 B-dots (BD-01) and a NorthStar high voltage probe (PVM-5 adapted to support a 50 ft cable). The B-dots were located every 90 degrees, and the load resistor placement was chosen in such a way that each B-dot was located directly in front of a load resistor as shown in Fig. 3.5. This was done to ensure that the current that passed the B-dot hole would be perpendicular to a vector normal to the loop area, which results in the largest signal. The NorthStar high voltage probe was connected to the cathode side of the load via a 1.2 m high voltage cable,

which connected to a 100kV DC high voltage vacuum feed through, to which the probe was connected.

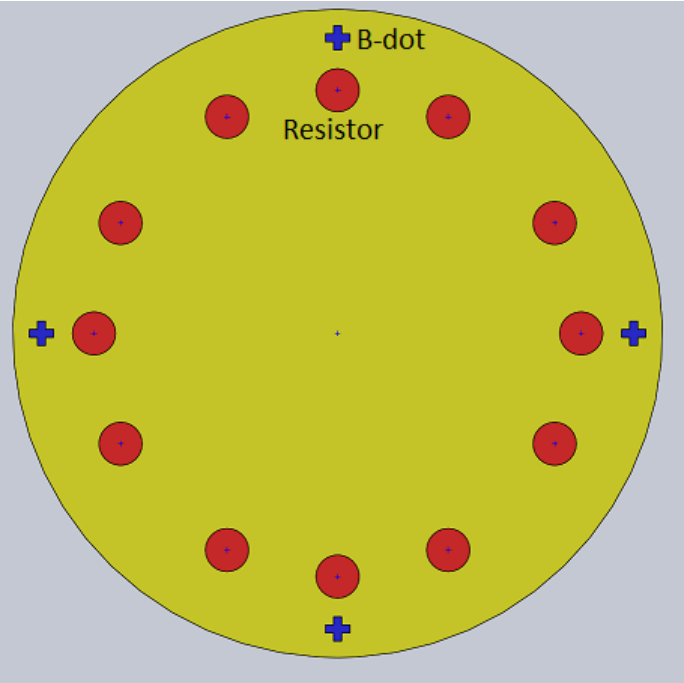

Fig. 3.5 Schematic diagram showing the location of the B-dot monitors (blue crosses) and the load resistors (red circles). There were 40 evenly-spaced holes for the load resistors and 12 resistors, which required the resistors to be slightly asymmetrically placed. Ideally they would be spaced every 30 degrees, but they were placed in a repeating pattern of 27, 27 and 36 degrees.

High voltage tests with the resistive load were conducted with an atmospheric-pressure SF_6 fill rather than vacuum. The nature of the resistive load prohibited vacuum operation. The 4 B-dot traces were integrated and then averaged. The average trace was scaled such that the peak amplitude matched the peak voltage divided by the resistance of the load

$$I_{peak} = V_{peak} / R_{load} . \tag{3.2}$$

The voltage traces had a significant level of ringing superimposed on the actual voltage signal in the higher charge-voltage cases, so the B-dot calibration factors were

determined for the 70 kV case and held constant for the 80 kV and 90 kV measurements. This is likely the result of reflections on the 1.2 m long connection between the high impedance probe and the low impedance resistive load. The period of the oscillations is 34 ns, which corresponds to a 17 ns one-way transit time. This transit time can be accounted for by the length of the cable, the feedthrough, and the electrode connection back to the other side of the load resistor. Traces from operation at charge voltages of +/- 70 kV, 80 kV, and 90 kV are shown in Fig. 3.6a-c.

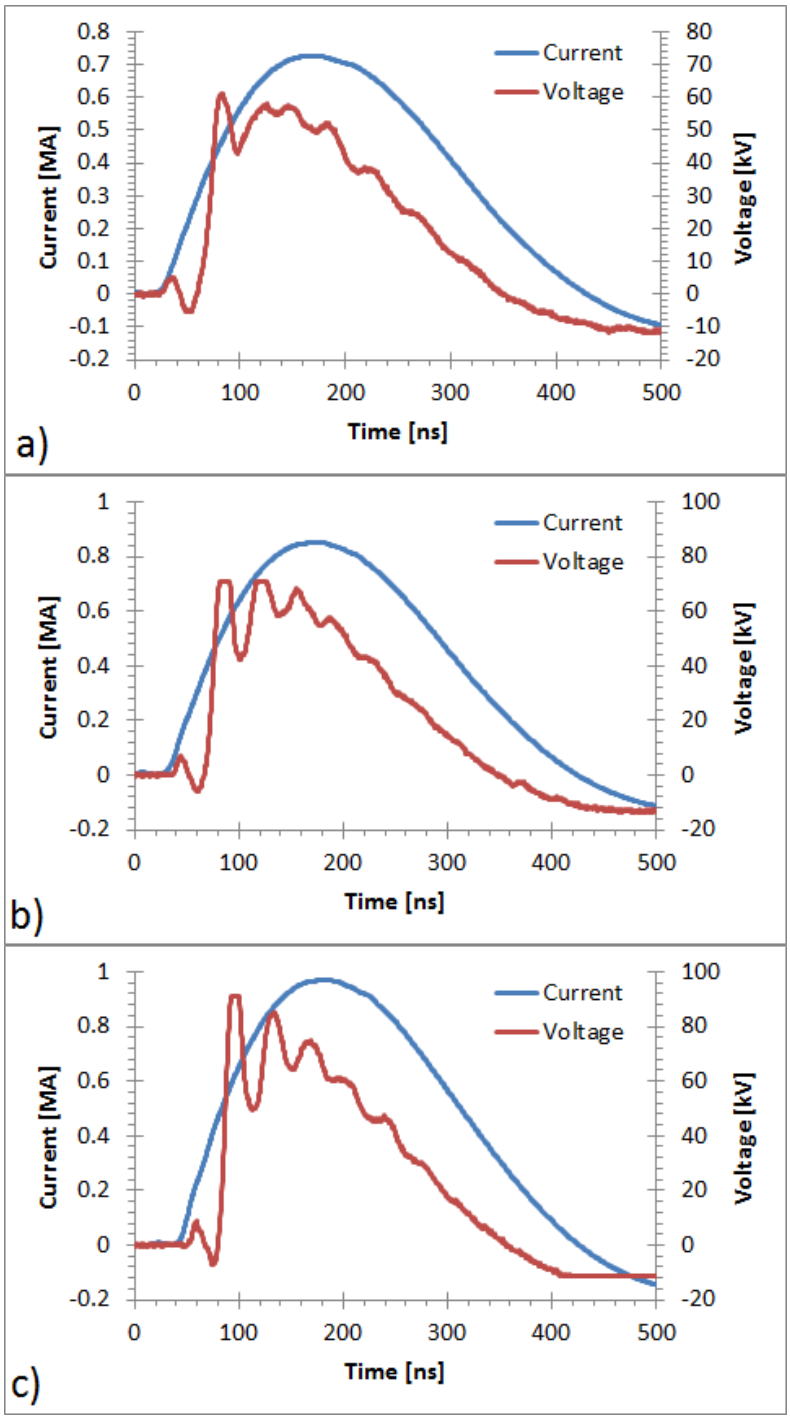

Fig. 3.6 Traces from the MAIZE resistive load tests; a) 70 kV charge voltage, b) 80 kV charge voltage, c) 90 kV charge voltage. In the 80 kV and 90 kV cases there is a significant level of ringing on the voltage signal; these fluctuations were clipped because they exceeded the maximum peak to peak range of the oscilloscope (100 V).

Operation of the LTD is possible without resetting the iron cores, but at the cost of significantly increased high voltage ring back. A comparison of the current traces with versus without the core reset is shown in Fig. 3.7. Without the core being reset (no Premag pulse), the peak amplitude of the current was reduced by more than 10%, and the current ring back was over 60% of the peak amplitude.

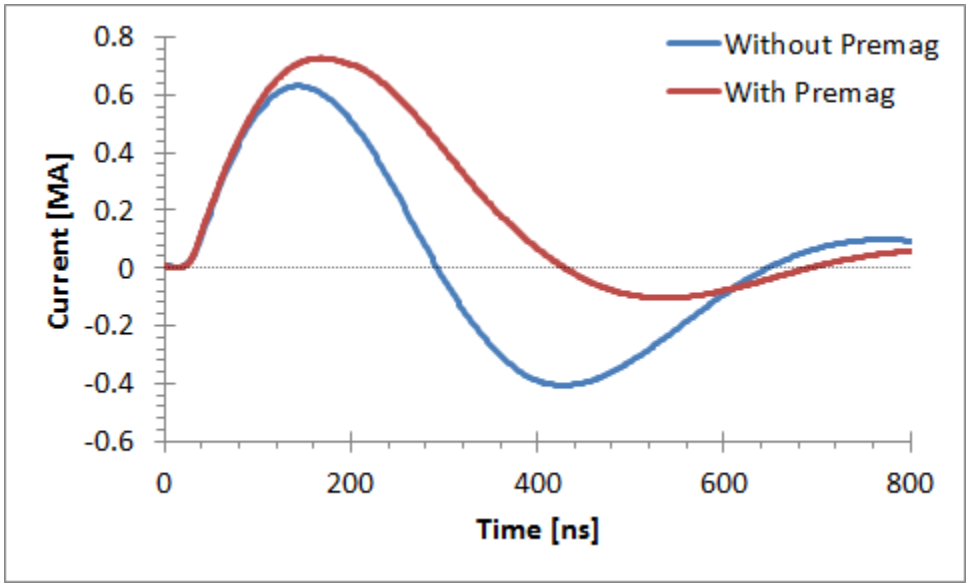

Fig. 3.7 Plot of the LTD current with versus without resetting the iron cores. Both shots used +/-70 kV charge voltage. In the case of no core reset, the peak current was lower and the amplitude of the ringing on the pulse was significantly greater than in the case where the core was reset.

3.1.3 PSpice Simulations

A discrete element circuit model of MAIZE has been developed using PSpice. The driver model contains 40 bricks in parallel. Each brick contains two oppositely charged capacitors and a switch in series. Switches in the bricks are closed in two 20 switch sets, temporally separated by 10 ns to account for the finite jitter in switch triggering.

The inductance of an individual brick has be estimated to be 232 nH (switch = 120 nH, capacitors = 25 nH each, the remainder due to connections between the components).

Since all of the bricks are identical, the inductance from each was combined in parallel to give roughly 6 nH. The outputs of all the bricks were combined in parallel and then passed through the 6 nH total internal inductance (3 nH on the anode side and 3 nH on the cathode side). The anode and cathode sides are joined through a resistor and inductor, which are set to the measured/calculated values for the load. A schematic of the circuit is shown in Fig. 3.8.

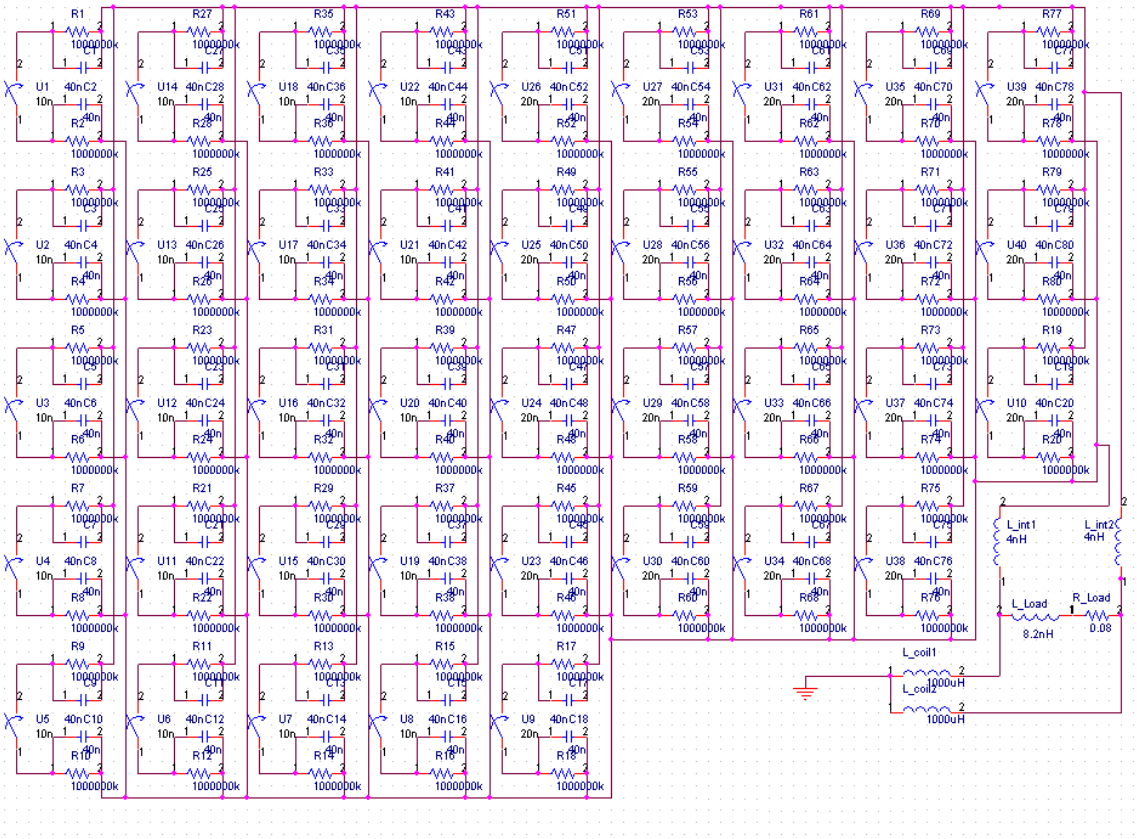

Fig. 3.8 Schematic of the circuit used in the PSpice simulations of the LTD resistive load tests. Forty bricks were connected in parallel and then passed through an internal inductance (varied from 5 nH to 8 nH, estimated to be 6 nH) and a load resistance (varied from 80 mOhm to 100 mOhm, measured to be 84 mOhm) and inductance (varied from 5 nH to 9 nH, calculated to be 5.9 nH). The measured/estimated/ calculated values for the resistance/inductances provided a reasonable match to the experimentally measured current.

The anode and cathode are coupled to ground through two large (~ mH) static inductors, which represent the iron cores. This is a good approximation during the rise of the pulse and through peak current, but it becomes a poor approximation when the cores saturate on the fall of the current. This is not particularly concerning, as most of the experiments planned for MAIZE take place during the rise of the current. Additionally, any dynamic load will cause the experimental current to deviate from the simulation long before the effect of the cores flipping is observed.

The critical values in these simulations were the current pulse shape and peak amplitude. An overlay of the simulated load current and a typical experimental trace is given in Fig. 3.9. The experimental and simulated traces match one another extremely well during the first 120 ns of the pulse (through the peak current). Later in time, the simulation over-estimates the current in the system. This is expected because the simulation does not take into account the time-changing inductance of the iron cores. The traces in Fig. 3.7 clearly show that in the case where the cores are not inductively isolating the driver from ground, the current drops more rapidly. Based on the accuracy of this model (through the interesting portion of the current pulse), the I-V characteristics of future static loads can be accurately estimated.

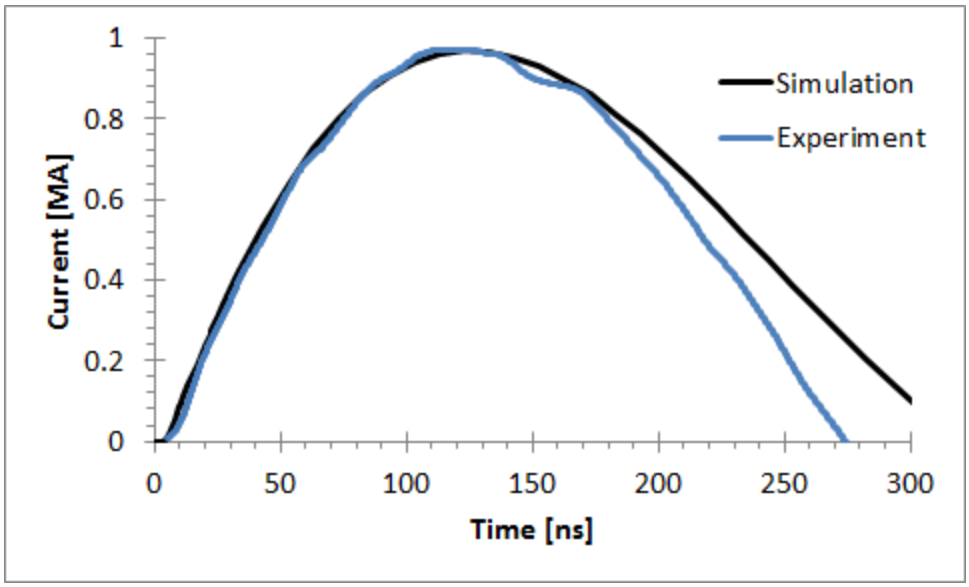

Fig. 3.9 Plot showing the experimental and simulated current for the resistive load experiments on MAIZE. The two signals overlay nicely through the current rise and peak current, but during the fall of the current, the experimental current drops much faster than the simulated current. This is due to the simulation not taking into account the time-changing inductance of the iron cores.

3.2 Transmission Line Design

The driver in MAIZE connects directly into a vacuum transmission line ($1x10^{-5}$ Torr) with no intermediate storage capacitors or pulse forming lines. The transmission line used in MAIZE was designed to keep manufacturing costs low, while maintaining an acceptable inductance. The relatively low voltage of MAIZE requires as low an inductance as possible in order to deliver the maximum current to the load. The transmission line is initially a 15 mm coaxial gap, which transmits the pulse up so a zero-degree diagnostic view of the load is possible. The coaxial line feeds into a nominally 11 mm gap, radial transmission line; Fig. 3.10 shows the coaxial and radial transmission line geometries. The radial line can couple to a variety of loads including a

conical feed to a wire array or thin foil, and a single post-hole convolute. The inductance of each section of the transmission line was calculated using the following equations

$$\text{Coaxial: } L[nH] = 2 * h[cm] * ln\left(\frac{R_2}{R_1}\right) \tag{3.3}$$

$$\text{Radial: } L[nH] = 2 * g[cm] * ln\left(\frac{R_2}{R_1}\right) \tag{3.4}$$

where h is the height of the coaxial cylinders, g is the gap between the radial plates, R_2 is the outer radius of the transmission line, and R_1 is the inner radius [50],[17].

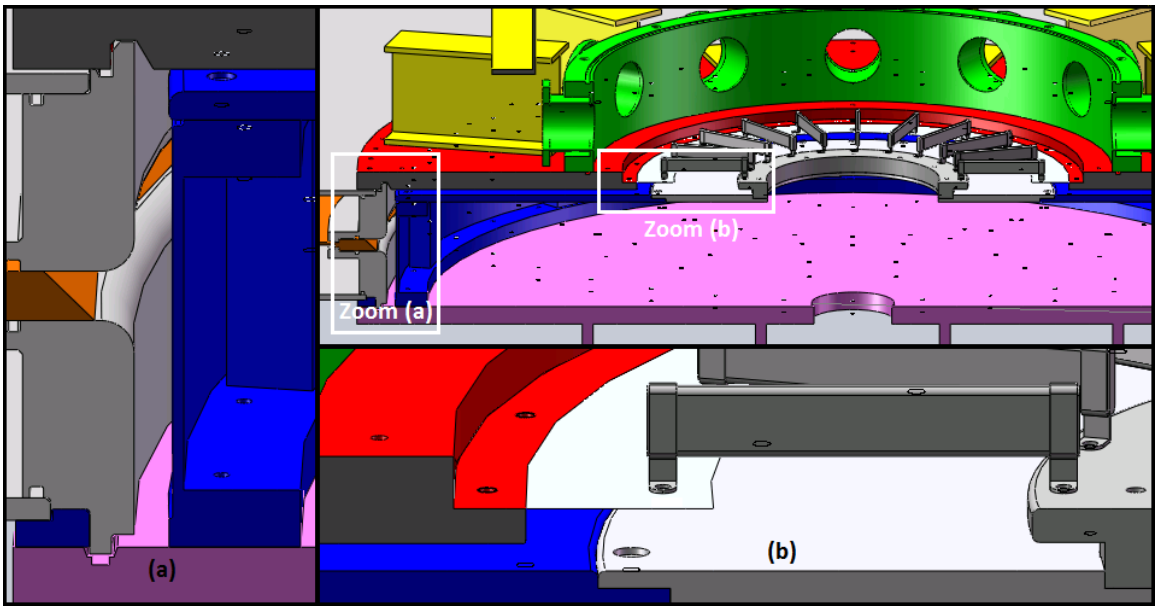

Fig. 3.10 The full transmission line is shown in the upper right image. Regions boxed in the upper right image are shown in insets (a) and (b). (a) shows the output of the LTD and the coaxial portion of the transmission line; (b) shows some of the radial transmission line and how the vacuum-resistive load is connected to the transmission line. The cathode is represented in blue and the anode in red.

When the system is under vacuum, the top vacuum plate, which also acts as the anode side of the transmission line, has approximately 50,000 pounds of atmospheric force on it. Despite the 30+ mm flange thickness and the array of I-beam supports, the flange still

bends under the atmospheric force. The deflection has been measured at a radius of 432 mm to be 1.5 mm. Thus the transmission line A-K gap reduces to 9.5 mm at this radius.

The transmission line inductance up to the load insert has an upper bound of 2.86 nH, assuming zero transmission line deflection. Assuming a linear transition from 11 mm at a radius of 794 mm to 9.5 mm at a radius of 432 mm, the inductance is 2.75 nH. In either case, load hardware designs with inductance in the 4-7 nH range will not significantly affect the peak current or rise-time.

3.2.1 Transmission Line Tests into Vacuum Resistive Load

Transmission line tests of MAIZE were conducted into a resistive load. The load consisted of a radial array of twenty-2 ohm ± 20% resistors in parallel; the total load resistance was 0.10 ohms. The resistors were Kanthal Globar ceramic resistors (6″ long, capable of dissipating 800 J/pulse). A set of plates were machined to allow the transmission line to be coupled to the resistors as shown in Fig. 3.11. This load hardware had a 3.96 nH inductance, which gave a total transmission line plus load inductance of 6.71 nH.

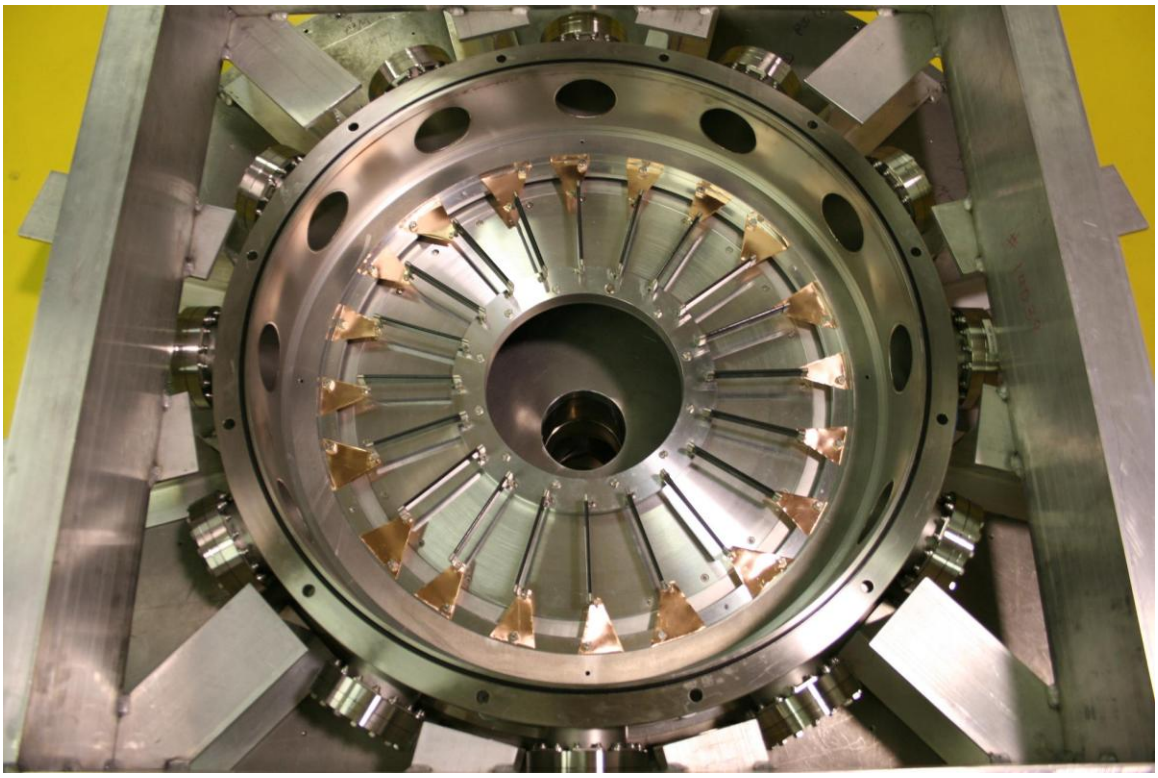

Fig. 3.11 Top down image of the MAIZE transmission line resistive load. Twenty resistors (2 ohms each) were connected in parallel to create a 0.1 ohm vacuum resistive load.

The BD-01-Mod-A B-dot monitors were used to monitor the current at the start of the transmission line. These monitors were the same ones used in the resistive load tests, but the loops were potted in Torr-Seal in an attempt to reduce the spurious signals generated by electron interactions with the probes. These monitors were located at the same 794 mm radius as in the resistive load tests. The signals recorded from these probes were processed in the same manner as in the resistive load tests. It should be noted that the calibration factors determined from the resistive load tests were not valid for the transmission line tests due to the vastly different geometry.

The RC-01 Rogowski coils were located around approximately every third load resistor (six coils for 20 resistors). Thus, the coils were used to measure a fraction of the load

current. The recorded signals were integrated and scaled according to the calibration factor determined using a calibration source. The signals were then weighted according to the resistance of the load resistor they were monitoring. The weighted signals were averaged to get the load current.

The BD-01-Mod-A and RC-01 probes were fielded on the same set of shots. A plot showing the traces from both diagnostics on a typical shot is shown in Fig. 3.12. The two methods of measuring the current match one another in amplitude to better than 5%, which is within the scatter of both the Rogowski coil and B-dot monitor measurement. The during most of the risetime, the signals match exactly, but as time progresses, the B-dot signal develops a slightly extended shape and deviates from the Rogowski coil signal. This is likely due to charge build-up on the epoxy that coated the B-dot monitors.

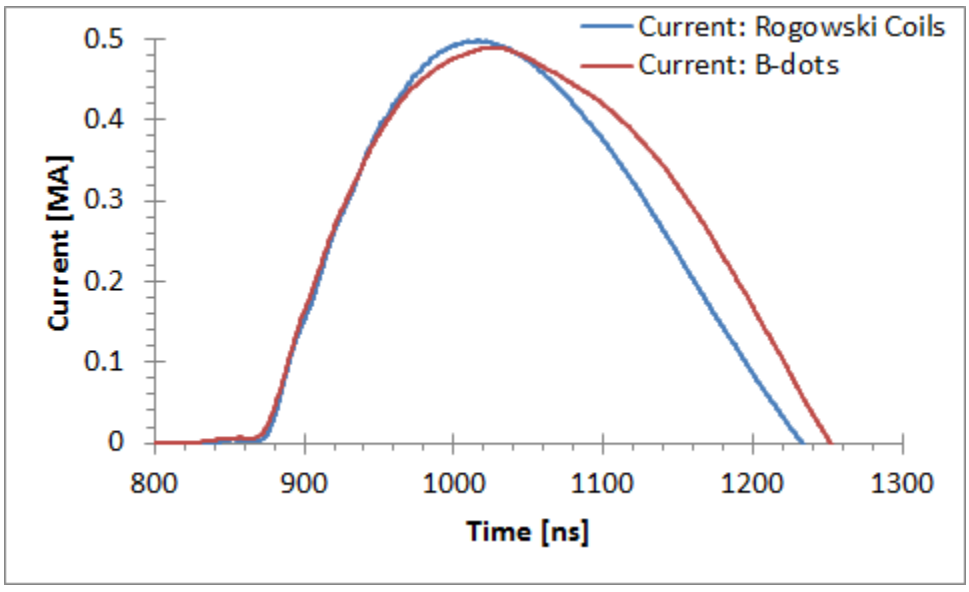

Fig. 3.12 Comparison of the current as measured by the set of six Rogowski coils at the load and the four B-dot monitors at the output of the driver on the same shot. The signals match very well for the rise of the pulse, but just before peak amplitude the B-dot signal deviates from the Rogowski signal.

In addition to the pulsed power diagnostics, a visible open pinhole camera was fielded during the transmission line tests. The purpose of this diagnostic was to look for light emission at the load, which indicates plasma formation. Ideally this type of load would not produce any emission. For a charge voltage of +/- 70 kV, very little light is observed as shown in Fig. 3.13a. When the charge voltage is increased to +/- 90 kV, more emission is observed as shown in Fig. 3.13b. The light is primarily observed at the metal ends of the load resistors, indicating plasma corona. Additional light observed at the lid of the vacuum chamber seems to indicate electron flow in the transmission line is passing through the load to strike areas throughout the vacuum chamber. When dielectrics were placed across the load anode-cathode gap (i.e. a resistive divider encased in a Lucite block), very bright plasma formed on the underside of the object as seen in Fig. 3.13c. This provides additional support for the argument that electron flow is reaching the load.

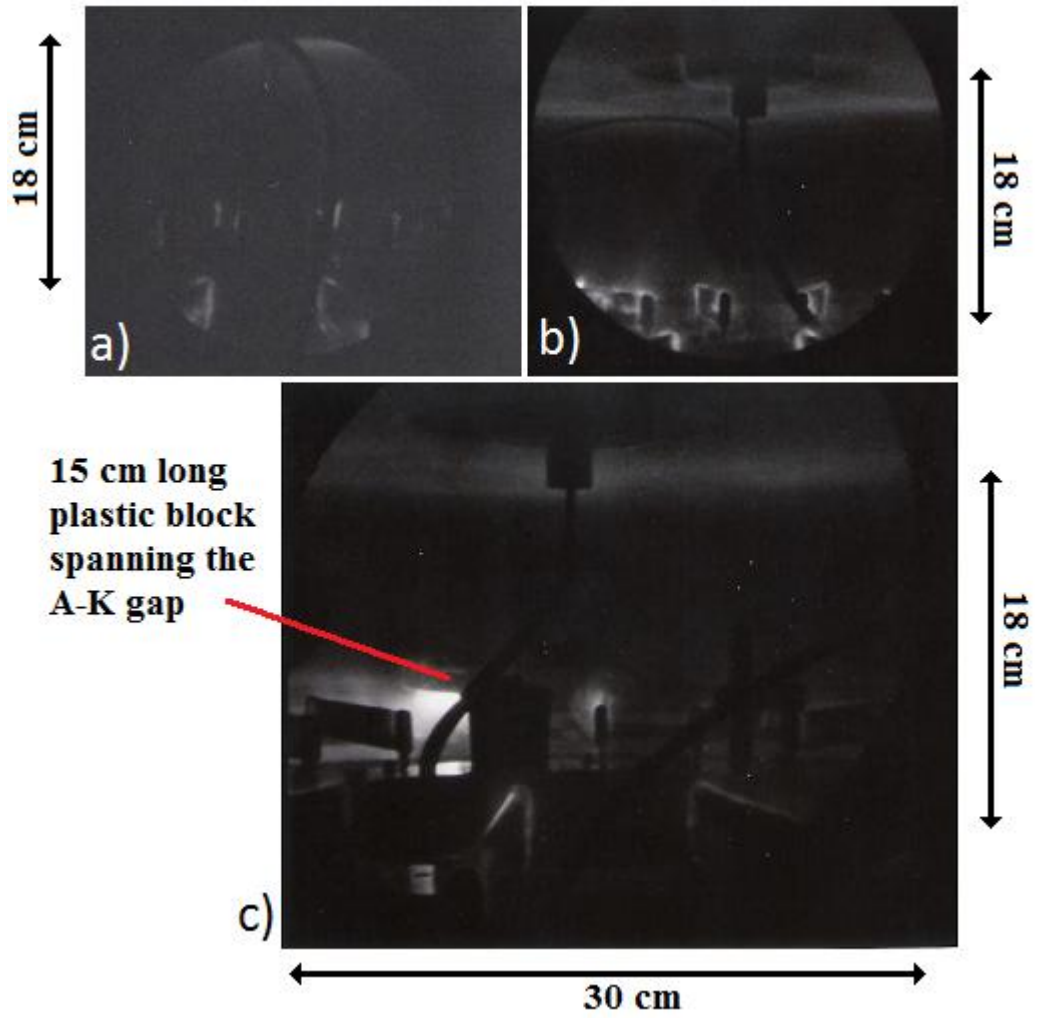

Fig. 3.13 Open pinhole images of the transmission line tests. a) image of the load during a 70 kV shot. The bright regions indicate emission and are located at the metal ends of the load resistors. The glowing is likely the result of coronal plasma. b) image of the load during a 90 kV shot. The ends of the resistors glow significantly more brightly in this shot; the vacuum chamber lid appears to be glowing as well, which could be due to significant electron flow striking its surface. c) image of the load during a 70 kV shot in which a resistive divider encased in a block of plastic spans the A-K gap at the load. The underside of the plastic block emits very brightly, which could be the result of electron flow striking the block and forming plasma.

On a subsequent set of shots, the BD-03 B-dot monitors were used to measure the current just downstream of the load resistors. These monitors were calibrated using the same system as the Rogowski coils. In the same manner as the other current monitors on previous shots, the signals were integrated and the appropriate scaling factor was applied to the traces. On this set of shots there were no other current monitors fielded.

These transmission line test shots were particularly important because they employ the current monitors that are presently being used for the thin-foil magneto-Rayleigh Taylor instability experiments. A plot comparing a shot with the resistive load and one with a MRT foil load is shown in Fig. 3.14. The resistance of the foil load is significantly less than that of the resistive load, thus the peak current is greater in the foil load case. The trace in the foil load case has a dip that likely corresponds to the time at which the foil has been accelerated to the center of the machine. This is the point of highest inductance, which would result in a dip in the current.

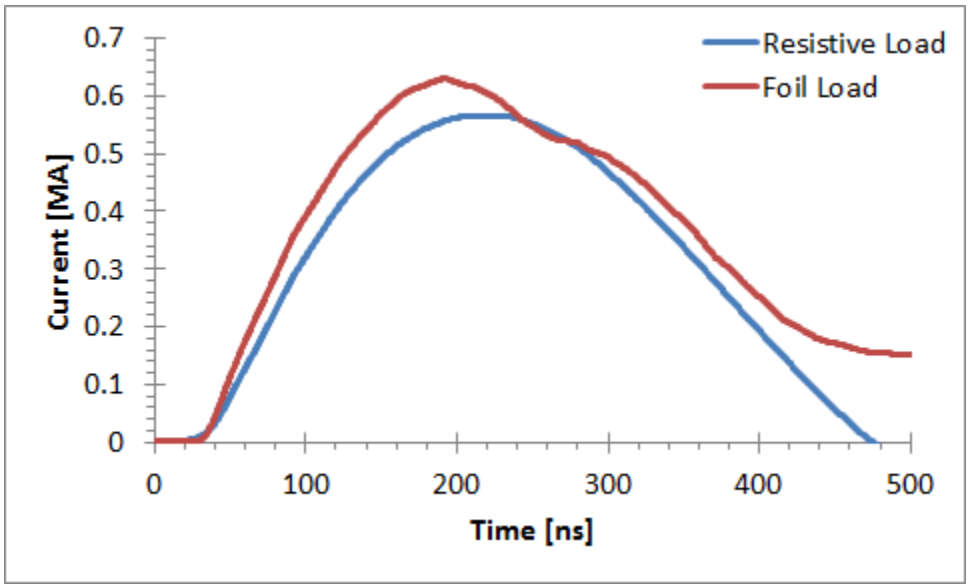

Fig. 3.14 Current traces obtained with the BD-03 model B-dot monitors for a resistive load shot (shot 275) versus a foil load shot (shot 321). The features on the foil load shot can be explained by the time changing inductance of the load. LTD charge voltage = +/- 70 kV.

3.2.2 Particle-In-Cell Simulations

Simulations of the transmission line tests on MAIZE were conducted using MAGIC PIC 3D [45]. A 100kV, 100 ns rise-time, 200 ns fall-time pulse was applied in the simulation at the vacuum insulator of the generator (see Fig. 3.15 for the simulation geometry). A

100 mOhm cylindrical conductance was used to simulate the load resistor array. The cathode surfaces were allowed to explosively emit uniformly throughout the transmission line when the electric field at the electrode surface reached 50 kV/cm. Cases were also run without emission and with the emission threshold set at 75 kV/cm and 100 kV/cm.

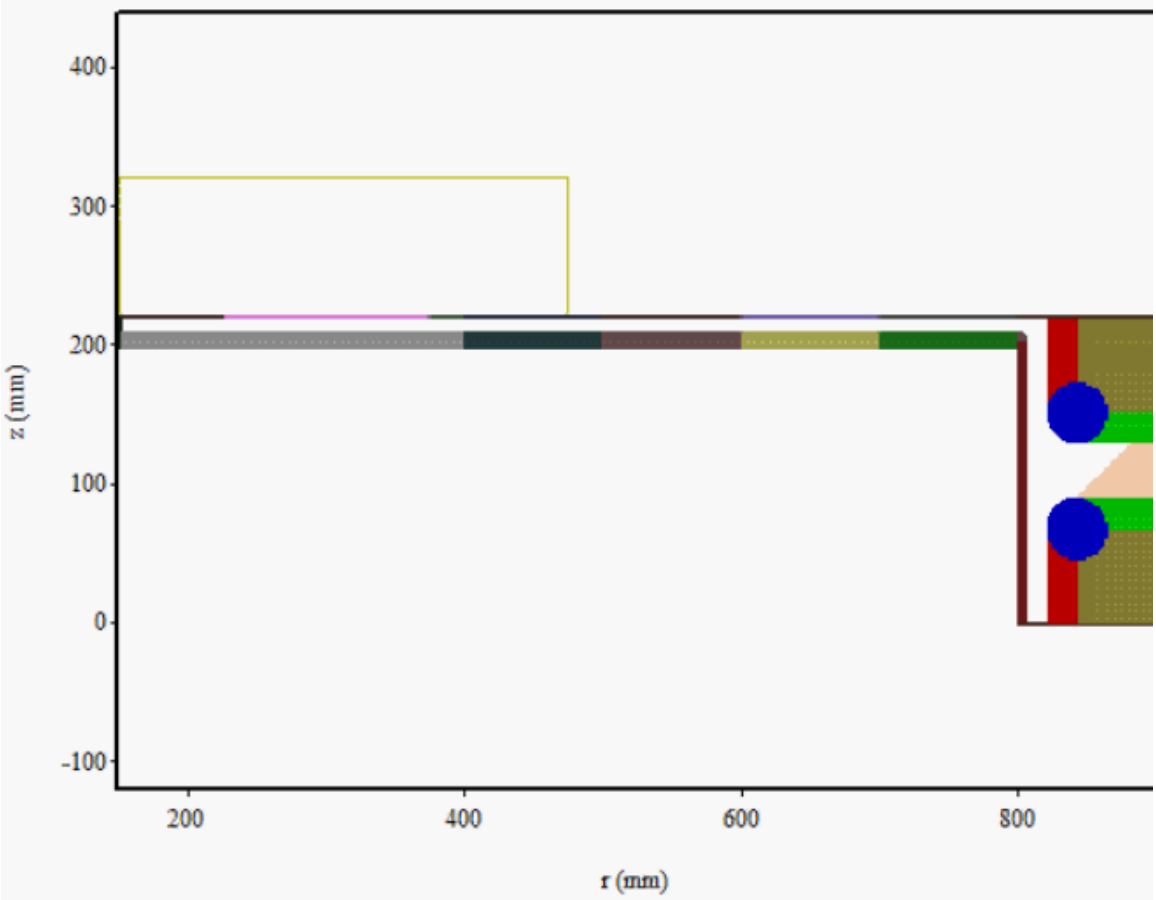

Fig. 3.15 R-Z cut of the simulation geometry used in the MAGIC PIC 3D simulations of the LTD and transmission line.

The input current and voltage were monitored at the vacuum insulator, while the load current and voltage were monitored through/across the load conductance. Additionally, the current is monitored as a function of axial position at 5 locations through the

transmission line. These measurements were made at the following radii: 0.4, 0.5 m, 0.6 m, 0.7 m, and 0.8 m. This allows the "height" of the electron flow as a function of radius to be determined. The simulated electron flow current passing through the load into the chamber was measured, and the current emitted by the cathode as a function or radius and the current collected by the anode as a function of radius were monitored as well.

A plot of the input current and load current is shown in Fig. 3.16. The difference between these signals accounts for the losses to electron flow (both the electrons that are lost to the anode and those magnetically insulated).

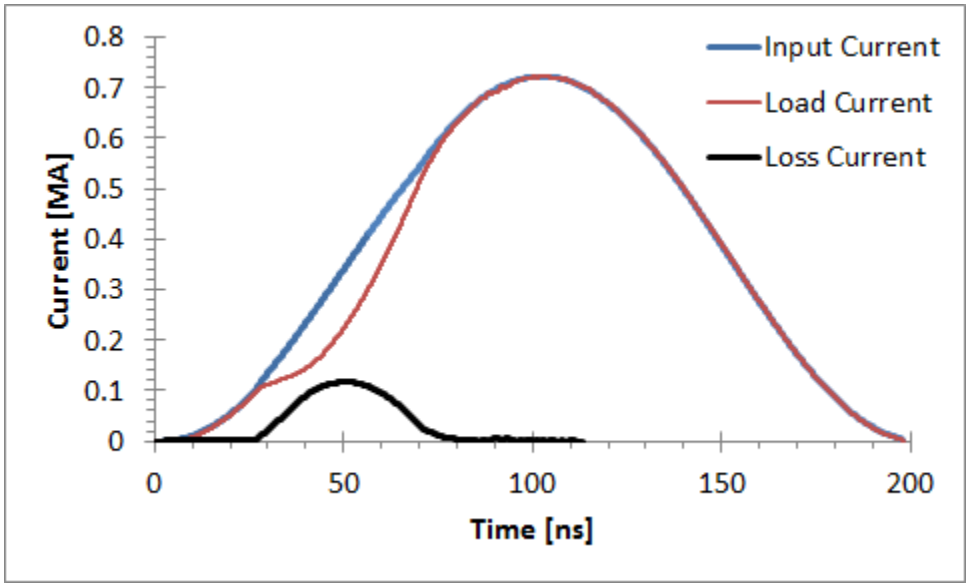

Fig. 3.16 Plot of the simulated input and load currents in MAIZE with a 50 kV/cm emission threshold. Early in time, the losses are zero because the emission threshold has not been passed; at ~ 30 ns, the losses start and are a significant fraction of the total current. At ~ 75 ns, the self-magnetic field exceeds the conditions necessary for self-magnetic insulation and the loss current drops back to nearly zero.

The hub height of the electron flow was determined by averaging the axial position of the electron flow at each radial location. These data are plotted for the three radial locations in the transmission line in Fig. 3.17. As the radius gets smaller, the current

density increases, which provides better magnetic insulation. This is very apparent from the average hub height at each radial location.

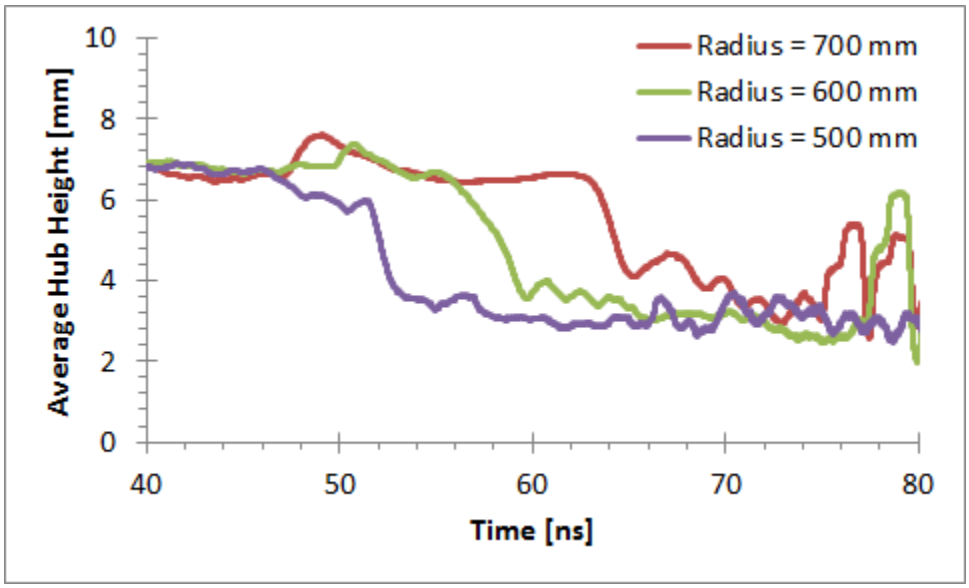

Fig. 3.17 A plot of the average hub height at three locations in the radial transmission line. Early in time, all three hub heights match (this is before magnetic insulation begins). As the current increases, the conditions for magnetic insulation are satisfied first at the smallest radius, and at progressively larger radii. This is shown in the plot where the hub height drops from ~ 7mm to ~ 3mm first in the 500 mm radius measurement, then the 600 mm measurement, and then the 700 mm measurement.

The electron flow passing through the load conductance is plotted in Fig. 3.18. The peak current is ~ 4 kA, which is a small fraction of the total current; however, it is still enough to strike the load and produce the light emission observed experimentally with the open pinhole camera.

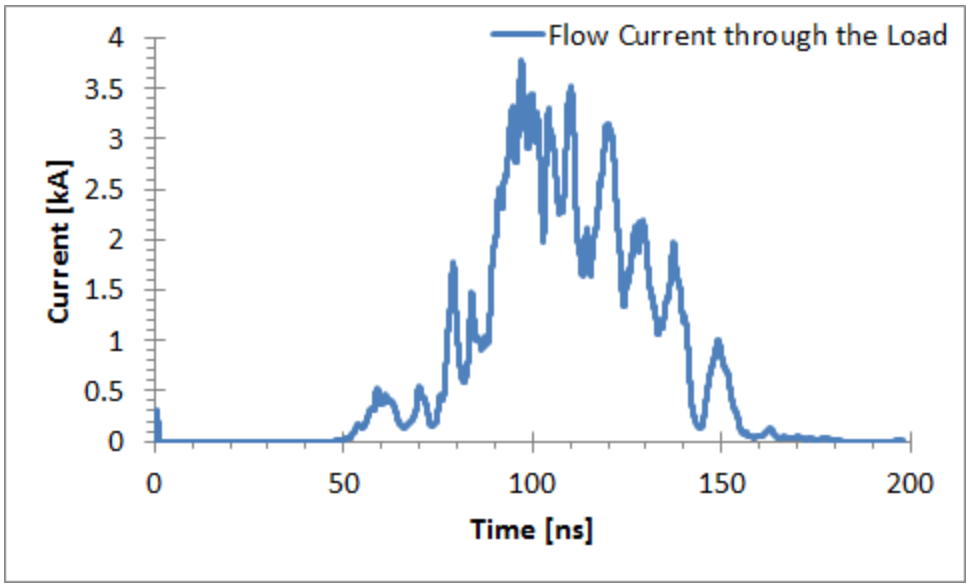

Fig. 3.18 Electron flow passing through the load conductance (the portion of the loss current that does not cross the A-K gap in the transmission line). The signal reaches a maximum value of nearly 4 kA, which is sufficient to produce a plasma on a dielectric that spans the A-K gap at the load.

The difference between the input and load currents shows the time evolution of magnetic insulation in the transmission line (Fig. 3.16). Initially, the current flow was well below the self-magnetic insulation threshold for the voltage applied. As a result, the current lost across the anode-cathode gap was a significant fraction of the total current. By peak current time the condition for self-magnetic insulation was satisfied, thus a negligible fraction of the current was lost across the anode-cathode gap; this is hinted at in the data shown in Fig. 3.17. The current emitted into the gap must go somewhere, and based on the measurements shown in Fig. 3.18, it appears that it passes through/strikes the load.

3.3 Summary

The preliminary pulsed power tests of MAIZE were a success. With a +/- 70 kV charge, MAIZE is capable of driving a 0.63 MA, 107 ns (10%-90%) rise-time pulse through the

transmission line coupled to a 0.1 Ohm resistive load. Discrete element circuit model simulations of MAIZE provide a good match to the experimental data, which indicates that the model of the system can be used to estimate current and voltage characteristics for a given static load impedance. Particle-in-cell simulations have corroborated the electron flow/current losses observed experimentally. These models will be an integral part of planning future experiments.

CHAPTER 4

MAIZE EXPERIMENTAL RESULTS AND SIMULATIONS

In this chapter, the single post-hole convolute experiments conducted on MAIZE are discussed. The hardware designs as well as the diagnostics utilized are described. The results of the experiments are also described, and the experimental results are compared with MAGIC PIC simulations.

4.1 Hardware Design

Post-hole convolutes are used to combine two or more parallel transmission lines into a single anode-cathode gap just upstream from the load. Typically, several post-hole sets are used in parallel to reduce the inductance of the convolute. In most cases of interest, the transmission lines being combined are in a radial or conical geometry. Inherent to this geometry is a limited (or non-existent) diagnostic access to the region of interest. The hardware used in these experiments was designed with the goal of maximizing the diagnostic access while maintaining the general post-hole convolute geometry.

For these experiments, the cathode plate of the transmission line was fed through the anode plate to form a pair of parallel plate transmission lines with a shared cathode, as shown in Fig. 4.1a. The cathode has a hole through which a post connects the two anode

plates to one another; thus forming a one post, single post-hole convolute. The vertical transmission lines upstream of the post-hole convolute starts at 309 mm wide and narrows to 88.9 mm; the transmission line continues as a constant with dual strip line until it reaches the convolute, as shown in Fig. 4.1b. Not only is this geometry convenient for diagnostic access, but it also allows for more simplistic data analysis (uniform direction of current flow, constant current density, etc.).

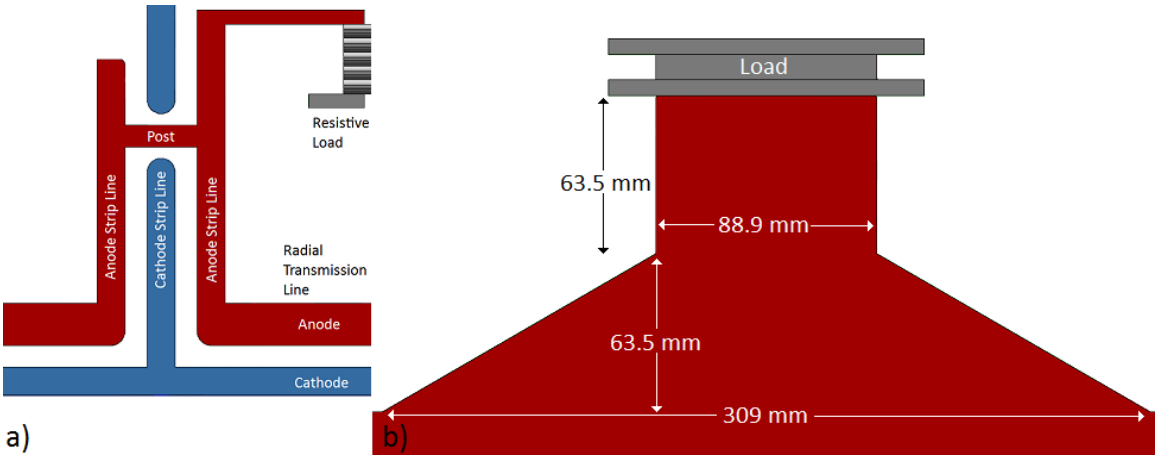

Fig. 4.1 a) Cutaway of post-hole convolute showing how the cathode strip line feeds through the anode transmission line plate to form a dual strip line geometry with a shared cathode. The post connects the two anodes through a hole in the cathode forming the post hole convolute. b) Side view of the strip line geometry. The strip line initially has a large width to lower inductance, but it tapers to a small width to increase the lineal current density in the transmission line.

The location of the post-hole was chosen such that it would be vertically centered in the diagnostic ports on the vacuum chamber. The tapered width of the strip line was chosen in order to reduce the inductance of the transmission line, and the anode-cathode gap was set to 1 cm in order to keep the voltage in the transmission line around 100 kV/cm. The inductance was estimated using the approximation for a pair of closely-spaced (A-K gap << width of transmission line) parallel plate transmission lines

$$L = \frac{\mu_0 * g * l}{w} \tag{4.1}$$

where μ_0 is the permeability of free space, g is the anode-cathode gap spacing, l is the length of the transmission line, and w is the width of the transmission line. A constant width (88.9 cm) dual parallel plate transmission line of the same length has an inductance of 8.8 nH. The width of the geometry used is described by

$$w = 309mm - 3.5216 * y \; for \; (0 < \; y < 62.5 \; mm) \tag{4.2}$$

$$w = 88.9mm \; for \; (62.5 < y < 125 \; mm) \tag{4.3}$$

where y is the position along the length of the transmission line(l). This geometry has an inductance of 6.6 nH (75% of the constant width case). The goal for the convolute, load, and transmission line inductance was 10 nH, which according to PSpice simulations would allow load currents on the order of 1 MA with 100 ns risetime for a +/- 100 kV charge voltage.

The convolute transmission line plates were fitted with replaceable inserts, as shown in Fig. 4.2. The inserts are necessary for the assembly of the geometry, but they also provide some experimental advantages. The inserts span the regions of the convolute that have typically exhibited damage in previous experiments; the inserts are small and relatively simple in design, which makes the hardware easy to replace if damaged. Additionally, the diagnostic access points are machined into the anode inserts (i.e. an array of holes that allow fiber optics to collect light emitted from the convolute), thus if the diagnostic setup needs to be modified; only this relatively simple part needs to be replaced. The cathode insert contains the hole through which the post passes. The

cathode insert and/or the post can be modified to affect the electric and magnetic fields within the post-hole. Adjusting the diameter of the post (or hole) would uniformly affect the magnitude of the electric and magnetic fields; changing the shape of the geometry (i.e. an elongated hole, an angled post, etc.) would allow sections of the post-hole region to be modified somewhat independently of other regions.

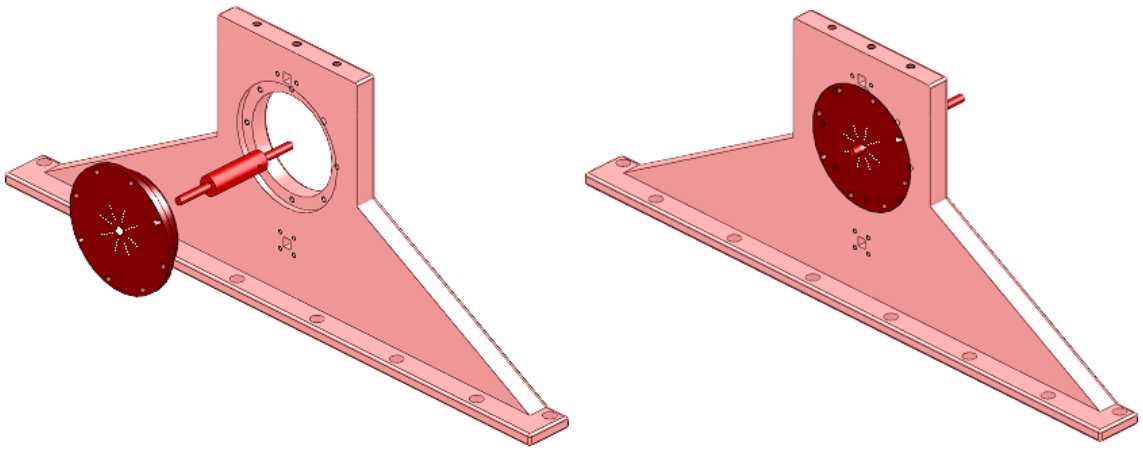

Fig. 4.2 The left image shows the exploded view of the anode strip line with the insert and post. The right image shows the parts assembled.

The materials used to construct the components of the post-hole convolute play an important role in the diagnostic setup of the convolute. Aluminum 6061, HPOF copper, and 304 Stainless Steel were chosen for the anode insert, post, and cathode insert respectively. The different materials were chosen to allow the origin of the plasma to be spectroscopically determined. This could be accomplished by looking for characteristic emission (or absorption) lines from each of the materials. Given the timing and location of the emission line, the origin and evolution of the plasma within the convolute could be determined. This is of particular importance in diagnosing the performance of the

convolute because the source of the impedance collapse in the post-hole region is still in question.

The output of the convolute was coupled to a static resistive load. While this removed the time changing load inductance that is normally present on the Z-Machine, it allowed for a high shot rate (up to one per minute) with reasonably good shot-to-shot reproducibility (because the same load was used on each shot). A resistive load was chosen over an inductive load to reduce the reflections sent back into the driver. The capacitors used in the LTD have a voltage rating of 100 kV with 10% voltage reversal. Thus it was important to limit voltage reflections, which would have been larger with a purely inductive load.

The target resistance for the load was 0.1 ohm, which matches the driver impedance. The design of a vacuum static resistive load capable of dissipating ~ 10 kJ per pulse while holding off ~ 100 kV was non-trivial. Metal and graphite shunts of a reasonable length would be too thin to survive multiple shots without being destroyed. Liquid resistors would require massive cross-sections or unreasonably short lengths to achieve the desired resistance. Additionally, liquid resistors are not known for being vacuum compatible.

Initial tests were run using ceramic composite resistors of the same type as those used in the transmission line resistive load. Twenty-four resistors were connected in parallel to form a 0.10 ohm load resistor. These resistors were 15 cm long and 2.54 cm wide; assuming a 1 cm A-K gap, the load inductance was approximately 18.6 nH, which was

considerably higher than the desired maximum value (~ 1 nH). This inductance was high enough to have significantly affected the risetime and peak current passing through the convolute.

4.2 Diagnostics

The diagnostics used to monitor the post hole convolute performance included open pinhole cameras, fiber coupled visible spectroscopy, B-dot monitors, and a high voltage probe. The pinhole cameras were used to record a time-integrated, spatially-resolved image of the emission from the convolute. The spectroscopic diagnostic recorded the time-integrated spectrally-resolved emission from four distinct locations in the convolute. The high voltage probe was attached to the cathode at the load, and the B-dot monitors (used to determine the current) were located just upstream and downstream from the convolute, as shown in Fig. 4.3, and at the output of the LTD.

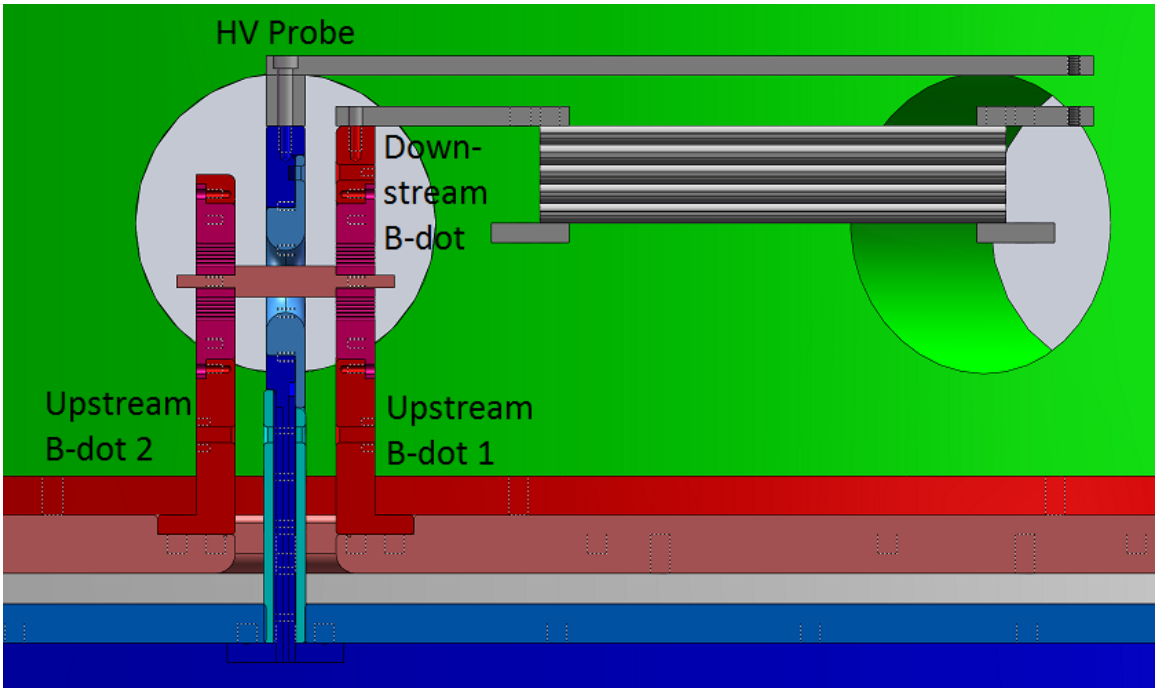

Fig. 4.3 R-Z cut through of the post-hole convolute and load showing the location of the convolute B-dots and the location of the high voltage probe.

The pinhole cameras were positioned as shown in Fig. 4.4. Typically they viewed the post horizontally through opposite ports on the vacuum chamber, but they were moved to other ports around the chamber in order to study plasma formation within the convolute and in the load.

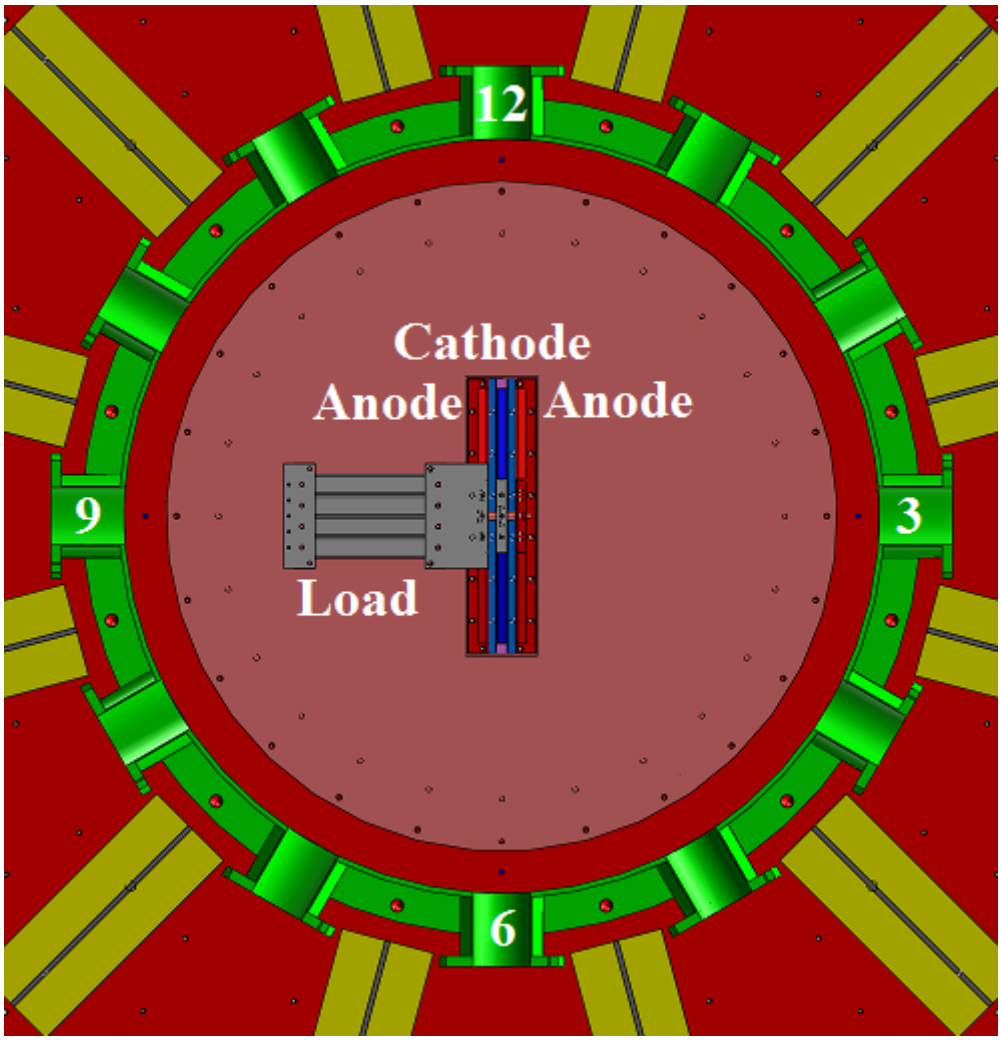

Fig. 4.4 Axial cut of MAIZE at the load region. The locations from which the pinhole cameras were fielded are shown as white numbers (3, 6, 9, and 12).

The anode inserts contained an array of 1 mm diameter holes at 1.25 mm spacing at eight locations around the post (see Fig. 4.5). The different azimuthal locations were used to determine the plasma origin and the plasma conditions around the post. The holes crossing the gap were used to measure the plasma parameters as a function of distance across the A-K gap. Four fiber optic cables were fed into the chamber and each one was positioned in one of the 48 holes. Shots were conducted in which the fibers were azimuthally located at 0°, 90°, 180°, and 270° (positions 3, 4, 2, and 1 respectively)

and radially at 5.5 mm (surface of the post). Additional shots were conducted in which the fibers were all azimuthally at 0°, and the radial position varied from 5.5 mm to 9.25 mm in 1.25 mm increments.

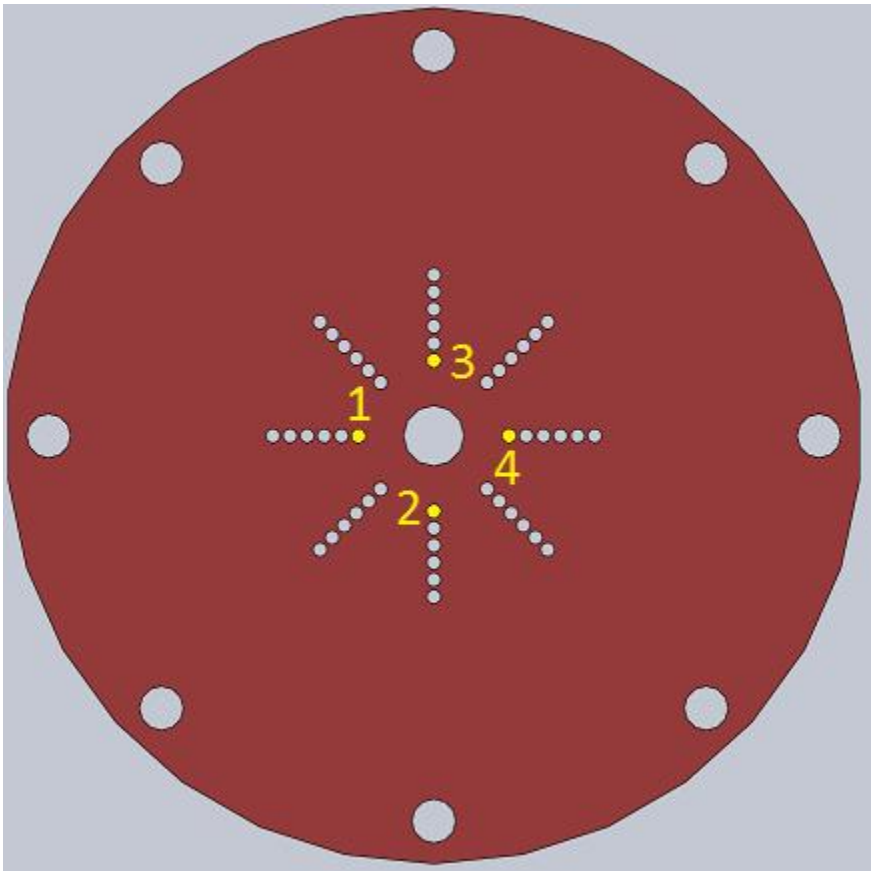

Fig. 4.5 A close-up of the anode insert showing the array of holes in which the fiber optics could be fielded. The regions used for the spectroscopy data shown below are colored yellow and labeled with yellow numbers (1-4).

The convolute B-dot monitors were of similar design to the BD-02 style monitor, which was briefly used in the MITL. The three convolute B-dot monitor locations each contained a B-dot set constructed as a dual-loop, dual-output, inverted pair. The locations of the B-dot monitors were chosen such that all of the current flowing into the convolute could be monitored, and all of the current leaving the convolute could be

measured. Subtracting these two signals gives the current lost in the convolute as a function of time. BD-01-Mod-A B-dot monitors were fielded at the output of the LTD. These were used as a quick check to verify that the current leaving the LTD was similar to that entering the convolute.

4.3 Experimental Results

Current and voltage traces from the post-hole convolute experiments are shown in Fig. 4.6. The MITL current indicates that the LTD is operating as expected. It reaches a peak value of 0.44 MA with a 153 ns 10%-90% risetime. It is clear from these traces that the convolute B-dots did not function properly. In all cases the integrated signal does not return to zero, but instead trails off to a high negative current. This is likely the result of unbalanced currents running along the ground of the cables. Subsequent experiments utilizing a similar style B-dot (see section 3.2.1) and cabling, but with better grounding techniques provided useful signals. Unfortunately, the post-hole convolute project terminated prior to determining the correct methods for fielding electrical diagnostics. Initially, the measured voltage spikes to 78 kV, which was expected due to the relatively high inductance of the resistive load. After approximately 37 ns, the voltage drops to zero and then rings back up to a lower voltage. This repeated through several more cycles. The voltage signal indicated that the load was shorting out, thus dropping the load voltage to zero; the frequency of the ringing indicates that the total round trip transit time through the system is approximately 30 ns.

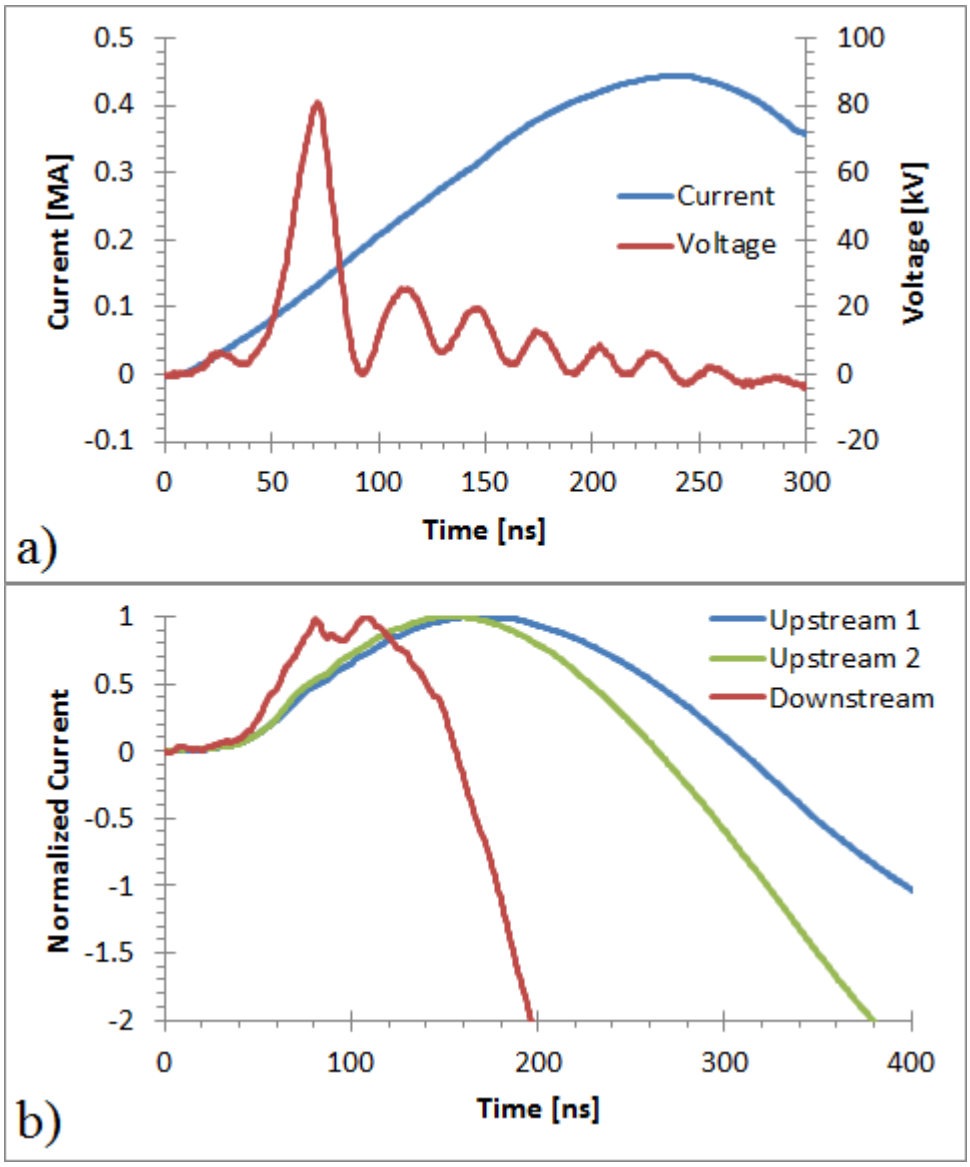

Fig. 4.6 Traces from a typical shot on MAIZE with the post-hole convolute load. a) shows the voltage as measured by the high voltage probe attached to the cathode and the LTD current as measured by the B-dots fielded at the start of the radial transmission line. b) shows the normalized current determined using the convolute B-dots. The downstream B-dot failed very early in the pulse, but the upstream B-dots looked reasonable through peak current. All three signals trailed off to a high negative current, indicating an issue with the diagnostics. Subsequent tests of new B-dot designs in similar environments indicate that the new designs would function through peak current, but these have not been fielded with the convolute hardware.

The pinhole images of the convolute confirm the theory that the load was being shorted out. In Fig. 4.7, there are two bright regions which indicate plasma formation. Neither emission region is close to the post-hole, but both can be easily explained. Plasma forms

near the load at the surface of a plastic spacer; this is the brighter of the two plasma regions (on the right). Plasma formation on the surface of the insulator is the result of electron flow striking the dielectric. Once the plasma has formed, it acts as a shunt impedance through which the majority of the current will pass. This results in a rapid drop in the voltage, as was observed in the electrical signals. The second region of plasma coincides with the location of a magnetic null in the system. The anode plate that does not connect to the load has no current passing through it, but there is a potential difference between this region of the anode and the cathode. Thus the electric field is similar in this region to that in the rest of the transmission line, but the magnetic field drops to zero (see Fig. 4.8); therefore, the requirements for magnetic insulation are not satisfied in this region, and electrons can stream directly across the A-K gap. The energy deposited by the electrons was sufficient to form plasma on the surface of the anode.

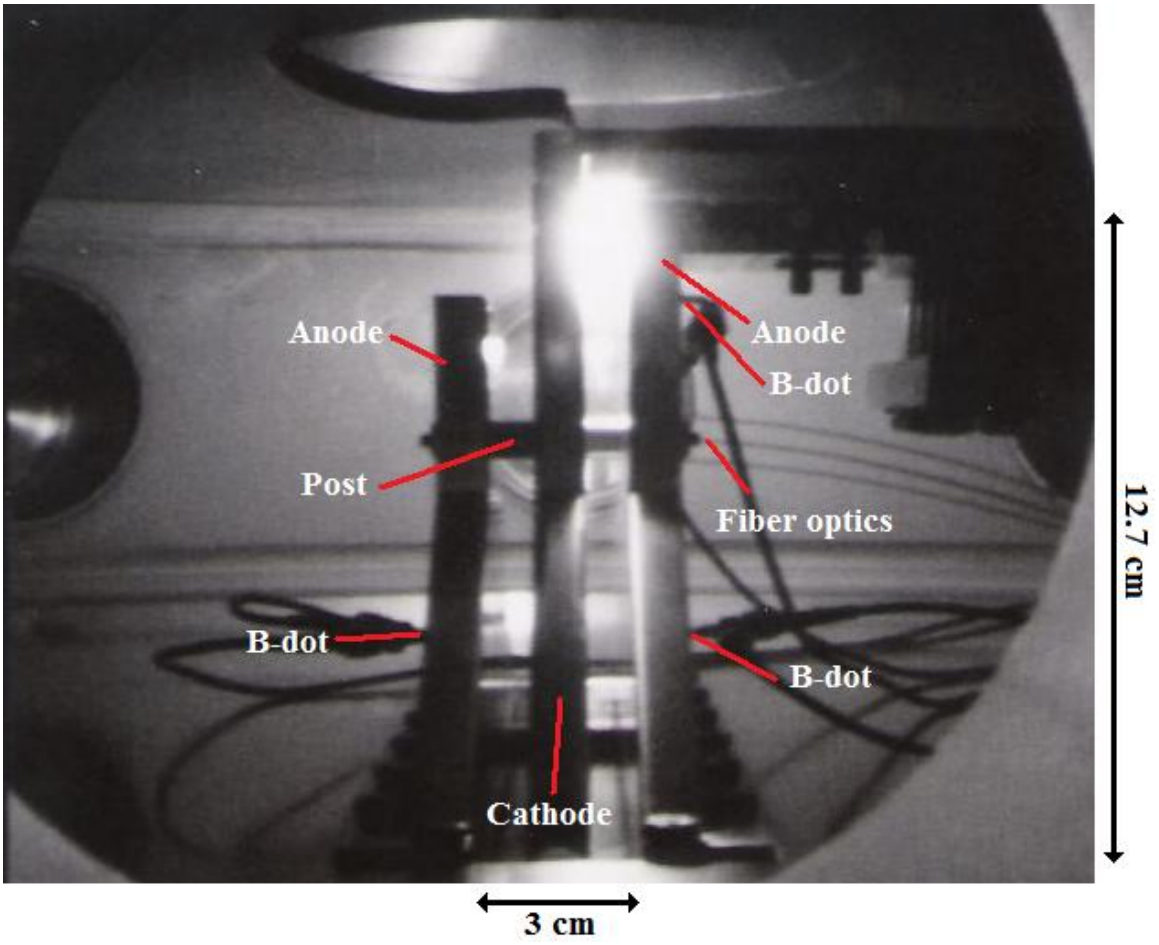

Fig. 4.7 Open pinhole image taken from position 9 showing the emission from the convolute integrated over the duration of the shot. Two obvious bright regions exist; the region on the left corresponds to a region of poor magnetic insulation, the region on the right is near a piece of dielectric that flashed over at the load.

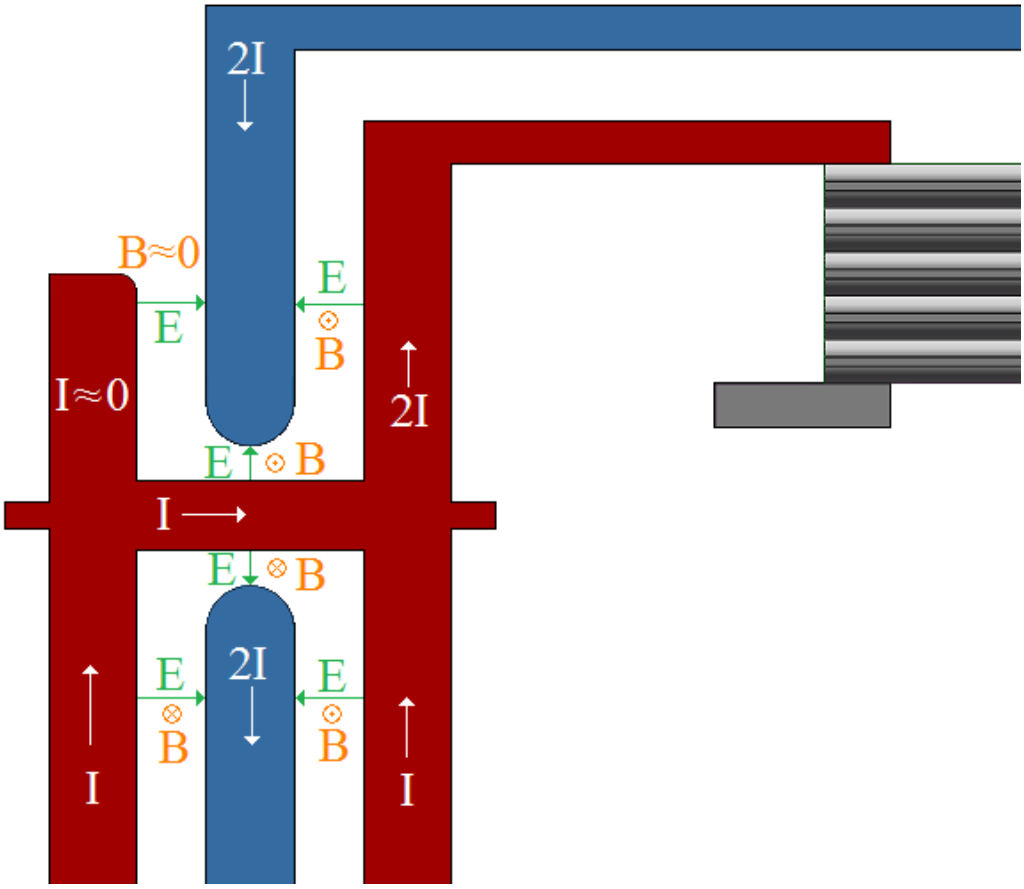

Fig. 4.8 Schematic showing the post-hole geometry, the current, and the electric and magnetic field orientations. The current is zero downstream of the post on the non-load side of the convolute (left), so the magnetic field approaches zero. In this region the conditions for magnetic insulation are not satisfied.

A third region of plasma, located on the short anode just upstream of the post, was observed in a few shots. Looking along the axis of the post (position 3 as shown in Fig. 4.4), the emission at the bottom of the post is significantly larger and brighter than it is at the top of the post, as shown in Fig. 4.9a. This is corroborated in another shot where the pinhole camera observes the convolute from position 12 (Fig. 4.9b).

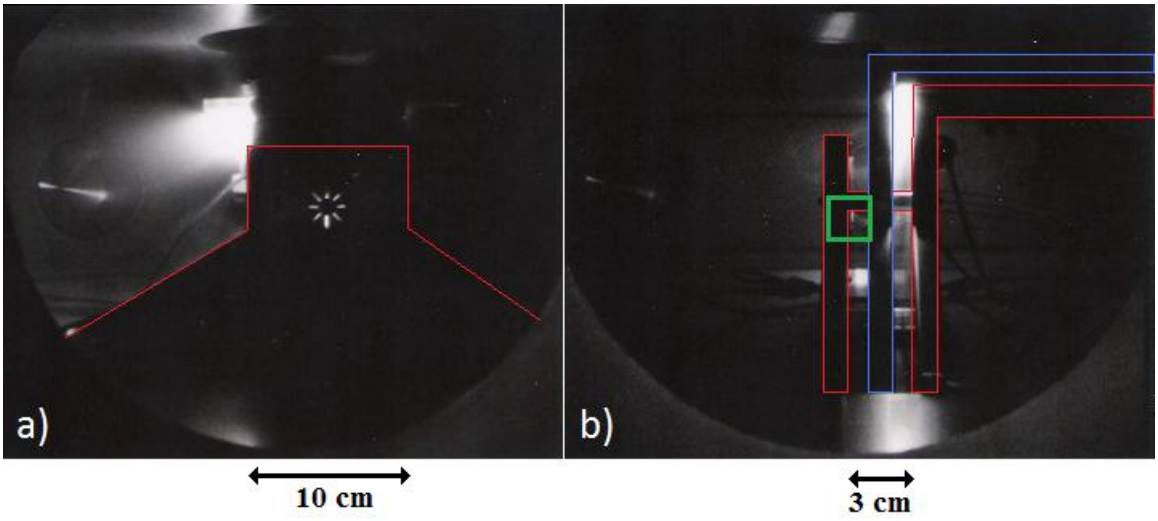

Fig. 4.9 a) open pinhole image from position 3. Light is observed through the diagnostic holes in the anode insert. The intensity of emission is greatest in the bottom holes, indicating plasma formation just upstream of the post. b) open pinhole image from position 12. A region of emission is boxed in green. This region corresponds to the location of emission shown in (a). The anode hardware is outlined in red, and the cathode is outlined in blue.

When the pinhole camera was positioned behind the load and directed along the axis of the post (position 9), the emission at the top of the post is significantly brighter than that at the bottom, as shown in Fig. 4.10a. When this is compared to a shot using the view from position 12 (Fig. 4.10b), it is plausible to assume that the emission observed is actually from plasma expanding down from the plastic at the load, or due to reflections of the emission from that plasma.

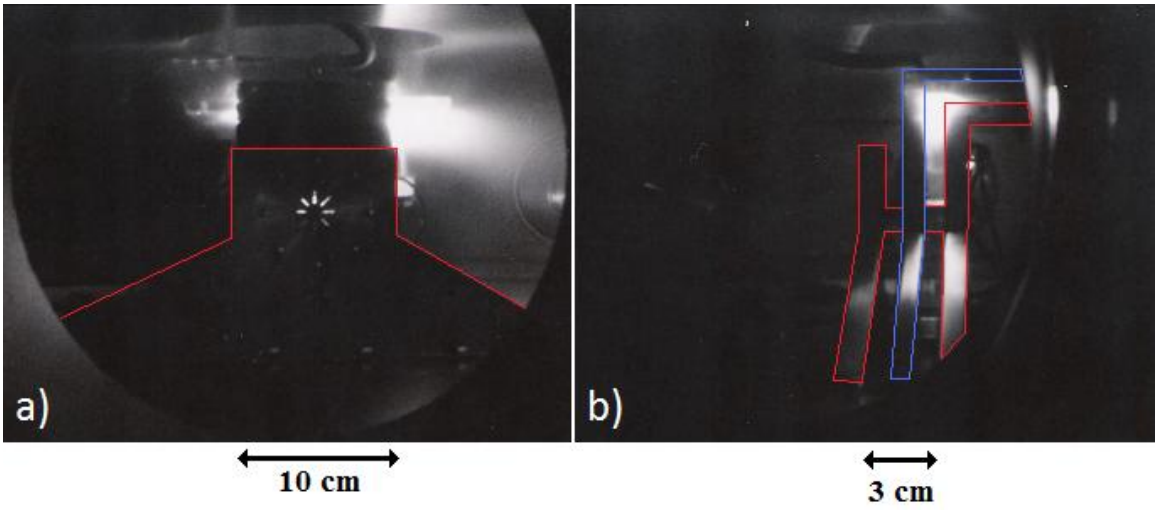

Fig. 4.10 a) open pinhole image from position 9. The emission intensity is greatest just downstream of the post. b) open pinhole image from position 12. This image shows that there is a considerable amount of emission at the load, which illuminates the convolute downstream of the post. There is no obvious emission upstream of the post. This matches the emission location observed in (a). The anode hardware is outlined in red, and the cathode is outlined in blue.

Spectroscopic measurements of the convolute plasma support the conclusions formed based on the data from the other diagnostics. The fibers for these measurements were positioned in the longer anode plate as shown in Fig. 4.5. The signal recorded using the fiber located at 0° (position 3) was always the most intense, but all of the signals showed roughly the same spectral features (see Table 4.1 and Fig. 4.11a-c). This is an indication that all of the light observed originates from plasma with similar parameters, but that some of the fibers are not collecting as efficiently as others. This could be the result of uniform plasma throughout the convolute being observed by some partially obscured fiber optics. Perhaps a more plausible explanation is that all of the light has the same origin (downstream from the convolute, where the load is breaking down) and the light collected by the fibers is due to reflections. The difference in the light collected in this

case would be the result of different reflection paths, as well as the post obscuring the lower fibers from the plasma.

Table 4.1 Summary of the emission lines observed in the time integrated spectra from the MAIZE convolute experiment.

Element	Wavelength [nm]	Oscillator Strength [s^{-1}]	Element	Wavelength [nm]	Oscillator Strength [s^{-1}]
Fe – I	282.6	$1.32x10^7$	Fe – I	484.0	$1.7x10^6$
Fe – I	296.5	$1.16x10^7$	Fe – I	486.0	$1.62x10^7$
Fe – I	310.1	$1.35x10^7$	Fe – I	489.1	$3.08x10^7$
Fe – I	360.9	$8.13x10^7$	Fe – I	492.1	$3.58x10^7$
Fe – I	385.6	$4.64x10^6$	Fe – I	512.2	$7.9x10^6$
Fe – I	387.9	$6.17x10^6$	Fe – I	513.7	$1x10^7$
Al – I	394.4	$4.93x10^7$	Fe – I	516.9	$2.72x10^6$
Al – I	396.2	$4.8x10^7$	Fe – I	519.1	$2.32x10^7$
Fe – I	410.7	$1.74x10^7$	Fe – I	523.3	$1.94x10^7$
Fe – I	415.7	$1.2x10^7$	Fe – I	540.4	$6.92x10^7$
Fe – I	429.9	$1.29x10^7$	Fe – I	543.0	$7.27x10^6$
Fe – I	448.6	$1.1x10^7$	Fe – I	546.3	$2.9x10^7$
Fe – I	455.6	$1.05x10^7$	Fe – I	558.7	$2.19x10^7$
Fe – I	470.5	$8.8x10^6$			

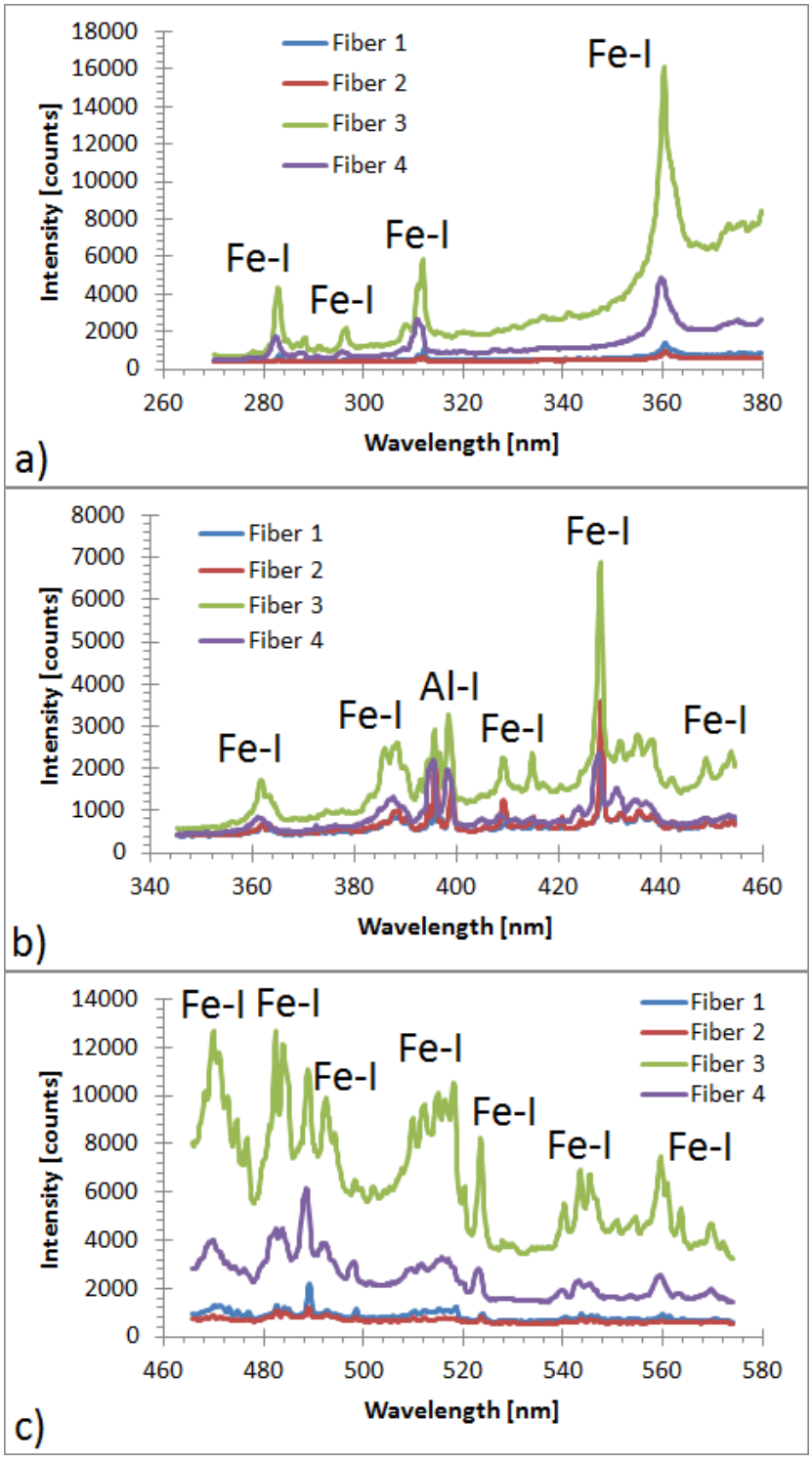

Fig. 4.11 Spectra recorded with the four fibers positioned as described in Fig. 4.5. All four fibers record similar features but with different intensities. The features observed are primarily neutral iron lines (originating from the 304 SS cathode insert); some neutral aluminum lines are also observed (originating from the Al 6061 anode insert).

The reflected light theory is particularly appealing because the fiber that received the most light was located closest to the proposed emission source. Additionally, the second most intense signal came from the side of the post with the asymmetrically higher emission as shown in Fig. 4.9a and Fig. 4.10a. The two lowest signals are obscured by the post from the brightest region of the plasma. Further support for this theory comes from subsequent experiments in which the plastic at the load was removed. In these experiments there was no plasma formation at the load and no significant emission was recorded from any of the fibers. A final point to note is that both Fe and Al lines are observed in the spectra, but no Cu lines are observed. If there was plasma crossing the A-K gap at the post, there would likely be some copper emission, but if the light being recorded originated at the plastic block near the load, only the aluminum and stainless steel would contribute atoms to the plasma.

4.4 Particle-In-Cell Simulations

A series of simulations of the post-hole convolute fielded on MAIZE were conducted using MAGIC PIC 3D [45] by D. M. French. The geometry used in these simulations is shown in Fig. 4.12. The load is purely resistive, which is not a good match to the experiment, but the rest of the geometry accurately reflects the experiment. A voltage pulse is supplied to both of the A-K gaps at the wide end of the transmission lines; the load voltage and load current pulses are shown in Fig. 4.13. The simulations assume a 100 kV/cm explosive emission threshold on a cell by cell basis; once electron emission begins, it continues until the electric field is reversed.

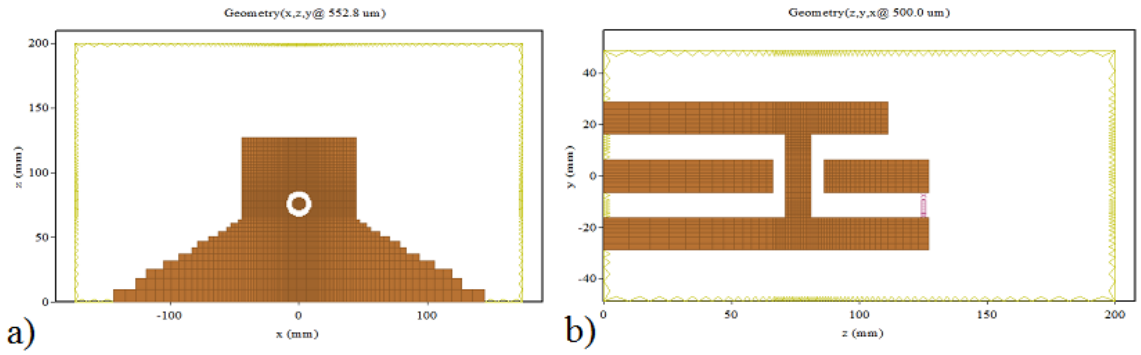

Fig. 4.12 Simulation geometry. a) X-Z cut showing the shape of the electrode and the hole/post. b) Y-Z cut showing the anode-cathode gap and the load resistor (red Xs).

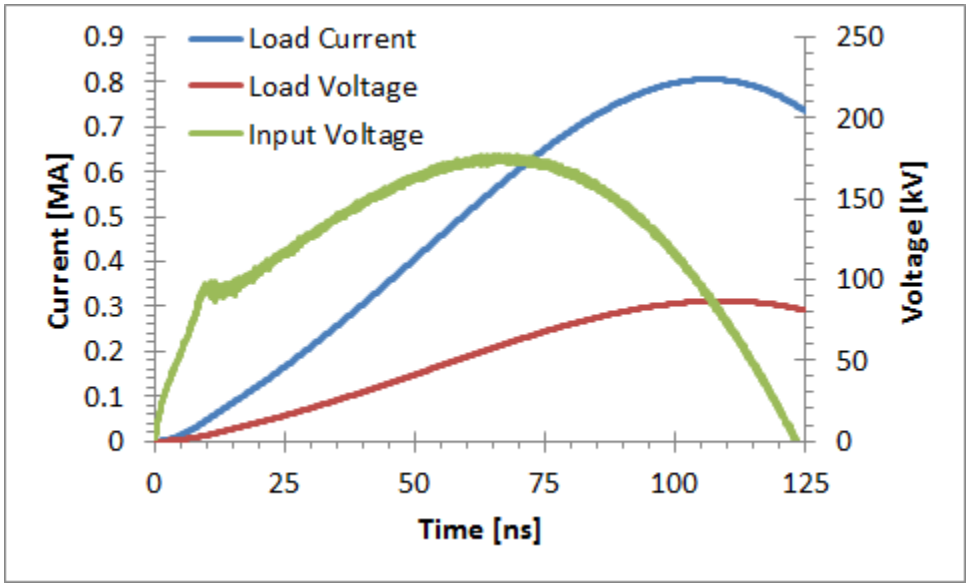

Fig. 4.13 Current and voltage traces from the MAGIC PIC 3D simulation of the post-hole convolute. (Courtesy of D.M. French)

Magnetic nulls are inherent to the convolute geometry, and as such, a magnetic null exists in the simulation. The magnetic fields at 90 ns into the simulation are shown in Fig. 4.14. A magnetic null spans from the cathode to the longer anode just upstream from the post. This is the result of the field generated by current flowing through the post cancelling the field generated by current flowing in the strip line. Progressing downstream from the post in the A-K gap with the shorter anode, the magnetic field

drops significantly, but does not go to zero within the A-K gap. There is no current flowing in this region of the transmission line, so no magnetic field is generated; current flowing in other regions of the convolute generate weak magnetic fields in the region. However, this weak magnetic field is sufficiently below the requirements for magnetic insulation, such that is can be treated as a lossy area, similar to a magnetic null.

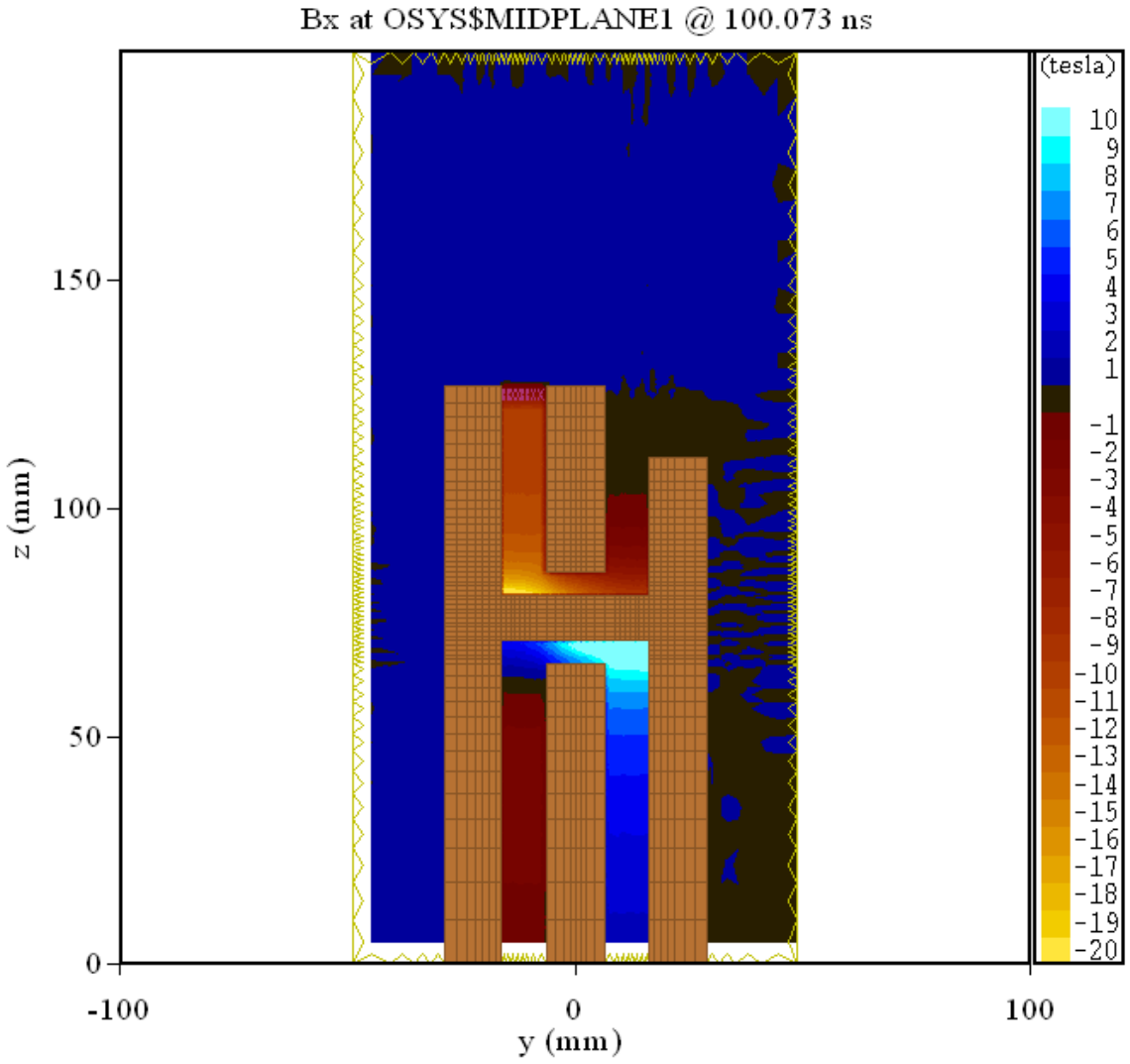

Fig. 4.14 Plot of the simulated magnetic fields in the convolute at 100 ns. The black regions show the locations of approximately zero magnetic field. (Courtesy of D.M. French)

As electrons stream across the A-K gap and strike the anode, energy is deposited in the material, and as a result, the temperature of the electrode rises. In these simulations, the energy deposited by electrons in the electrodes was monitored on a cell by cell basis, and the rise in temperature was estimated based off of the deposited energy. A plot of the energy deposited in the electrodes is shown in Fig. 4.15a and the resultant rise in temperature is shown in Fig. 4.15b.

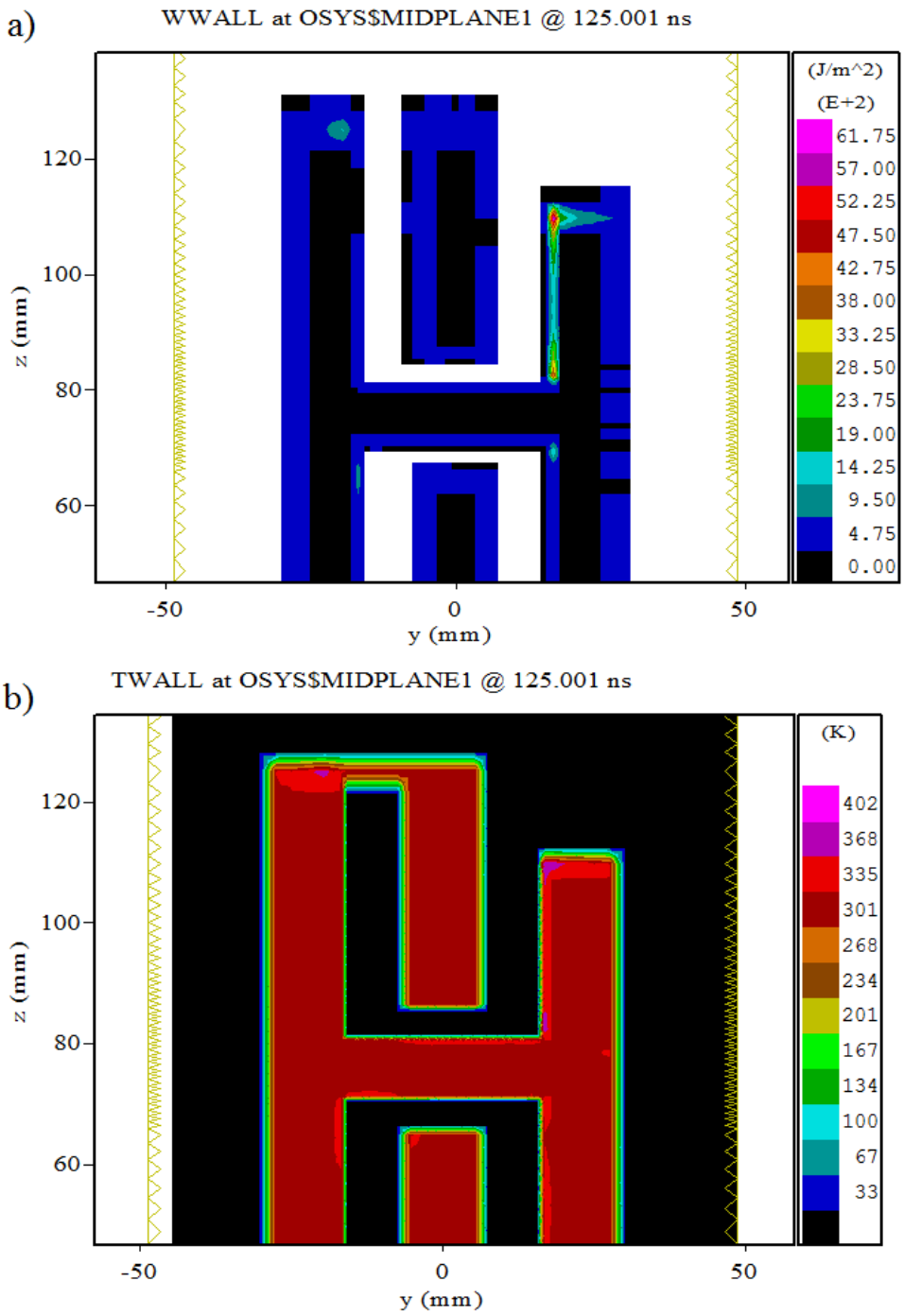

Fig. 4.15 a) Plot of the simulated energy deposited by flow electrons in the electrodes as a function of position. The region of largest energy deposition approximately corresponds to the region of low magnetic field. b) Plot of the simulated temperature of the electrodes due to the energy deposited by electrons. (Courtesy of D.M. French)

The location of energy deposition in the simulations qualitatively matched the location of plasma light emission in the experiments. Fig. 4.7 shows that a bright region of plasma on the shorter anode (non-load) side of the convolute downstream of the post was observed experimentally. This is the location predicted by the simulations to have the greatest energy deposition. Energy deposition in the anode heats the material, which desorbs contaminants. The liberated materials can be ionized by additional electron flow creating plasma, which would emit light, as was seen experimentally.

Typically, the anode transmission lines stop at the post (no material extends past the post) such that the flow electrons in the A-K gap stream out of the transmission line rather than striking the anode (i.e. the region where plasma was observed in these experiments does not exist in the Z-Machine post-hole convolute). However, plasma formed in this region should have similar parameters to plasma formed with similar electron flow and electric field elsewhere in the convolute.

CHAPTER 5

Z-MACHINE FACILITY AND DIAGNOSTIC DESCRIPTIONS

In this chapter, background information for the experiments conducted on the Z-Machine at Sandia National Labs are presented. A brief description of the pulsed power and vacuum sections of the machine is given. Additionally, the streaked visible spectroscopy diagnostic setup and convolute light plasma diagnostic probe design are included. A series of bench measurements and calibration procedures for the diagnostic are presented as well.

5.1 Z-Machine Description

The Z-Machine is a large pulsed power driver capable of producing load currents up to 26 MA. This current can be used to drive a number of loads including wire array z-pinches and dynamic materials loads. Risetime of the Z-machine current pulse is approximately 100 ns in short pulse mode, but it can be stretched to 300 ns and the shape of the rise can be set to some degree. When erected, the Marx voltage is on the order of 5 MV (60 capacitors x 80 kV charge); by the time the pulse reaches the load, the peak voltage drops to 1-2 MV.

The Z-Machine consists of three main sections: the energy storage section, the pulse compression section, and the vacuum transmission line. The energy storage section is immersed in an oil tank and is composed of 36 Marx banks. Voltage pulses from these Marx banks are transmitted to a set of intermediate storage (IStore) capacitors (part of the pulse compression section). Gas switches hold the voltage in the IStore capacitors until triggered by short-pulse UV lasers; the voltage then passes into the pulse forming lines (located in the water section). Pulse forming lines connect through self-breaking output switches to the insulating stack, which couples the water section to the vacuum section. A cross-section of the pulsed power section of the Z-machine is shown in Fig. 5.1.

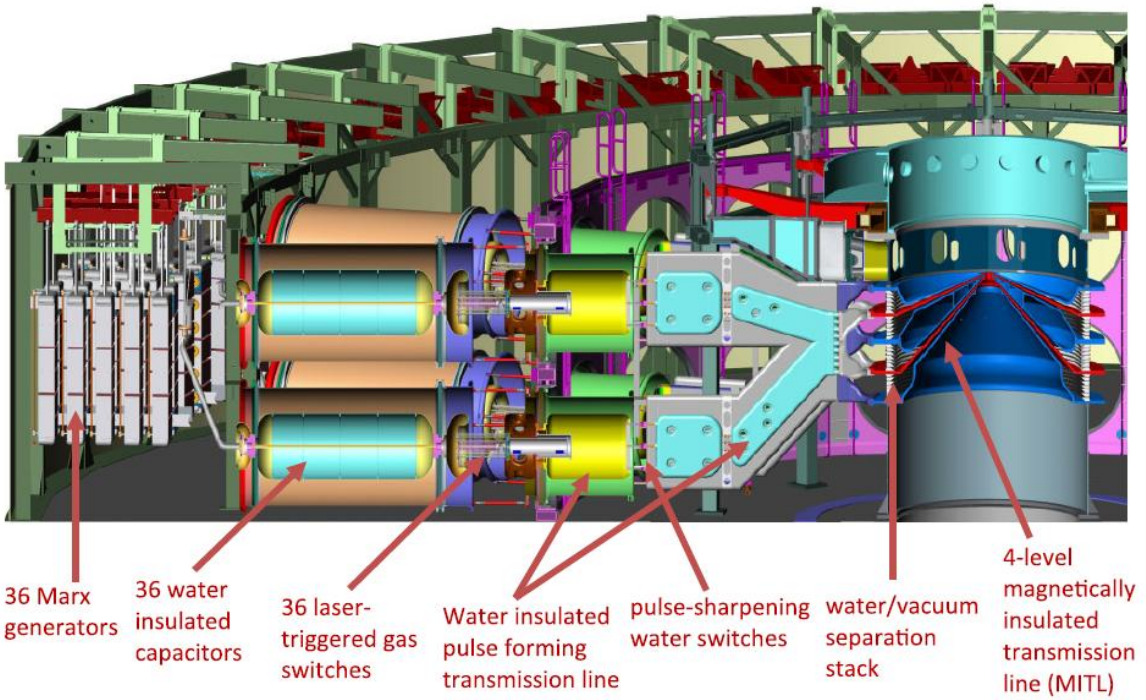

Fig. 5.1 A cross section of the Z-Machine pulsed power section. (Figure courtesy of K. R. LeChien et al. [35].)

The capacitors in the 36 Marx generators at the outside edge of the accelerator are used to initially store the energy, and then the Marx banks erect the voltage. This energy is transferred to the water capacitors, which compress the pulse from microseconds to sub-microsecond. Once the laser-triggered gas switches are fired, the energy passes into the pulse forming network and through the self-breaking water switches. At this point the pulse has been compressed to roughly 100 ns. It then passes through the vacuum insulated stack to the MITLs.

The vacuum section of the Z-Machine contains the self-magnetically insulated transmission lines (MITLs) as well as the post-hole convolute and the load. The MITL geometry is shown in Fig. 5.2. Four anode-cathode (A-K) gaps are used to reduce the inductance of the transmission line. Loads require there to be only one A-K gap, thus the four transmission lines are joined together using a double post-hole convolute. The geometry of the post-hole convolute used on Z is shown in Fig. 5.3. The output of the convolute is connected to the load via the final feed gap.

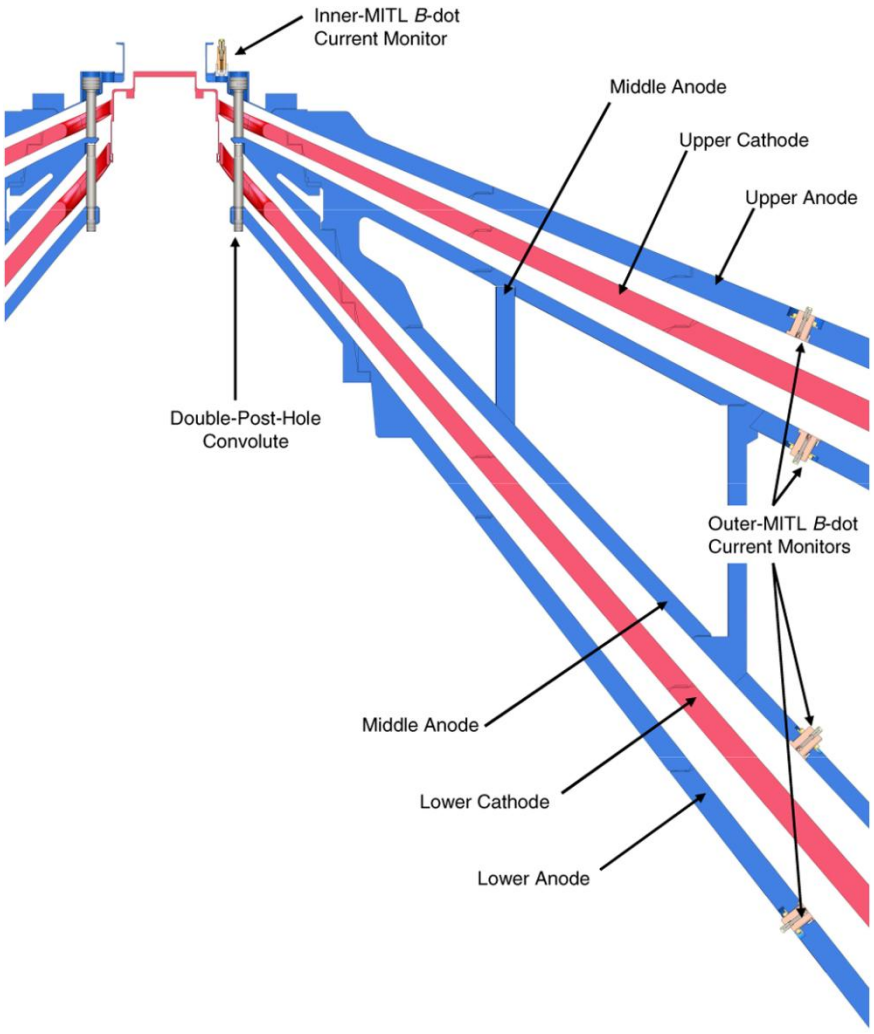

Fig. 5.2 Magnetically Insulated Transmission Line geometry used on the Z-Machine. There are 4 MITLs in parallel from the insulator stack. The post-hole convolute converts the 4 A-K gaps into a single A-K gap at the load. There are outer MITL B-dot monitors in each of the four anodes, thus the current in each transmission line is measured. The inner MITL B-dot monitors are also located in the anode and are used to measure the current that exits the convolute. Transmission lines and convolute designed by M. E. Savage and W. A. Stygar of Sandia National Laboratories. (Figure courtesy of D. V. Rose et al. [36].)

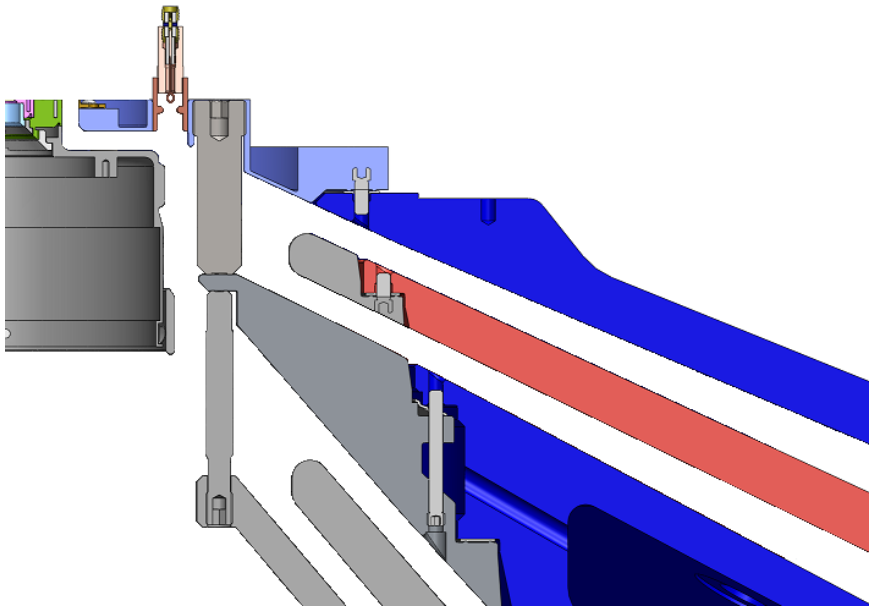

Fig. 5.3 R-Z cut of double post-hole convolute used on the Z-Machine. The double post-hole convolute combines the signal from 4 parallel anode-cathode gaps into a single gap across which the load is connected. The convolute connects the three anode sections with two posts. The two cathode sections have holes through which the posts pass. The cathode sections are connected to one another downstream from the convolute. (SolidWorks models of the Z Machine courtesy of J. Cisneros and M. Vigil.)

5.2 Diagnostic Description

Temporally resolved spectra were recorded using a 1 meter McPherson 2061 scanning monochromator coupled to an EG&G CA-24 streak camera as shown in Fig. 5.4. A similar diagnostic system was previously used on the Z-Machine by J. E. Bailey et al. [51-53]. The streak camera output light is amplified through a micro-channel plate (MCP) onto a film cassette. The streak camera entrance slit was located at the focal plane of the spectrometer output such that the direction of spectral dispersion was perpendicular to the direction of the streak sweep. Thus the axes on the film are spectral and temporal.

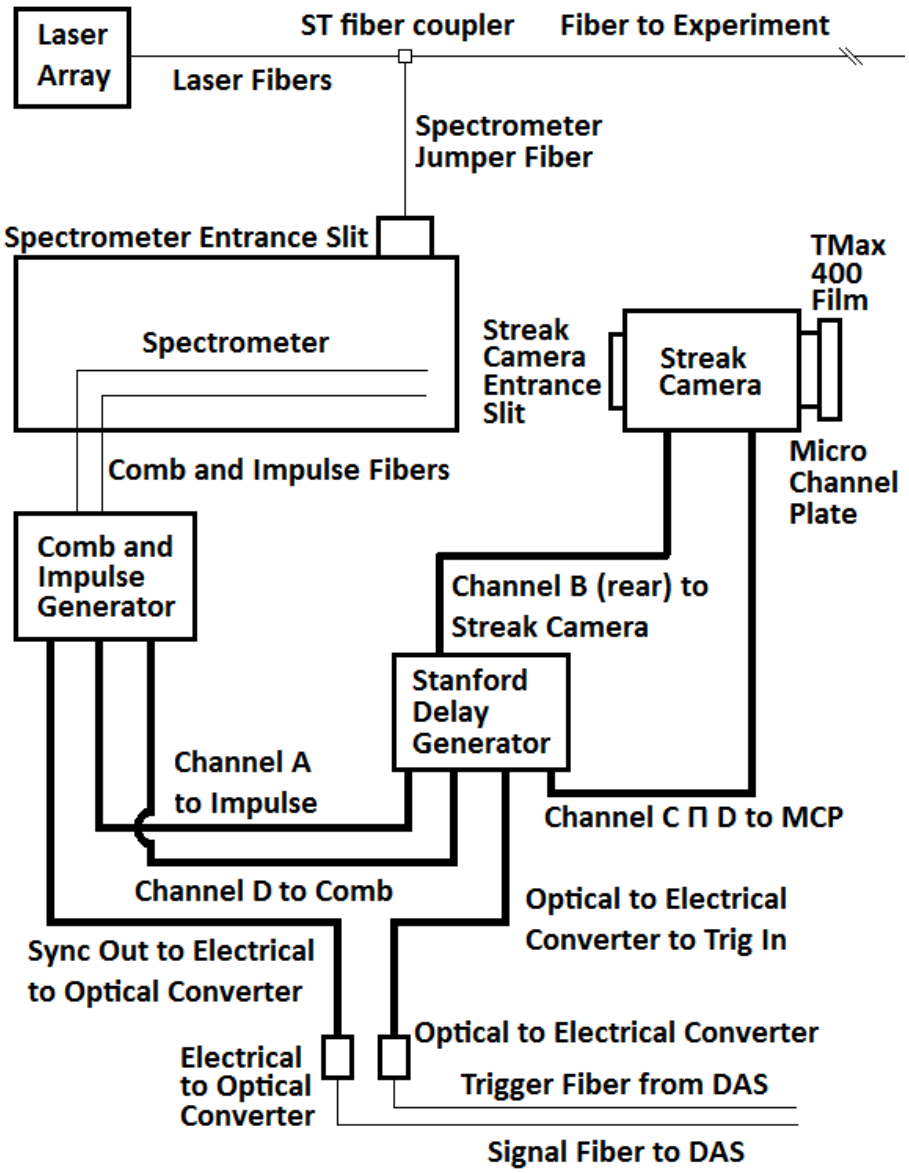

Fig. 5.4 Schematic of the diagnostic setup. At the input of the spectrometer, the spectrometer jumper fiber is either connected to the experimental fiber (for recording data during the shot) or one of the laser fibers (for wavelength fiducials). Output of the spectrometer is coupled to the input of the streak camera. Streak camera signal is amplified through a micro-channel plate onto a piece of film. Coaxial cables are shown as bold lines and fiber optic cables are shown as thin lines.

A series of diffraction gratings were available for use in the spectrometer. The spectral range of the survey grating is 265 nm; the finest grating has 1/16 the spectral range of the survey grating, but 16 times the spectral resolution (16.5 nm range, 0.2 nm resolution).

The spectrometer optics are designed to vertically focus at a point just past the output port of the spectrometer. At this location the vertical spot size of the light is roughly the same as the diameter of the fiber. The spectrometer has a numerical aperture (NA) of 7, but the fiber optic has a NA of 0.22. For a light source with a smaller NA than that of the detector, some of the signal is wasted. Thus a lens coupling system was used to convert from the NA of the fiber to the NA of the spectrometer.

The streak camera can be set to 5 discrete sweep durations ranging from 30 ns to 480 ns. The input slit to the streak camera is approximately 3 mm tall. This does not affect the temporal resolution of the streak camera since the vertical focus of the spectrometer is much smaller. The streak camera output light is transmitted into a 40 mm diameter gated MCP with adjustable gain setting. Since the streak camera tube is approximately 50 mm in diameter, some of the possible spectral and temporal ranges are lost. The 265 nm range quoted above takes into account the loss in spectral range. Because the streak tube is circular, the observed spectral range changes as a function of time; the quoted spectral range is the maximum. Streak sweep durations listed above do not take the loss due to the undersized MCP into account. A 480 ns sweep duration setting on the streak camera yields a 440 ns record on the MCP. A green phosphor is used to convert the signal from the MCP into light, which is recorded on TMax 400 film. After exposure, the film is developed along with an additional piece of film with a step wedge, which is used to correct for non-linear film response.

Comb and impulse generators produce timing fiducials on the film. The impulse signal is a single, precisely-timed, sub-ns laser pulse, and the comb signal is a train of sub-ns laser pulses spaced by 4 ns. Wavelength for both the comb and impulse lasers is 800 ± 20 nm. The comb and impulse signals are coupled into the spectrometer via fiber optic cable and focused through a pair of lenses onto the input slit of the streak camera. Both comb and impulse signals are completely separate from the diffraction grating in the spectrometer, thus they remain in approximately the same location regardless of the wavelength setting of the spectrometer. When the impulse light signal is sent to the streak camera, an electrical impulse sync signal is sent to be recorded on an oscilloscope. This is used to determine the absolute timing of the impulse on the film. The comb is used to determine the relative timing on the film.

A laser array consisting of 2 HeNe lasers (543.5 nm and 632.8 nm) and two diode lasers (650 ± 10 nm and 670 ± 10 nm) are lens-coupled into individual fiber optic cables. The HeNe laser fibers are connected to the spectrometer jumper fiber, which allows the laser light to enter the spectrometer, be deflected off the diffraction grating, and reach the streak camera entrance slit at the spectrally correct location. Placing two laser lines on the film sets both the absolute and relative wavelength scale. Additionally, the line width of a HeNe laser line is roughly 10^{-5} nm, which is orders of magnitude less than the measured line width, thus the width of the laser lines on the film gives a measurement of the spectral resolution of the diagnostic. A sample streak image with only spectral and temporal fiducials (no experimental data) is shown in Fig. 5.5.

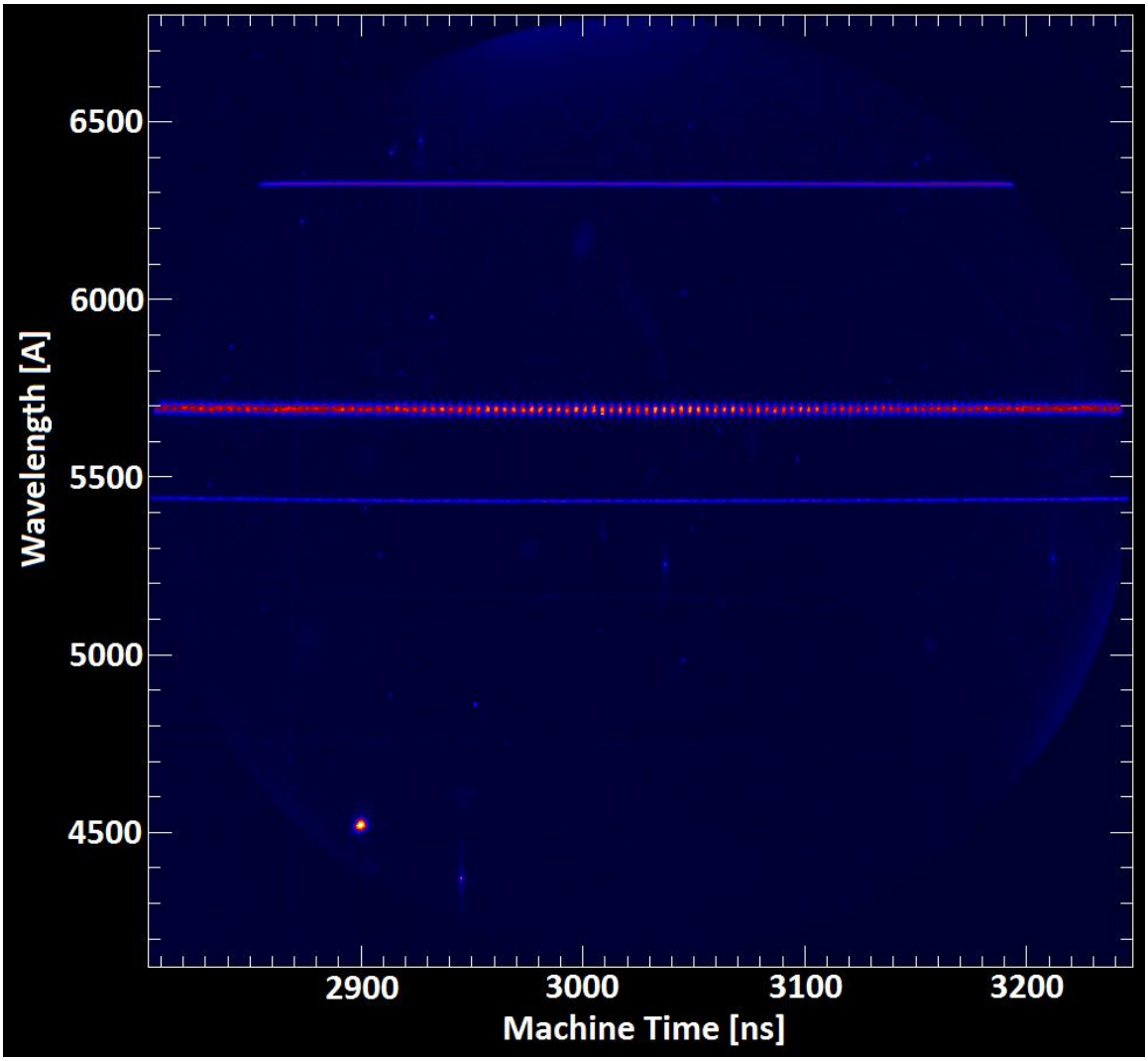

Fig. 5.5 Streak image showing timing and spectral fiducials. The impulse fiducial (absolute timing) is located at Machine Time = 2900 ns and Wavelength = 4500 A. The comb fiducial (relative timing) is located at Wavelength = 5700 A and spans the entire time base. The wavelength fiducials are produced by HeNe lasers and are located at Wavelength = 5435 A and 6328 A.

A Stanford delay generator was used to trigger the system. The timing of the impulse relative to the streak sweep was held constant for each sweep duration setting. The impulse signal was located as early as possible in the sweep to avoid overlap with the shot signal. Typically, the sweep was timed such that the shot signal turn-on would be centered on the sweep, thus it was recorded with the largest available spectral range.

5.2.1 Probe Description

The convolute light/plasma diagnostic (CLPD) probe consists of a fiber optic cable with a limiting aperture mounted in a fixture that appears electrically similar to the B-dot monitors used on the Z-Machine. Since these optical probes could be inserted into conventional B-dot probe locations and were non-perturbing to most experimental goals, there were opportunities to collect data in a "ride-along" mode on many experiments. The CLPD probe is inserted in place of a B-dot monitor in the upper anode plate as shown in Fig. 5.6a. The probe can measure light emitted in the convolute region from this location. An alternate location for the B-dot monitor/CLPD probe is shown in Fig. 5.6b.

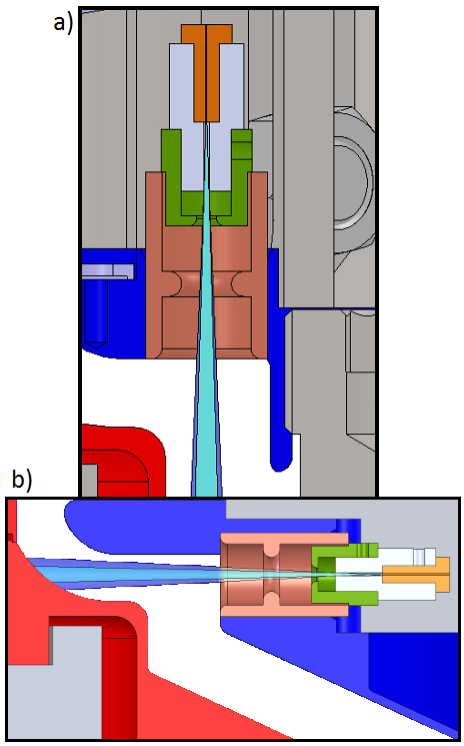

Fig. 5.6 a) Example of CLPD probe inserted in a vertical B-dot hole. The probe is located at the same azimuthal position as a post. b) Example of CLPD probe inserted in a horizontal B-dot hole. The probe is located azimuthally between two posts. The view in a) looks down into the convolute, while the view in b) looks at the feed gap. (SolidWorks models of the Z Machine courtesy of J. Cisneros and M. Vigil.)

The fiber optic cable used in the probe had a 0.22 numerical aperture; both 100 micron and 200 micron diameter core fibers were used. Larger diameter fibers increased the sensitivity of the probe, but also decreased the spectral resolution of the diagnostic. The entrance slit on the spectrometer was increased to accommodate the larger fiber diameter, which inherently reduced the spectral resolution of the diagnostic.

The CLPD can be set at four angles: 0, 5, 7.5 and 20 degrees. The 0, 5, and 7.5 degree views look down into the convolute; primarily they view the cathode, gap, and anode, respectively. Additionally, the probe can be installed in reverse, which allows the probe to view the cathode outside of the convolute region. The 20 degree view only observes the plasma inside of the B-dot cup. The secondary location, shown above in Fig. 5.6b,

was also used with the 0 and 7.5 degree probes. The actual view used for each shot is shown along with the data in chapter 6.

The probe utilizes a fiber within the vacuum chamber (probe fiber) which was typically 2.4 m or 3.7 m. This fiber is connected to one side of a 1.5 m fiber optic vacuum feedthrough (feedthrough fiber). The other end of the feedthrough is connected to a 29.9 m fiber connecting to the diagnostic (transit fiber). The probe fiber was destroyed on each shot; thus a new probe fiber was used for each shot. The exact length of the total fiber run was measured with an optical time domain reflectometer (OTDR). There is a wavelength dependent propagation time in the fiber. This effect is on the order of a few ns for this fiber length [54].

5.2.2 Calculated Probe Collection Efficiency

The limiting aperture of the probe was varied from 0.5 mm diameter to 2.0 mm diameter. The limiting aperture forcibly under-filled the fiber for all diameters chosen. Increasing the diameter of the aperture increased the sensitivity of the probe, but decreased the spatial resolution of the measurement. For a large planar light source, the light collected by the probe is described by

$$A_{source} = \pi \left(\frac{L_s D_a}{2L_a}\right)^2 \tag{5.1}$$

$$\Omega = \frac{\pi D_f^2}{4L_s^2} \tag{5.2}$$

$$\Omega_{total} = \Omega * A_{source} = \frac{\pi^2 D_a^2 D_f^2}{16 L_a^2} \tag{5.3}$$

where A_{source} is the area of the source, L_s is the distance from the source to the fiber, L_a is the distance from the end of the aperture to the fiber, D_a is the diameter of the aperture, D_f is the diameter of the fiber, D_s is the diameter of the source, and Ω_{total} is the total solid angle subtended by the fiber summed over the entire area of the source. Fig. 5.7 shows the geometry used in the above equation.

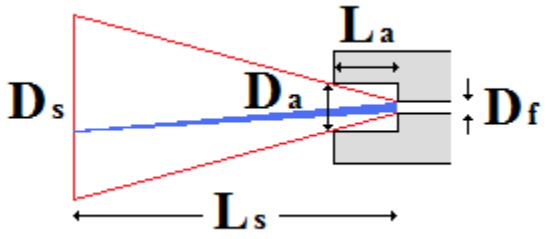

Fig. 5.7 Schematic showing the collection geometry of the probe. The source is assumed to be a uniform planar source that emits isotropically. The distance L_s is assumed to be much greater than D_a such that the solid angle subtended by the fiber with diameter D_f can be described as $D_s^2/(16L_s^2)$.

The probe views one cone completely and a second larger cone partially. This is shown schematically in Fig. 5.8. For a fixed aperture size, and a larger fiber diameter, the "complete" cone narrows slightly, while the "partial" cone expands. The light collected by the partial cone is described by

$$\Omega_{total} = \int_{R_{smin}}^{R_{smax}} \Omega(R_s) * 2\pi * dR_s \tag{5.4}$$

where $\Omega(R_s)$ is the solid angle subtended by the fiber at a given radial location in the source, R_{smax} is the largest radial point in the source from which any light can reach the fiber, and R_{smin} is the largest radial point in the source from which all of the fiber is visible. For the case of a 100 micron fiber and a 0.5 mm aperture with a uniform planar

light source, this accounts for ~33% of the total signal collected. This analysis ignores reflections off the inside of the B-dot cup.

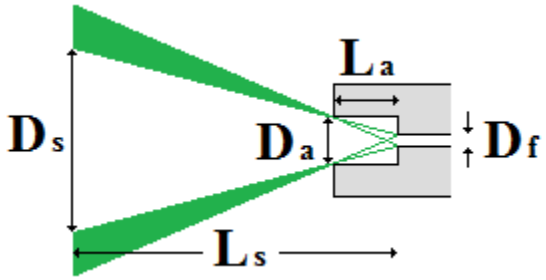

Fig. 5.8 Schematic showing the region of the collection cone that is only partially viewed by the fiber. At Ds/2, the fiber is not obscured by the aperture; when the radial location of the source is increased, the aperture obscures more of the fiber until the source location is outside of the field of view of the fiber.

5.2.3 Diagnostic Calibration

A fiber-coupled spectroscopic system must be calibrated to take into account the wavelength dependent losses associated with the collection optics, the fiber optic run, any relay optics, the spectrometer, and the detector, which in this case is a streak camera with a gated MCP output recorded on film. The efficiency of each component in the diagnostic can be determined individually, or a sub-set of the components can be calibrated through at the same time [55]. For these experiments, the efficiency of the collection optics was measured separately from the efficiency of the rest of the system (fiber through to film).

In order to absolutely calibrate a spectroscopic diagnostic, a light source of known intensity as a function of wavelength must be measured by the diagnostic. The response of the diagnostic to the known light source gives the calibration factor as a function of wavelength that must be applied to the data. Ideally, the diagnostic is calibrated with

identical settings to the shot. In the case of a very intense experimental signal, a well characterized light source of similar intensity can be difficult to find.

Black body spectral calibration sources emit a spectrum that can be well known, but they are typically not intense enough to provide an adequate signal. In order to artificially increase the diagnostic response to a calibration signal, the MCP gain can be increased, or the spectrum can be recorded many times. The flaws with both of these techniques are discussed below.

DC arc lamps are commonly used as the spectral calibration source for high signal intensity applications. In an arc lamp, the arc is typically large compared to the distance from the source to the detector, i.e. the source cannot be treated as a point. The arc does not emit a power uniformly throughout its volume, thus the signal measured is dependent on which region of the arc the detector views. As a result arc lamps are not well characterized in spectral intensity, so the intensity must be measured as a function of wavelength using a power meter. In order to properly determine the calibration, the collection end of the component being calibrated must be placed at the same location and view the same region of the arc as the power meter.

Typically, the power meter is calibrated for a specific wavelength, so a bandpass filter is placed between the arc lamp and the meter to only allow that wavelength through. The same setup must be used for the component being calibrated. Each of these measurements provides a signal point where the a calibration factor is known, but this cannot be done for all wavelengths in the spectrum of interest, so typically a set of

calibration points are collected and some form of interpolation or line fitting is used to determine the calibration factor for the points in between. It is important to note that an arc lamp spectrum may contain discrete lines, which can result in a skewed measurement if they fall within the bandwidth of one of the filters. It should also be noted that arc lamps can generate outputs up to 1 kW, but this is spread over a few hundred nm and 4π steradians; often the bandpass filters must have a 10 nm full-width at half-maximum (FWHM) in order to provide sufficient signal, and in some cases it is still inadequate for calibrations. For a larger FWHM, the signal will be greater but so will the error in measured signal intensity. One final note about using high powered DC arc lamps: there is a significant hazard associated with the operation of these devices, which inherently makes operation of them more difficult and less desirable.

An array of lasers at various wavelengths can also be used as a calibration source. Similarly to using an arc lamp for calibration, lasers can only provide a series of discrete points at which the calibration factor is known. However, the lasers used for calibration operate at a well-known, discrete wavelength, thus the power meter measurement of the intensity can be made more accurately. An array of lasers is an advantageous calibration source because the power per wavelength can be more than an order of magnitude greater than high power DC arc lamps. The directionality of the lasers is both a positive and a negative. It further increases the available signal passing through the system, but the collection optics may not behave the same with highly directionalized light as they do with the experimental signal. For class 3a or 3r lasers and below, there are no significant safety restrictions that would limit operation of the calibration source.

5.2.3.1 Laser Power Measurements

In order to use an array of lasers as the calibration source for the diagnostic, the laser power should be stable, and the level of fluctuation must be well known in order to quantify the uncertainty in the calibration. Each of the four lasers (two diode, two HeNe) was coupled to the power meter with the wavelength set to 544, 633, 650, or 670 nm depending on the laser being measured. The power output was measured once every 10 seconds for 5 minutes; the power for each laser is given in Table 5.1. The power stability of each laser was better than 2%, thus they can effectively be used as a calibration source.

Table 5.1 Five minute time-averaged power for the four lasers used in the calibrations. The laser power was measured once every 10 seconds for 5 minutes with the power meter. All four lasers showed standard deviations of less than 2% for the 5 minute average.

Wavelength [nm]	Laser power [μW]	Power Stability [%]
535	133 +/- 2	1.7
633	342 +/- 1	0.3
658	578 +/- 3	0.5
674	638 +/- 8	1.1

Diode lasers can fluctuate in wavelength as well. Since the power meter relies on knowing the input wavelength, it is important to know the laser wavelength at the time of the measurement. In this case, the exact wavelength was not easily known, so a reasonable substitute was to know how the power meter reading varies with wavelength. The 650 nm diode laser was coupled into the power meter, and the

wavelength was shifted from 640 nm to 660 nm in 1 nm increments. The measured power versus wavelength is shown in Fig. 5.9a. This process was repeated with the 670 nm diode laser; the power meter wavelength range for this case was 660 nm to 680 nm. These data are plotted in Fig. 5.9b.

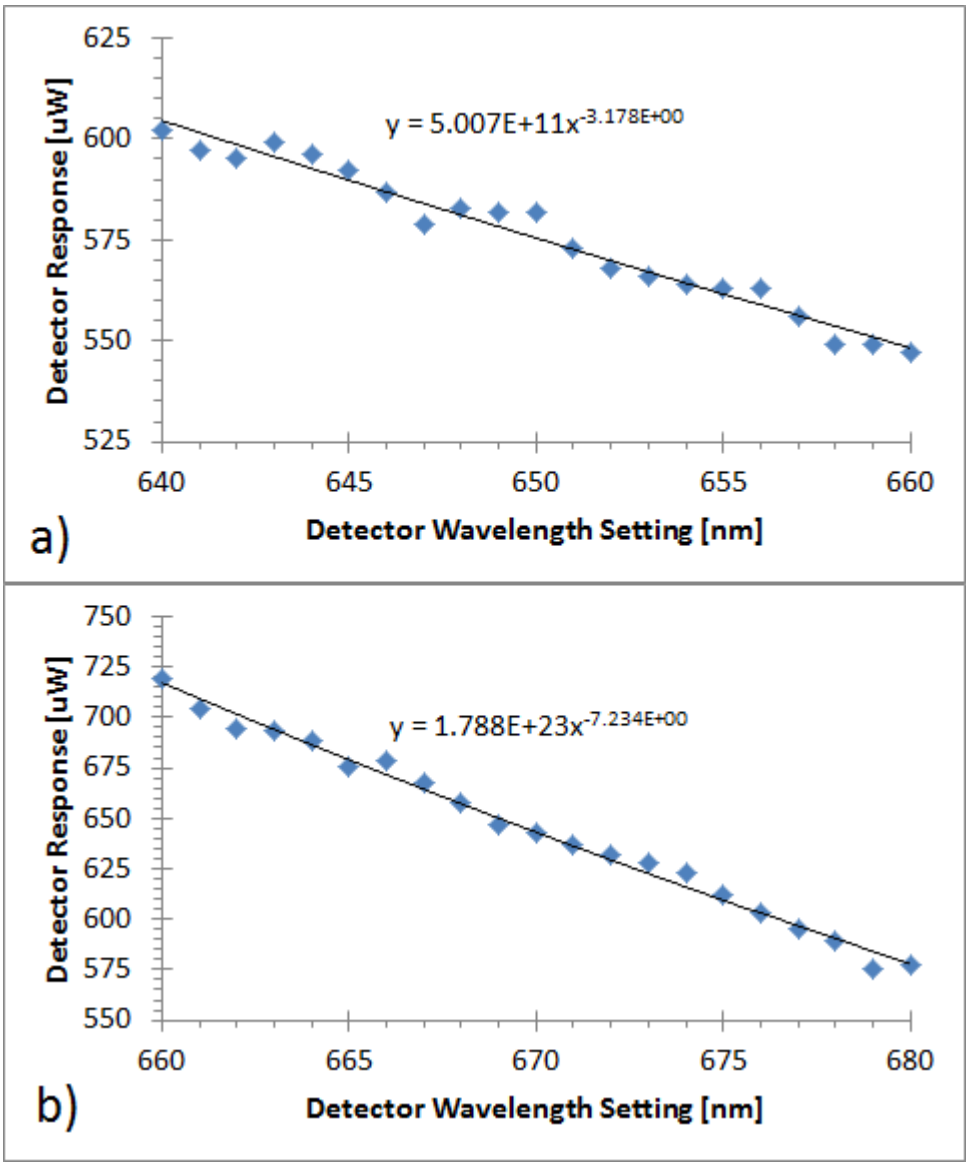

Fig. 5.9 Comparison of detector response versus wavelength setting for the power meter. Plot a) shows the results from the nominal 650 nm diode laser, and plot b) shows the results from the nominal 670 nm diode laser. A line was fit to each data set, and the equations were used to correct data that were collected assuming the laser was 650 nm (or 670 nm) after the correct wavelength had been determined.

5.2.3.2 Step Wedge Film Response Correction

Film does not respond linearly to exposure throughout its entire dynamic range; the response is fairly linear at the center of the range, but rolls off as it approaches both low and high levels of exposure. This is often referred to as an "s-curve." In order to compensate for the effect that the non-linear response has on the data, a neutral density (ND) step wedge is placed between a flash lamp and a piece of TMax 400 film. When the flash lamp emits, the regions of the film are exposed to light of varying intensity as a result of the different levels of ND. The ND opacity for each step is well known, thus, while the intensity of the flash lamp is not well known, the expected difference in intensity between two steps is well known. The step wedge film is developed at the same time as the data to ensure that the chemical processes are identical, thus the step wedge can be used to determine the relative intensity reaching the film from the film response.

5.2.3.3 Streak Camera Flat Field

A flat-field test was performed to determine the film response to a uniform illumination of the streak camera entrance slit. This type of test is useful in determining if there are any defects in the photocathode at the input of the streak camera or in the gated MCP and phosphor on the output of the camera. A defect in the photocathode would result in a non-uniformity on the film that was relatively constant in time (i.e. a vertical band that is lighter or darker than the surrounding region). A defect in the MCP or phosphor

would result in spotting that is localized on the time and space axes. The flat-field can also be used to determine the streak camera response throughout the sweep (i.e. does the signal intensity vary as a function of time for a uniform light source). The flat field image is shown in Fig. 5.10a, a series of horizontal lineouts (fixed time) are plotted in Fig. 5.10b, and a series of vertical lineouts (fixed wavelength) are plotted in Fig. 5.10c.

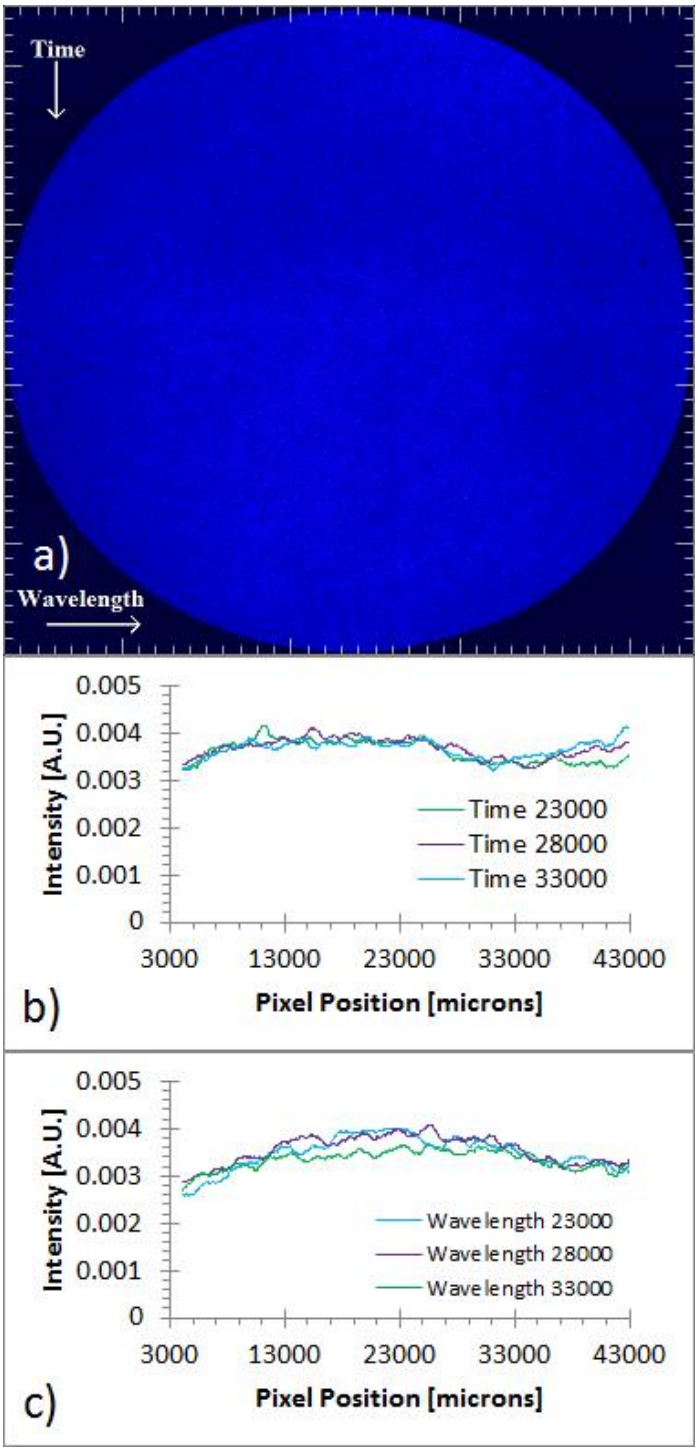

Fig. 5.10 a) Flat-field image obtained with the streak camera when the entrance slit was uniformly illuminated with a white light source. b) Horizontal lineouts of the image at three vertical locations. There is an approximately 5% drop in response at approximately pixel position 27000, which is consistent for all three line outs. c) Vertical lineouts of the image at three horizontal locations. The signal has a roughly parabolic shape; the peak signals occurs at approximately pixel position 23000 and the drop in signal is as much as 20% at very early and late times.

The flat-field contains some spotting, but this may be the result of a low photon count. There is on the order of a 5% dip in the signal from horizontal pixel position 27000 to 37000. The vertical lineouts show a more significant effect on the signal near the edges of the sweep. The difference in signal between the peak position and the edges is on the order of 20%.

5.2.3.4 Linearity of Streak Camera Response

The response of the streak camera may not be linear with intensity. In other words, the streak camera response to an input intensity, 2I, is not necessarily twice the response it produces for in input intensity, I. Additionally, there may be some threshold intensity below which the streak camera will not respond. In an effort to test this, a 632.8 nm HeNe laser was coupled through the spectrometer onto the streak camera entrance slit. Various laser intensities were used as given in Table 5.2. All exposures were done with the same piece of film, which required shifting the streak camera horizontally between shots. Care was taken to ensure that the light from the spectrometer did not get clipped by the entrance slit of the streak camera.

Table 5.2 Laser powers and film response values for the calibrations testing the linearity of film response to the input laser energy. The normalized values for the laser power and film response that were plotted in Fig. 5.11 are also included. It is clear from the data set that the streak camera response cannot be assumed to be linear with no threshold value.

Laser power [μW]	Normalized Laser Power	Film Response [A.U.]	Normalized Film Response
80	0.107	77.4	0.042
145	0.193	220	0.119
250	0.333	448	0.241
300	0.400	535	0.288
390	0.520	853	0.459
505	0.673	1170	0.632
625	0.833	1660	0.894
750	1.000	1860	1.000

The area under each peak was integrated to get the total film response to the input photons. These values were normalized and plotted versus the normalized input laser intensity as shown in Fig. 5.11. The data follow a linear trend with a positive offset. This indicates that the streak camera response is linear with intensity, but that there is a threshold intensity, below which the signal cannot be recorded.

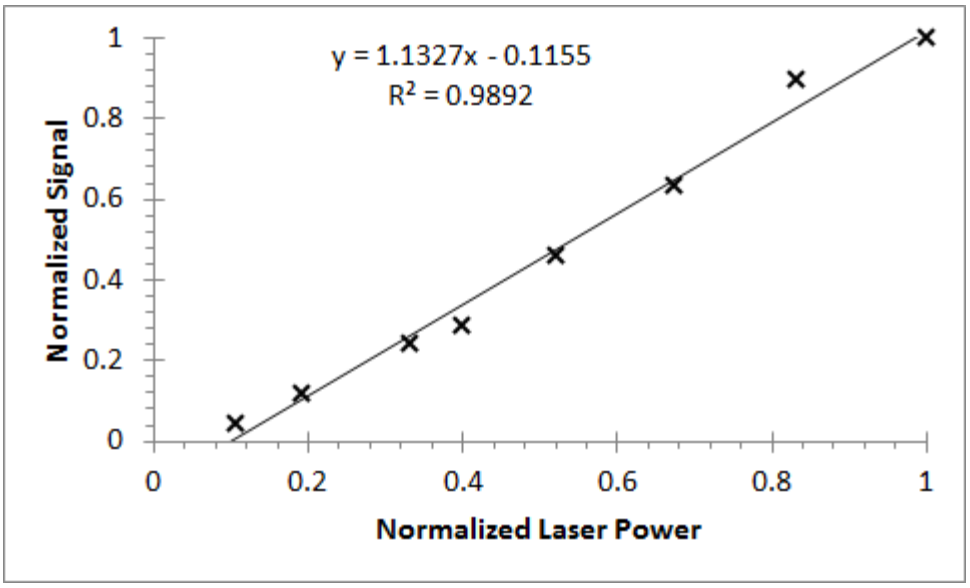

Fig. 5.11 Plot of the normalized film response versus normalized laser power for these tests. Based on the data, it was assumed that there was a threshold intensity below which the streak camera response was negligible.

5.2.3.5 Repeated Exposures

Statistically speaking, a low intensity light source with a well-known spectral output could be used to expose a detector many times, thus giving a similar total photon flux to a more intense light source [56]. There are two options for the repeated exposure when using film as the final detector. The first is to expose each piece of film once and use an extremely large amount of film. This method is both monetarily and temporally expensive, which makes it not a realistic option. The second option is to expose the same piece of film multiple times. The advantage of this method is only one piece of film need be loaded, developed, and scanned.

In order to test if this is a viable method of calibration, a piece of film was exposed multiple times at the same location to determine the effect of overlaying multiple

exposures. Specifically, the spectrometer was set to be centered at 632.8 nm, and a 0.75 ± 0.005 mW, 632.8 nm, HeNe was sent into the input of the spectrometer and the film was exposed. The streak camera was shifted horizontally such that none of the spectrometer settings were changed but a new region of the film would be exposed. It was verified that the light from the laser was still entering the streak camera without clipping on the entrance slit. A piece of ~ 0.7 ND filter was placed in front of the laser in order to reduce the laser power entering the spectrometer to 0.15 ± 0.005 mW. At this setting the streak camera was fired 5 times at 1 second intervals, thus approximately the same number of photons reached the film as in the previous case. The streak camera was shifted horizontally a second time, and an additional piece of ~ 0.7 ND filter was placed in front of the laser (1.4 ND total), which further reduced the laser power entering the spectrometer to 0.03 ± 0.005 mW. The streak camera was fired 25 times, which, again, allowed approximately the same number of photons to reach the film as the first case.

The total number of photons reaching the film was calculated using the following equation

$$N_{total} = m * N_{streak} = m * \frac{P_{laser} * t_{collection}}{\left(\frac{hc}{\lambda}\right)} \tag{5.5}$$

where N_{total} is the number of photons reaching the film, m is the number of times the streak camera is fired with the same piece of film, N_{streak} is the number of photons reaching the film per streak, P_{laser} is the laser power, $t_{collection}$ is the duration of the sweep over which the photons are counted, h is Planck's constant, c is the speed of light, and λ is the wavelength of the photons. The number of photons reaching the film (normalized

to 1) and the normalized response of the film is plotted for the three cases in Fig. 5.12. The film response is well outside of the uncertainty in the power measurements; therefore, these data show that the film response drops off with multiple overlaid exposures. Thus, overlaying exposures is not a viable option for increasing signal from a low intensity calibration source.

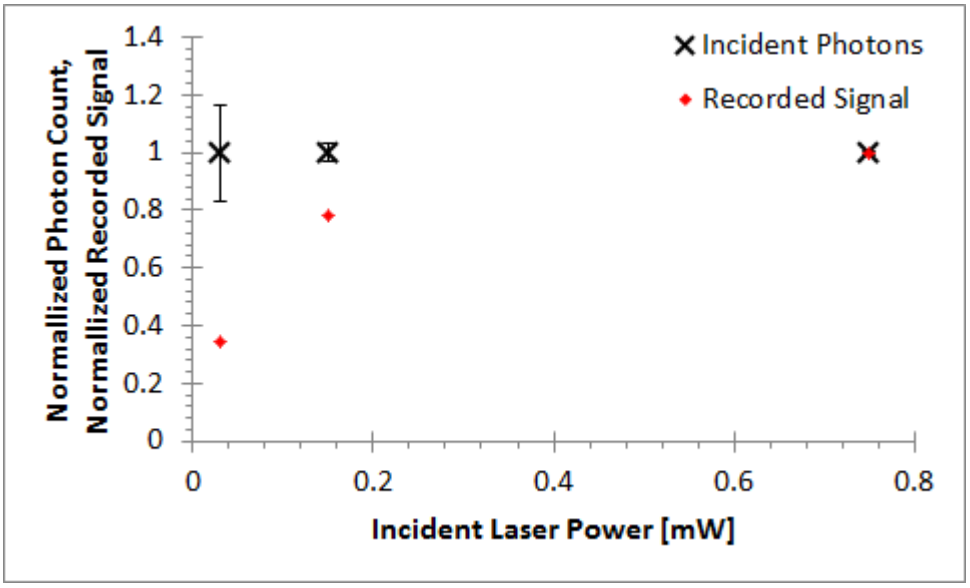

Fig. 5.12 A plot of the recorded signal on the film and number of photons reaching the film for three cases: a single 750 μW sweep, five 150 μW sweeps, and twenty-five 30 μW sweeps. In each case, the total number of photons reaching the film should be the same, with the exception of the uncertainty in the measured power. The recorded signal on the film does not match the photons collected. When multiple signals are overlaid, they do not cause the film to respond in the same way that a single sweep with an equivalent number of photons would.

5.2.3.6 Microchannel Plate Gain Response

The MCP at the output of the streak camera has an adjustable gain. Thus, for a given input signal, the film response is dependent on the MCP gain setting. It is a valuable exercise to determine the film response as a function of the MCP applied voltage. The

relationship between MCP voltage and the signal on the film is useful in determining experimental settings.

A 632.8 nm HeNe laser was coupled through the spectrometer onto the input of the streak camera. ND filters were used to reduce the laser power to 0.14 mW and 0.08 mW for the two sets of measurements. At 0.14 mW, the MCP voltage was set to 425 V, the streak camera was fired and then shifted horizontally, the voltage was increased by 25 V, and the process was repeated until the voltage reached 600 V. The laser power was decreased to 0.08 mW and the MCP voltage was set to 500 V, and the above process, again, was repeated until the voltage reached 600 V.

A temporally integrated lineout was taken across the film, the counts per peak were recorded and have been plotted in Fig. 5.13 versus the applied MCP voltage for both the 0.08 mW and 0.14 mW cases. Fitting a power function to each data set yields an equation of the form

$$y = Ax^b \tag{5.6}$$

where A is a constant based on the input laser power, b = 9.84 for the 0.14 mW case and b = 9.44 for the 0.08 mW, x is the MCP applied voltage and y is the film response. This indicates that the relationship between input voltage and signal output is roughly x^{10}, which is the commonly quoted value.

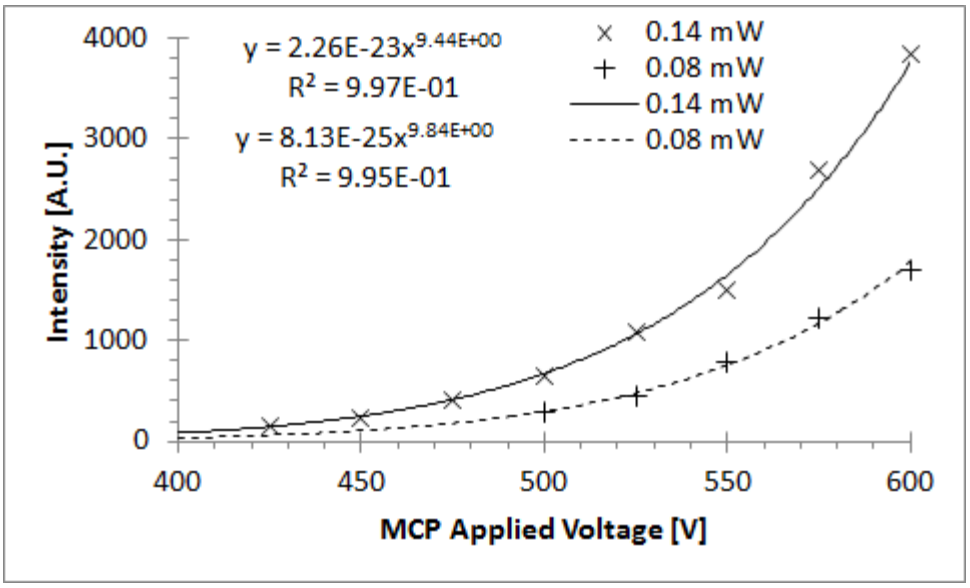

Fig. 5.13 Plot of the Intensity of the film response as a function of the voltage applied to the MCP. Two cases are shown; one with 0.14 mW input laser power and the other with 0.08 mW. The intensity is proportional to the voltage to the 9.44 and 9.84 respectively. The difference in these values implies that there is a dependence of the exponent on the input intensity. Further tests at additional input intensities are necessary to confirm this.

5.2.3.7 Experimental Calibration Shots

Each experimental setup requires a calibration shot to determine the wavelength dependent response of the system. Ideally, calibrations would be performed prior to each shot with the fibers and connections used during the shots. This was not possible giving the time and resources available for these experiments. As a result, a calibration was performed for each combination of fiber lengths/diameters used. The calibrations were performed using four lasers, two were HeNe lasers at 543.5 nm and 632.8 nm and the other two were diode lasers at 650 ± 10 nm and 670 ± 10 nm. Each laser's power was attenuated using ND filters such that it would show a clear, distinct line on the film in the roughly linear region of the s-curve (avoiding saturation).

The following procedure was repeated for all four lasers. The power meter was set to measure the wavelength of the laser being used. The power was measured before entering a secondary transit fiber (~ 30 m) going up to the probe fiber (point A), which was connected through the chamber and feedthrough fibers to the primary transit fiber as shown in Fig. 5.14. The power at the other end of the fiber chain (point C) was also measured. The end of the primary transit fiber was then connected to the spectrometer jumper fiber, and the streak camera was fired. The power was measured again at both point C and point A to verify that the power had not significantly changed.

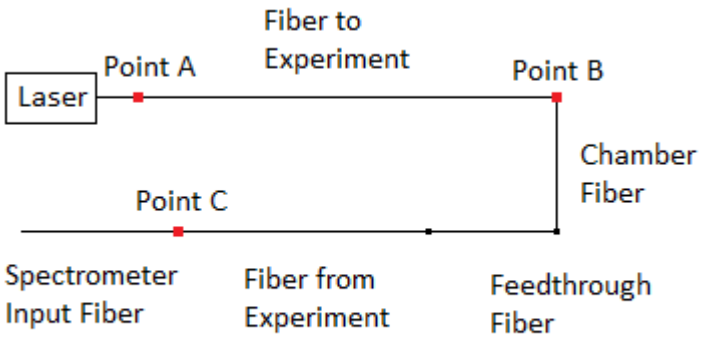

Fig. 5.14 Schematic diagram showing how the fibers were connected during the calibrations and the locations at which the power was measured (points A, B, and C shown in red).

After processing the film, the exact wavelengths of the diode lasers were determined. The measured laser power at points A and C from above was corrected using the curves from the power meter reading versus wavelength. The nominally 650 nm laser was actually 658 nm, and the nominally 670 nm laser was actually 674 nm.

A series of measurements were performed to correct for the attenuation due to the secondary transit fiber. In these measurements, the power was measured at point A,

point C, point B, and then at point C and point A a second time. All 5 measurements were made within a 3 minute period, thus the power fluctuations should have been similar to those observed in the 5 minute power stability tests. These measurements were made for each of the four lasers and for the four different fiber optic setups. The signal attenuation at each point for each setup and each laser is listed in Table 5.3. Based on these measurements, the power input into the system for the calibrations was adjusted to account for the attenuation due to the secondary transit fiber.

Table 5.3 The fraction of input laser power measured at points B and C for the 4 wavelengths used in the calibrations. The values are tabulated for the three fiber optics configurations used in the experiments.

100 micron diameter fiber, 12 foot long chamber fiber				
Wavelength [nm]	544	633	658	674
Point B	0.844	0.867	0.899	0.837
Point C	0.550	0.599	0.612	0.571
200 micron diameter fiber, 12 foot long chamber fiber				
Wavelength [nm]	544	633	658	674
Point B	0.856	0.862	0.942	0.967
Point C	0.428	0.521	0.591	0.596
200 micron diameter fiber, 8 foot long chamber fiber				
Wavelength [nm]	544	633	658	674
Point B	0.813	0.847	0.933	0.952
Point C	0.422	0.526	0.609	0.632

5.2.4 Background tests

The probe used in these spectroscopic measurements was located within 25 cm of the most powerful x-ray source in the world. Radiation from the z-pinch could interact with

the fiber optic cable creating Cherenkov radiation fluorescence. As a result, there was some concern over the background that would be superimposed on the data. In order to determine the effect that the x-ray source would have on the fiber used in the probe, a series of null experiments were performed.

The background (or null) tests were fielded using the geometry shown in Fig. 5.15. One end of the fiber was connected to the feed through as usual; the other end of the fiber was covered with a piece of copper tape to prevent light from being collected. The fiber was placed in the chamber so the copper taped end was located directly next to the B-dot hole where the probe normally was fielded.

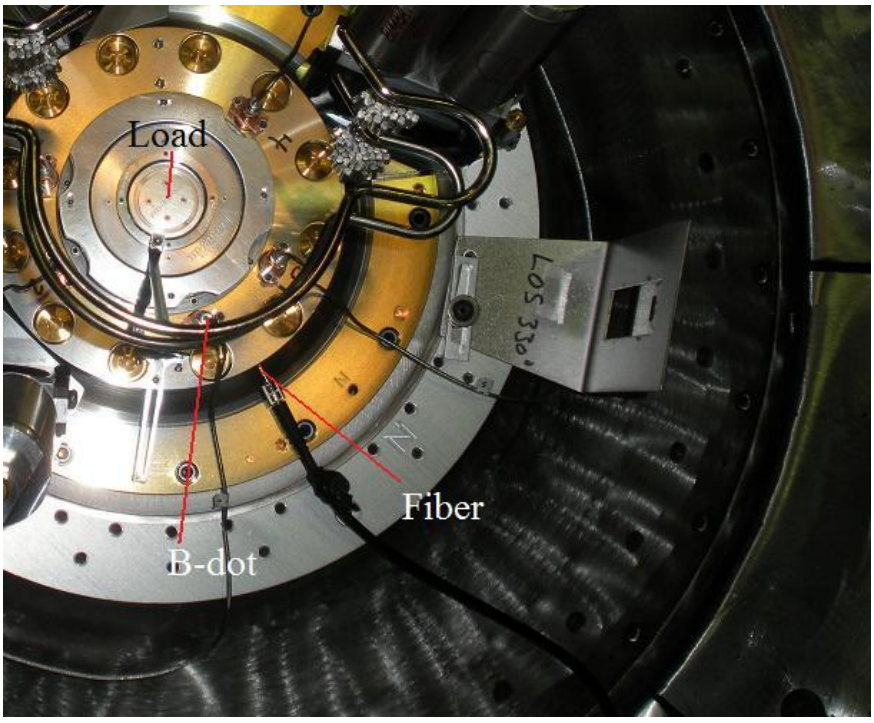

Fig. 5.15 Picture of the chamber fiber during a background test. The end of the fiber is covered with copper tape to prevent any light from entering the fiber; this end of the fiber is located next to the B-dot, thus it receives a similar radiation dose as it would during a shot that observes the convolute.

Two of the background tests were conducted on Lincoln shots (high mass imploding liners, relatively low x-ray yield), and one test was conducted on a C7 shot (high velocity wire array implosion, more intense and harder x-ray yield). On one of the Lincoln shots, the probe fiber was shielded using ~ 1 mm thick flexible steel tubing, and on the other shot, the fiber was unshielded. The streak images from the Lincoln shots are shown in Fig. 5.16a and b. The unshielded fiber had an unacceptable background level due to the x-ray interactions in the fiber; the shielded fiber had a negligible background level.

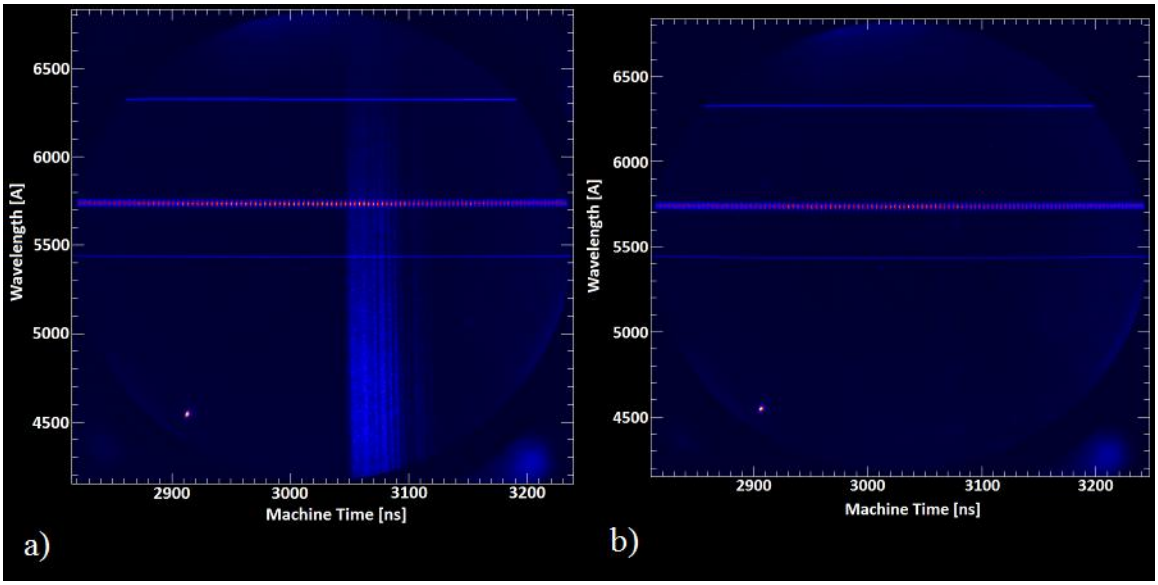

Fig. 5.16 Background tests on two Lincoln shots (imploding solid liner – shots 2058 and 2060). In a) no shielding was used and there is an observable signal starting at 3050 ns and persisting until 3100 ns, at which point it fades but is still visible until 3130 ns. In b) the flexible steel tubing was used to shield the fiber and there is no observable signal. This indicates that the shielding is effective in eliminating the background for the Lincoln series shots.

While the shielding was adequate for reducing the background during a Lincoln shot, it may not have been sufficient to stop the x-ray flux produced in the C7 shots. Thus, an additional background test was performed during a C7 shot; these data are shown in Fig. 5.17. These data show that the background generated in the C7 shots is greater than

that in the Lincoln shots, but is small enough to not significantly affect the measurements.

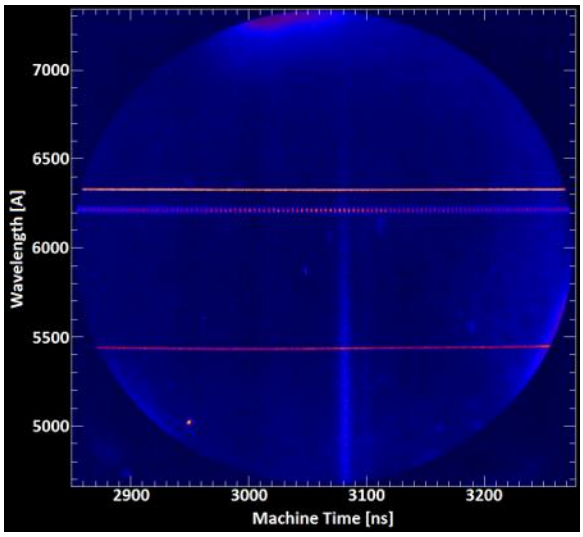

Fig. 5.17 Background test from a C7 shot (K Shell radiator load - shot 2123). At 3080 ns there is a dim emission signal that is the result of x-ray interactions in the fiber. The signal persists for approximately 10 ns. This shot used a gain ~ 60x higher than that used on a typical shot, and the signal was still relatively low, thus the background on K Shell Radiator load shots can also be neglected when using the fiber shielding.

The corrections applied to the data and the uncertainties associated with the calibrations are described in Appendix D.

CHAPTER 6

Z-MACHINE EXPERIMENTAL RESULTS

In this chapter are presented the raw data from experiments performed on the Z-machine at Sandia National Labs. These experiments were performed as "ride-along" experiments so the choice of parameters and diagnostic locations were not always optimal for convolute studies. Line-outs, temporal evolution of diagnostic signals, and analysis of these data are presented in Chapters 7 and 8.

It will be shown that the primary feature of the measurements was the strong continuum. Additionally, on many shots spectral lines were observed in absorption. This indicates very dense optically thick or long plasmas. The lack of even weak emission lines early in the pulse was surprising. This may indicate the sensitivity and collection efficiency of the probe should be improved. Additional issues include a complex geometry, limited flexibility in probe location, the possibility for optical reflections, and low spatial resolution of the probe. The effect of these issues on the observed signal needs to be evaluated.

Many different configurations were used to conduct the different sets of experiments as described in Table 6.1 and Table 6.2. Shots 2058, 2060, and 2123 were used to determine

the background signal. Shots 2062-2076, 2081, 2106, 2108, and 2119 were used to determine the spectral features for various views. Shots 2077, 2079, and 2080 were used to determine the emission timing in the convolute. Shots 2078, and 2120-2122 were used to determine the effect of diagnostic sensitivity on the spectrum. Shots 2082, 2083, 2107, 2110, 2116, and 2118 were used to study the H-alpha absorption feature in greater detail. Shots 2104 and 2105 were used to determine the effect of plasma within the B-dot cup. Shots 2115-2118 utilized localized dopants in the convolute to verify the location of the observed signal.

Table 6.1 List of first 15 shots in which the emission from the Z-Machine post hole convolute was measured. This diagnostic was fielded on a total of 30 shots over 7 shot series. The table describes the experimental/diagnostic configuration for each shot. The time stated in the load column is the nominal current risetime. The diagnostic settings column includes the diffraction grating and the sweep duration.

Shot #	Load	CLPD View	Diagnostic Settings	Dopant Location	Shot Objective
2058	Lincoln (100 ns)	N/A	150 G/mm 480 ns	N/A	Background
2060	Lincoln (100 ns)	N/A	150 G/mm 480 ns	N/A	Background
2062	Lincoln (100 ns)	Cathode	150 G/mm 480 ns	N/A	Spectral components
2063	Taos (100 ns)	Cathode	150 G/mm 480 ns	N/A	Spectral components
2064	Lincoln (100 ns)	Anode	150 G/mm 480 ns	N/A	Spectral components
2065	Taos (100 ns)	Anode	150 G/mm 480 ns	N/A	Spectral components
2075	C7 (100 ns)	Gap	150 G/mm 480 ns	N/A	Spectral components
2076	C7 (100 ns)	Cathode feed gap	150 G/mm 480 ns	N/A	Spectral components
2077	C7 (100 ns)	Cathode	150 G/mm 120 ns	N/A	A-K gap closure
2078	C7 (100 ns)	Cathode	150 G/mm 120 ns	N/A	Emission turn-on time
2079	C7 (100 ns)	Anode	150 G/mm 120 ns	N/A	A-K gap closure
2080	C7 (100 ns)	Gap	150 G/mm 120 ns	N/A	A-K gap closure
2081	C7 (100 ns)	Below	150 G/mm 240 ns	N/A	Spectral components
2082	C7 (100 ns)	Gap	600 G/mm 240 ns	N/A	H-alpha high resolution
2083	C7 (100 ns)	Gap	1200 G/mm 240 ns	N/A	H-alpha high resolution

Table 6.2 List of last 15 shots in which the emission from the Z-Machine post hole convolute was measured. This diagnostic was fielded on a total of 30 shots over 7 shot series. The table describes the experimental/diagnostic configuration for each shot. The time stated in the load column is the nominal current risetime. The diagnostic settings column includes the diffraction grating and the sweep duration.

Shot #	Load	CLPD View	Diagnostic Settings	Dopant Location	Shot Objective
2104	Lincoln (100 ns)	B-dot cup (B5)	150 G/mm 240 ns	N/A	Spectral components
2105	Lincoln (100 ns)	B-dot cup (B2)	150 G/mm 240 ns	N/A	Spectral components
2106	Lincoln (100 ns)	Between posts	150 G/mm 240 ns	N/A	Spectral components
2107	Lincoln (100 ns)	Gap	600 G/mm 240 ns	N/A	H-alpha high resolution
2108	Union (200 ns)	Cathode	150 G/mm 480 ns	N/A	Spectral components
2110	Union (200 ns)	Gap	600 G/mm 240 ns	N/A	H-alpha high resolution
2115	Cibola (100 ns)	Anode	150 G/mm 480 ns	Top post-lower	Localized dopant
2116	Cibola (100 ns)	Anode	600 G/mm 480 ns	Top post-upper	H-alpha high resolution
2117	Cibola (100 ns)	Anode w/ lens	150 G/mm 480 ns	Top post-upper	Localized dopant
2118	Cibola (100 ns)	Anode	300 G/mm 240 ns	Top post-upper	Localized dopant
2119	C7 (100 ns)	Gap (horiz.)	150 G/mm 480 ns	N/A	Spectral components
2120	C7 (100 ns)	Gap (horiz.)	150 G/mm 480 ns	N/A	Spectral components
2121	C7 (100 ns)	Gap (horiz.)	150 G/mm 480 ns	N/A	Spectral components
2122	C7 (100 ns)	Anode (horiz.)	150 G/mm 480 ns	N/A	Spectral components
2123	C7 (100 ns)	N/A	150 G/mm 480 ns	N/A	Background

6.1 LiF Dopant Experimental Results

The post-hole convolute on the Z-machine both has a complex geometry and is made from reflective materials. Typically a non-specularly reflective gold coating is applied to the upper anode and cathode, and the remaining electrodes are polished stainless steel. This allows reflected light from many locations to reach the probe, which reduces the spatial resolution of the probe. This issue was resolved by depositing a small amount of a foreign material onto the convolute at a specific location. Since this material was not normally found in the convolute, any spectral emission or absorption features characteristic of the material can be attributed to the dopant. The localized nature of the dopant permitted the location of the continuum emission source to be more accurately determined.

Lithium fluoride (LiF) was used as the dopant to determine the location of light emission within the convolute. Specifically, lithium was the desired dopant because it has a strong ground state transition at 6708 Angstroms. LiF was used because lithium is highly reactive; LiF is more stable. Lithium has not been used in any previous convolute experiment, and previous spectra showed no spectral features around the 6708 Angstrom transition of interest.

Aside from determining temperature and/or density based on the line profile, the 6708 Angstrom Li transition is susceptible to Stark shift for fields on the order of 10 MV/cm [57-59]. Thus any shift in the line would allow the electric field to be determined within the convolute, and no shift in the line indicates an upper bound on the electric field. In

addition to the 2s-2p transition at 6708 Angstroms, lithium also has a somewhat weaker transition (2p-3d) at 6104 A. The relative intensity of these transitions gives some information about the temperature of the plasma, and the 6104 A transition Stark shifts at lower electric fields.

In these experiments, one of the top posts in the convolute was coated with a 1 mm tall, 1 micron thick, 360 degree band of LiF. The axial location of the coating was varied between the shots. Fig. 6.1a-c show the position of the LiF band and the region of the convolute viewed by the probe for three shots. The LiF was directly within the line of sight of the probe for one of the shots, but it was located further down in the convolute (Fig. 6.1b). For the other cases, the Li had to expand out into the post-hole gap in order to be observed (Fig. 6.1a, 6.1c). In each case, the probe was pointed at the same location within the convolute, but the field of view was varied by changing the fiber optic and limiting aperture diameters.

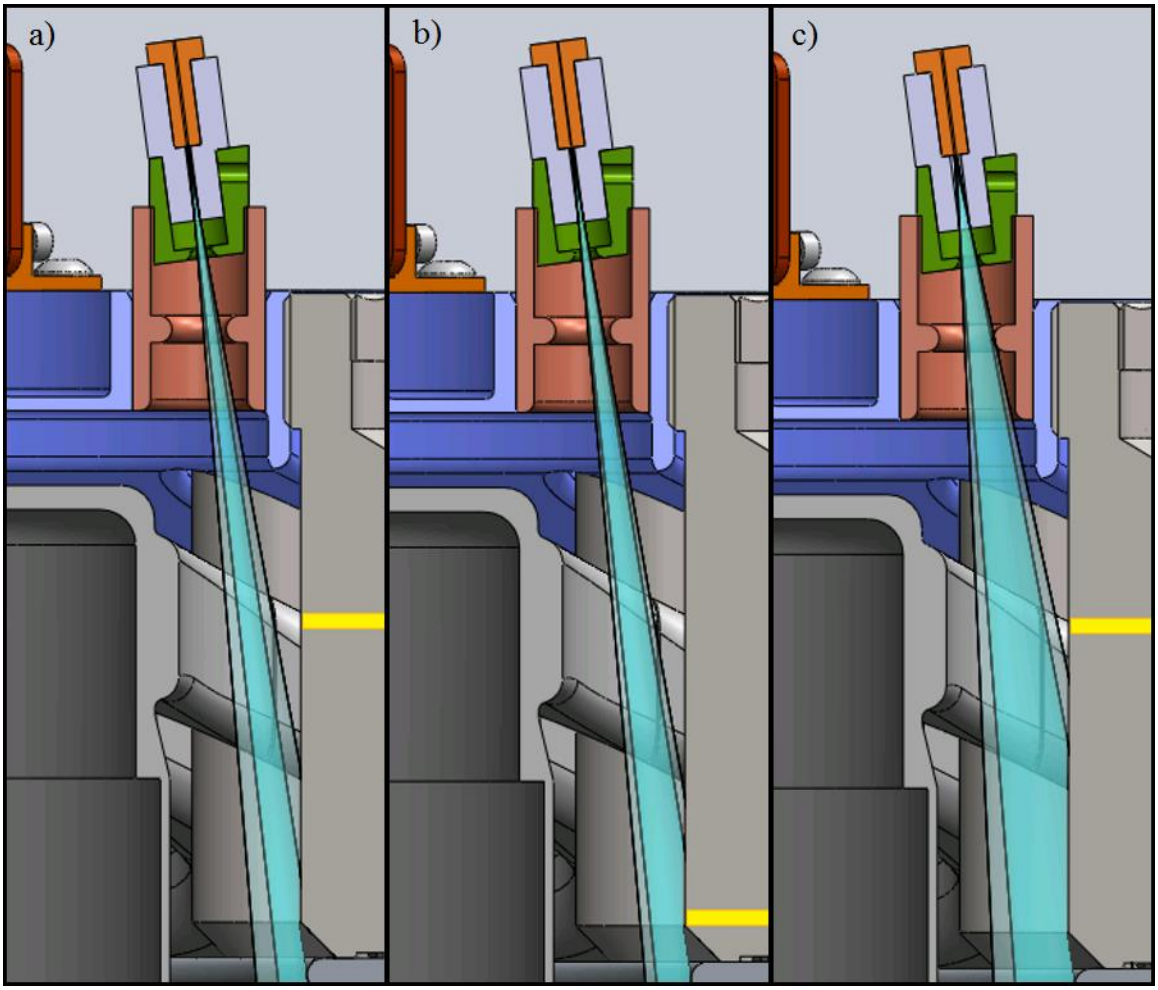

Fig. 6.1 Diagnostic views for the localized LiF dopant experiments: a) 200 micron diameter fiber with 500 micron diameter limiting aperture, LiF band located in upper position (axially centered in upper hole); b) 100 micron diameter fiber with 500 micron diameter limiting aperture, LiF band located in lower position (bottom of cylindrical portion of top post, directly viewed by probe); c) 200 micron diameter fiber with 1 mm diameter limiting aperture, LiF band in upper position. All cases used the "anode view" (7.5 degree probe). (SolidWorks models of the Z Machine courtesy of J. Cisneros and M. Vigil.)

The streak image for the case where the LiF is located at the top position on the post and the probe has a narrow view (Fig. 6.1a) is shown in Fig. 6.2. The image shows a strong continuum, which was observed on every shot, but no emission lines. Absorption features are superimposed on the continuum; this includes the Balmer series H-alpha transition at 6562 Angstroms and the Li 2s-2p transition at 6708 Angstroms. Both absorption features are observed at the start of the continuum and persist for the

duration of the streak sweep. The H-alpha feature broadens as a function of time; there is no obvious change in the shape of the Li transition. The Li feature remains at 6708 Angstroms for the duration of the sweep (i.e. no Stark shift). The spectral range of the diagnostic on this shot did not include the 6104 Angstrom Li transition.

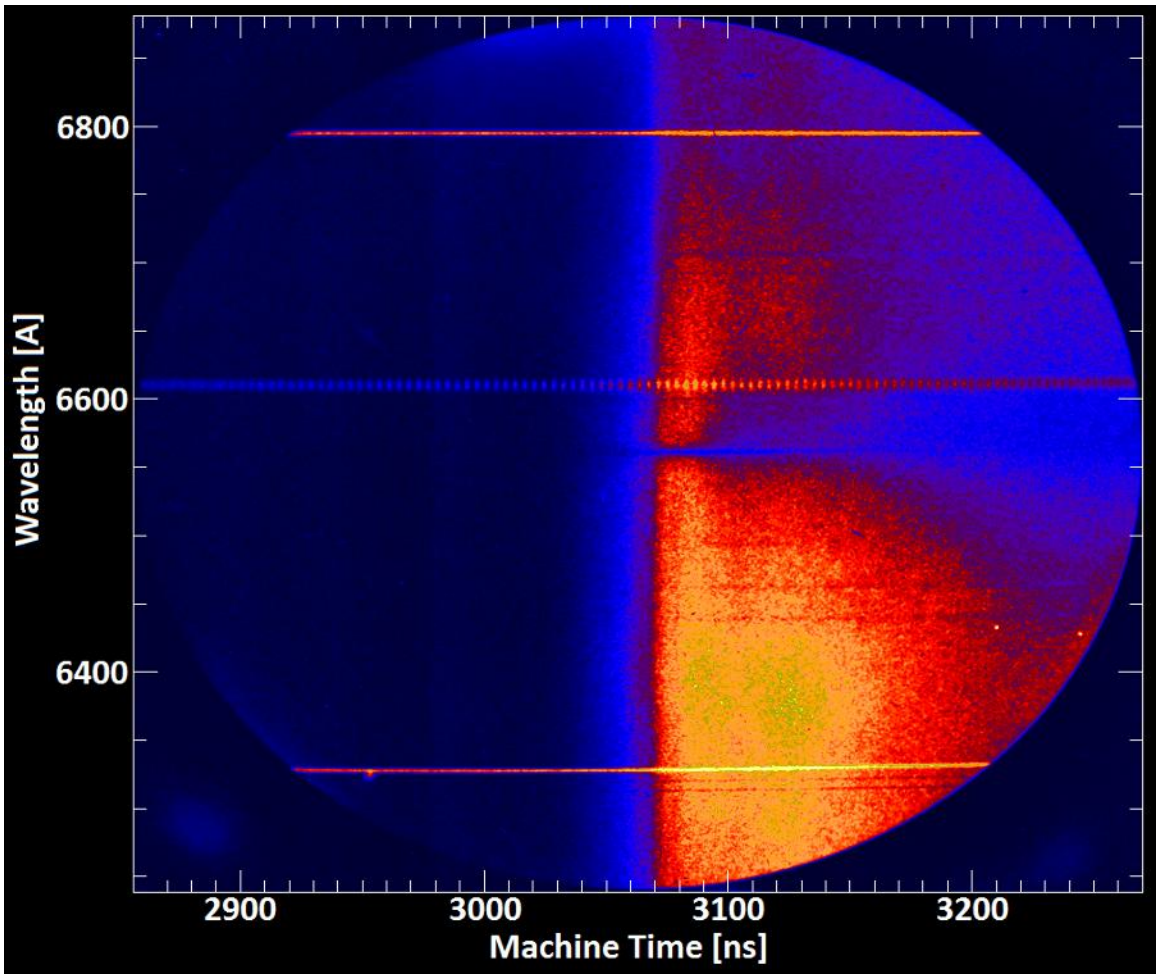

Fig. 6.2 Streak image obtained on Z Machine shot 2116. Early in time, no signal is observed. The continuum emission starts at approximately 3070 ns. There is an absorption feature at 6562 A (Hα) and one at 6708 A (Li-I 2s-2p).

For the shot with the LiF at the lower position (Fig. 6.1b), the spectrum looks similar to the previous case, but does not include the 6708 Angstrom feature. The spectral range for this shot included 6104 Angstroms, but the Li 2p-3d transition was also absent from

the spectrum. The streak image for this shot is shown in Fig. 6.3. The continuum and H-alpha feature are observed, as in the case above. Additionally, an absorption feature at 5890 Angstroms is observed. This is believed to be the sodium 3s-3p doublet. This feature was outside of the observed spectral range on the previous experiment, thus it could not have been observed. This feature was observed in the majority of the data sets collected (with the obvious exception of those observing a different spectral region). The most probable source of the feature is contamination due to perspiration. The transition is strong enough that a small quantity of sodium (perhaps from an improperly cleaned piece of hardware, or from handling during installation) would account for the observed signal.

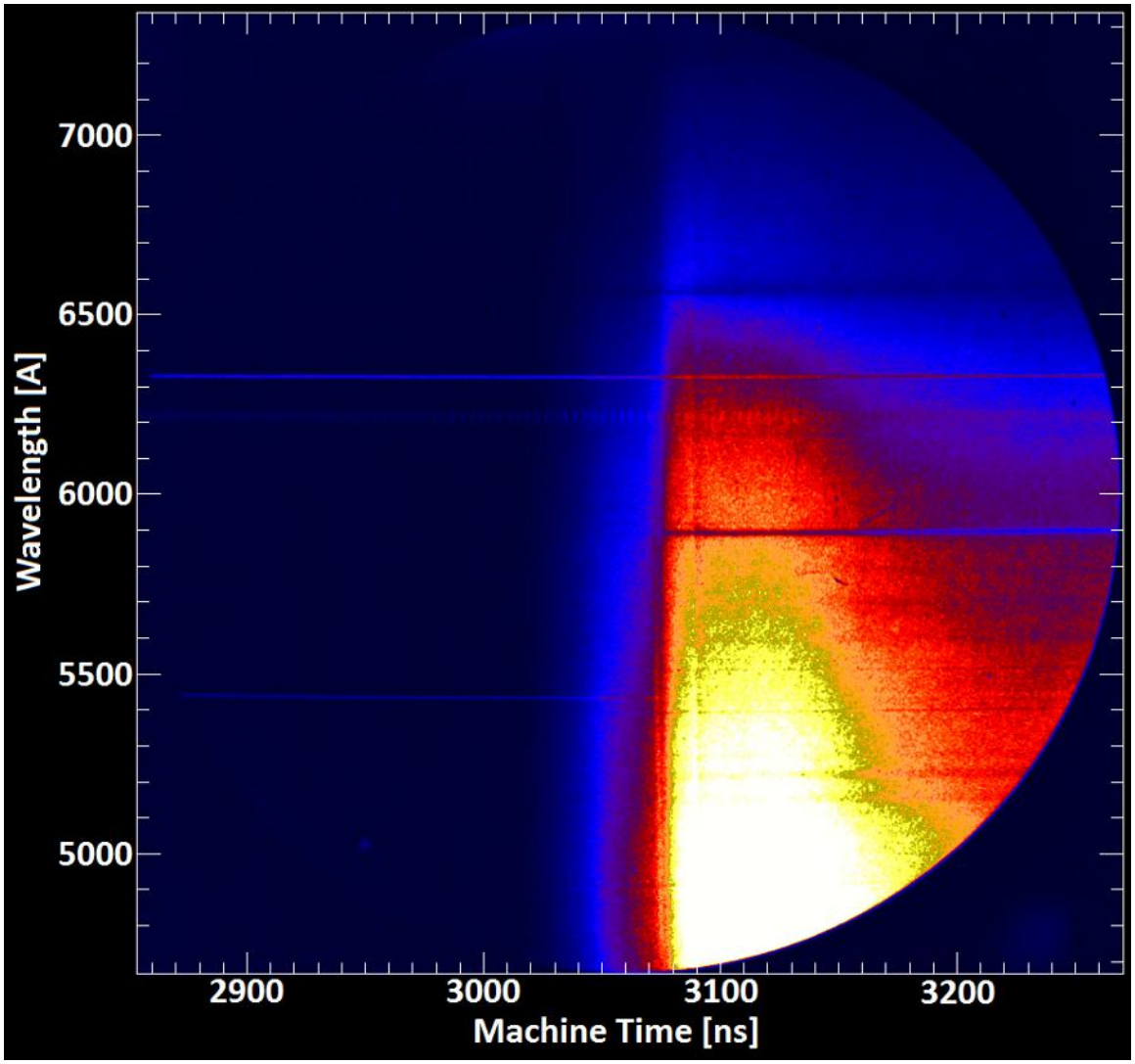

Fig. 6.3 Streak image obtained on Z Machine shot 2115. Spectral features are similar to those in shot 2116. No signal is observed until continuum emission starts at approximately 3070 ns. There is an absorption feature at 6562 A (Hα) and one at 5890 A (Na-I 3s-3p).

A second shot with LiF at the top position (view shown in Fig. 6.1c) yielded the streak image shown in Fig. 6.4. The region that the probe viewed was increased in order to improve sensitivity; the goal was to observe emission lines prior to the continuum turn on. However, these data looked similar to the other two; spectra consisted of continuum emission with absorption lines. The strong Li absorption feature was not observed.

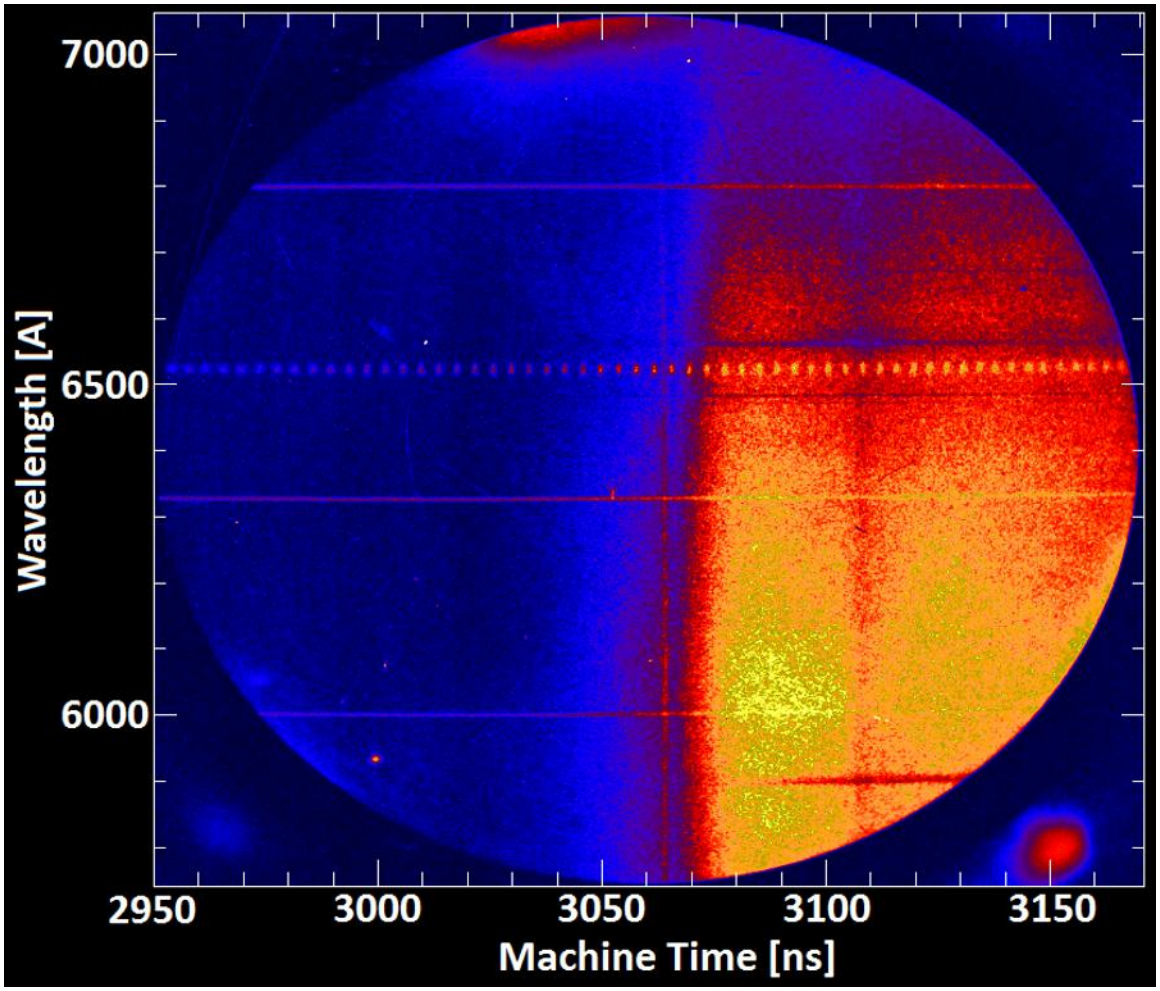

Fig. 6.4 Streak image obtained on Z Machine shot 2118. Spectral features are similar to those in shots 2115 and 2116. A sub-ns, broadband flash of light is observed at ~ 3065 ns; sustained continuum emission starts at approximately 3070 ns. There is an absorption feature at 6562 A (Hα) and one at 5890 A (Na-I 3s-3p). A faint absorption feature exists at 6708 A (Li-I 2s-2p).

The above data sets show that the observed continuum originates in the convolute. In order for the Li absorption feature to be observed, either the continuum source must backlight the Li plasma, or the Li could be mixed in with the continuum source. In either case, the observation of the Li absorption line indicates that the diagnostic probe is an effective way of measuring plasma emission from the convolute.

These data also give some indication as to the specific location of plasma in the convolute. The views shown in Fig. 6.1a and b are similar but the axial location of the dopant varies. The observation of a Li feature with the view in Fig. 6.1a and the lack of the feature with the view in Fig. 6.1b indicate that the source of some of the observed continuum is located between the regions on the post that were coated with Li.

6.2 Emission Turn-On Timing

A primary objective of the post-hole convolute measurements was to determine when and where the plasma forms. Additionally, it is important to establish if the turn-on time of the bright plasma continuum emission is correlated to the time when the load current deviates from the MITL current. The turn-on time was measured for multiple views; based on these measurements, the spatial evolution of plasma in the convolute and feed gap was determined. Theoretically, once the plasma is observed throughout the gap, significant current losses are possible through this secondary path to ground. Prior to complete plasma shorting across the gap, electron emission from the expanding cathode plasma reaches the anode electrode, thus resulting in current loss in the convolute.

6.2.1 Probe Angle Sweep

A series of experiments were conducted where the spectroscopic diagnostic and probe settings were identical with the exception of the angle of the probe (probe sensitivity, gain settings, wavelength range, and sweep duration were all held constant). On these shots, the z-pinch load was also held constant, thus the convolute behavior should have

been similar on each shot. The purpose of this set of experiments was to determine the turn-on time for each view, and, based on that, estimate the rate at which the dense, continuum-emitting plasma traveled across the anode-cathode gap in the convolute. The three views used in this series of experiments are shown in Fig. 6.5a-c.

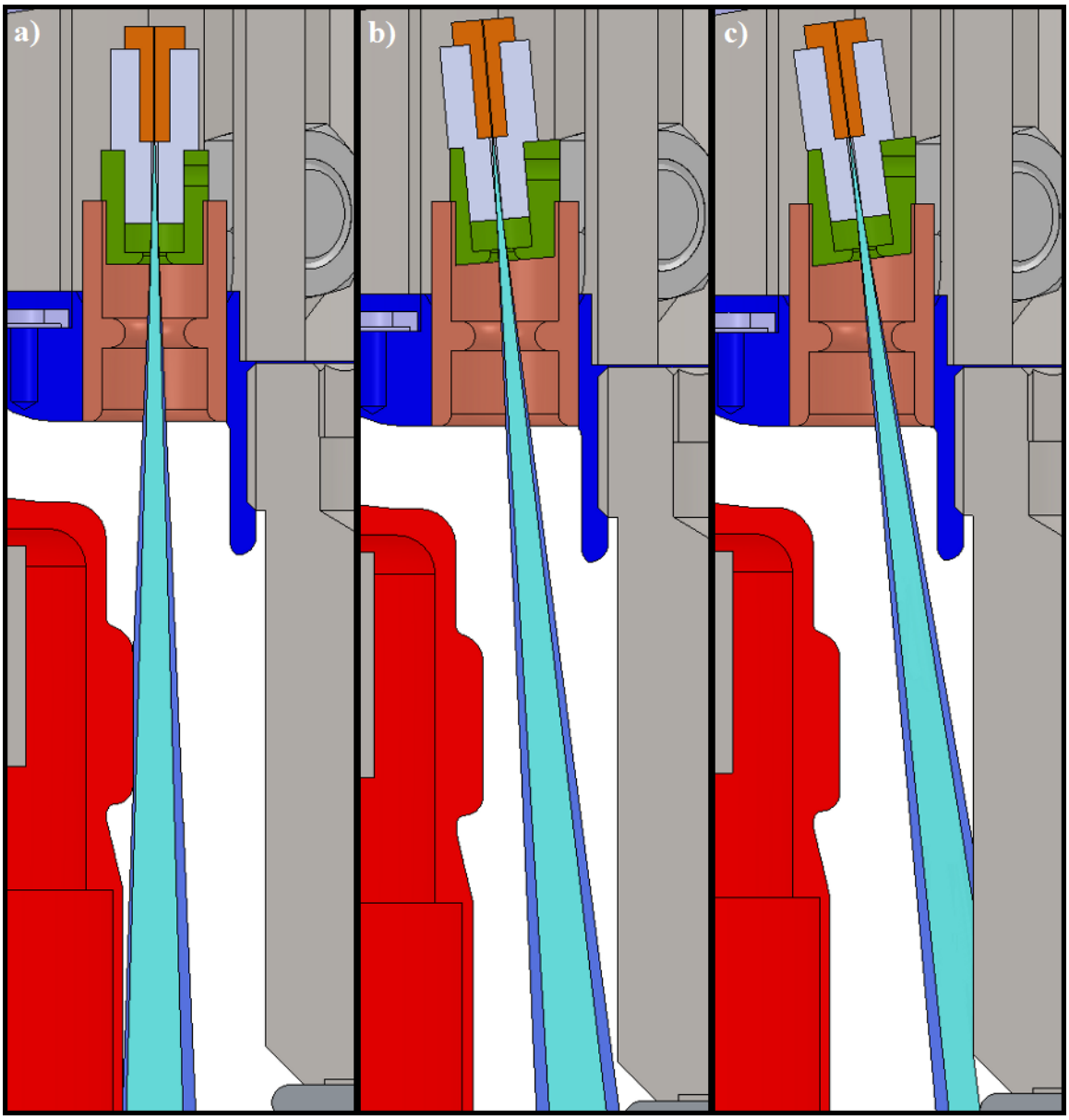

Fig. 6.5 Diagnostic views used to monitor plasma movement across the anode-cathode gap in the upper post-hole region: a) "cathode view" using 0 degree probe; b) "gap view" using 5 degree probe; c) "anode view" using 7.5 degree probe. All views used 100 micron fiber with 500 micron limiting aperture. (SolidWorks models of the Z Machine courtesy of J. Cisneros and M. Vigil.)

The views in Fig. 6.5a-c yielded the streak images shown in Fig. 6.6a-c. These data sets each consist of continuum with a strong absorption feature at 5890 Angstroms (sodium) and a few weaker absorption features. The most important information from these data sets is timing of the continuum turn-on, thus the absorption features were neglected during the analysis. From examination of the data, there is a clear trend in the turn-on time of each view. Specifically, the continuum starts later as the views progress from anode to cathode.

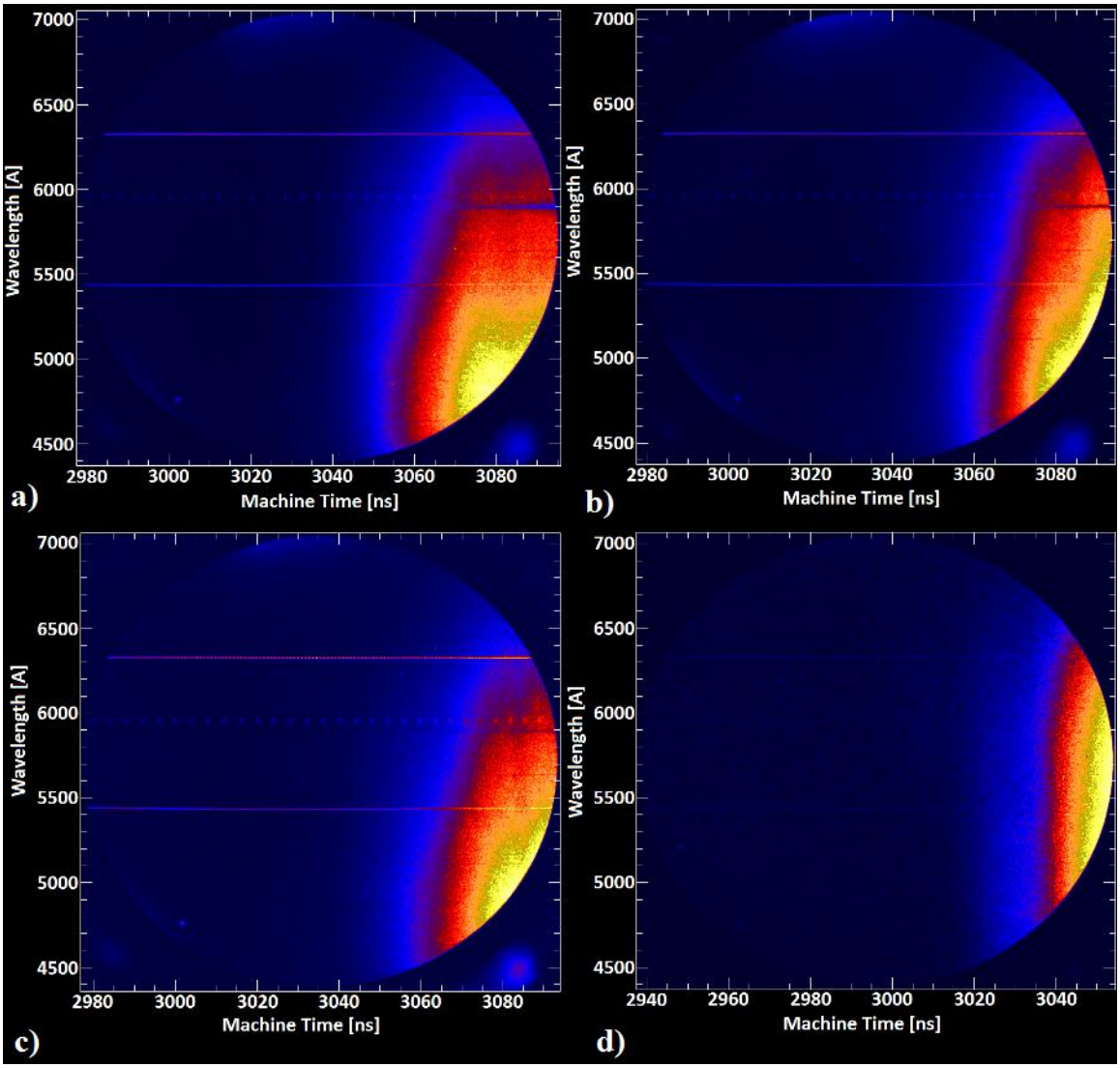

Fig. 6.6 Streaked spectra from a) shot 2077 (cathode view), b) shot 2080 (gap view), c) shot 2079 (anode view), d) shot 2078 (cathode view, high gain). As the shot views progress from cathode to anode, the turn-on time of the continuum occurs later. The higher gain shot shows emission earlier than the equivalent low gain shot, which indicates a lower bound for the sensitivity of the diagnostic.

A forth data point was taken using the view shown in Fig. 6.5a, but with a factor of ~58 higher gain. The trigger time for the streak camera was also changed so the continuum turn-on time at the lower gain setting was at the end of the time record. This produced the streak image shown in Fig. 6.6d. This image also consists of continuum, but no obvious emission or absorption features exist.

6.2.2 Alternative Probe Locations

Several regions outside of the convolute were also observed using the streaked visible spectroscopy system. This information is useful in putting together a more complete picture of the plasma evolution in and around the convolute. The primary purpose of these measurements was to determine the continuum turn-on time for each view. An additional objective was to determine if the spectral features observed in any other region of the vacuum transmission line section significantly deviated from those observed in the convolute.

A series of experiments were performed in which the hardware had horizontal mounting B-dots. These holes were azimuthally located between the posts of the convolute. The final feed gap was visible from the horizontal B-dot holes as shown in Fig. 6.7a-d. It is important to note that there is only a 1-2 bounce path for light from the wires to reflect into the probe view.

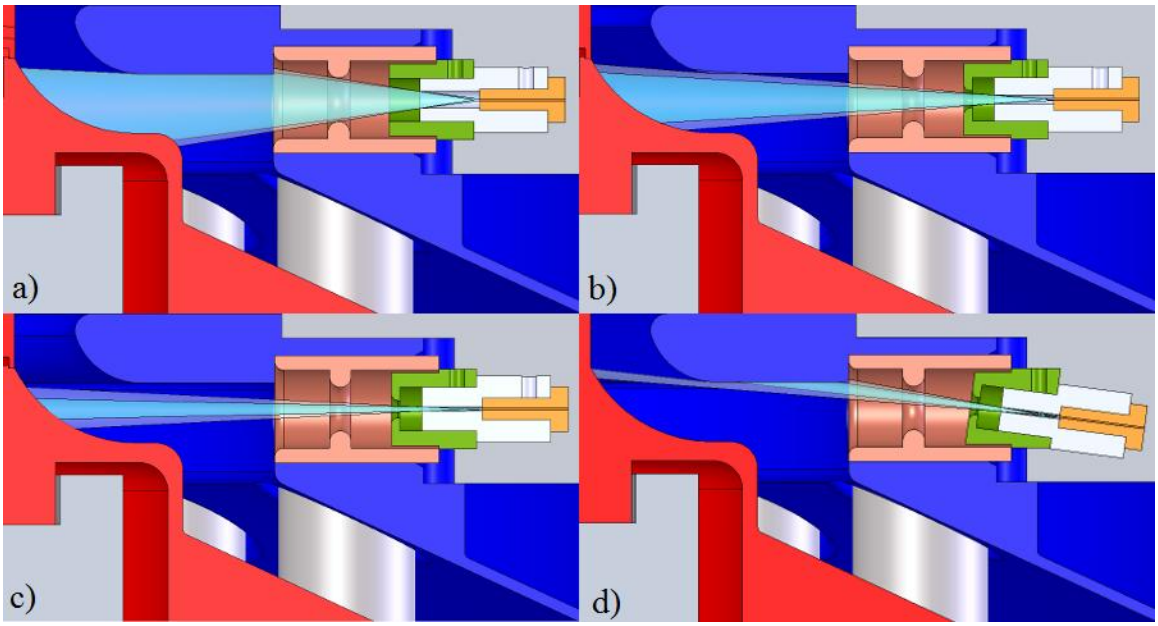

Fig. 6.7 Diagnostic views for shots with horizontal b-dot holes: a) 200 micron fiber with 2 mm limiting aperture, "gap view" (0 degree probe); b) 200 micron fiber with 1 mm limiting aperture, "gap view"; c) 200 micron fiber with 500 micron limiting aperture, "gap view"; d) 200 micron fiber with 500 micron limiting aperture, "anode view". It should be noted that the feed gap curves up to the load, thus in all of the cases, the probe directly viewed the cathode power flow surface. (SolidWorks models of the Z Machine courtesy of J. Cisneros and M. Vigil.)

For these experiments, the diameter of limiting aperture for the probe was increased from 0.5 mm to 1 mm to 2 mm. This was done to increase the sensitivity of the probe, with the expectation that emission lines might be observed early in time. The streak images for the three aperture sizes are shown in Fig. 6.8a-c. Similarly to previous spectra, these images consist of continuum emission with absorption features. No obvious emission features were observed. For one shot, the probe was pointed towards the anode (Fig. 6.7d) in order to compare the continuum turn-on time and intensity to a previous view that only observed the cathode (Fig. 6.7c). The two shots had similar spectral features (continuum with absorption lines) but with different timing as shown in Fig. 6.8c and d.

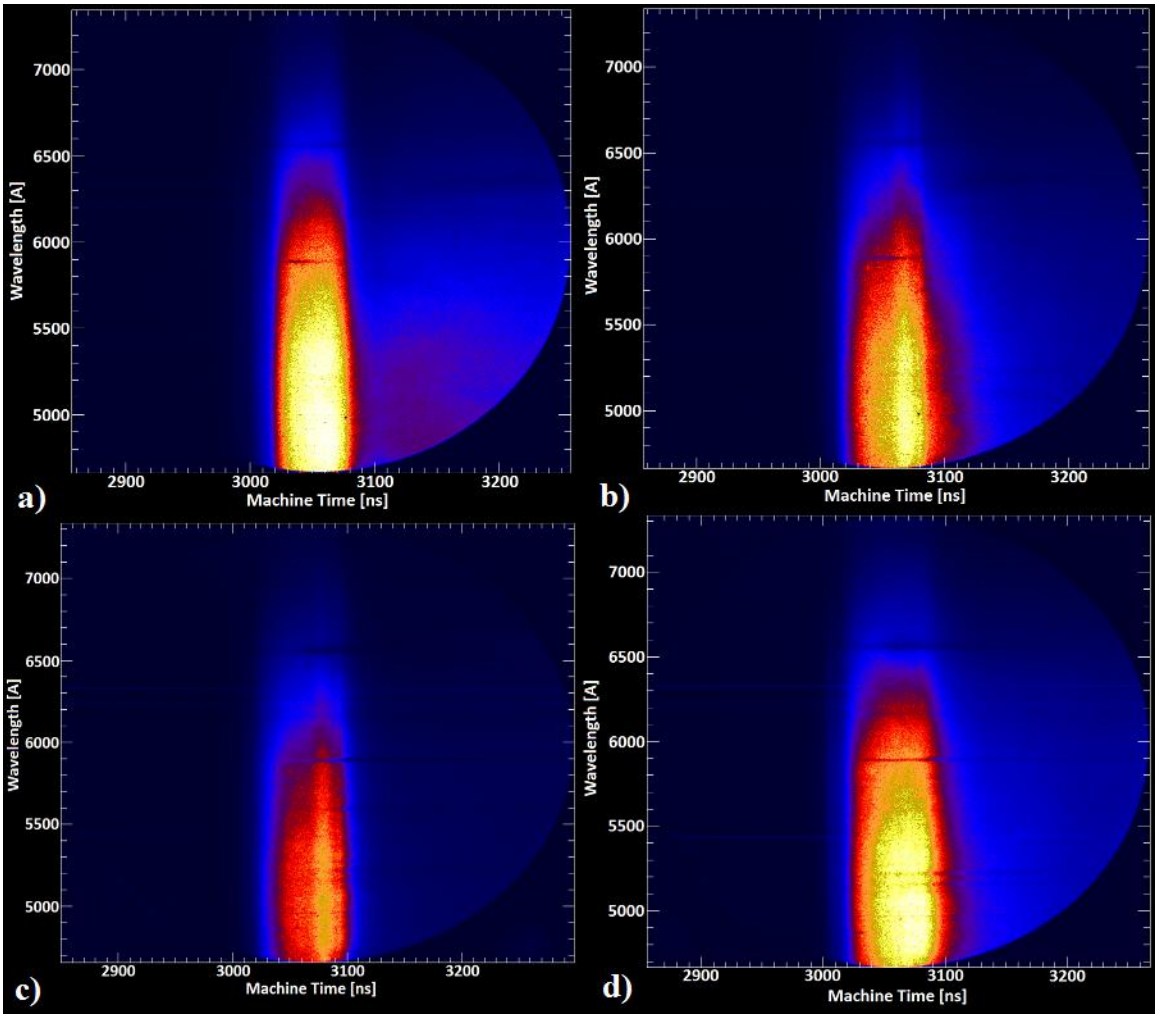

Fig. 6.8 Streak images from the four shots with the horizontal b-dot view. The top left image (a) was recorded using the view in Fig. 6.7a, (b) was recorded using the view in Fig. 6.7b, (c) used the view in Fig. 6.7c, and (d) used Fig. 6.7d. Progressing from a) to c), the spatial resolution of the probe increased, but the probe sensitivity decreased. The images in c) and d) have identical spatial resolution and probe sensitivity, but c) views the cathode and d) views the anode.

Inserting the 7.5 degree probe in the normal location backwards, yields the view in Fig. 6.9a. This probe setting views only the cathode in the region just downstream of the convolute. This view falls in between the standard convolute view and the view from the horizontal B-dot hole. The streak image from this view is shown in Fig. 6.10a. The spectral features are similar to those observed from the other views, and the turn-on time of the continuum falls somewhere in between the two cases.

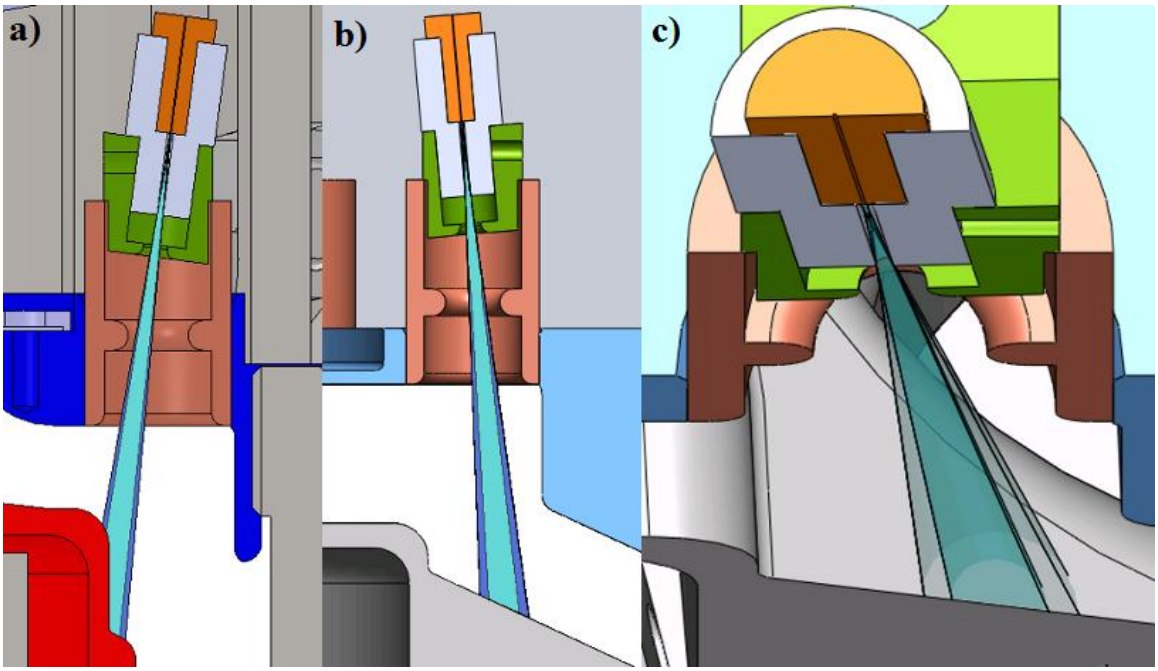

Fig. 6.9 Additional diagnostic views: a) 100 micron fiber with 500 micron limiting aperture, direct view of cathode downstream of the convolute (7.5 degree probe inserted backwards); b) 100 micron fiber with 500 micron limiting aperture, direct view of upper cathode between two holes (5 degree probe); c) the same view as (b) but from another angle. (SolidWorks models of the Z Machine courtesy of J. Cisneros and M. Vigil.)

A 5 degree probe was inserted in a vertical B-dot hole at the normal radius, but azimuthally located between two convolute posts. The probe views the cathode on a narrow bridge between two holes as shown in Fig. 6.9b and c.

The observed spectrum consists of continuum, which turns on at ~ 3030 ns (Fig. 6.10b). This turn on time is similar to that observed with the -7.5 degree probe. In both cases the probe looks directly at the cathode, thus at a relatively thin, dense plasma. A similar set of absorption features were observed in both cases, namely a set of features clustered around 4750 A and another set near 5200 A. The source of these absorption lines is yet unknown. The H-alpha and Na absorption features are also visible in these spectra.

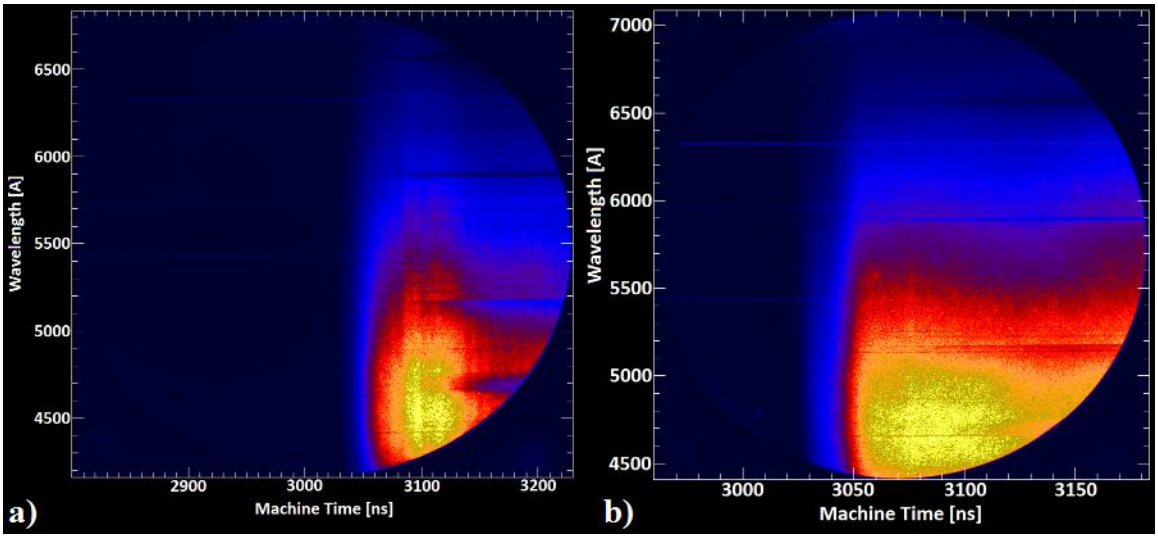

Fig. 6.10 Streak images for the views shown in Fig. 6.9. The image on the left (a) is from the view that directly observes the cathode just downstream of the convolute. The image on the right (b) is from a view that looks directly at the upper cathode between holes. It should be noted that (a) was taken on a C7 (K-Shell radiator) shot, while (b) was taken during a Lincoln (imploding solid liner) shot.

6.3 B-dot Cup Plasma Measurements

There was some concern that the signal observed by the probe in these experiments may have been the result of plasma generated in the B-dot cup itself. Simulations of the electron flow in the convolute region show that the localized heating in the B-dot cup is sufficient to desorb trapped gas and form plasma [36]. In order to examine the possibility that the observed signal was due to the B-dot cup, a series of tests were performed that only looked at the signal generated inside of the B-dot cup. These experiments used the 20 degree probe, which viewed the cup aperture as shown in Fig. 6.11; one of the measurements used the B-2 style B-dot cup, and the other used the B-5 style. The B-5 cup aperture is recessed by 5 mm compared the B-2 cup aperture. The streak images for these shots are shown in Fig. 6.12a-b. The images are very similar to those that view the convolute.

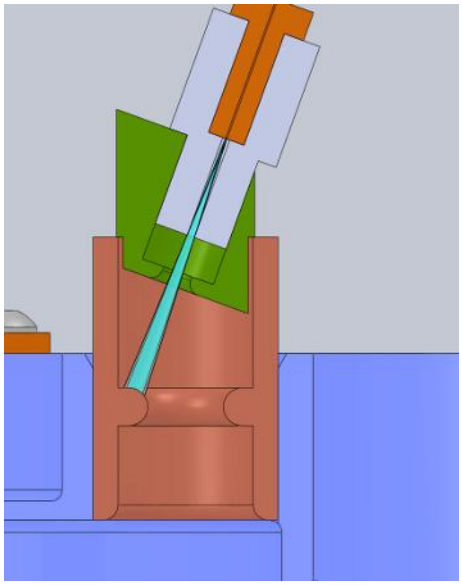

Fig. 6.11 Diagnostic view for B-dot cup plasma measurements: 100 micron diameter fiber with 500 micron diameter limiting aperture, direct view of cup aperture (20 degree probe). This image shows the B-5 style b-dot cup. SolidWorks models of the Z Machine courtesy of J. Cisneros and M. Vigil.

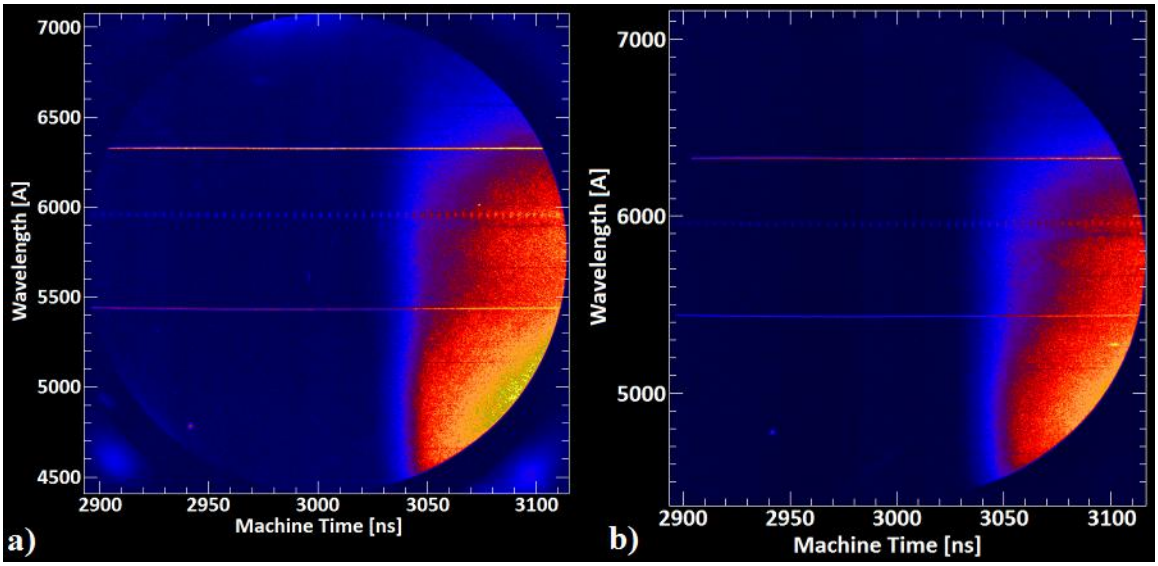

Fig. 6.12 Streak images from the shots where the probe only viewed the inside of the b-dot cup. The image on the left (a) used a B-5 style cup, and the image on the right (b) used a B-2 style cup. These experiments were both conducted on a Lincoln series shot (imploding solid liner). The intensity scales on the two images are not the same.

This result by itself would indicate that the plasma observed is located inside the cup; however, when combined with the observation of Li absorption (section 6.1), this

indicates that one or more of the following is true: a) the observed continuum from the cup is due to reflections and originates outside of the B-dot cup, b) a plasma forms within the B-dot cup and generates light, but when the probe is directed towards the convolute, this cup plasma contributes a negligible amount of signal, or c) the continuum emission from the cup and from the gap are similar. Treatment of the convolute and B-dot cup surfaces are similar (cleaning, handling, etc.) and the vacuum conditions are the same in both locations. The surface and bulk contaminants in both regions should be similar, thus the plasma formation in both regions could be similar as well.

The convolute should be similarly heated (compared to the B-dot cup) via current passing through the material [60] and flow electrons bombarding the surface [36]. Assuming there was enough hydrogen desorbed within the B-dot cup to create the observed absorption feature, there should be a similar amount of hydrogen in the convolute. Thus, characterizing the hydrogen density is important, even if the source of the absorption feature is from within the B-dot cup. A detailed spectroscopic analysis of the H-alpha absorption feature is provided in Chapter 7.

6.4 View from Below the Convolute

The spectroscopic measurements of the convolute through B-dot holes view a well-defined region of space, but the plasma conditions in that volume likely vary significantly along the line of sight. The field of view expands due to the collection optics only consisting of a limiting aperture. In addition, the angled views integrate

over different radial positions in the anode-cathode gap for the top and bottom post-holes. Confusion about the location of the emission can complicate the analysis of the data.

All of the spectroscopic measurements of the convolute through the B-dot holes directly viewed an electrode surface, where it is assumed a dense plasma forms [28],[30],[31],[47]. Thus the expected spectrum for each of these shots was continuum. A lens coupled system on the bottom of the machine would allow a collimated view through the convolute at a well-defined radial position in the post-hole gap, and, on future hardware sets, the top anode could be machined with a hole at the location where the probe would view the electrode.

The experimental setup used on this shot did employ a lens coupled system that viewed the convolute from below; however, the probe directly viewed the top anode. The probe observed a cylindrical region with a ~ 4 mm diameter at the center of the anode-cathode gap of a post-hole as shown in Fig. 6.13. This setup still integrates signal from a long region of the convolute, which likely contains regions with vastly different plasma parameters.

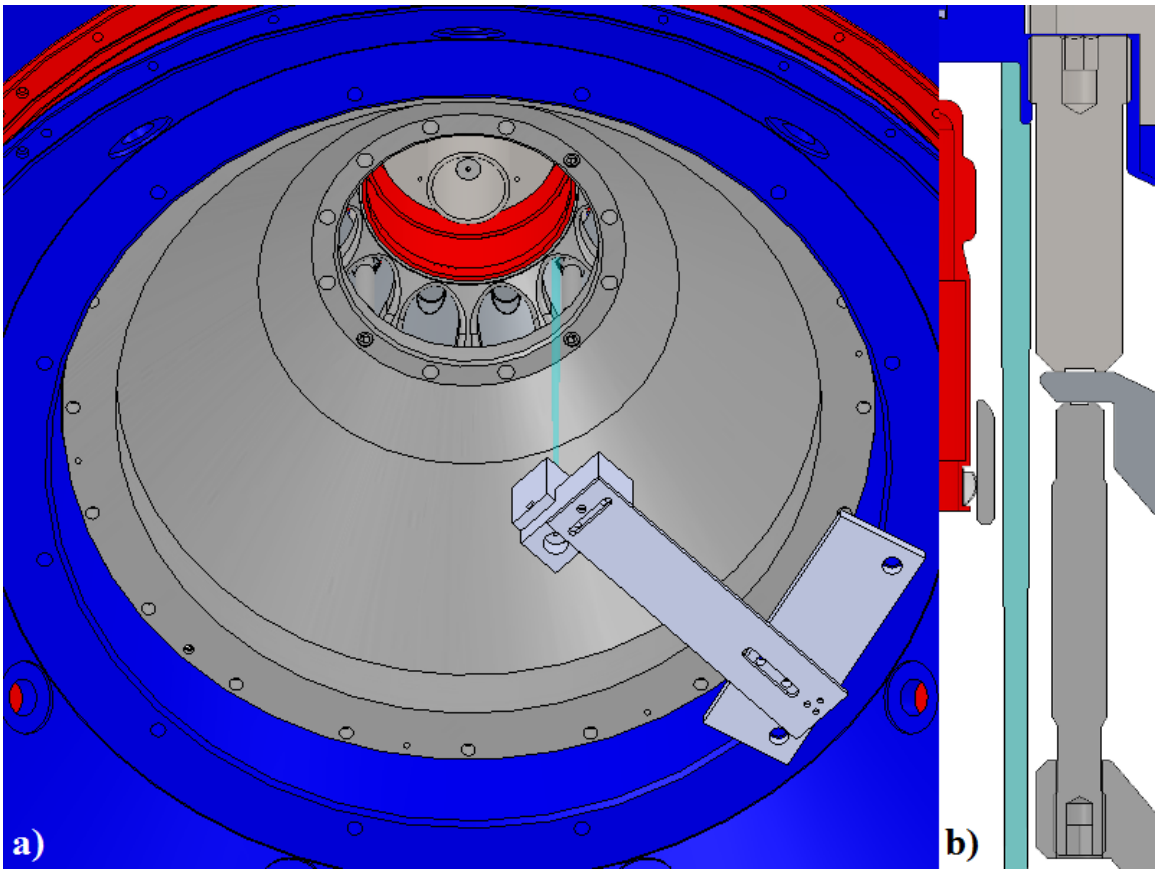

Fig. 6.13 Diagnostic view from below the convolute: a) perspective view of probe attached to bottom anode; probe consists of a 6.35 mm focal length, 6.35 mm diameter lens with a 100 micron diameter fiber at located 6.35 mm from the central plane of the lens; b) region of convolute from which light is collected; view is an approximately collimated, 4 mm diameter beam, which is on the down-stream side of the post. The only power-flow surface directly viewed is the top anode. (SolidWorks models of the Z Machine courtesy of J. Cisneros and M. Vigil.)

The streak image for this setup in shown in Fig. 6.14. There are two distinct emission times observed, one approximately matches the turn-on time of the other convolute measurements from the B-dot aperture probe positions, and the other occurs ~ 30 ns earlier in time at about 3015 ns. The late time emission roughly matches shape and duration of the emission in previous shots. The early time emission must originate at a location that the diagnostic cannot view from the top of the convolute. Based on the view shown in Fig. 6.13, the only region from which the signal could originate is on the

top anode just downstream of the post. At early times, the anode-cathode gap is not yet magnetically insulated, and, as a result, electrons can cross the gap and bombard the anode. This could result in significant emission early in time. Once the conditions for magnetic insulation are satisfied, the energy deposited in the anode by electrons drops to nearly zero, at which point the emission from the anode would also decrease significantly.

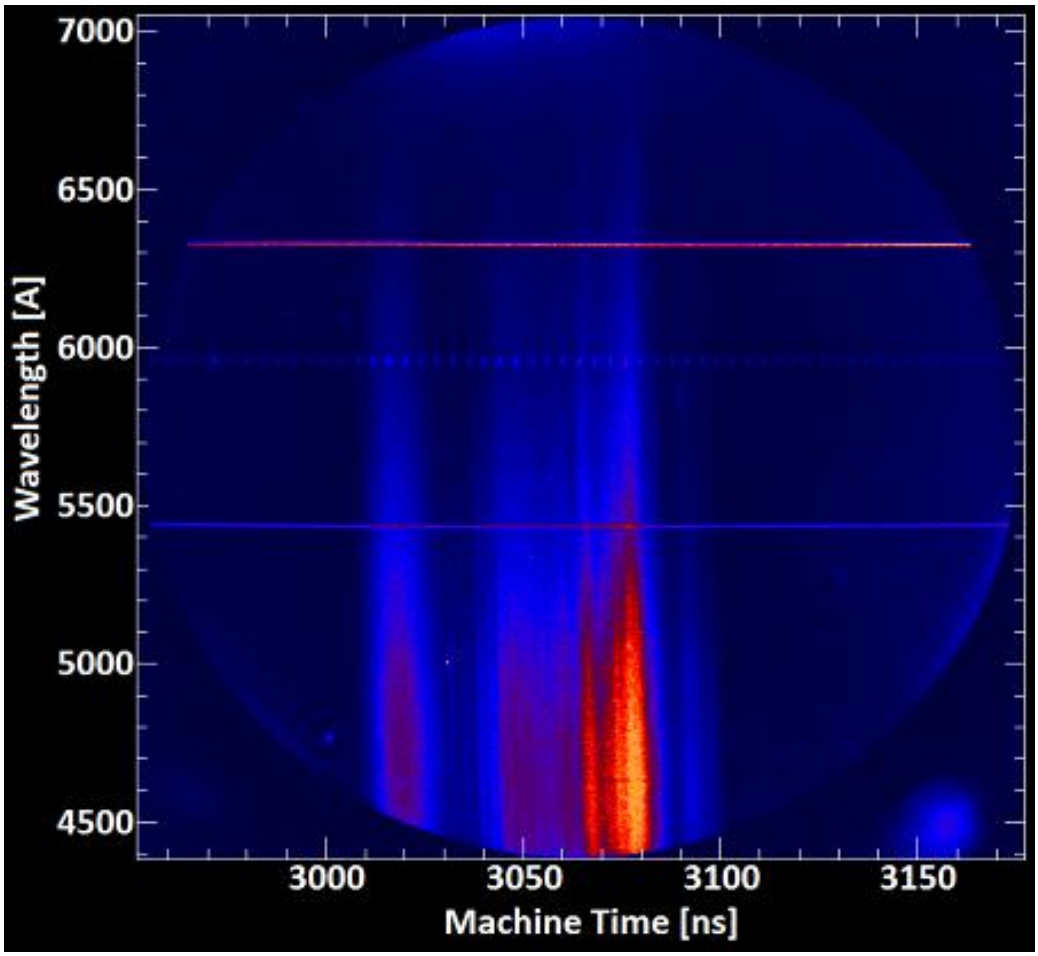

Fig. 6.14 Streak image recorded with the view shown in Fig. 6.13. This view was fielded on a C7 (K Shell Radiator) shot.

The signal observed with this diagnostic view is strong on the short wavelength end of the spectrum but weak on the long wavelength end. As a result of this, no absorption

features were observed at 6563 A (hydrogen) or 5890 A (sodium). One possible explanation for the significant drop in signal with increasing wavelength is that the lens used to focus the signal into the fiber has a wavelength-dependent focal length. As a result of this, the location within the convolute most efficiently viewed by the probe is wavelength dependent. Assuming that the plasma within the convolute is non-uniform, it is expected that certain regions emit more strongly. Thus the light collected from a certain region of the spectrum (in this case blue-green) could be significantly greater than the rest of the spectrum. In future experiments, this can be accounted for through a spectral calibration. Due to the limited number of shots and on those shots a significant number of restrictions on probe location; this view was only fielded once. A number of additional shots with adjustments to the probe view and diagnostic settings would be necessary to get a full picture of what is being observed with the bottom view.

6.5 High Resolution H-Alpha Absorption Feature Measurements

An absorption feature at 6563 Angstroms was observed in all of the streak images with large enough spectral and temporal ranges with the exception of the bottom view. In many images, the width and depth of the absorption feature changed as a function of time, thus indicating a time changing temperature and density of the hydrogen plasma. The absorption feature may be a result of hydrogen located in the B-dot cup itself (as suggested in section 6.3), but the presence of hydrogen in the B-dot cup indicates that it also exists elsewhere in the convolute. There is sufficient electrode heating to desorb

hydrogen from the metal somewhere in the field of view, thus there is likely hydrogen neutrals and and associated plasma formed from neutral ionization throughout the convolute.

The machine settings and load dynamics have a significant affect on the current delivered to the load, thus it seems reasonable that they would also have an affect on the plasma dynamics in the convolute. The line shape of the H-alpha feature was measured for a number of different loads/machine settings to determine the effect the changes had on plasma parameters in/around the convolute. The three measurements used the probe views in Fig. 6.15a – c.

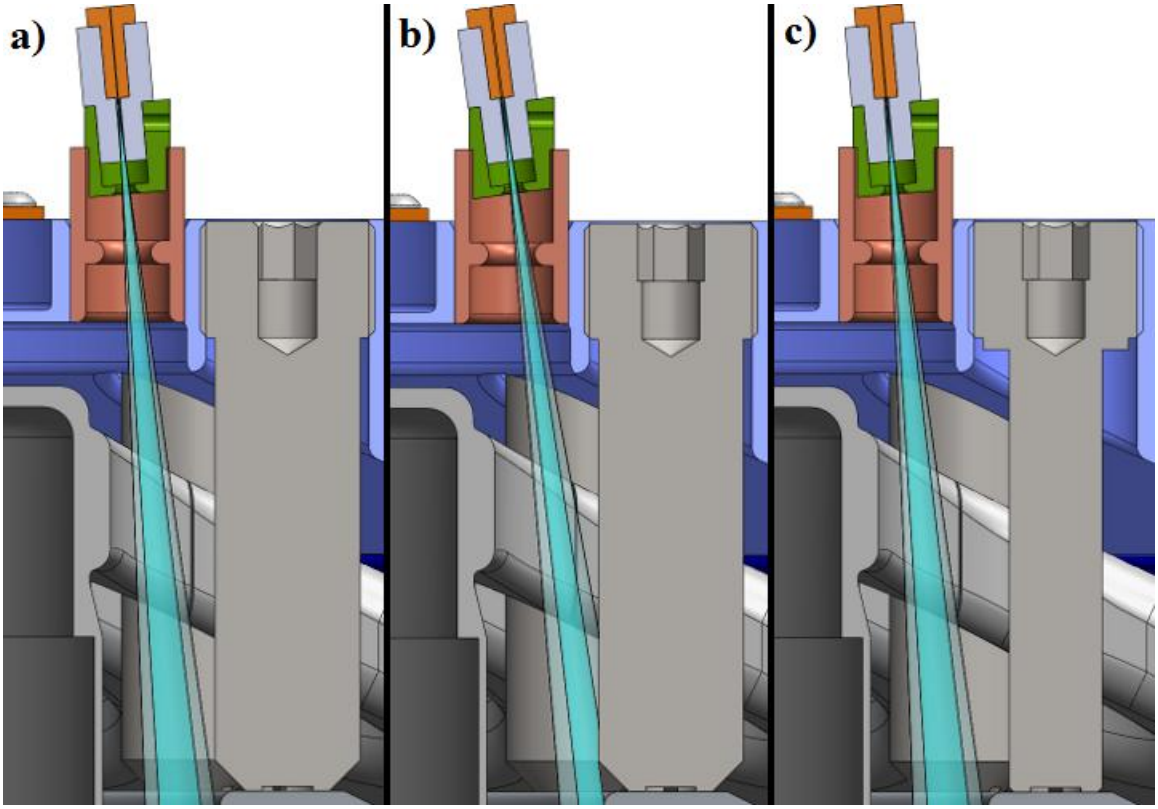

Fig. 6.15 Diagnostic views used for the high spectral resolution measurements of the Balmer series H-alpha absorption feature: a) 100 micron diameter fiber with 500 micron diameter limiting aperture, "gap view", large diameter upper post (15.88 mm); b) 200 micron diameter fiber with 500 micron diameter limiting aperture, "anode view", large diameter upper post; c) 100 micron diameter fiber with 500 micron diameter limiting aperture, "gap view", small diameter upper post (10.06 mm). (SolidWorks models of the Z Machine courtesy of J. Cisneros and M. Vigil.)

The data from the three shots are shown in Fig. 6.16 and Fig. 6.17 and Fig. 6.18. A low initial inductance, high time changing inductance load was fielded for the data set in Fig. 6.16. The load used for the data in Fig. 6.17 had a moderate initial inductance and time changing inductance. The final data set (Fig. 6.18) utilized a high initial inductance and a very low time changing inductance; additionally, on this shot the machine was fired in long pulse mode. It is clear from looking at the three streak images that there is a difference in the absorption feature shape for the three cases.

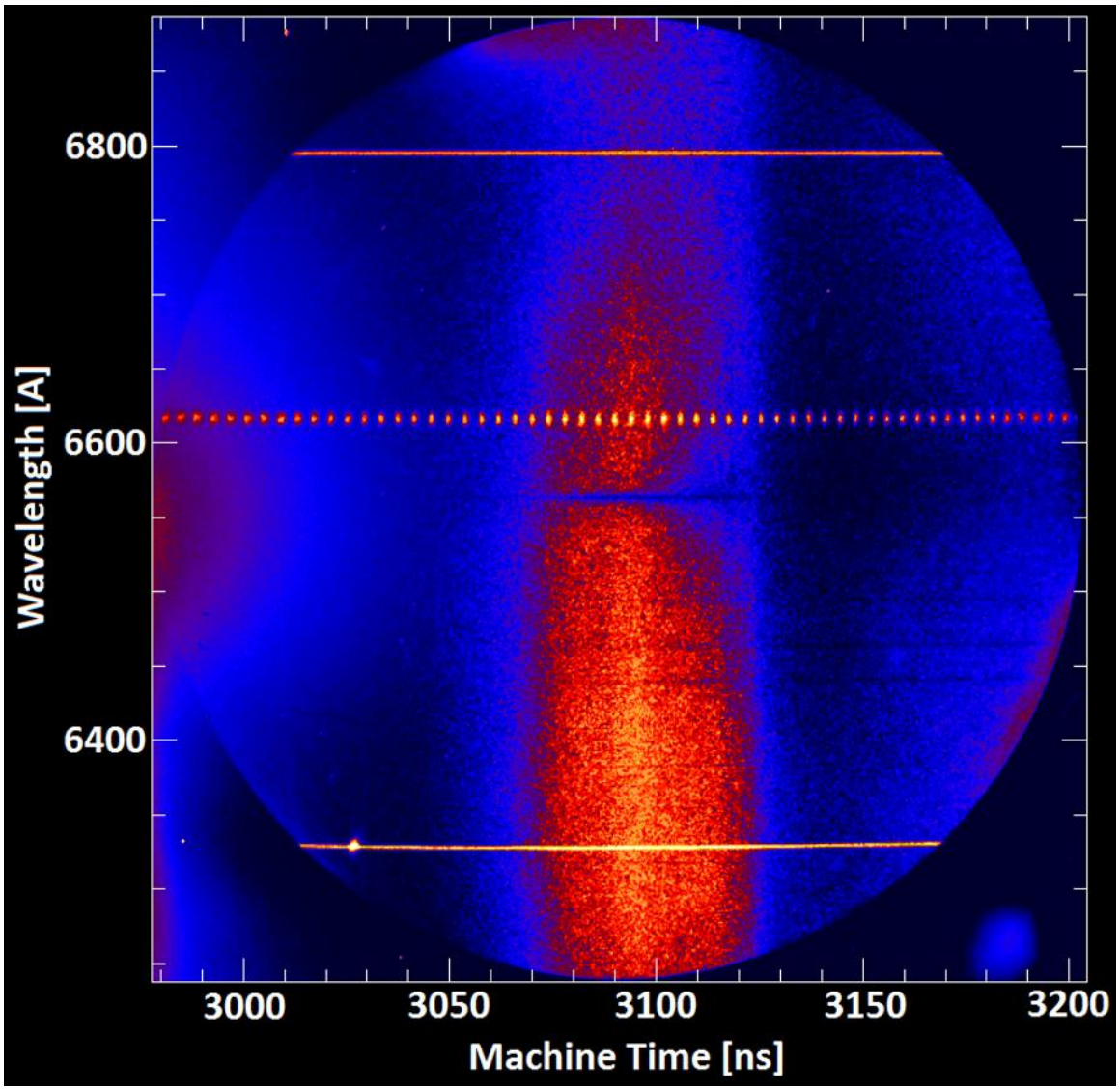

Fig. 6.16 Streak image from shot 2082 (K Shell Radiator load). The H-alpha absorption feature is spectrally centered on the image. As time increases, the feature broadens significantly.

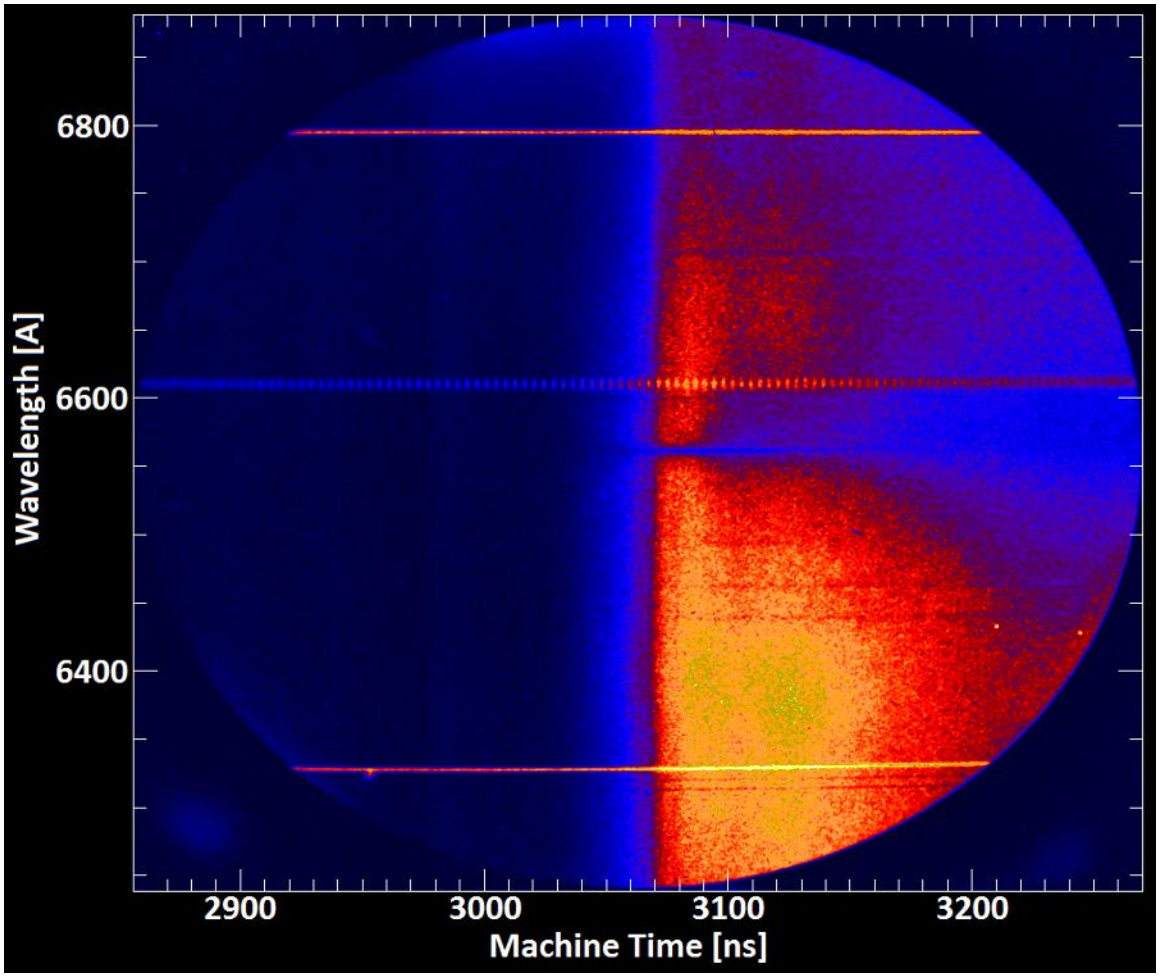

Fig. 6.17 Streak image from shot 2116 (Inertial Confinement Fusion load). Similarly to the K Shell Radiator shot shown in Fig. 6.16, the H-alpha feature starts narrow and then broadens significantly later in time.

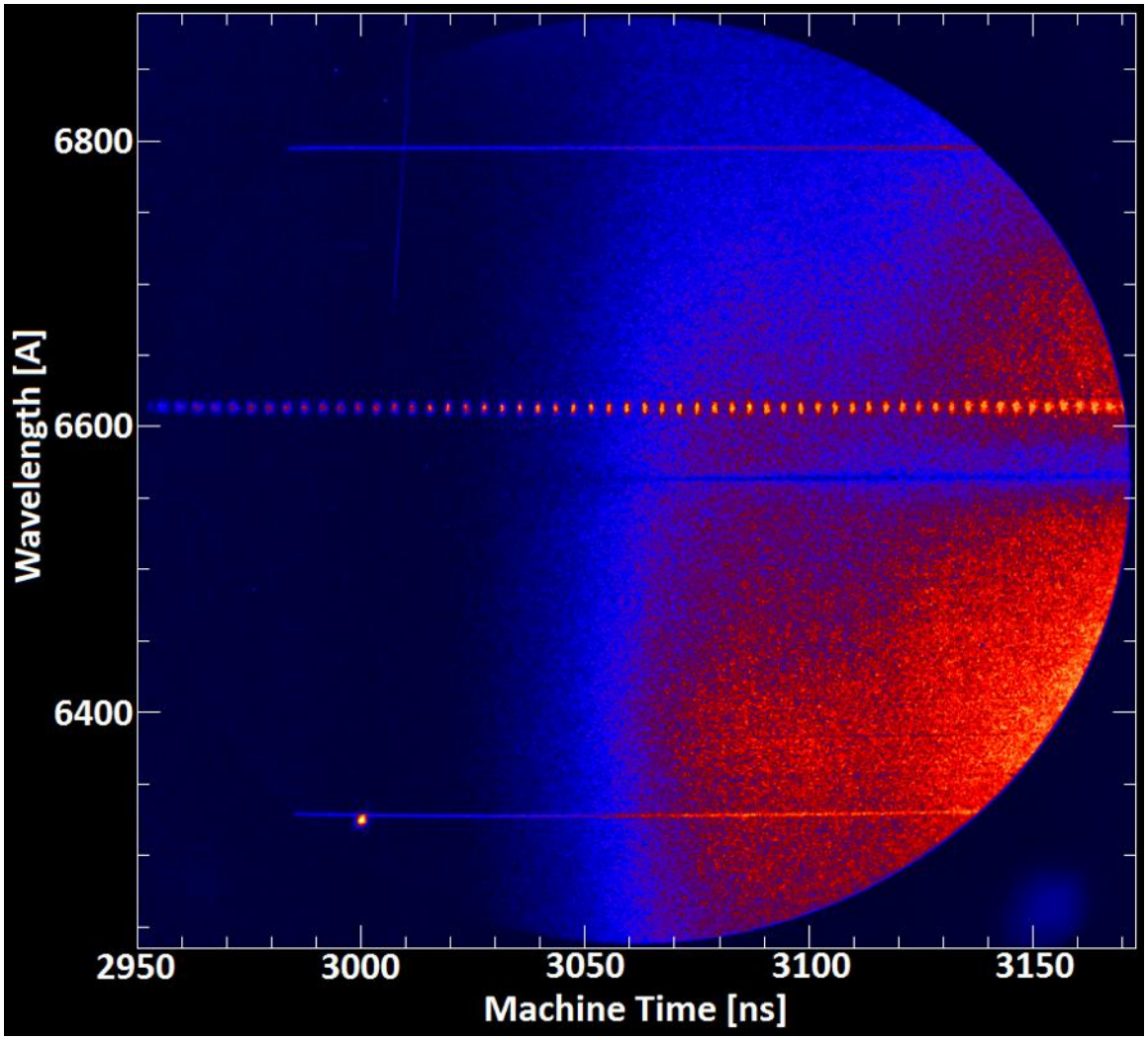

Fig. 6.18 Streak image from shot 2110 (Isentropic Compression Experiment). The H-alpha feature is prominent in this spectrum as well, but it does not broaden as much or as quickly as it does on the other two shots.

CHAPTER 7

SPECTRAL LINEOUT ANALYSIS OF Z-MACHINE DATA

In this chapter the spectral analysis of the data collected during experiments performed on the Z-Machine will be presented. Data sets were corrected using the procedures described in Appendix D. Temporally and spectrally resolved emission from the convolute was used to determine plasma density as a function of time using Stark broadening [58],[61-66]. A typical optical spectrum consists of continuum emission with a number of absorption lines. The continuum emission is produced by dense plasma; the absorption features are the result of that dense plasma backlighting a second region of plasma. In these experiments, the most prominent absorption lines are at approximately 5890 A (neutral sodium) and 6563 A (neutral hydrogen). A subset of these experiments contained a lithium-fluoride dopant, which produced an absorption feature at 6708 A. The widths of these features were used to estimate the density of the different plasma components.

7.1 Spectral Analysis of LiF Dopant Shots

As indicated in section 6.1, three shots were successfully conducted with LiF on the upper convolute post. For two of the shots, the dopant was located at the upper position

on the post (approximately centered within the hole of the upper cathode), and for the other shot, the dopant was located at the lower position on the post (approximately where the upper post meets the middle anode). The location of the dopant for each case is shown in Fig. 7.1.

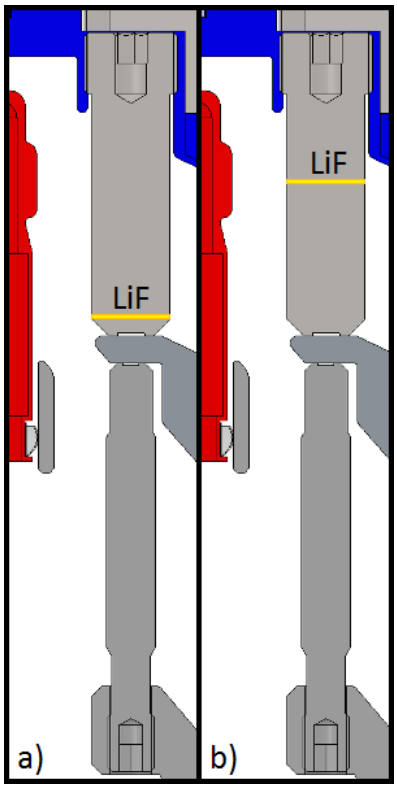

Fig. 7.1 R-Z cross-section of the Z-Machine double post-hole convolute showing the location of the lithium fluoride localized dopant. In both cases, the 1mm tall, 1 micron thick dopant band was located on the upper post, but a) shows the lower position (the lowest portion of the post that is cylindrical) and b) shows the upper position (axially centered within the upper cathode hole). (SolidWorks models of the Z Machine courtesy of J. Cisneros and M. Vigil.)

A series of spectral lineouts were taken of the case with the dopant at the lower location (shot 2115). The lineouts were taken every 10 ns and each lineout averages the signal intensity over a 10 ns period (+/- 5 ns from the quoted time). The lineouts were taken starting ~ 30 ns prior to peak x-ray production from the z-pinch and continued until ~ 60

ns after. The spectra are plotted from 6690 A to 6720 A in Fig. 7.2 (range is approximately centered about 6708 A, which is the location of the feature of Li interest).

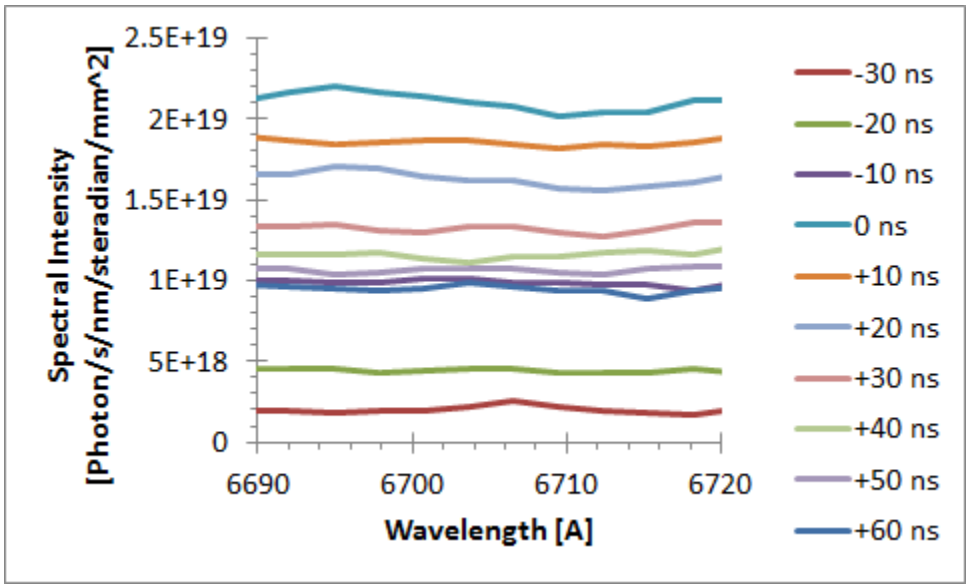

Fig. 7.2 Lineouts of the streak image shown in Fig. 6.3 (Shot 2115). Each line represents a 10 ns average of the data. Times given are relative to peak x-ray production because electrical signals were not available for this series. There are no prominent features at ~6708 A (Li-I 2s-2p), with the possible exception of the peak on the "-30 ns" trace.

Early in time (-30 ns), there is an obvious peak at 6707 A, which is likely due to Li 2s-2p emission (6708 A). At this time the continuum exists but is significantly weaker than at its peak. A Lorentzian profile was fit to the line (Fig. 7.3), and the full-width at half maximum (FWHM) was measured to be 5 A. The density of the lithium was estimated using a PrismSpect simulation of a ~ 1eV pure Lithium neutral plasma. Simulated Li plasma density was approximately 5×10^{16} cm^{-3} for a spectral feature with FWHM ~ 5 A.

The diagnostic probe directly views the location at which the Li was deposited on the post, thus it is plausible that an emission line from the Li would be observable. The density of solid LiF is 6×10^{22} cm^{-3}; the measured plasma density would be significantly

lower than solid density, but it is probable that the density measured at the source would be higher than the density measured further out in the A-K gap.

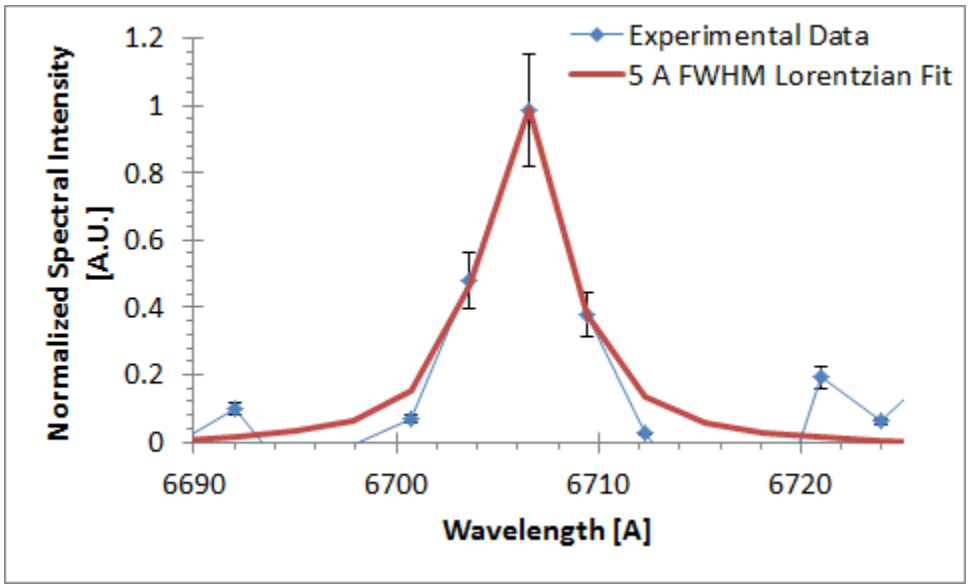

Fig. 7.3 Lineout of Shot 2115 at -30 ns (averaged over a 10 ns window) relative to peak x-ray time and a Lorentzian fit to the peak at 6707 A. The peak has a FWHM equal to 5 A.

At -20 ns, the emission line is washed out by continuum emission. For all subsequent time steps, there are no obvious spectral features in the range of interest. The lack of an obvious absorption feature can be explained by the schematic shown in Fig. 7.4. The Li plasma is back lit by plasma in the lower convolute (as shown to exist in Rose's simulations, an example of which is shown in Fig. 7.4b), which produces a Li absorption feature. A second region of plasma exists in the upper convolute, which cannot backlight the Li at its lower position on the upper post. Photons from the upper convolute plasma also reach the detector, thus any spectral features due to the lower plasma can be washed out by the upper plasma. Due to the angle at which the probe viewed the convolute for this shot, the region of the lower plasma that was viewed by

the probe was closer to the anode than the region of the upper plasma viewed by the probe. The simulations indicate that in general, the density of the plasma in the convolute decreases from cathode to anode. The intensity of continuum emission is proportional to the square of the plasma density. Thus, the expected contribution to the observed signal by the upper convolute plasma is greater than that of the lower convolute plasma. This results in the Li absorption feature (which can only be the result of the lower convolute plasma) being washed out by a stronger continuum source (which does not contain the absorption feature).

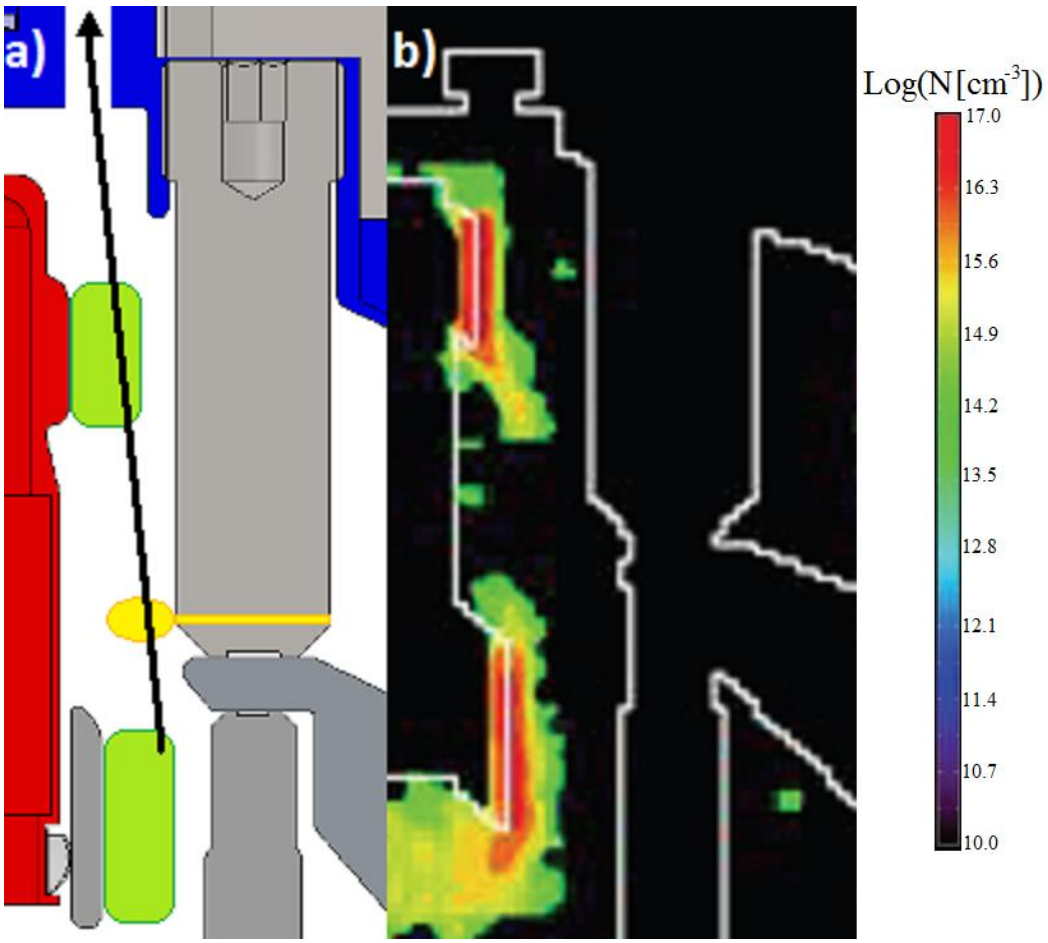

Fig. 7.4 a) R-Z cross-section of the Z-Machine double post-hole convolute showing a possible explanation for the relatively non-existent spectral feature at 6712 A. Cathode plasma is shown in green and LiF is shown in yellow. The spectrum is collected through the hole in the top electrode. An arrow shows a possible path for photons to leave the plasma in the lower convolute, pass through the Li plasma, which is expanding from the post, enter the upper convolute plasma, and then reach the detector. In that case, the lower plasma would be backlighting the Li, which creates the absorption feature, but then the photons enter the upper plasma, which may fill in the observed signal. b) Plasma density from Rose's PIC simulation of the Z-machine post-hole convolute [31]. The location of the plasma in the simulation qualitatively supports the theory that less dense lower convolute plasma could backlight the Li, but the upper convolute plasma would wash out the signal. (SolidWorks models of the Z Machine courtesy of J. Cisneros and M. Vigil.)

A second series of spectral lineouts were taken of the case with the dopant at the upper location (shot 2116). Once again, the lineouts were taken every 10 ns and each lineout averages the signal intensity over a 10 ns period (+/- 5 ns from the quoted time). The

lineouts started at -30 ns relative to peak x-ray production and persisted until +60 ns. The spectra are plotted from 6690 A to 6720 A in Fig. 7.5.

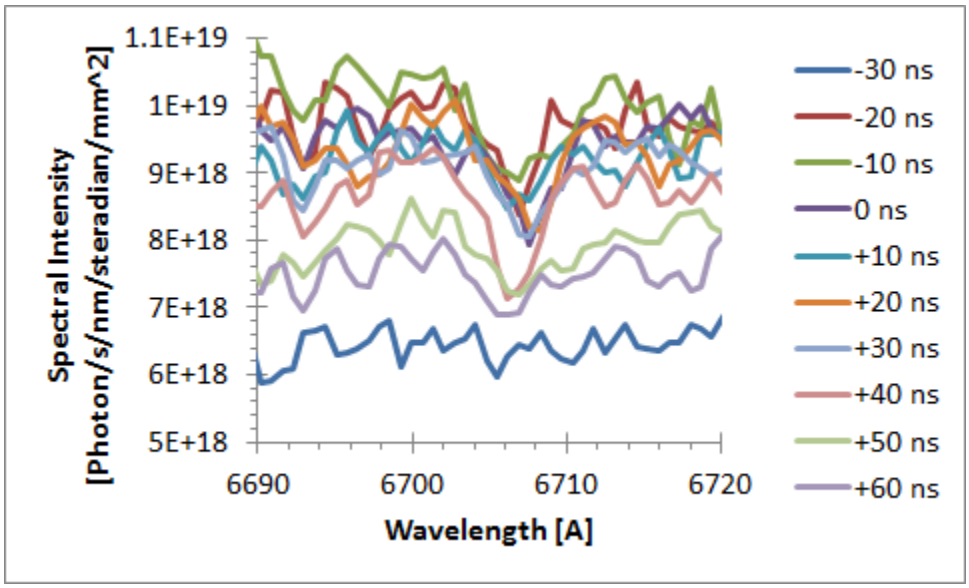

Fig. 7.5 A plot of a series of spectral lineouts of shot 2116 zoomed in to observe the Li 2s-2p transition at 6708 A. There is an obvious absorption feature on all lineouts from -20 ns to +40 ns.

All of the lineouts shown in Fig. 7.5 have an apparent absorption feature at 6708 A; from -20 ns to +40 ns the absorption features are significantly above the noise level. A time average of all of the lineouts was calculated and the resultant lineout (at +15ns with range +/- 50ns) is plotted in Fig. 7.6. A series of PrismSpect simulations were run in which hydrogen plasma with temperature varying from 0 to 1 eV and density varying from 10^{14} to 10^{20} cm^{-3} was backlit by a 1 eV blackbody emitter. The simulated spectrum that best matched each experimental data set was determined. A plot of the density and temperature for the best fit cases is plotted in Fig. 7.6. The simulated plasma temperature varies from 0.90 eV to 0.95 eV; the simulated plasma density increases from

~ $3x10^{16}$ cm^{-3} at -20 ns to ~ $7x10^{16}$ cm^{-3} just after peak x-ray, and then drops back down again.

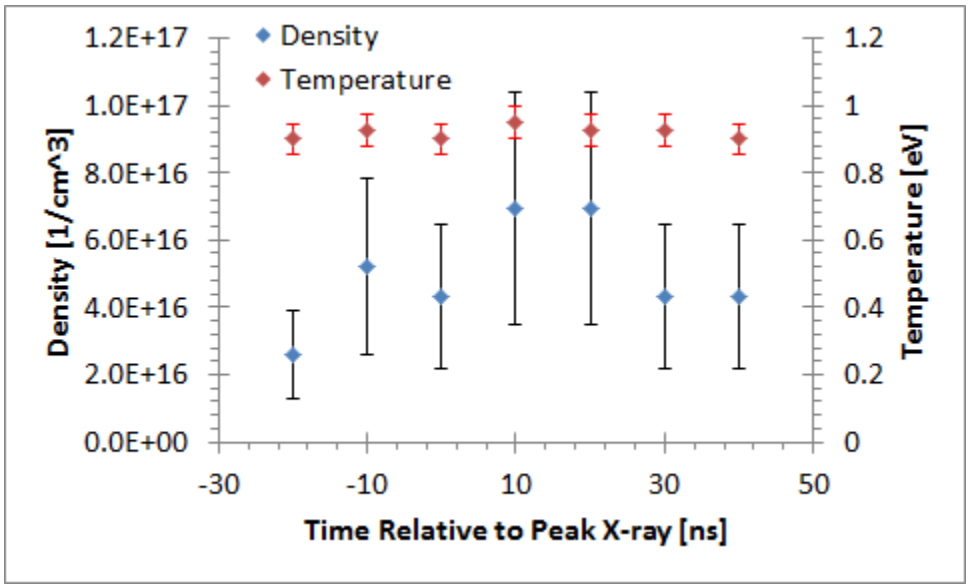

Fig. 7.6 Plot of the simulated plasma parameters from shot 2116. The simulated temperature holds relatively constant at 0.9-0.95 eV; the simulated density increases by more than a factor of two from -20 ns to +10 ns. Peak simulated density is $7x10^{16}$ cm^{-3}.

The observation of the Li transition for this geometry further supports the physical explanation suggested in Fig. 7.4. In this case, the Li dopant is located higher up on the post, which allows it to be back-lit by the upper convolute plasma as is shown in Fig. 7.7. In this case, fewer photons emitted by the plasma that are within the probe acceptance cone can miss the Li plasma. This is more likely to result in the absorption feature being observable. It should be noted that the plasma shown in the figure below is a schematic representation of the upper and lower convolute plasma locations and the Li expanding into the gap. According to Rose's simulations, there is significantly more structure to the plasma; the plasma that extends out far enough to be observed by the probe is all located

below the Li dopant. Thus most photons collected by the probe had to pass through the Li, and it is not possible for the absorption feature to be washed out.

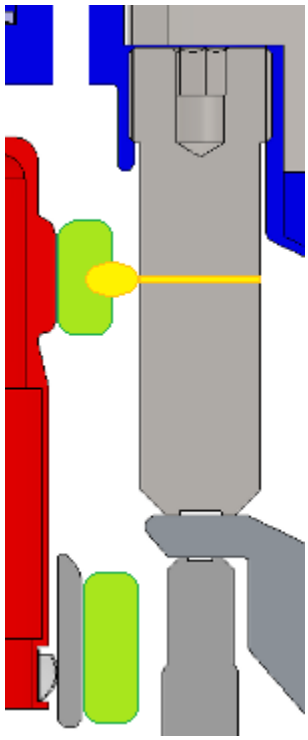

Fig. 7.7 R-Z cross-section of the Z-Machine double post-hole convolute showing possible locations for the Li with upper and lower convolute plasmas that would produce the observed spectral absorption feature. Cathode plasma is shown in green and LiF is shown in yellow. The spectrum is collected through the hole in the top electrode. The upper plasma backlights the Li, which creates the absorption feature. SolidWorks models of the Z Machine courtesy of J. Cisneros and M. Vigil.

7.2 Spectral Analysis of Balmer Series H-Alpha Absorption Feature

The Balmer series H-alpha transition was observed prominently on many shots as an absorption feature. In some cases the absorption line width significantly increased as a function of time, which indicates a significant change in the neutral hydrogen density. Measurements of the cup plasma (data presented in section 6.3) show the absorption feature within the cup itself, thus the H plasma likely persists throughout the entire

vacuum A-K gap. There is reason to believe that the plasma is not uniform between the cup and the rest of the convolute, and as a result, it is necessary to deconvolve the spectral contribution of the cup plasma from that which originates within the convolute.

A series of three high spectral resolution shots of the convolute with different load parameters showed that the load can significantly affect the shape of the absorption feature (data presented in section 6.5). In the following sections the density of the H plasma in the convolute (as well as within the B-dot cup) will be determined.

7.2.1 H Plasma within the B-dot Cup

As described in section 6.3, several shots were dedicated to observing the plasma that forms within the B-dot cup. The probe was angled such that all of the light collected came from within the cup, thus the spectral features observed (continuum and H-alpha absorption, see Fig. 6.12) originate from within the cup. It is interesting to note that the absorption feature that is typically observed at 5890 A (assumed to be the Na-I 3s-3p doublet) is not observed in these shots. This indicates that the contaminant that is producing that absorption feature is located within the convolute, but not within the B-dot cup. The lack of the Na absorption feature may be explained as follows. While the B-dot cup and the convolute are both cleaned in the same manner, the inside of the cup is likely not handled after cleaning. The convolute has greater exposure to personnel during the installation process, which allows for possible contamination.

A series of spectral lineouts were taken every 10 ns, each of which averages the signal over a 10 ns window. The timing of these lineouts and the traces from the shot are

shown in Fig. 7.8. The spectral lineouts are shown in Fig. 7.9. The earliest lineout (60 ns) does not have an absorption feature, thus prior to this point the H liberated from the electrodes is not sufficiently dense to produce an observable feature. Fitting a Voigt profile to each of these data sets, the FWHM was determined and tabulated in Table 7.1. The instrument broadening is Gaussian and the Stark broadening is Lorentzian, thus the total broadening is a convolution of the two (known as a Voigt profile). The Lorentzian FWHM was determined using the following equation

$$\lambda_V = \frac{\lambda_L}{2} + \sqrt{\left(\left(\frac{\lambda_L}{2}\right)^2 + \lambda_G^2\right)} \tag{7.1}$$

where λ_V is the measured FWHM, λ_G is the Gaussian FWHM associated with instrument broadening (7 A for this shot), and λ_L is the Lorentzian FWHM.

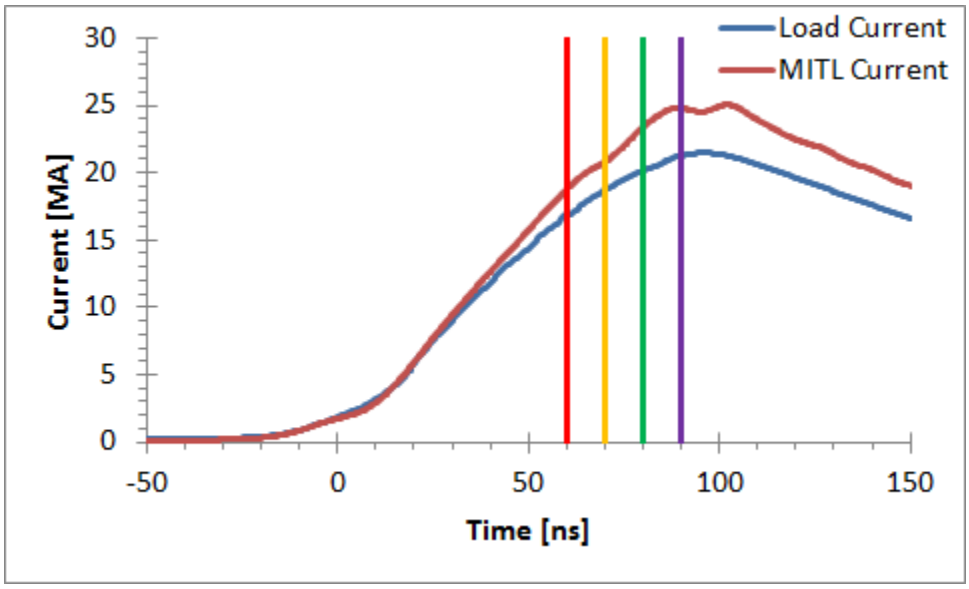

Fig. 7.8 A plot of the MITL and load currents for shot 2104 (B-dot cup plasma measurement shot). Also included are the times of the four spectral lineouts shown in Fig. 7.9 below.

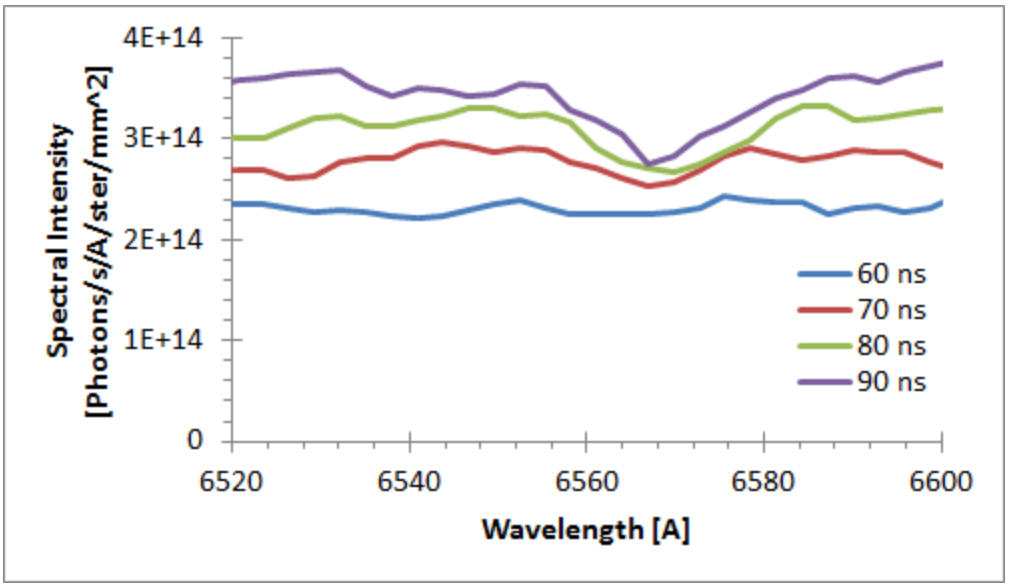

Fig. 7.9 A plot of the four spectral lineouts of shot 2104 (B-dot cup plasma measurement shot) zoomed in around the 6563 A absorption feature. The lineout at 60 ns has no absorption feature, but the other three do. The feature becomes more prominent as time progresses.

Table 7.1 Compilation of information about the lineouts of shot 2104 (B-dot cup plasma measurements. The table includes the full-width at half-maximum (FWHM) of the Voigt profile fit to the data, the FWHM of the deconvolved Lorentzian, and the plasma density as calculated using Equation 7.4.

Time [ns]	Voigt FWHM [A]	Lorentzian FWHM [A]	Density [cm^{-3}]
60	N/A	N/A	Unknown
70	12.5	8.5	$9\pm3 \times 10^{16}$
80	18	15.25	$2.1\pm0.8 \times 10^{17}$
90	15	11.75	$1.5\pm0.6 \times 10^{17}$

The electron density (N_e) and thus the H plasma density was determined by plugging the Lorentzian FHWM into the following equation for Stark Broadening in a H plasma

$$\lambda_{FWHM} = (2.50\ x\ 10^{-9})\alpha_{1/2} N_e^{2/3} \tag{7.2}$$

where $\alpha_{1/2}$ is taken from Griem's spectral broadening reference [61] (and is tabulated in Table 7.2). The calculated plasma density ranges from $9\pm3 \times 10^{16}$ cm^{-3} to $2.1\pm0.8 \times 10^{17}$

cm^{-3}; these values are also listed in Table 7.1. The calculations assume the plasma temperature is 3 eV, as suggested in [28-31],[33]. There is approximately a +/-10% difference in the calculated density for +/-1 eV change in assumed temperature.

Table 7.2 Values for $a_{1/2}$ at several temperatures and densities for the Balmer series H-Alpha (n=2 to n=3) transition. These values are listed in the appendix of Griem [61].

Density	$a_{1/2}$ ($5x10^3$ K)	$a_{1/2}$ (10^4 K)	$a_{1/2}$ ($2x10^4$ K)	$a_{1/2}$ ($3x10^4$ K)	$a_{1/2}$ ($4x10^4$ K)
10^{15}	$9.69x10^{-3}$	$7.77x10^{-3}$	$6.01x10^{-3}$	$4.98x10^{-3}$	$4.50x10^{-3}$
10^{16}	$1.49x10^{-2}$	$1.34x10^{-2}$	$1.14x10^{-2}$	$1.00x10^{-2}$	$9.22x10^{-3}$
10^{17}	$1.89x10^{-2}$	$1.86x10^{-2}$	$1.75x10^{-2}$	$1.66x10^{-2}$	$1.58x10^{-2}$
10^{18}		$2.15x10^{-2}$	$2.26x10^{-2}$	$2.25x10^{-2}$	$2.23x10^{-2}$
10^{19}			$2.35x10^{-2}$	$2.57x10^{-2}$	$2.69x10^{-2}$

7.2.2 H Plasma with K-Shell Radiator Load

The load for this series of experiments was a large diameter wire array z-pinch, which at early times has a low inductance, but during the implosion, the time derivative of the inductance is very high. Thus, the voltage at the load, which can be described by

$$V = IR + L\frac{dI}{dt} + I\frac{dL}{dt} \tag{7.3}$$

becomes large late in time when both I and L-dot are large. This causes the electric fields within the convolute to increase, which can increase the current losses in the region as well. The increased energy deposition in the convolute desorbs more H from the electrodes; thus the density of the H plasma should increase with the increase in current losses within the convolute.

A plot of the electrical signals (current and voltage) for shot 2082 is shown in Fig. 7.10. Spectral lineouts that averaged a 10 ns window were taken at 10 ns intervals starting at 80 ns. The lineouts are plotted in Fig. 7.11. The lineouts show a significant change in spectral line-shape with time, which, in this case, indicates increasing plasma density. Additionally, the H-alpha features appear to be the superposition of two Lorentzian profiles, which indicates that there are two regions of significantly different plasma density. The low density plasma is assumed to be located within the B-dot cup, and the higher density plasma is assumed to be in the convolute itself.

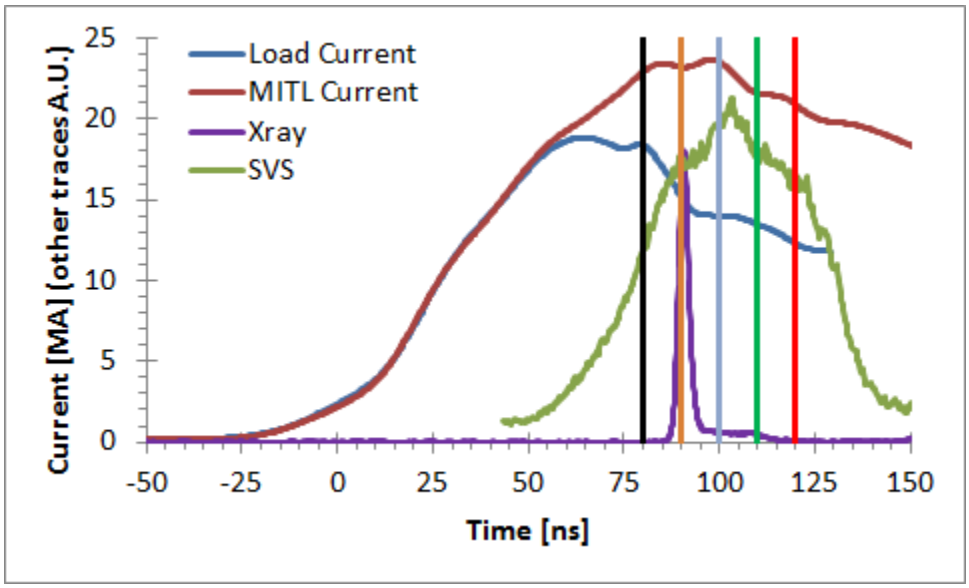

Fig. 7.10 Traces from shot 2082 (K-shell radiator load). In addition to the MITL and load current signals, a PCD signal showing the x-ray timing is shown in purple, and a temporal lineout of the streaked visible spectroscopy (SVS) film is shown in green. The timings of the five spectral lineouts of the SVS film are also shown.

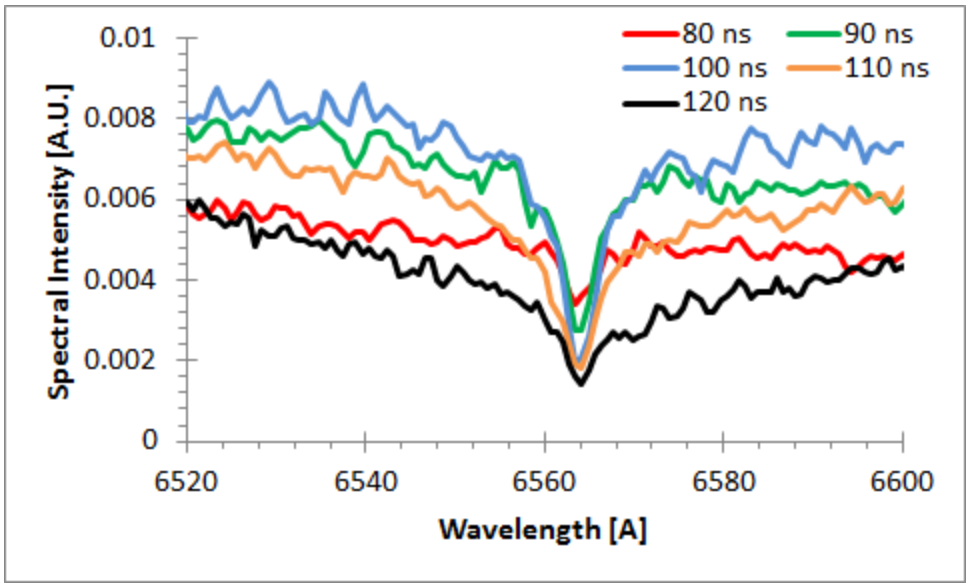

Fig. 7.11 Spectral lineouts of the data from shot 2082 (K-shell radiator load). The absorption feature at 6563 A is prominently visible in all traces shown. As time progresses, the width and depth of the absorption feature change significantly.

The superposition of two Lorentzian profiles was fit to each of the lineouts (an example is shown in Fig. 7.12), and the FWHM for each Lorentzian at each time is reported in Table 7.3. The narrower Lorentzian was assumed to be the result of the B-dot cup plasma. Note that the density calculated here is significantly lower than that determined in Section 7.2.1; a possible explanation for the difference will be discussed later. Using Equation 6.3 and the values listed in Table 7.3, the density of the plasma was determined to range from 6×10^{16} cm^{-3} to 1×10^{18} cm^{-3}.

Table 7.3 Compilation of information about the lineouts of shot 2082 (K-shell radiator load). Included in the table are the FWHMs of the Lorentzian profile fits to the data and the plasma density as calculated using Equation 7.4. Subscripts denote the different Lorentzians superimposed on one another to fit the experimental data. The subscript 1 is used for the Lorentzian with the larger FWHM possibly associated with the convolute. The two Lorentzian fits describe two different regions of plasma that are being observed by the probe.

Time [ns]	$FWHM_1$ [A]	$FWHM_2$ [A]	$Density_1$ [cm^{-3}]	$Density_2$ [cm^{-3}]
80	6	2.2	$7.3\pm1.7 \times 10^{16}$	$2.4\pm0.9 \times 10^{16}$
90	12	3	$1.5\pm0.3 \times 10^{17}$	$3.6\pm1.4 \times 10^{16}$
100	16	3.2	$2.2\pm0.5 \times 10^{17}$	$3.8\pm1.4 \times 10^{16}$
110	36	6	$6.3\pm1.4 \times 10^{17}$	$7.4\pm2.8 \times 10^{16}$
120	56	3.8	$1.0\pm0.2 \times 10^{18}$	$4.6\pm1.7 \times 10^{16}$

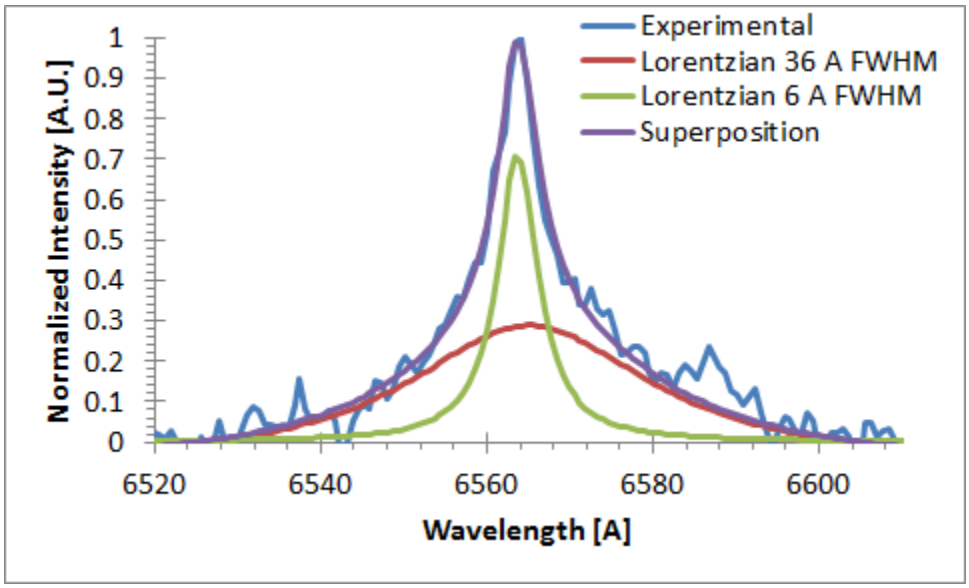

Fig. 7.12 Lineout at 110 ns from shot 2082. A line was fit to the continuum around the absorption feature from which the experimental signal was subtracted to isolate the line. The line was normalized such that the peak value was equal to unity. A superposition of two Lorentzians (purple trace) was fit to the experimental data. This fit was used to determine the FWHMs of the absorption feature.

A simple calculation to estimate the monolayer desorption rate within the B-dot cup was performed using the above data. The smaller FWHM was assumed to be the result of H plasma within the B-dot cup itself. The peak density inferred from this FWHM was 6.6 x

10^{16} cm^{-3}. The B-dot cup has a volume approximately equal to 0.86 cm^3, thus at the estimated density, there are 5.7 x 10^{16} H atoms. The surface area of the cup is approximately 3.8 cm^2; this gives 1.5 x 10^{16} H/cm^2, which over the 110 ns of the current pulse gives a desorption rate of 1.4 x 10^{14} H/cm^2/ns. Rose's simulations assume a desorption rate on the order of 0.1 monolayers/ns; a monolayer is approximately the equivalent of 10^{15} H/cm^2, thus Rose's simulations assume a desorption rate of ~ 10^{14} H/cm^2/ns, which is in good agreement with the experimental data.

7.2.3 H Plasma with Isentropic Compression Load

For this case, a cylindrical liner was shocklessly compressed as part of an isentropic compression experiment (ICE). When compared to a wire array, the liner slowly implodes onto the axis, thus the L-dot is smaller than that in the previous case. Additionally, the Z-machine was fired in long pulse mode for this shot, which means that I-dot was also decreased. As a result, the load voltage was significantly lower than in the previous case. Furthermore, a small diameter upper convolute post was used in this experiment, and because the anode-cathode gap was also increased, the electric field in the convolute was significantly lower than in the previous case. As a result of this, the loss in the convolute is expected to decrease, which will also cause the energy deposited in that region to decrease, thus the desorbed H should decrease as well. The expected consequence of the decreased plasma density (relative to the wire array case) is a narrower absorption line profile.

Spectral lineouts of the streak image were taken at 10 ns intervals. The timing of the lineouts and the shot traces are shown in Fig. 7.13; the lineouts are shown in Fig. 7.14. A superposition of at least two Lorentzian curves was fit to each lineout and the FWHM for each time was recorded in Table 7.4. Earlier in time, two Lorentzians centered at 6563 A (H-alpha) were used to describe the experimental data. At late times, additional absorption features were observed at 6578 and 6583 A, which correspond to C-II, thus a total of 4 Lorentzians were necessary to describe the data as shown in Fig. 7.15. This is an indication that in addition to H desorption from the electrodes, there are hydro-carbon contaminants in the convolute as well. The long risetime of the pulse (2x the normal risetime) allows the carbon to expand into the field of view. The carbon clearly travels slower than the hydrogen, which explains why it was not observed on the previous shots with short current risetimes.

Table 7.4 Compilation of information about the lineouts of shot 2110 (Isentropic Compression Experiment). Included in the table are the FWHMs of the Lorentzian profile fits to the data and the plasma density as calculated using Equation 7.4. Subscripts denote the different Lorentzians superimposed on one another to fit the experimental data. The subscript 1 is used for the Lorentzian with the larger FWHM. The two Lorentzian fits describe two different regions of plasma that are being observed by the probe.

Time [ns]	$FWHM_1$ [A]	$FWHM_2$ [A]	$Density_1$ [cm^{-3}]	$Density_2$ [cm^{-3}]
100	N/A	N/A	Unknown	Unknown
125	10	2.2	$1.2\pm0.3 \times 10^{17}$	$2.4\pm0.9 \times 10^{16}$
150	16	3.6	$2.3\pm0.5 \times 10^{17}$	$4.4\pm1.7 \times 10^{16}$
175	28	4	$4.7\pm1.1 \times 10^{17}$	$4.9\pm1.9 \times 10^{16}$
200	38	5.6	$6.7\pm1.5 \times 10^{17}$	$6.9\pm2.6 \times 10^{16}$

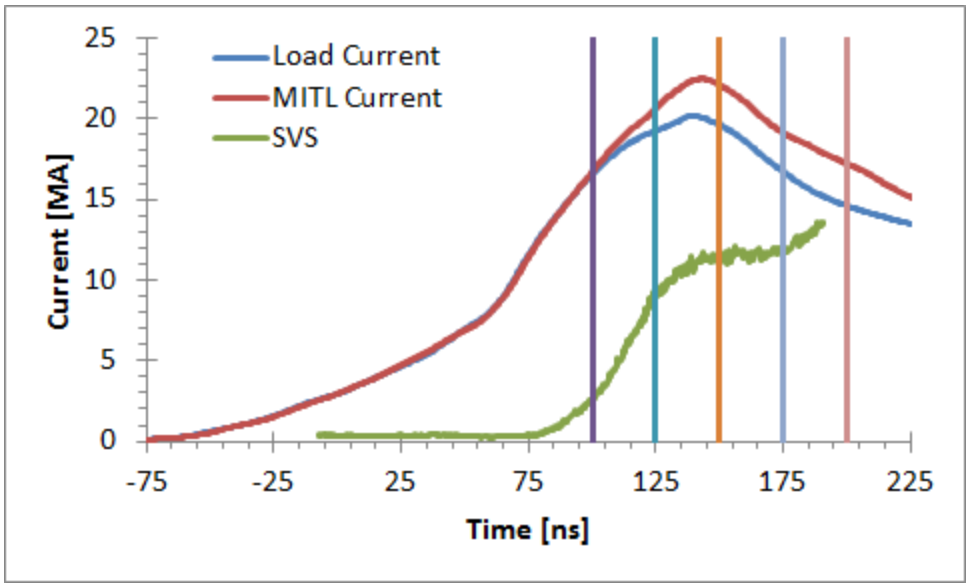

Fig. 7.13 Traces from shot 2110 (Isentropic Compression Experiment). In addition to the MITL and load current signals, a temporal lineout of the streaked visible spectroscopy (SVS) film is shown in green. The timings of the five spectral lineouts of the SVS film are also shown.

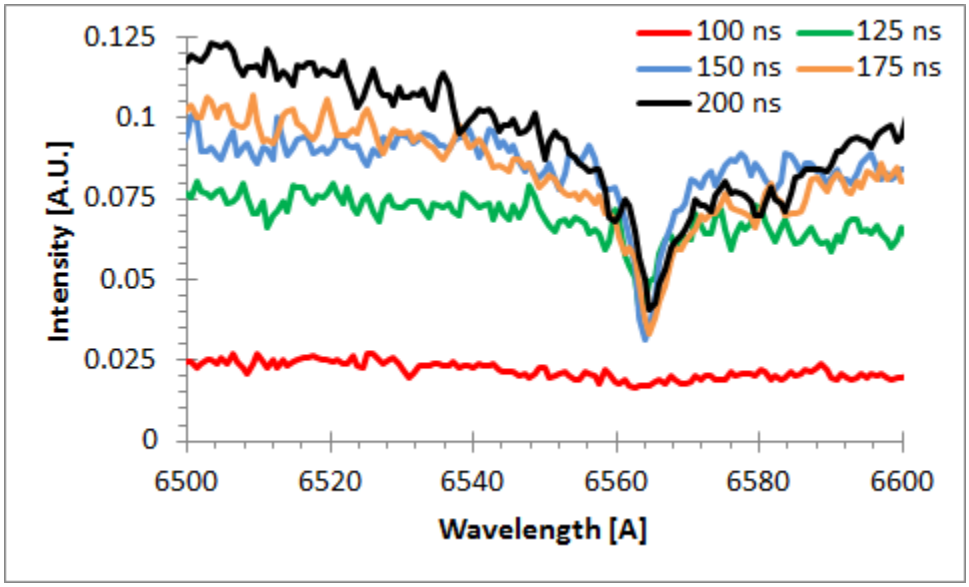

Fig. 7.14 Spectral lineouts of the data from shot 2110 (Isentropic Compression Experiment). The H-alpha absorption feature at 6563 A is not observed in the first trace, but is prominently visible in the other four traces shown. As time progresses, the width and depth of the absorption feature change significantly. Additionally absorption peaks are observed at 6578 A and 6583 A, which are likely the result of C-II.

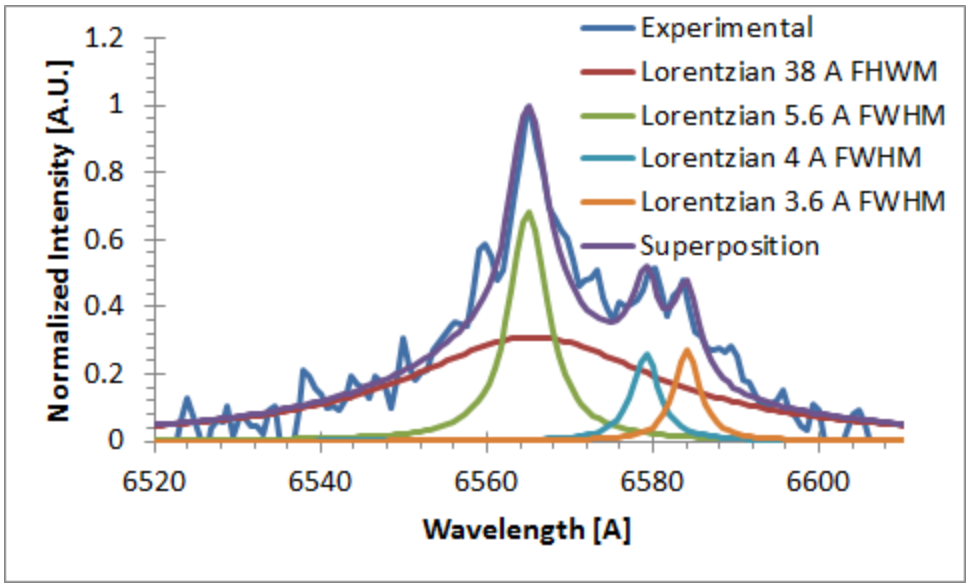

Fig. 7.15 Lineout at 200 ns from shot 2110. A superposition of four Lorentzians was fit to the experimental data. Two of the Lorentzians were centered at 6563 A (one for the convolute H-alpha and one for the B-dot cup H-alpha). The other two Lorentzians were centered at 6578 A and 6583 A; both are singly ionized carbon features.

Compared to the wire array load, the H density becomes observable later and increases at a slower rate. The portion of the absorption that was attributed to the B-dot cup plasma is similar to that in the wire array load data set. Using Equation 7.3 and the FWHM in Table 7.4, the density of the H plasma in the convolute was calculated for each time. The calculated densities ranged from 2.4×10^{16} cm^{-3} to 6.7×10^{17} cm^{-3}.

7.2.4 H Plasma with Inertial Confinement Fusion Load

For this shot, the Z-machine was fired in short pulse mode (the same as the K-shell radiator shot); the large diameter upper convolute posts were used. As a result, the load voltage (and the electric field) should be similar to the K-shell case. Thus, the expected current loss and H plasma density are expected to be similar to the K-shell case.

The current and voltage traces for this shot are unavailable; however, some estimates about the current can be made. Using the knowledge that the machine was operated in short pulse mode, the time of peak x-ray occurs at roughly 3100 ns machine time, which is typically ~10 ns after peak current, and the peak current is roughly 20 MA; therefore, a very crude estimate of the MITL current is given in Fig. 7.16. Spectral lineouts were taken of the data at 10 ns intervals with 10 ns windows. The timing of these lineouts is plotted in Fig. 7.16, and the lineouts themselves are shown in Fig. 7.17.

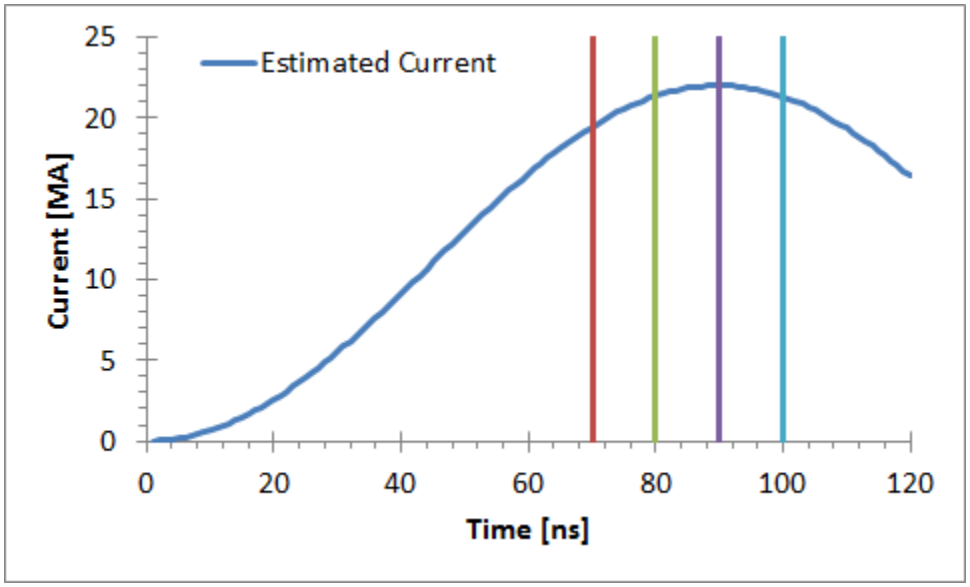

Fig. 7.16 Estimated current trace from shot 2116 (Inertial Confinement Fusion Experiment). The timings of the four spectral lineouts of the SVS film are also shown.

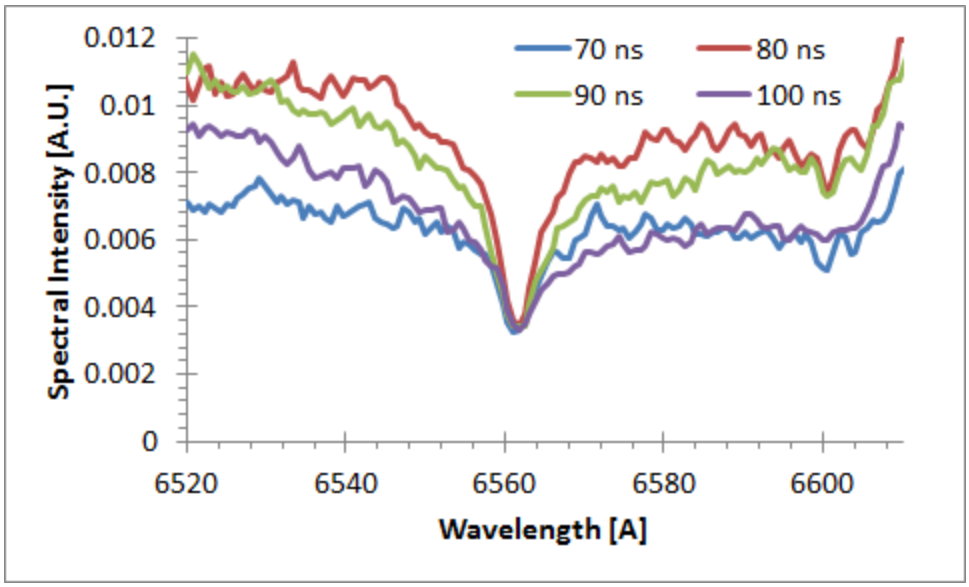

Fig. 7.17 Spectral lineouts of the data from shot 2116 (Inertial Confinement Fusion Experiment). The H-alpha absorption feature at 6563 A is observed on all traces. As time progresses, the width and depth of the absorption feature change significantly.

Fitting a superposition of two Lorentzians to each lineout, the FWHMs were determined and tabulated in Table 7.5. The narrower Lorentzian gives similar results to the previous cases, as is expected, assuming that the absorption comes the B-dot cup plasma.

Table 7.5 Compilation of information about the lineouts of shot 2116 (Inertial Confinement Fusion Experiment). Included in the table are the FWHMs of the two Lorentzian profile fits to the data and the plasma density as calculated using Equation 7.4. Subscripts denote the different Lorentzians superimposed on one another to fit the experimental data. The subscript 1 is used for the Lorentzian with the larger FWHM. The two Lorentzian fits describe two different regions of plasma that are being observed by the probe.

Time [ns]	$FWHM_1$ [A]	$FWHM_2$ [A]	$Density_1$ [cm^{-3}]	$Density_2$ [cm^{-3}]
70	12	3.6	$1.5\pm0.3 \times 10^{17}$	$4.4\pm1.7 \times 10^{16}$
80	16	4.6	$2.3\pm0.5 \times 10^{17}$	$5.7\pm2.2 \times 10^{16}$
90	24	6	$3.9\pm0.9 \times 10^{17}$	$7.4\pm2.8 \times 10^{16}$
100	24	4	$3.9\pm0.9 \times 10^{17}$	$4.9\pm1.9 \times 10^{16}$

CHAPTER 8

DISCUSSION OF POST-HOLE CONVOLUTE DATA FROM THE Z-MACHINE

In this chapter, plasma densities (calculated in Chapter 7) are compared for several different convolute/load setups on the Z-Machine at Sandia National Labs (see Table 8.1). Experimental data are also compared to LSP simulations performed by Rose et al. The impedance of the convolute was calculated as a function of time for several cases. Additionally, plasma closure velocity was estimated using three different techniques.

Table 8.1 Compilation of the maximum inferred plasma density in the convolute and B-dot cup. The load types include Inertial Confinement Fusion (ICF), Imploding Liner for Magneto-Inertial Fusion (MIF), K-Shell Radiator (KSR), and Isentropic Compression (ICE). The spectral lines used were Li-I (6708 A) and H-I (6563 A).

Shot #	Load Type	Spectral Line	Convolute Density [cm^{-3}]	Cup Density [cm^{-3}]	Technique
2115	ICF	6708 A (Li-I)	$5\pm2 \times 10^{16}$	N/A	PrismSpect Sim.
2116	ICF	6708 A (Li-I)	$7\pm3 \times 10^{16}$	N/A	PrismSpect Sim.
2104	MIF	6563 A (H-I)	N/A	$2.1\pm0.8 \times 10^{17}$	Stark Broadening
2082	KSR	6563 A (H-I)	$1.0\pm0.2 \times 10^{18}$	$7.4\pm2.8 \times 10^{16}$	Stark Broadening
2110	ICE	6563 A (H-I)	$6.7\pm1.5 \times 10^{17}$	$6.9\pm2.6 \times 10^{16}$	Stark Broadening
2116	ICF	6563 A (H-I)	$3.9\pm0.9 \times 10^{17}$	$4.9\pm1.9 \times 10^{16}$	Stark Broadening

8.1 Comparison of H Plasma Densities for Different Loads

The H plasma densities recorded in the previous three sections were compiled and plotted versus time in Fig. 8.1. The times have been shifted such that the zero time from each case is overlaid (the zero time was calculated as the time at which a line extrapolated from 75% of the peak to 25% of the peak passes through zero). The K-shell radiator shot and the Fusion shot turn on at roughly the same time, but the density on the K-shell shot increases more rapidly than the density on the Fusion shot. The ICE shot turns on much later than the other two, and it increases slowly compared to the other two cases.

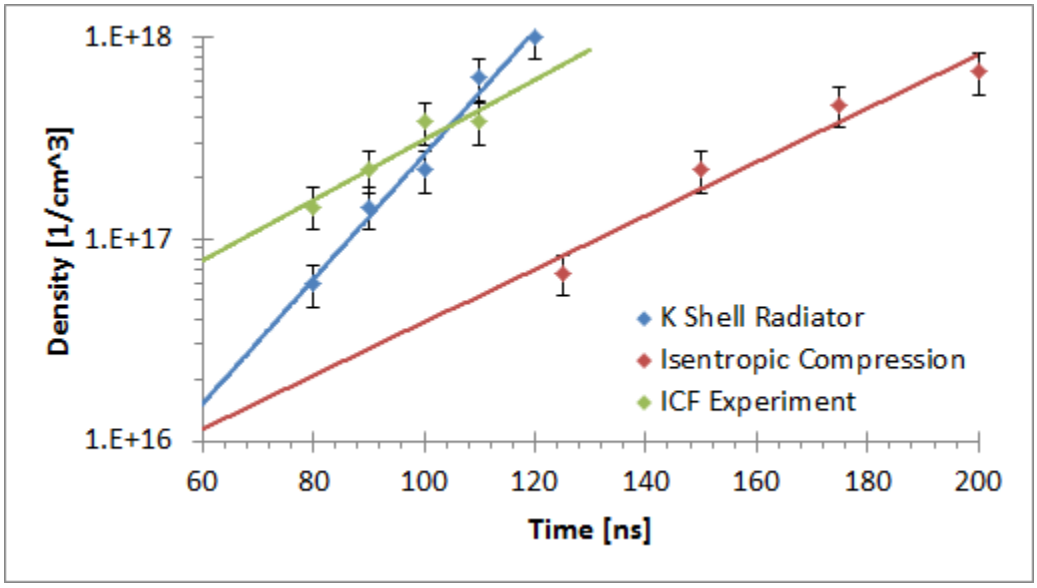

Fig. 8.1 Plot of the measured density as a function of time for three experimental cases. The K Shell Radiator and ICF shots used the Z-Machine in short pulse mode, while the ICE shot used long pulse mode. This explains the difference in start time between the cases.

Without extensive knowledge of the inertial confinement fusion experiment load, nothing definitive can be said about the expected plasma density. However, in other previous ICF experiments, the wire array load diameter was typically considerably

smaller than that in K-shell radiator experiments. Based on this, one could assume that the initial inductance of the ICF wire array would be slightly higher than that in the K-shell radiator, and that the L-dot would be lower in the ICF wire array case. This indicates that the convolute voltage (thus the H density) should be higher early in time for the ICF experiment case, but once the K-shell wire array begins imploding on axis, the convolute voltage (thus the H density) in the K-shell case should overtake the ICF experiment. The convolute voltage is related to the energy deposited in the region, and consequently the contaminant desorption rate. For a greater desorption rate, a faster increase in plasma density is expected. This explanation fits with the observed plasma densities.

The H density in the ICE case is expected to become observable later and to increase more slowly than the other two cases. This is the result of both the machine being fired in long-pulse mode and the load voltage remaining relatively low (additionally, the loss current in the convolute is much smaller for a longer time); there is a longer time before the energy deposited in the convolute region is sufficient to liberate an observable quantity of H. The data support this conclusion as well.

The inferred plasma density in the B-dot cup and the inferred density in the convolute disagree. The density inferred from the measurements than only viewed inside the cup (see Fig. 6.12) lies in between the low density that was assumed to be from the B-dot cup, and high density that was assumed to be from the convolute in the other measurements. A possible explanation for this discrepancy follows. In the case where the probe only

views the interior of the B-dot cup, it is looking directly into the cup surface where there is likely dense plasma that forms on the surface of the cup. This plasma is observed with the B-dot cup view, but not with the convolute views as is shown in Fig. 8.2. Assuming this explanation is correct, the plasma near the surface of the B-dot cup is up to an order of magnitude greater than that at the center of the cup, but approximately an order of magnitude less than the maximum density within the convolute itself.

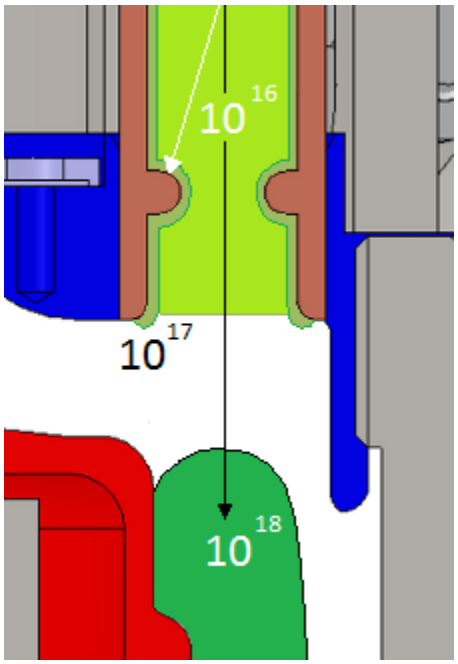

Fig. 8.2 A schematic diagram of the location of different plasma densities that would explain the results observed above. Plasma is represented by the different shades of green. The lightest green represents the least dense plasma, and the darkest represents the most dense plasma. The white arrow indicates the region viewed by in the B-dot cup measurements. In that case, the probe looks through the 10^{16} cm^{-3} density plasma at the 10^{17} cm^{-3} density plasma. The black arrow indicates the region viewed by the probe when it is pointed into the convolute. In that case, the probe views through the 10^{16} cm^{-3} density plasma at the 10^{18} cm^{-3} density plasma. (SolidWorks models of the Z Machine courtesy of J. Cisneros and M. Vigil.)

8.2 Comparison between Simulated and Experimental Densities

A series of simulations of the Z-machine double post-hole convolute have been performed by Rose et al. using a hybrid particle-in-cell and fluid code known as LSP. The simulation geometry matches that of the experiment, and the load used was a K-shell radiator similar to the load used for these measurements. In these simulations, neutral hydrogen is desorbed from the electrodes in the convolute and expands out into the A-K gap from the cathode. A line was drawn through the simulation that matches the view of the fiber in the actual experiment. The density of the H plasma in the cells along this line was determined at 10 ns intervals and is shown in Table 8.2.

Table 8.2 Results from Rose's simulations. The density is measured along the axis of the experimental probe view. The time of the density measurements is relative to the start of the current. The start of current is determined by extrapolating a line from 75% of peak current through 25% of peak current to zero current.

Time [ns]	Density [cm^{-3}]
-2	0
8	1.00×10^{14}
18	2.33×10^{15}
28	9.19×10^{15}
38	1.60×10^{16}
48	2.32×10^{16}
58	2.68×10^{16}

A comparison between the results from Rose's simulations (of the K-shell radiator case) and the K-shell radiator experimental data is shown in Fig. 8.3. The two datasets do not include overlapping time scales, thus it is difficult to make a direct comparison between the two. However, it is clear that both data sets show the H density increasing with time. Additionally, the simulated densities measurements were all made prior to the experimental measurements, and all of the simulated densities are below the experimental densities. Based on these data, it is plausible that the data sets could agree with one another at later times.

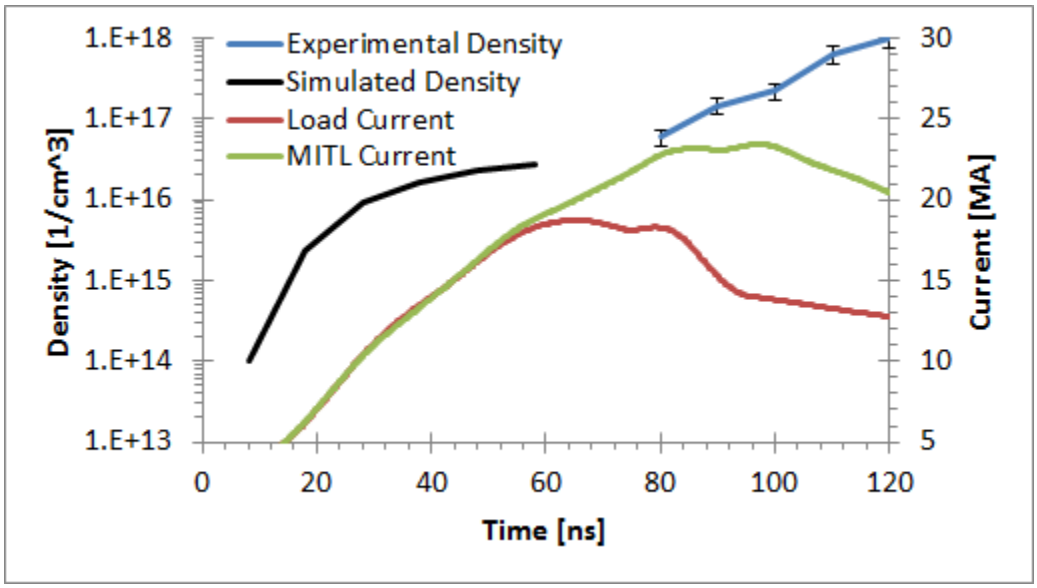

Fig. 8.3 A plot of the experimental and simulated plasma density on a semi-log plot. The MITL and load currents have been included for timing. The simulation only provides information about the density until ~ 60 ns, and the experimental data are not available until ~ 80 ns, thus a direct comparison between the two cannot be made. There is a general trend that the simulated data points increase with time, and the last simulated data point represents an earlier time but only slightly lower density than the first experimental data point.

In order to verify if the data sets match, there would need to be an overlap in the time at which the H densities were measured. The experimental data is limited by the time at which the H-alpha feature becomes observable. Thus, with higher spectral resolution

and increased probe sensitivity, the density may be able to be measured experimentally at earlier times. The simulated data is ultimately limited by the duration of the simulation. Assuming the physics in the simulation continues to hold, longer simulations could be run, and comparison to measurements of the H density should be possible at later times.

8.3 Current Losses in the Post-Hole Convolute

Signals from the B-dot current monitors upstream and downstream from the convolute were used to determine the "lost current" in the convolute. The outer MITL measurement was losslessly propagated to the load in order to determine what the load current could have been (calculations courtesy of Ryan McBride [67],[37]). The inner MITL measurement is used to determine the actual load current. Subtracting the "expected" load current from the measured load current gives the lost current as a function of time. Additionally, the stack voltage is losslessly propagated to the load in order to determine the expected load voltage. Dividing the expected load voltage by the loss current gives the effective shunt impedance of the convolute. This analysis was performed on the traces from the K-shell radiator shot and the ICE shot from sections 7.2.2 and 7.2.3, and the results are plotted in Fig. 8.4a, b, and c. The shunt impedance for the ICE case has been shifted 52 ns earlier in time in order to directly compare to the K Shell Radiator case. The shunt impedance for the two cases is roughly equal at the point at which the lost current starts. As time progresses the ICE shunt impedance remains

higher for a longer time. The shunt impedance for the ICE case takes approximately 30% longer to drop from 100 ohm to 0.1 ohm.

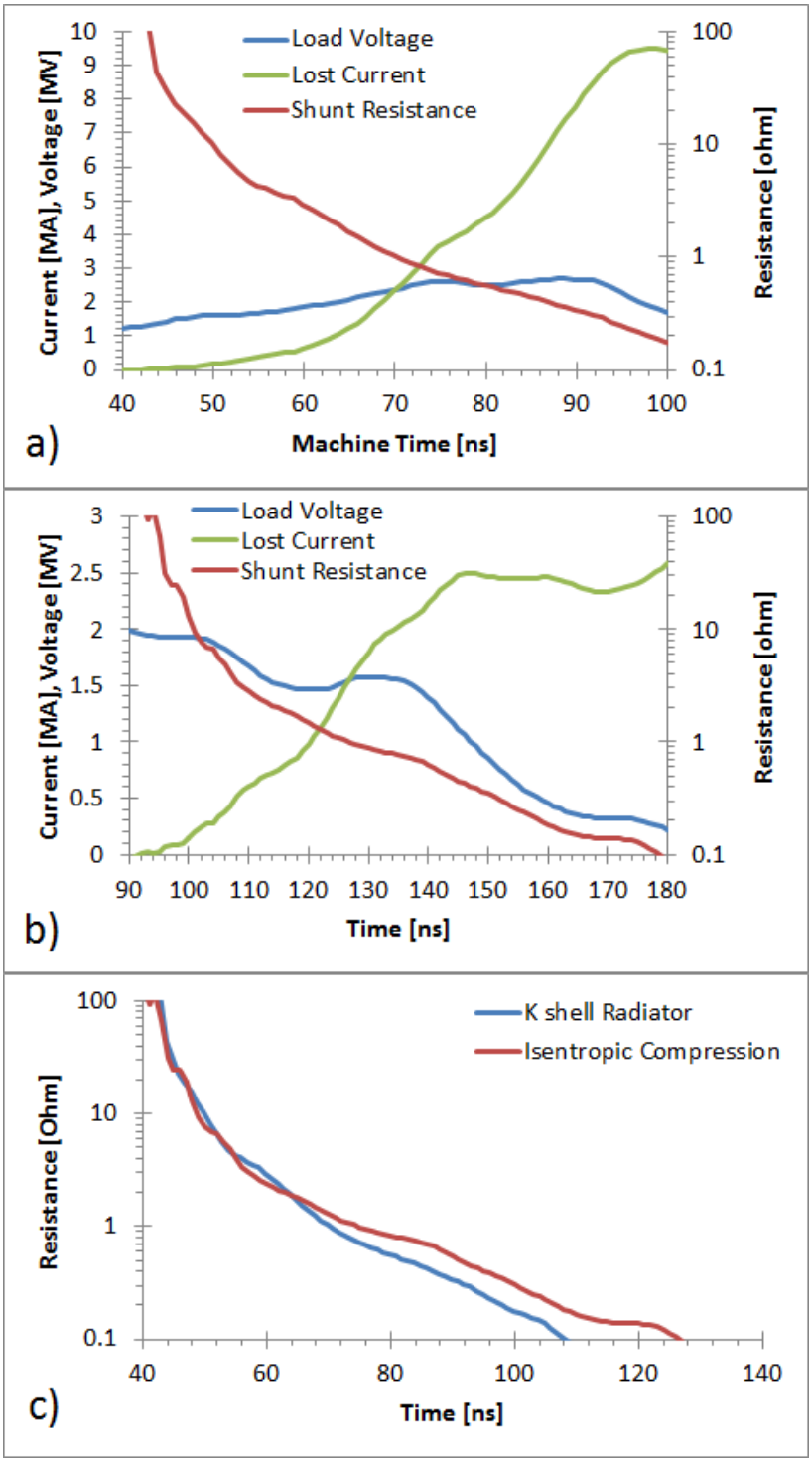

Fig. 8.4 Plots showing the Load Voltage, Lost Current, and Shunt Resistance. Plot a) shows the three traces for a K Shell Radiator Shot (2077), plot b) shows the traces for an Isentropic Compression Experiment (2110), and plot c) shows the Shunt Resistance for both cases with the ICE time shifted backwards by 52 ns.

The timing of the current losses with respect to the convolute emission turn-on time is of considerable importance as well. The measured turn-on time of the convolute emission is dependent on the sensitivity of the detector, which means that as the gain on the streak camera MCP is increased (greater applied voltage), the emission from the convolute will appear to start earlier in time. In an effort to record the earliest emission, the sensitivity of the system was set as high as possible. There would still likely be emission earlier in time, but it is at a rate of less than 7×10^{12} photons/s/nm/ster/mm^2. A temporal lineout of the high gain data is shown in Fig. 8.5 along with the traces for the shot. A low gain temporal lineout is shown on the same plot, in order to show the significance of the gain setting.

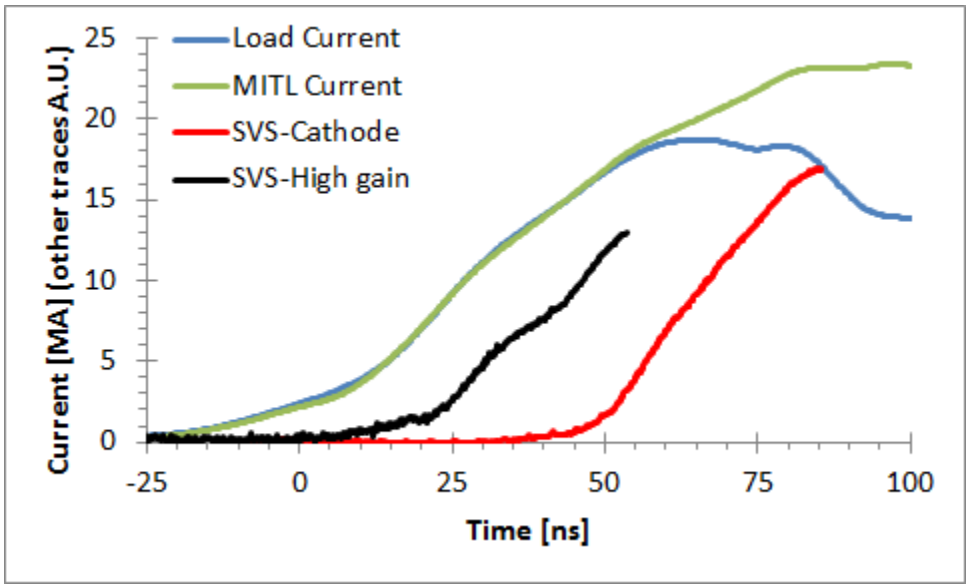

Fig. 8.5 Plot of the two current traces and a temporal lineout of the streaked visible spectroscopy (SVS) film for shot 2077 (K Shell Radiator Load). Also included is the SVS signal for shot 2078 (SVS – High Gain), which used an identical load and had nearly identical current traces.

The data from Rose's convolute simulations (presented in Table 8.3) were compared to the continuum emission measurements from the convolute. The square of the density

scaled by an arbitrary constant was plotted along with the experimental data in Fig. 8.6. The density of the plasma is related to its continuum emission intensity as follows

$$\int_{\lambda}^{\lambda+\Delta\lambda} I_z(\lambda)d\lambda = \frac{2^5\sqrt{\pi}E_H c z^2}{3^{3/2}\lambda^2}\left(\frac{E_H}{kT}\right)^{1/2}\Delta\lambda\int dx$$
$$\times\left\{\xi_{fb}(\lambda,T)\left[1-exp\left(\frac{-\hbar\omega}{kT}\right)\right]+\xi_{ff}(\lambda,T)exp\left(\frac{-\hbar\omega}{kT}\right)\right\}$$
$$\times exp\left(\frac{\Delta E_L-\Delta E_Z}{kT}\right)(\alpha a_0)^3 N_Z N_e$$

or

$$\int_{\lambda}^{\lambda+\Delta\lambda} I_z(\lambda)d\lambda \propto N_Z N_e \tag{8.1}$$

where N_Z is the ion number density and N_e is the electron number density, and in the case of a hydrogen plasma N_Z is assumed to be equal to N_e [62]. An arbitrary constant was chosen because the experimental data were collected over a cone, while the simulation values were measured along a line of cells at the center of that cone.

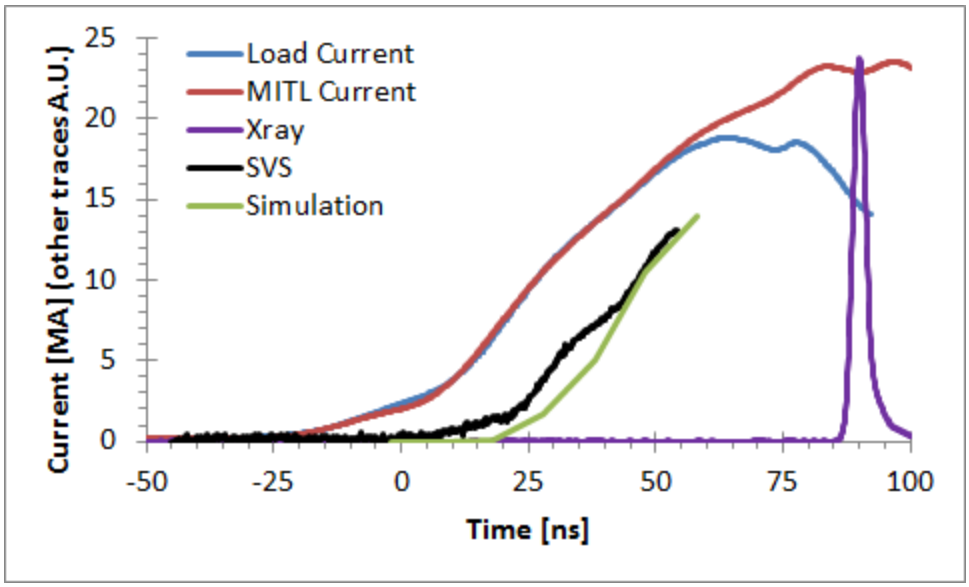

Fig. 8.6 Plot of the traces for shot 2078 (K Shell Radiator Load). The simulated density was squared and scaled by an arbitrary constant to match it to the experimental SVS lineout.

The experimental data match the simulated data in both timing and shape. Although the slopes cannot be directly compared due to the scaling factor applied to correct for the difference in collection volume, the shapes match in that both are roughly linear with no local minima or plateaus. This indicates that the emission turn-on time in the convolute is at roughly 20 ns (or earlier). The measured load current deviates from the expected load current at 45 ns, thus, the convolute continuum emission begins at least 25 ns prior to the start of the lost current.

8.4 Gap Closure Velocity Calculations

Anode-cathode gap closure in a crossed field device has been studied previously, but the double post-hole convolute has an extremely complex geometry that differentiates this measurement from those previously performed. Several methods of estimating the gap closure velocity are presented below.

8.4.1 Optical Turn-on Time to Current Loss

The effective gap closure velocity can be roughly estimated by dividing the gap distance by the time it takes for the plasma to cross the gap. This is represented by

$$v = \frac{d}{t_2 - t_1} \tag{8.2}$$

where d is the distance across the A-K gap, t_1 is the time at which a plasma forms at the surface of the cathode, and t_2 is the time at which the load current begins to deviate from the MITL current. This analysis requires several assumptions. First, it assumes that the plasma eventually spans from the cathode to the anode. Additionally, it assumes that prior to the plasma completely crossing the gap, there is not a measurable amount of current shunted away from the load. Finally, it requires that either the area of the plasma spanning the gap, or the conductivity of the plasma in the gap increases with time to account for the increasing fraction of current shunted away from the load.

The gap between the upper post and the hole in the upper cathode is 11.4 mm, the turn on time according to the data presented in Section 8.3 was 20 ns, and the time at which the load current deviates from the MITL current was 45 ns. Based on these values and equation 8.2, the effective average gap closure velocity was estimated to be 46 cm/μs.

As a side note, the conductivity of the plasma can be estimated using the Spitzer resistivity

$$\eta \simeq 10^{-4} \frac{Z ln\Lambda}{T^{\frac{3}{2}}(eV)} ohm - m \tag{8.3}$$

where Z is the ion charge number (for hydrogen Z = 1), lnΛ is ~ 10 and T is the plasma temperature in eV [68],[69]. Assuming 3 eV hydrogen plasma, conductivity is $2x10^{-4}$ ohm-m. Given the geometry of the convolute, and assuming uniform plasma of the conductivity calculated above fills the entire A-K gap and there are 24 gaps in parallel (area ~ 240 cm^2, length ~ 1 cm), the impedance of the gap is 10^{-4} ohms. This is considerably lower than the measured convolute impedance (0.1 to 100 ohms). Thus one or more of the assumptions cannot be correct.

8.4.2 Optical Turn-on Time across the Gap

A second technique for estimating the plasma closure velocity utilizes time resolved emission measurements at several locations throughout the gap (an optical time of flight measurement). The turn-on time at each location was determined from the collected data, and assuming an axial position that lines up with the post-hole (see Fig. 8.7) the distance across the gap between the measurements was calculated. Based on these values the average optical closure velocity can be determined using the following

$$v = \frac{d_{2,3} - d_1}{t_{2,3} - t_1} \tag{8.4}$$

where $d_{1,2,3}$ are the distance from the surface of the electrode to the cathode view, gap view, and anode view, respectively, and $t_{1,2,3}$ are the turn-on times of the cathode view, gap view, and anode view respectively.

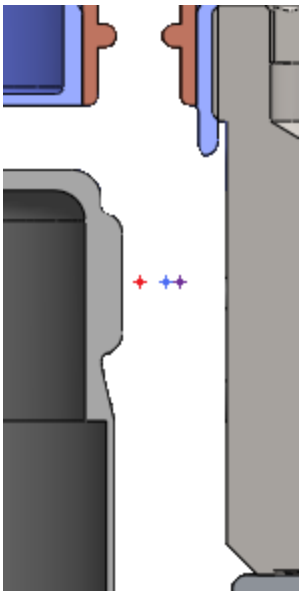

Fig. 8.7 R-Z cut of the upper post hole convolute showing the locations that the measurements were assumed to be made. The red point denotes the cathode measurement, the blue point denotes the gap measurement, and the purple point denotes the anode measurement. The points were chosen to lie on the intersection between the axis of the probe view and a line connecting the vertical center of the upper cathode hole to the anode post. (SolidWorks models of the Z Machine courtesy of J. Cisneros and M. Vigil.)

This calculation requires a set of assumptions as well. The axial position at which the light emission originates is assumed to be at the same height as the downstream side of the hole in the upper cathode. The views collect light from a volume, but the plasma location is assumed to be at the axis of the collection cone. The turn-on time is assumed to be the point at which the emission signal reaches 50% of its maximum signal.

The three different views were fielded on three shots with identical wire-array loads and identical instrument sensitivity. The streak images from these shots are presented in Section 6.2.1. Temporal lineouts of these data sets were taken at 5500 +/- 1000 A and are shown in Fig. 8.8. As the probe view progresses across the anode-cathode gap, the turn-on time becomes progressively later. This indicates that the plasma may be traveling across the anode-cathode gap. Using the distances and turn-on times listed in Table 8.3

and Equation 8.4, the optical plasma closure velocities for the two cases were determined to be 40 cm/μs and 51 cm/μs. Averaging these values gives 46 cm/μs, which is the same value that was calculated using the optical emission to current loss technique.

Table 8.3 Distance between the three CLPD views and the turn-on time for each location.

Location	Distance from Cathode [mm]	Turn on time [ns]
Cathode	N/A	63.6
Gap	2.9	70.8
Anode	4.5	72.4

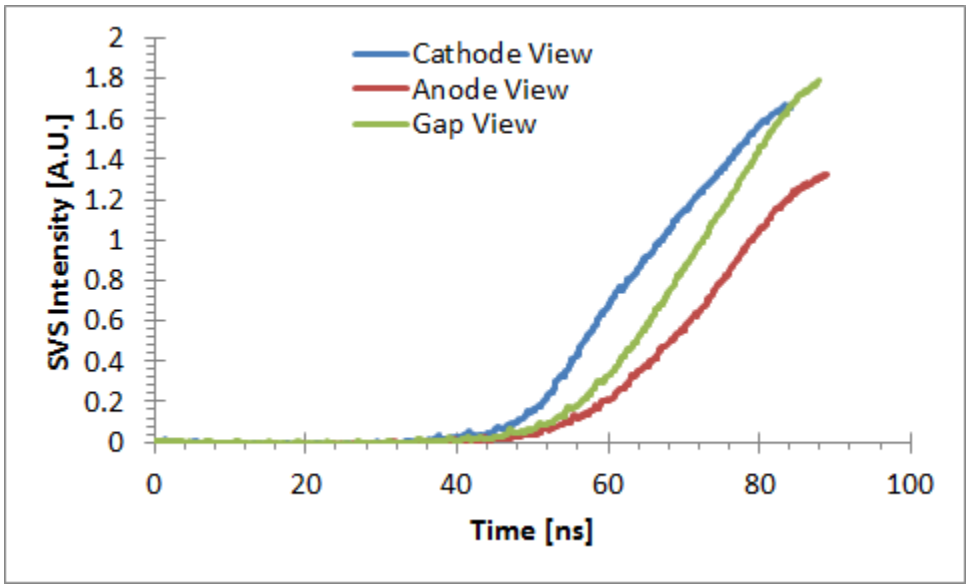

Fig. 8.8 Plot of the temporal lineouts of the SVS signal from shots 2077 (cathode), 2079 (anode), and 2080 (gap). Each shot used identical diagnostic settings with the exception of the probe angle, and the loads for the three shots were identical as well.

8.4.3 Space Charge Limited Current Loss

The final method of calculated closure velocity utilizes the electrical signals from the experiment and the Child-Langmuir Law

$$J = \frac{I}{A} = \frac{4}{9}\varepsilon_0 * \sqrt{\frac{2e}{m}} * \frac{V^{3/2}}{d^2} \tag{8.5}$$

where J is the current density, I is the current, A is the area of emission, e is the electron charge, m is the electron mass, ε_0 is the permittivity of free space, V is the gap voltage, and d is the distance across the A-K gap [48],[70]. The MITL current is measured prior to the convolute, and the stack voltage is lossless propagated to the load, thus approximations of V and I are known. Assuming an area, A, based on Rose's convolute simulations [31] as shown in Fig. 8.9, the gap distance, d, was calculated using

$$d = \sqrt{\frac{A}{I}} * \left(\frac{32e{\varepsilon_0}^2}{81m}\right)^{\frac{1}{4}} * V^{3/4} \tag{8.6}$$

A plot of d vs time is shown in Fig. 8.10. The time derivative of the gap distance gives the instantaneous gap closure velocity, which is also shown in Fig. 8.10.

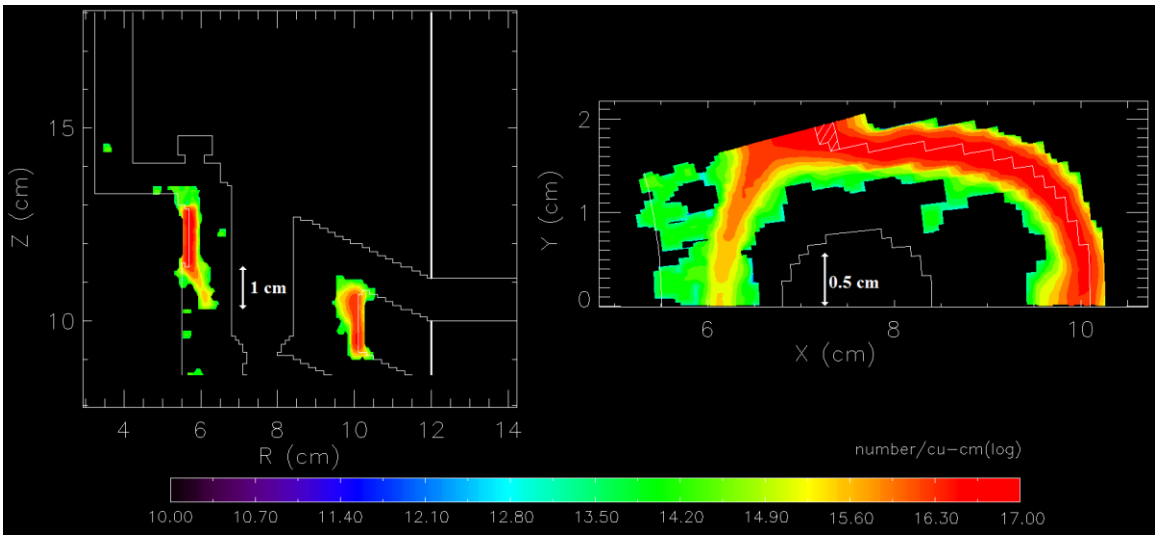

Fig. 8.9 Data from Rose's simulation [31]. R-Z and X-Y cut of the post-hole convolute with H density plotted. Based on these images, the plasma crossing the gap is assumed to have a cross-sectional area of approximately 1 cm². This is assumed to be the case for all upper and lower posts. Used with the permission of D. V. Rose.

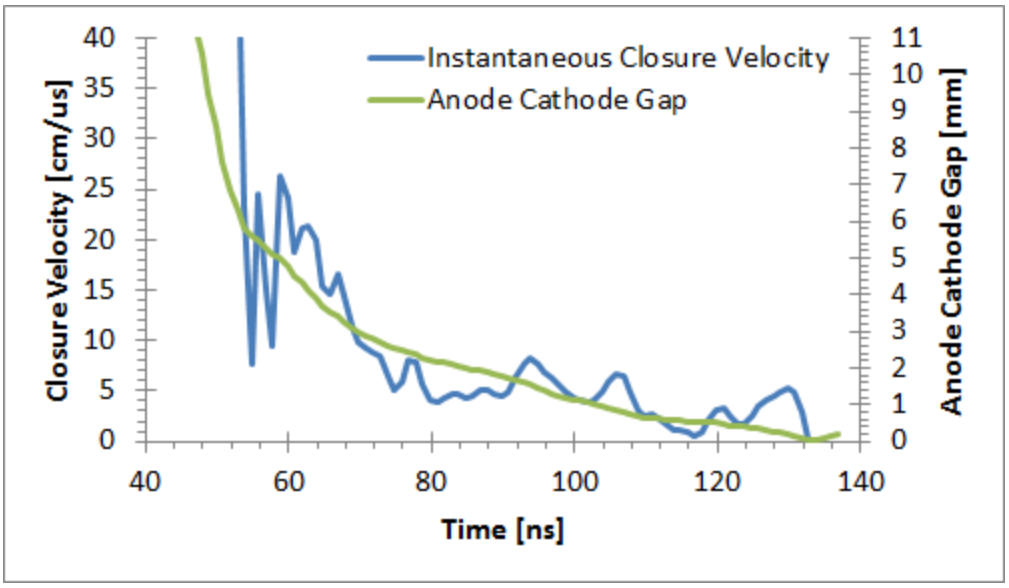

Fig. 8.10 A plot of the anode-cathode gap and closure velocity as a function of time. The gap decreases from the initial size of the A-K gap (11.4 mm) at the start of the lost current to approximately 1 mm at peak current. The closure velocity starts out at approximately 20 cm/μs, but eventually drops to approximately 5 cm/μs.

At approximately the time at which the MITL current begins deviating from the load current, the estimated gap distance is equal to the actual A-K distance. The gap closes to less than one mm by the peak of the lost current. Initially, the calculated closure velocity is high (~ 20 cm/μs), but as the plasma crosses the gap, the velocity rapidly drops until it reaches a relatively steady state of approximately 5 cm/μs.

This method of calculating the gap closure velocity requires assuming the main loss mechanism in the convolute is dense plasma originating from the cathode, emitting space charge limited flow across the gap, which is the suggestion given in Rose's paper. The calculations here assume that all of the current is lost to the posts and that all 24 convolute post-holes behave identically. The plasma is assumed to have a constant emission area, and emission associated with the rest of the convolute is assumed to be negligible. Finally, the Child-Langmuir Law used ignores the crossed-field transport

effects of the large magnetic fields within the convolute, which would act to limit the electron flow across the A-K gap. It should be noted that the effective gap would decrease if magnetic field effects were included, and would increase if the emission associated with the rest of the convolute (beyond the 1 cm^2 emission region) is not negligible. The gap is directly related to the square root of the emission area, so if the emission region was larger than the assumed value, the effective gap would need to be larger as well.

Equations 8.5 and 8.6 assume relativistic effects can be ignored as well. A relativistic version of the Child-Langmuir law was previously developed [71], however only a numerical solution to Poisson's equation is possible. A plot of the exact numerical solution compared to the non-relativistic case (low-energy approximation) is shown in Fig. 8.11. This plot shows that if the voltage and current density are known, the effective A-K gap will be smaller for the exact solution than for the non-relativistic case. The peak voltage is ~ 3 MV, thus the peak value for τ is ~ 6. At $\tau = 6$, the effect of neglecting the relativistic effects is less than 25%; for the majority of the pulse, $\tau < 3$ at which point the effect is less than 10%.

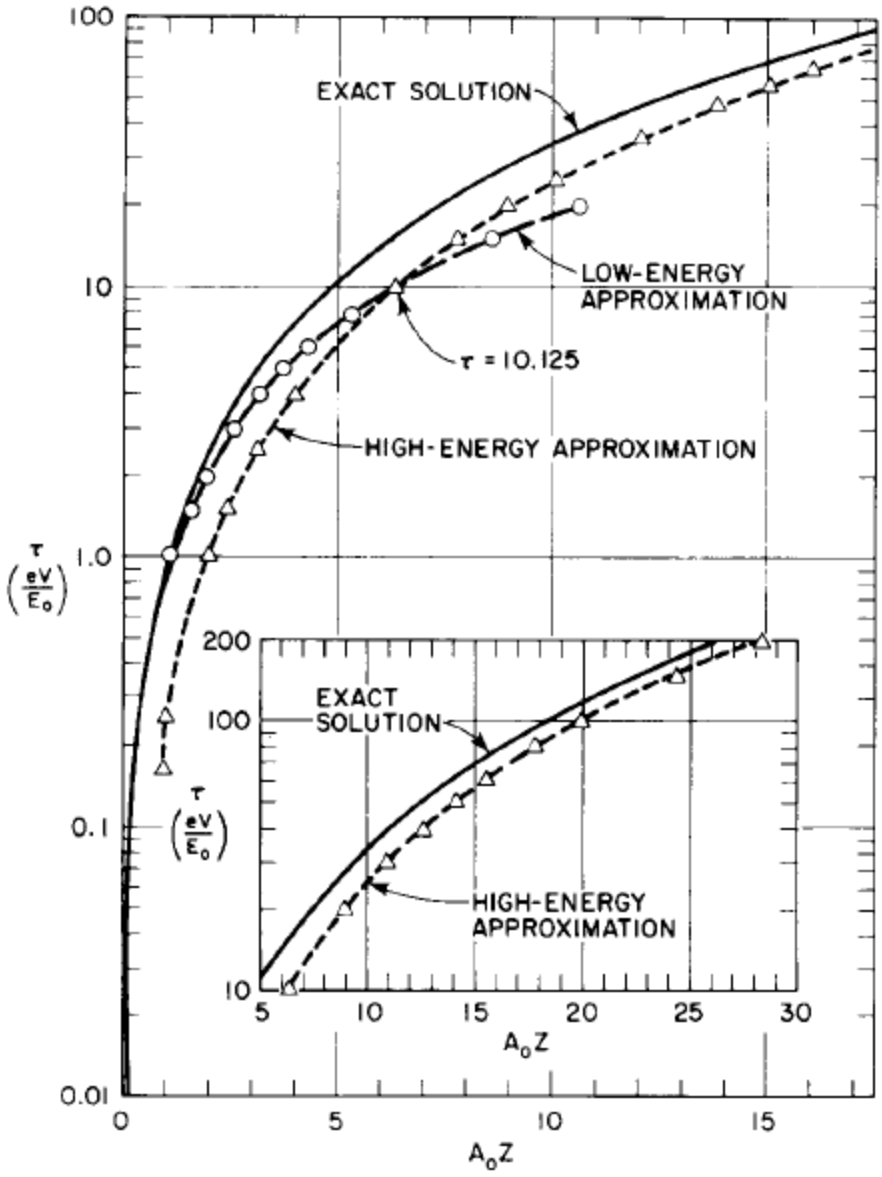

Fig. 8.11 Comparison of the exact solution of the relativistic Child-Langmuir law to the Low- and High-Energy Approximations. Figure courtesy of S. V. Yadavalli and R. L. Bollen [71].

8.4.4 Comparison of Different Gap Closure Measurements

The three techniques for estimating the anode-cathode gap closure described above give similar results to one another. The first two methods match each other to within 10%, but they are roughly double the early time closure velocity as estimated with the third method. In Rose's simulations, the gap closure velocity was determined to be between

20 and 30 cm/μs. The simulated value matches the early time value estimated by the third method.

CHAPTER 9

CONCLUSIONS AND FUTURE WORK

In this dissertation, original research was presented with application to pulsed power systems, specifically post-hole convolutes. Design and operation of the mega-Ampere-class Michigan Accelerator for Inductive Z-pinch Experiments (MAIZE) was described. Experimental results were given utilizing a geometrically-simplified version of a single post-hole convolute as the load on MAIZE. Extensive post-hole convolute research on the Z-Machine at Sandia National Laboratories was also included. In this chapter, the results from the previous chapters are summarized, and recommendations for future work are made.

9.1 Summary of MAIZE Experimental Results

The Linear Transformer Driver (LTD) based MA-class facility, MAIZE, has been assembled and is fully operational. Resistive load tests of the pulsed power driver showed proper operation, i.e. with a charge voltage of +/- 90 kV and an 84 mOhm load, the current through the load was 0.97 MA. A model of the pulsed power driver was constructed in PSpice in order to predict the effect of the resistance/inductance of a static load on the current driven through the load. Utilizing the measured load resistance and

the calculated load inductance of the resistive load tests mentioned above, the experimental and simulated currents matched one another to within 1% in both risetime and peak amplitude. At later times the simulation deviates from experiment because it does not include the effects of the time-changing inductance (saturation) of the LTD iron cores. The effect of the iron cores on the LTD pulse shape was also investigated. On shots in which the magnetic flux in the iron cores was not reset, the peak amplitude of the current dropped by more than 10% and the undershoot of the current quadrupled when compared to the standard case.

Tests of the transmission line utilized in MAIZE were successful. The transmission line was designed to minimize inductance while maintaining a reasonable cost. Minimum anode-cathode gaps were set to ensure that the transmission line would be self-magnetically insulated, which was necessary because the gaps exceeded the electric field threshold for electron emission. Electromagnetic Particle-In-Cell simulations of the transmission line using MAGIC PIC 3D showed that early in time the electron flow in the A-K gap is not well insulated, i.e. some flow current is lost to the anode, but as the current flowing in the transmission line increased, the electron hub height drops, and the current lost to the anode approaches zero. The MAGIC simulations predicted for a charge voltage of +/- 100 kV, a load resistance of 0.1 Ohm, and a load inductance equal to 6.7 nH, the peak current would be approximately 700 kA (or around 70% of the ideal value). Experimental tests of the transmission line with a resistive load of the same resistance/inductance used in the MAGIC simulations were conducted. In these tests several different current monitoring diagnostics were used. In earlier tests, the signals

from the B-dots and Rogowski coils showed that the current was 0.46-0.49 MA for a +/- 70 kV charge voltage (66% - 70% of the ideal value). In more recent tests, the anode-cathode gap in the radial section of the transmission line was increased by 10% (from nominally 10 mm to 11 mm). Subsequent resistive load transmission line tests with precisely calibrated B-dots produced peak currents of 0.54 MA for a charge voltage of +/- 70 kV (77% of the ideal value). The increase in current delivered to the load can be explained by the reduced electric field in the transmission line, which reduces the electron emission into the gap, and thus reduces the losses. However, the A-K gap cannot be increased to an arbitrary size, because the inductance scales with the gap, and eventually the negative effect of the increased inductance will outweigh the positive effect of reduced electron losses.

Post-hole convolute experiments conducted on MAIZE were successful in reducing the complicated, diagnostically inaccessible geometry of the standard post-hole convolute, into a more experimentally-friendly setup. The experimental setup allowed spatially-resolved, fiber-coupled visible spectroscopy of the post-hole region parallel to the axis of the post. Pinhole imaging of the visible emission from the plasma was typically performed along a view perpendicular to the axis of the post. Voltage and current monitors were fielded as well. The object of the measurements was to correlate plasma formation with current loss in the convolute. Once this relationship was confirmed, the origin, evolution, and parameters of the plasma were to be determined. The electric fields and localized energy deposition involved in these experiments did not create plasma in the post-hole region, thus no correlation between the plasma formation and

current loss could be formed. Plasma did form in another region of the convolute, and a series of MAGIC simulations conducted by D. M. French showed qualitative agreement with the experiment in the location of the plasma formation. This plasma formed in a region of the experiment that normally would not exist in the standard convolute geometry, as a result, it was helpful in showing that the experiment was behaving as expected in the simulation, but it was not useful in extrapolating a loss mechanism to the convolute used on the Z-Machine.

9.2 Summary of Z-Machine Experimental Results

Measurements of the Z-Machine post-hole convolute were made using a fiber-optically-coupled, visible spectrometer, the output of which was coupled to a streak camera. This diagnostic provided spectrally- and temporally-resolved data from a specific region of the convolute. The probes were designed to allow different regions of the convolute to be viewed depending on the probe used in the measurement. In addition to the streaked visible spectroscopy diagnostic, B-dot and D-dot monitors, and X-ray diodes were used to determine the current, voltage, and X-ray timing, respectively.

Experiments were conducted in which a small band of lithium-fluoride was placed on the upper convolute post as a localized tracer element. Li has a strong line at 6708 A, and is not normally found in the convolute, so when this feature was observed (or not observed), information about the location of the source of the signal was determined. Specifically, when the Li was centered in the upper post-hole it was observed in absorption, and when it was located at the bottom of the upper post, it was briefly

observed in emission early in time, and then not noticeably observed. This result indicates that the location of one source of the continuum emission is located axially in between the two dopant locations. There may be a continuum emission source located below the lower position as well, but this cannot be proven with the data available. This result qualitatively agrees with the LSP simulations performed by Rose et al.

Additional measurements were made of the Balmer series H-alpha transition at 6563 A. The lineshape of the absorption feature was measured as a function of time for several different cases. For the K-shell radiator load, which has a high convolute E-field (high L-dot, high I-dot, and large diameter upper posts), the Full-Width at Half-Maximum (FWHM) increased to 60 A over approximately 30 ns. With an Isentropic Compression Experiment (ICE) load, which has a lower convolute E-field (low L-dot, low I-dot, and small diameter upper posts), the FWHM only reached 30-40 A in 100 ns. These broadening data indicate H peak plasma density of $1.0 \pm 0.1 \times 10^{18}$ cm^{-3} for the K-shell case, and only $7 \pm 1 \times 10^{17}$ cm^{-3} for the ICE case. Additionally, in the ICE case, the plasma density in the convolute increases at a lower rate, thus lower amplitude loss current is expected (was observed). In both cases, a less dense (approximately 6×10^{16} cm^{-3}) region of H plasma was observed. This plasma could have been located within the B-dot cup where the probe was fielded, or it could have been a region of the convolute with significantly lower density.

Experimental H plasma densities were compared to simulated densities for the K-shell radiator case. Unfortunately, the times at which experimental data were recorded did

not overlap with the times at which the simulations had values for the plasma density. The simulation shows that as time increases, so does plasma density. Approximately 20 ns after the last simulation point, the first experimental point is available. The first experimental data point ($6\pm1 \times 10^{16}$ cm^{-3}) is close, but higher than the last (highest density) simulated point (3×10^{16} cm^{-3}), and the experimental data continue to trend upward.

The plasma closure velocity in the post-hole A-K gap was estimated using three different techniques. Two techniques gave 40-50 cm/μs (optical emission to current loss and optical emission across the A-K gap), and the other gave initial values of approximately 20 cm/μs, which then decreased to around 5 cm/μs later in time (space-charge-limited emission). Simulations by Rose predict that the closure velocity is in the range of 20-30 cm/μs, which is a good match to the early time value determined using space-charge-limited (SCL) emission. The closure velocity of the plasma in the simulation was determined prior to 60 ns (last data point for simulated density), which is prior to the point that the experimentally measured SCL emission velocity drops to around 5 cm/μs. Thus, the simulation quantitatively agrees with the experimental measurement of closure velocity.

9.3 Future Work

While the original research presented in this dissertation provides some useful insight about the operation of post-hole convolutes, it leaves plenty of room for additional work. Based on this work, any additional convolute research conducted on MAIZE

would require a cathode plasma source. The electric field necessary to produce electrode plasma (240 kV/cm) is not easily achievable on a nominally 100 kV driver. The A-K gap could be reduced to produce the necessary E-field, but the gap-closure time would be too short to be useful. The electric field can be geometrically increased using carbon fiber emission regions (Fowler Nordheim or explosive emission) on the cathode. This method of increasing the electric field allows the gap to remain an appropriate size. Interferometry or laser induced fluorescence measurements of plasma density could be performed on the MAIZE convolute.

Additional measurements are being planned for the Z-Machine post-hole convolute. The previously conducted localized Li dopant shots were useful in determining the location of anode plasma originating on the post. Similar measurements could be made with varying axial position of the Li on the post on each shot. The intensity and timing of the absorption feature would provide useful information about the location and evolution of the post plasma.

Dopant measurements could be made in which the Li was coated onto a region of the cathode. Placing a dopant on downstream side of the hole would be useful in following the cathode plasma across the A-K gap. Plasma parameters from these measurements could be compared to the results from the anode measurements. Previous simulations indicate that the plasma originating at the anode is less dense than that from the cathode. Simulations also show that plasma from the upstream side of the hole moves along the magnetic field lines and collects on the downstream side of the post. If Li were

located on the upstream side of the hole and observed downstream of the post, this result could be confirmed. Multiple different dopants could be used in different locations on the same shot.

A single measurement of the convolute was made from below, and the data show an interesting feature that was not observed on any other shot. Additional measurements from below with different diagnostic settings/probe locations would be useful in determining what caused the feature seen in the one measurement to date.

In future measurements, the diagnosis of the post-hole convolute may be a primary (or at least significant) goal of the experiment (as opposed to a ride-along). In this instance, it may be possible to modify hardware in such a way that the probe can view the A-K gap without directly viewing any electrodes. With this setup it is plausible that emission lines might be observed without significant continuum. Additional views that still directly observe electrodes but require hardware modifications are also be possible, i.e. a view that looks radially through the cathode from the hole to the post. This view could be used with a dopant to determine the A-K gap closure velocity by measuring at the Doppler shift of the spectral line. A similar measurement could be made of the plasma velocity in the final feed gap using a dopant and the horizontal B-dot holes described in chapter 6.

Improvements need to be made to the data collection and analysis procedures. This includes more sensitive probe, better collimation, and improved collection optics. These

improvements will help push the experimental data collection earlier in time, which is necessary to make comparisons between the simulations and experiments.

Additional simulations of the convolute using LSP should also be conducted. Once a large enough experimental data set is available, the plasma parameters in the simulations can be benchmarked against the experiment. This would allow certain "knobs" in the simulation to be fixed, thus, the code could be used to design and "test" more efficient convolute geometries. Once these new designs have been validated in simulations, they could be more confidently fielded on the Z-Machine.

APPENDICES

APPENDIX A

LINEAR TRANSFORMER DRIVER ASSEMBLY

The following is a series of steps used to assemble the LTD when it was first delivered to the University of Michigan. Subsequent upgrades and modifications of the systems may both make some of these steps unnecessary and require additional steps not listed here in order to properly assemble the LTD.

Remove internal LTD components

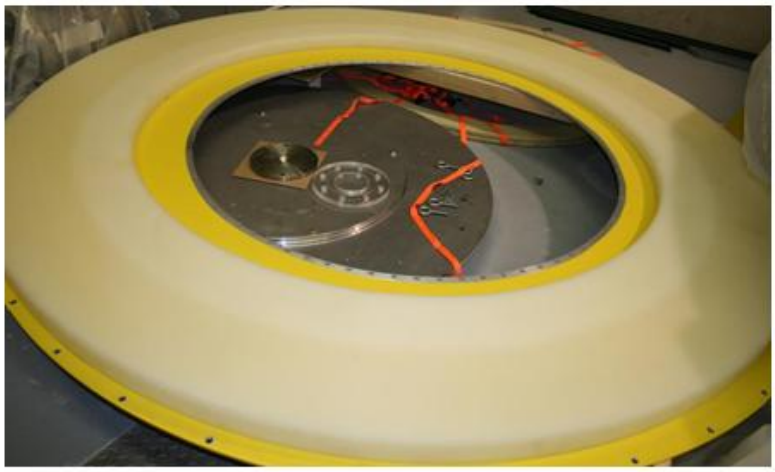

- Lift off the plastic insulator by hand with ~ 4 people
  - Suction cups may be necessary if insulator has swollen with oil

Remove internal LTD components

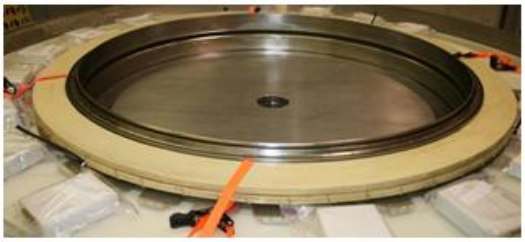

- Remove the top iron cores
  - Attach straps to the crane and lift out the cores
  - Attach 4 nylon straps to the cores by sliding down at the I.D. and pulling under the cores
  - Lift out with crane

Install the bottom capacitors

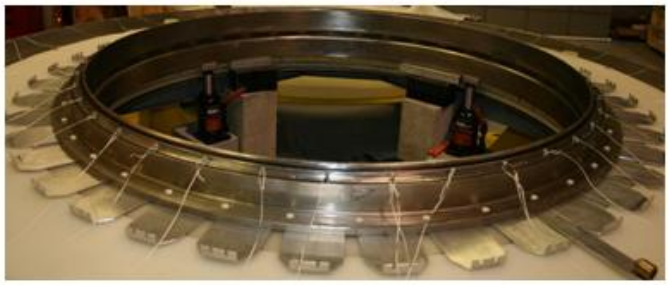

- Attach 40 M6 bolts in the top stainless steel electrode (skipping one hole between bolts) and tie one end of a ~ 4 foot piece of wax string to each bolt

Install the bottom capacitors

- Prep the bottom capacitors
  - Loosely attach the metal clamping plates to each end of 40 of the capacitors
  - Insert the metal capacitor-switch coupler in the high potential end of the capacitor (assuming bottom capacitors charged positively)
  - Tighten the screws on the high potential end of the capacitor to secure the metal capacitor-switch coupler in place

Install the bottom capacitors

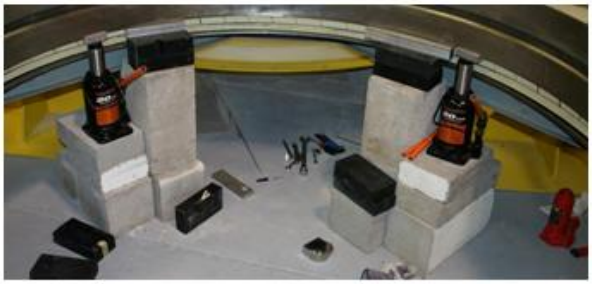

- Lift the center stack of the LTD
  - Remove the 80 M6 bolts holding in the iron ring that clamps the bottom plate to the bottom stainless steel electrode and remove the iron ring
  - Place 4 hydraulic jacks with at least 6 inches of travel on stacks of cinderblocks
  - Place 4 aluminum blocks on top of the jacks to protect the o-ring surface
  - Adjust the height of the jacks to just reach the center stack of the LTD
  - Raise all 4 jack simultaneously so the center stack is supported by all four jacks until the entire stack is raised by ~ 6 inches
  - Place a set of secondary supports in for safety incase the jacks fail

Install the bottom capacitors

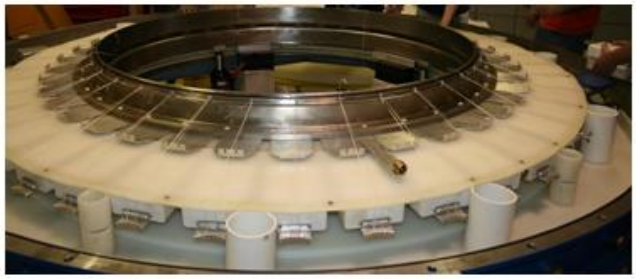

- Prop up the mid-plane insulator with ~ 10 PVC tube supports
- Attach the bottom set of capacitors
  - Slide capacitor in under the mid-plane insulator and lift capacitor up so it is flush with the insulator
  - Make sure the metal clamping plate on the capacitor fits over the slotted metal sheet that is attached to the bottom stainless steel electrode.
  - Using a short Phillips head screw driver bolt the capacitor in place
  - Pull the wax string through the slots on the capacitor-switch coupler and tie the other end to the M6 bolt

Install the bottom capacitors

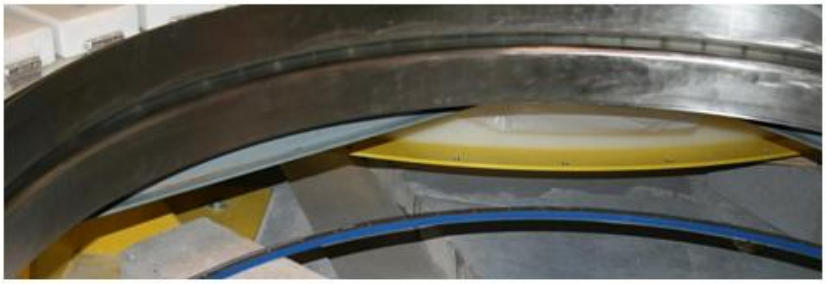

- Lower the center stack of the LTD
  - Remove the secondary supports
  - Remove pieces propping up mid-plane insulator and have ~ 4 people support the insulator
  - Slowly release all 4 hydraulic jack valves simultaneously
  - Make sure center stack seats properly on oil o-ring
  - Bolt iron ring to bottom electrode
- Remove the wax strings from bottom set of capacitors

Install the remaining components

- Prep the top capacitors
  - Loosely attach the metal clamping plates to each end of the 40 remaining capacitors
  - Insert the metal capacitor-switch coupler in the low potential end of the capacitor
- Prep the slotted rings
  - Loosen the bolts that pull the ring together
  - Flex the ring to increase the size of the ring slightly
  - 2 of the 80 rings have an extra tapped hole in them
  - Attach the special charging resistor to the tapped hole

Install the remaining components

- Install the trigger resistor holders
  - FIRST TIME ONLY: remove the small threaded pins holding the trigger wire in place inside the mid-plane insulator from the top and insert from the bottom (Only done if charging bottom capacitors positively)
  - Pry the sheets of the trigger resistor holders open with a flathead screwdriver so the trigger resistors easily slide in and out of the holder
  - Loosely screw the trigger resistor holders to the mid-plane insulator

Install the remaining components

- Mid-plane Insulator
  - The insulator is not rotationally fixed
  - It must be oriented so the trigger resistor clamps are centered between capacitors
  - This is most easily done with only a few top capacitors loosely placed in position

Install the remaining components

- Insert the PE shims into the mid-plane insulator
- Insert the bottom slotted rings
  - Place 40 of the 80 slotted rings underneath the capacitor-switch coupler
  - The bolt must be located under capacitor-switch coupler to line up charging resistors correctly
  - Orient the rings so all face the same direction (access to the bolt from the right side seems preferable)
  - Place one of the special rings to the left of the positive charging cable input

Install the remaining components

- Install the bottom charging resistors (~ 1 kohm)
  - Insert one end of a charging resistor into a hole in a slotted ring
  - Bend the resistor slightly taking care not to kink the resistor
  - Insert the other end of the resistor into a hole in the next slotted ring
  - Continue this process around the LTD until all rings have been resistively linked together

Install the remaining components

- Position the switch
  - Find one of the four Legris gas line fittings in the LTD
  - Insert one of four Legris Tees in the Legris fitting in the LTD
  - Place a switch on the slotted ring to the right of the Legris fitting
  - Make sure the switch number is facing up
  - Orient the switch so the Legris fittings point towards the insulator
  - Attach a ~ 1 kohm trigger resistor to the left Legris fitting on the switch.
  - Make sure the resistor points away from the mid-plane insulator or else the resistor will likely kink when installing

Install the remaining components

- Install the switch
  - Slide the switch into the bottom slotted ring
  - Pull up on the ring so it rests against the plastic portion of the switch
  - Tighten the bolt in the slotted ring until the switch is held tightly in place.
  - Slide the trigger resistor into the right slot of the trigger resistor holder
  - Do not tighten the trigger resistor holder screw until both resistors have been placed

Install the remaining components

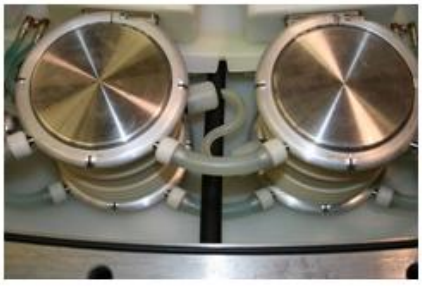

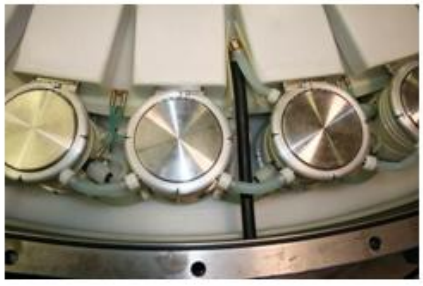

- Install the HV Cables
  - Only perform if a cable is to be installed to the directly to the right of the switch that is currently being installed
  - Slide one end of the black PE guiding tube into the metal cap on the mid-plane insulator and slide the other end into the hole in the LTD wall
    - 2 x Long – Premagnetizer, 2 x Medium – Charging, 4 x Short – Trigger
  - Insert the cable making sure that the cable is seated properly and tighten the compression fitting
  - Twist the PE guiding tubes so the holes face upward

Install the remaining components

- Assemble the gas fittings
  - Place one of the o-ring gaskets on a gas line s-bends and then add a plastic cap
  - Repeat this for the other end of the s-bend
  - Insert one end into the Legris fitting on the right side of the switch
  - Make sure the tube is completely seated in the fitting and is not kinked
  - Slide the plastic cap down until it covers the metal threads on the switch
  - Use the o-ring gasket to hold the plastic cap in place

Install the remaining components

- Gas fittings Exceptions
  - The four Legris fittings in the LTD are used to couple gas into and out of the switch chain
  - The Legris Tees are used to couple to the switches to both the left and the right of the LTD Legris fittings
  - A long s-bend is used to couple to the switch to the right, and a short tight s-bend is used to couple to the switch to the left
  - New s-bends can be made from 1 cm O.D. PE tubing by slowly heating the plastic with a heat gun and bending it to shape

Install the remaining components

- Attach the top capacitor
  - Slide capacitor down on the mid-plane insulator so it is flush with the insulator
  - Make sure the metal clamping plate on the capacitor fits over the slotted metal sheet that is attached to the top stainless steel electrode.
  - Using a Phillips head screw driver bolt the capacitor in place

Install the remaining components

- Install the top slotted ring
  - Slide the slotted ring down over the switch until it seats
  - The bolt must be positioned over the capacitor-switch coupler to allow the charging resistors to be installed
  - Insert one end of a charging resistor into the hole on the right side of the metal ring
  - Leave the ring loose until the other end of the resistor has been attached to the next switch

Install the remaining components

- Charging cables
  - The special charging resistors must be oriented to allow the charging cables to properly seat
  - The top slotted ring is oriented with the bolt to the left to allow this to work
  - Plastic U channels are inserted to make sure the charging cables (and trigger cables) do not get too close to the capacitors.

Install the remaining components

- Install the rest of the Bricks (repeat previously described steps)
  - Position the next switch so it sits to the right of the last one
  - Orient the Legris fittings so they point in the opposite direction as the ones did on the last switch
  - Connect a trigger resistor to the opposite Legris fitting used on the last switch
  - Slide the switch into place
  - Insert the other end of the tubing from the last switch in the left Legris fitting and slide the plastic cap on and fix it in place with the o-ring gasket
  - If necessary twist the switch slightly to avoid kinking the gas tubing
  - Make sure the switch is properly seated in the bottom slotted ring and tighten the bolt in the ring
  - Place a new s-bend of tubing in the right Legris fitting slide the plastic cap on and fix it in place with the o-ring gasket
  - Slide the other end of the trigger resistor into the trigger resistor holder
  - Make sure that the trigger resistors have not kinked during installation
  - If the trigger resistor holder has a resistor in each slot, tighten the screw to clamp the resistors in place
  - Install the top capacitor
  - Place the top slotted ring over the switch
  - Make sure that the switch to the right of the negative charging cable input has the other special slotted ring
  - Insert the other end of the charging resistor from the previous switch in the top slotted ring
  - Tighten the slotted ring on the previous switch
  - Continue this process until all 40 bricks are assembled

APPENDIX B

ADDITIONAL SPECTRAL LINEOUTS

On shot 2075, the streaked spectrum contained a noticeable dip at 5167 A. This feature corresponds to the $3d^7(^4F)4s - 3d^6(^5D)4s4p(^3P^o)$ Fe–I feature. A lineout of the spectrum at 3180 ns (90-100 ns past peak current) is shown below. The Fe feature is of particular importance because the B-dot cup is made from high purity copper and coated in gold. Thus the Fe feature could not come from the B-dot cup, and likely is a result of absorption with in the convolute. Since the continuum is back lighting the Fe feature, the continuum must also come from within the convolute. A second point worth noting is that the upper convolute is made from stainless steel and primarily coated in ~ 3 micron thick gold. Observation of the Fe line implies that the gold coating is ablated from the electrodes during the shot and some of the stainless steel below is also ablated. This can be confirmed by post-shot visual inspection of the convolute, which shows that the parts that were gold coated prior to the shot are no longer coated post-shot.

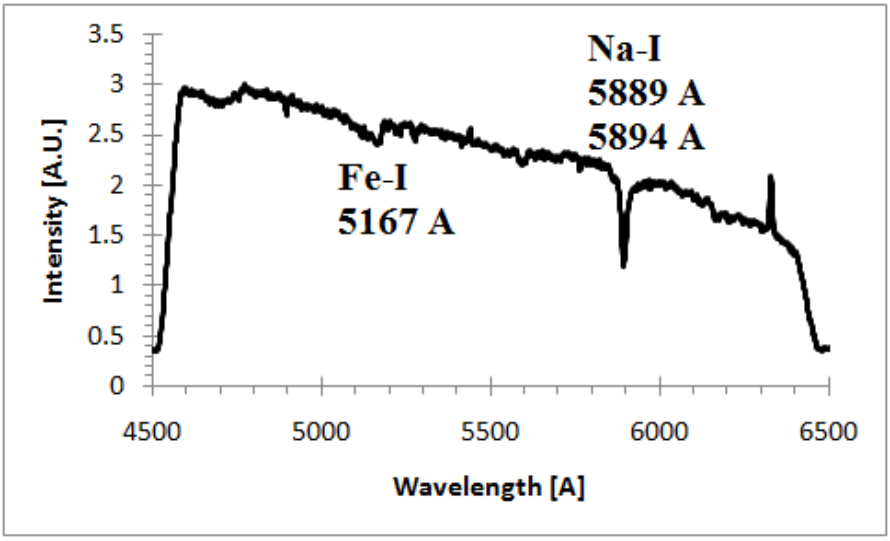

APPENDIX C

TEMPERATURE CALCULATIONS FROM CONTINUUM SLOPE

The temperature of the blackbody radiator was calculated based on the following equation

$$I'(\lambda, T) = \frac{A\lambda^{-5}}{exp\left(\frac{B}{\lambda * T}\right) - 1}$$

Where A and B are constants, T is the temperature of the radiator, and λ is the wavelength of the radiation [62],[72],[73]. Data from Shot 2075 was plotted against curves using the above equation. Lineouts were taken at 70 ns, 80 ns, and 90 ns. Based on the plot shown below, the temperature of the blackbody continuum irradiator appears to increase with time from 2 eV at 70 ns to 4 eV at 90 ns. Beyond 90 ns, the slope of the continuum is relatively constant, indicating that the temperature is also relatively constant.

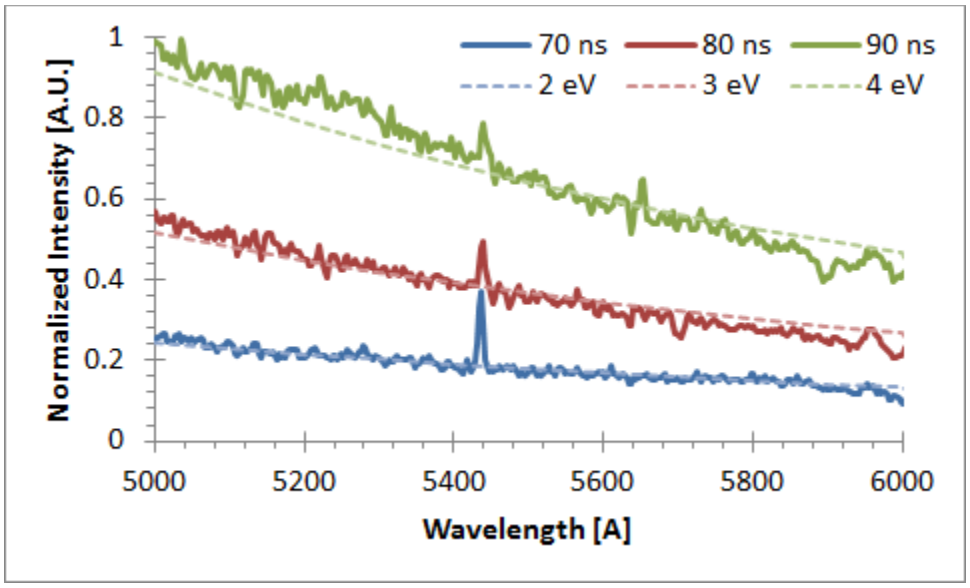

APPENDIX D

CALIBRATION/CORRECTIONS APPLIED AND PLASMA DENSITY UNCERTAINTY ESTIMATES

The following corrections were applied to the data in the following order. First the raw data had the step wedge applied to it; then the wavelength and time scales were applied. A wiggle correction was applied to account for the shift due to imperfections in the streak tube. The linearity of response correction was applied to account for the low signal threshold, and the wavelength calibration was applied. The wavelength calibration itself also had corrections applied to it. First the step wedge, then the linearity of response, and last the laser power stability correction.

The uncertainty in the plasma density calculations is the result of several factors: application of the calibration, temperature assumption, and the Lorentzian fits to the data. The uncertainty in the calibration consists of several individual uncertainties: application of the step wedge (10%), linearity of response of the streak camera (6%) and the wavelength calibration (12%). The wavelength calibration takes into account the 2% stability in the power of the laser sources used in the calibration, as well as the uncertainty in the step wedge correction (10%), and the linearity of the streak camera response (6%). The total uncertainty in the calibration is 17%. This is included with the ~10% uncertainty associated with the assumed temperature and the 12% associated with the Lorentzian fits to the data to get a total uncertainty on the order of 23%.

APPENDIX E

LTD RESISTOR SOLUTIONS

Charging resistors:

1/2″ inner diameter

4 3/8″ long

22.3 g/L copper sulfate solution

Resistance @ 100 kHz ~ 600 ohms

Trigger resistors:

3/16″ inner diameter

4 1/2″ long

279 g/L copper sulfate solution

Resistance @ 100 kHz ~ 620 ohms

APPENDIX F

PSPICE SIMULATION INPUT

```
**** 05/27/09 18:18:27 ******* PSpice 10.0.0 (Jan 2003) ******* ID#
1111111111
 ** Profile: "SCHEMATIC1-LTD"  [ H:\Private\LTD-100kV\ltd-
pspicefiles\schematic1\ltd.sim ]


 ****     CIRCUIT DESCRIPTION


*******************************************************************************
*******




** Creating circuit file "LTD.cir"
** WARNING: THIS AUTOMATICALLY GENERATED FILE MAY BE OVERWRITTEN BY
SUBSEQUENT SIMULATIONS

*Libraries:
* Profile Libraries :
* Local Libraries :
* From [PSPICE NETLIST] section of s:\CAEN\pspice-
10.0\tools\PSpice\PSpice.ini file:
.lib "nom.lib"

*Analysis directives:
.TRAN  0 1000ns 0
.PROBE V(alias(*)) I(alias(*)) W(alias(*)) D(alias(*)) NOISE(alias(*))
.INC "..\SCHEMATIC1.net"



**** INCLUDING SCHEMATIC1.net ****
* source LTD
C_C12         N01497 N24280  40n IC=-100kV
C_C43         N08721 N23149  40n IC=100kV
R_R66         N16401 N24280  1000000k
C_C71         N18843 N23149  40n IC=100kV
R_R50         N10617 N24280  1000000k
C_C24         N03675 N24280  40n IC=-100kV
X_U24         N09975 N09951 Sw_tClose PARAMS: tClose=0n ttran=10n
Rclosed=0.01
+  Ropen=1Meg
X_U34         N17205 N17181 Sw_tClose PARAMS: tClose=0n ttran=10n
Rclosed=0.01
```

```
+  Ropen=1Meg
R_R77         N21471 N23149  1000000k
R_R37         N07011 N23149  1000000k
X_U9         N02505 N02481 Sw_tClose PARAMS: tClose=0n ttran=10n
Rclosed=0.01
+  Ropen=1Meg
R_R11         N01473 N23149  1000000k
C_C72         N18867 N24280  40n IC=-100kV
C_C44         N08745 N24280  40n IC=-100kV
R_R23         N03651 N23149  1000000k
C_C67         N17181 N23149  40n IC=100kV
X_U29         N13365 N13341 Sw_tClose PARAMS: tClose=0n ttran=10n
Rclosed=0.01
+  Ropen=1Meg
C_C47         N09951 N23149  40n IC=100kV
C_C17         N02481 N23149  40n IC=100kV
X_U1         N00131 N00124 Sw_tClose PARAMS: tClose=10n ttran=10n
Rclosed=0.01
+  Ropen=1Meg
X_U20         N07587 N07563 Sw_tClose PARAMS: tClose=10n ttran=10n
Rclosed=0.01
+  Ropen=1Meg
X_U38         N20601 N20577 Sw_tClose PARAMS: tClose=0n ttran=10n
Rclosed=0.01
+  Ropen=1Meg
R_R71         N18843 N23149  1000000k
R_R43         N08721 N23149  1000000k
R_R78         N21495 N24280  1000000k
R_R38         N07035 N24280  1000000k
X_U30         N14097 N14073 Sw_tClose PARAMS: tClose=0n ttran=10n
Rclosed=0.01
+  Ropen=1Meg
X_U28         N12651 N12627 Sw_tClose PARAMS: tClose=0n ttran=10n
Rclosed=0.01
+  Ropen=1Meg
R_R12         N01497 N24280  1000000k
C_C68         N17205 N24280  40n IC=-100kV
C_C57         N13341 N23149  40n IC=100kV
C_C48         N09975 N24280  40n IC=-100kV
C_C18         N02505 N24280  40n IC=-100kV
X_U7         N01815 N01791 Sw_tClose PARAMS: tClose=10n ttran=10n
Rclosed=0.01
+  Ropen=1Meg
C_C39         N07563 N23149  40n IC=100kV
C_C75         N20577 N23149  40n IC=100kV
R_R24         N03675 N24280  1000000k
X_U11         N03267 N03243 Sw_tClose PARAMS: tClose=10n ttran=10n
Rclosed=0.01
+  Ropen=1Meg
C_C59         N14073 N23149  40n IC=100kV
C_C55         N12627 N23149  40n IC=100kV
R_R72         N18867 N24280  1000000k
C_C1         N00124 N23149  40n IC=100kV
R_R44         N08745 N24280  1000000k
C_C58         N13365 N24280  40n IC=-100kV
R_R47         N09951 N23149  1000000k
R_R67         N17181 N23149  1000000k
```

```
R_R17          N02481 N23149  1000000k
C_C13          N01791 N23149  40n IC=100kV
X_U27          N11955 N11931 Sw_tClose PARAMS: tClose=0n ttran=10n
Rclosed=0.01
+  Ropen=1Meg
X_U31          N14847 N14823 Sw_tClose PARAMS: tClose=0n ttran=10n
Rclosed=0.01
+  Ropen=1Meg
C_C40          N07587 N24280  40n IC=-100kV
C_C76          N20601 N24280  40n IC=-100kV
C_C21          N03243 N23149  40n IC=100kV
C_C56          N12651 N24280  40n IC=-100kV
C_C60          N14097 N24280  40n IC=-100kV
C_C2          N00131 N24280  40n IC=-100kV
R_R57          N13341 N23149  1000000k
L_L_coil1          0 N475113  1000uH
C_C14          N01815 N24280  40n IC=-100kV
C_C53          N11931 N23149  40n IC=100kV
C_C61          N14823 N23149  40n IC=100kV
R_R39          N07563 N23149  1000000k
R_R75          N20577 N23149  1000000k
X_U2          N00405 N00381 Sw_tClose PARAMS: tClose=10n ttran=10n
Rclosed=0.01
+  Ropen=1Meg
C_C22          N03267 N24280  40n IC=-100kV
R_R48          N09975 N24280  1000000k
R_R68          N17205 N24280  1000000k
R_R55          N12627 N23149  1000000k
R_R18          N02505 N24280  1000000k
R_R59          N14073 N23149  1000000k
X_U3          N00651 N00627 Sw_tClose PARAMS: tClose=10n ttran=10n
Rclosed=0.01
+  Ropen=1Meg
L_A_L_TL          N691909 N475113  25n
L_L_int1          N475113 N24280  4nH
R_R13          N01791 N23149  1000000k
C_C54          N11955 N24280  40n IC=-100kV
C_C62          N14847 N24280  40n IC=-100kV
C_C3          N00381 N23149  40n IC=100kV
R_R58          N13365 N24280  1000000k
R_R21          N03243 N23149  1000000k
R_R1          N00124 N23149  1000000k
C_C5          N00627 N23149  40n IC=100kV
X_U16          N05487 N05463 Sw_tClose PARAMS: tClose=10n ttran=10n
Rclosed=0.01
+  Ropen=1Meg
X_U15          N05007 N04983 Sw_tClose PARAMS: tClose=10n ttran=10n
Rclosed=0.01
+  Ropen=1Meg
R_R76          N20601 N24280  1000000k
R_R40          N07587 N24280  1000000k
X_U26          N11277 N11253 Sw_tClose PARAMS: tClose=0n ttran=10n
Rclosed=0.01
+  Ropen=1Meg
X_U32          N15615 N15591 Sw_tClose PARAMS: tClose=0n ttran=10n
Rclosed=0.01
+  Ropen=1Meg
```

```
R_R60          N14097 N24280  1000000k
R_R56          N12651 N24280  1000000k
X_U4          N00915 N00891 Sw_tClose PARAMS: tClose=10n ttran=10n
Rclosed=0.01
+  Ropen=1Meg
X_U23          N09351 N09327 Sw_tClose PARAMS: tClose=0n ttran=10n
Rclosed=0.01
+  Ropen=1Meg
X_U35          N18027 N18003 Sw_tClose PARAMS: tClose=0n ttran=10n
Rclosed=0.01
+  Ropen=1Meg
R_R61          N14823 N23149  1000000k
R_R53          N11931 N23149  1000000k
C_C4          N00405 N24280  40n IC=-100kV
R_R2          N00131 N24280  1000000k
R_R14          N01815 N24280  1000000k
C_C6          N00651 N24280  40n IC=-100kV
C_C31          N05463 N23149  40n IC=100kV
X_U17          N05985 N05961 Sw_tClose PARAMS: tClose=10n ttran=10n
Rclosed=0.01
+  Ropen=1Meg
C_C29          N04983 N23149  40n IC=100kV
X_U21          N08157 N08133 Sw_tClose PARAMS: tClose=10n ttran=10n
Rclosed=0.01
+  Ropen=1Meg
X_U37          N19725 N19701 Sw_tClose PARAMS: tClose=0n ttran=10n
Rclosed=0.01
+  Ropen=1Meg
R_R22          N03267 N24280  1000000k
C_C63          N15591 N23149  40n IC=100kV
X_U14          N04545 N04521 Sw_tClose PARAMS: tClose=10n ttran=10n
Rclosed=0.01
+  Ropen=1Meg
C_C51          N11253 N23149  40n IC=100kV
C_C7          N00891 N23149  40n IC=100kV
C_C45          N09327 N23149  40n IC=100kV
C_C69          N18003 N23149  40n IC=100kV
R_R3          N00381 N23149  1000000k
C_C32          N05487 N24280  40n IC=-100kV
C_C33          N05961 N23149  40n IC=100kV
R_R5          N00627 N23149  1000000k
R_R62          N14847 N24280  1000000k
R_R54          N11955 N24280  1000000k
C_C30          N05007 N24280  40n IC=-100kV
C_C73          N19701 N23149  40n IC=100kV
C_C41          N08133 N23149  40n IC=100kV
X_U8          N02151 N02127 Sw_tClose PARAMS: tClose=10n ttran=10n
Rclosed=0.01
+  Ropen=1Meg
C_C27          N04521 N23149  40n IC=100kV
C_C52          N11277 N24280  40n IC=-100kV
C_C64          N15615 N24280  40n IC=-100kV
C_C8          N00915 N24280  40n IC=-100kV
C_C46          N09351 N24280  40n IC=-100kV
C_C70          N18027 N24280  40n IC=-100kV
X_U10          N02877 N02853 Sw_tClose PARAMS: tClose=0n ttran=10n
Rclosed=0.01
```

```
+  Ropen=1Meg
R_R_int         N674740 N140654  0.033
C_C34          N05985 N24280  40n IC=-100kV
X_U5          N01197 N01173 Sw_tClose PARAMS: tClose=10n ttran=10n
Rclosed=0.01
+  Ropen=1Meg
R_R31          N05463 N23149  1000000k
X_U18          N06501 N06477 Sw_tClose PARAMS: tClose=10n ttran=10n
Rclosed=0.01
+  Ropen=1Meg
R_R29          N04983 N23149  1000000k
X_U40          N22407 N22383 Sw_tClose PARAMS: tClose=0n ttran=10n
Rclosed=0.01
+  Ropen=1Meg
R_R4          N00405 N24280  1000000k
C_C74          N19725 N24280  40n IC=-100kV
C_C42          N08157 N24280  40n IC=-100kV
C_C15          N02127 N23149  40n IC=100kV
C_C28          N04545 N24280  40n IC=-100kV
R_R51          N11253 N23149  1000000k
R_R63          N15591 N23149  1000000k
R_R7          N00891 N23149  1000000k
R_R6          N00651 N24280  1000000k
R_R45          N09327 N23149  1000000k
R_R69          N18003 N23149  1000000k
C_C19          N02853 N23149  40n IC=100kV
X_U13          N04101 N04077 Sw_tClose PARAMS: tClose=10n ttran=10n
Rclosed=0.01
+  Ropen=1Meg
R_R33          N05961 N23149  1000000k
C_C9          N01173 N23149  40n IC=100kV
L_A_L_load         N691909 N690612  5n
C_C35          N06477 N23149  40n IC=100kV
C_C79          N22383 N23149  40n IC=100kV
R_R73          N19701 N23149  1000000k
R_R41          N08133 N23149  1000000k
X_U33          N16401 N16377 Sw_tClose PARAMS: tClose=0n ttran=10n
Rclosed=0.01
+  Ropen=1Meg
X_U25          N10617 N10593 Sw_tClose PARAMS: tClose=0n ttran=10n
Rclosed=0.01
+  Ropen=1Meg
C_C16          N02151 N24280  40n IC=-100kV
R_R27          N04521 N23149  1000000k
R_R32          N05487 N24280  1000000k
C_C20          N02877 N24280  40n IC=-100kV
R_R30          N05007 N24280  1000000k
C_C25          N04077 N23149  40n IC=100kV
R_R52          N11277 N24280  1000000k
R_R64          N15615 N24280  1000000k
R_R8          N00915 N24280  1000000k
R_R46          N09351 N24280  1000000k
R_R70          N18027 N24280  1000000k
C_C10          N01197 N24280  40n IC=-100kV
C_C36          N06501 N24280  40n IC=-100kV
C_C80          N22407 N24280  40n IC=-100kV
C_C65          N16377 N23149  40n IC=100kV
```

```
C_C49         N10593 N23149  40n IC=100kV
R_R15         N02127 N23149  1000000k
L_L_coil2         0 N140654  1000uH
R_R34         N05985 N24280  1000000k
R_R19         N02853 N23149  1000000k
R_R42         N08157 N24280  1000000k
R_R74         N19725 N24280  1000000k
C_C26         N04101 N24280  40n IC=-100kV
R_R28         N04545 N24280  1000000k
R_R9         N01173 N23149  1000000k
R_R79         N22383 N23149  1000000k
R_R35         N06477 N23149  1000000k
C_C66         N16401 N24280  40n IC=-100kV
C_C50         N10617 N24280  40n IC=-100kV
X_U19         N07035 N07011 Sw_tClose PARAMS: tClose=10n ttran=10n
Rclosed=0.01
+  Ropen=1Meg
X_U39         N21495 N21471 Sw_tClose PARAMS: tClose=0n ttran=10n
Rclosed=0.01
+  Ropen=1Meg
L_L_int2         N140654 N23149  4nH
R_A_R_load         N690612 N674740  0.05
X_U6         N01497 N01473 Sw_tClose PARAMS: tClose=10n ttran=10n
Rclosed=0.01
+  Ropen=1Meg
R_R25         N04077 N23149  1000000k
R_R16         N02151 N24280  1000000k
R_R20         N02877 N24280  1000000k
X_U12         N03675 N03651 Sw_tClose PARAMS: tClose=10n ttran=10n
Rclosed=0.01
+  Ropen=1Meg
R_R49         N10593 N23149  1000000k
R_R65         N16377 N23149  1000000k
C_C77         N21471 N23149  40n IC=100kV
C_C37         N07011 N23149  40n IC=100kV
R_R10         N01197 N24280  1000000k
R_R80         N22407 N24280  1000000k
R_R36         N06501 N24280  1000000k
C_C11         N01473 N23149  40n IC=100kV
X_U22         N08745 N08721 Sw_tClose PARAMS: tClose=10n ttran=10n
Rclosed=0.01
+  Ropen=1Meg
X_U36         N18867 N18843 Sw_tClose PARAMS: tClose=0n ttran=10n
Rclosed=0.01
+  Ropen=1Meg
C_C23         N03651 N23149  40n IC=100kV
R_R26         N04101 N24280  1000000k
C_C78         N21495 N24280  40n IC=-100kV
C_C38         N07035 N24280  40n IC=-100kV

**** RESUMING LTD.cir ****
.END
```

```
**** 05/27/09 18:18:27 ******* PSpice 10.0.0 (Jan 2003) ******* ID#
1111111111
 ** Profile: "SCHEMATIC1-LTD"  [ H:\Private\LTD-100kV\ltd-
pspicefiles\schematic1\ltd.sim ]


 ****     Voltage Controlled Switch MODEL PARAMETERS


*********************************************************************
*******



               X_U24.Smod      X_U34.Smod      X_U9.Smod
X_U29.Smod
         RON     .01             .01             .01             .01
        ROFF    1.000000E+06    1.000000E+06    1.000000E+06
1.000000E+06
         VON    1               1               1               1
        VOFF    0               0               0               0


               X_U1.Smod       X_U20.Smod      X_U38.Smod
X_U30.Smod
         RON     .01             .01             .01             .01
        ROFF    1.000000E+06    1.000000E+06    1.000000E+06
1.000000E+06
         VON    1               1               1               1
        VOFF    0               0               0               0


               X_U28.Smod      X_U7.Smod       X_U11.Smod
X_U27.Smod
         RON     .01             .01             .01             .01
        ROFF    1.000000E+06    1.000000E+06    1.000000E+06
1.000000E+06
         VON    1               1               1               1
        VOFF    0               0               0               0


               X_U31.Smod      X_U2.Smod       X_U3.Smod
X_U16.Smod
         RON     .01             .01             .01             .01
        ROFF    1.000000E+06    1.000000E+06    1.000000E+06
1.000000E+06
         VON    1               1               1               1
        VOFF    0               0               0               0


               X_U15.Smod      X_U26.Smod      X_U32.Smod
X_U4.Smod
         RON     .01             .01             .01             .01
        ROFF    1.000000E+06    1.000000E+06    1.000000E+06
1.000000E+06
         VON    1               1               1               1
```

```
        VOFF    0               0               0               0


                X_U23.Smod      X_U35.Smod      X_U17.Smod
X_U21.Smod
         RON     .01             .01             .01             .01
        ROFF    1.000000E+06    1.000000E+06    1.000000E+06
1.000000E+06
         VON    1               1               1               1
        VOFF    0               0               0               0


                X_U37.Smod      X_U14.Smod      X_U8.Smod
X_U10.Smod
         RON     .01             .01             .01             .01
        ROFF    1.000000E+06    1.000000E+06    1.000000E+06
1.000000E+06
         VON    1               1               1               1
        VOFF    0               0               0               0


                X_U5.Smod       X_U18.Smod      X_U40.Smod
X_U13.Smod
         RON     .01             .01             .01             .01
        ROFF    1.000000E+06    1.000000E+06    1.000000E+06
1.000000E+06
         VON    1               1               1               1
        VOFF    0               0               0               0


                X_U33.Smod      X_U25.Smod      X_U19.Smod
X_U39.Smod
         RON     .01             .01             .01             .01
        ROFF    1.000000E+06    1.000000E+06    1.000000E+06
1.000000E+06
         VON    1               1               1               1
        VOFF    0               0               0               0


                X_U6.Smod       X_U12.Smod      X_U22.Smod
X_U36.Smod
         RON     .01             .01             .01             .01
        ROFF    1.000000E+06    1.000000E+06    1.000000E+06
1.000000E+06
         VON    1               1               1               1
        VOFF    0               0               0               0
```

```
**** 05/27/09 18:18:27 ******* PSpice 10.0.0 (Jan 2003) ******* ID#
1111111111
 ** Profile: "SCHEMATIC1-LTD"  [ H:\Private\LTD-100kV\ltd-
pspicefiles\schematic1\ltd.sim ]


 ****     INITIAL TRANSIENT SOLUTION       TEMPERATURE =   27.000 DEG C


*********************************************************************
*******



 NODE   VOLTAGE     NODE   VOLTAGE     NODE   VOLTAGE     NODE
VOLTAGE


(N00124) 100.0E+03 (N00131)-100.0E+03 (N00381) 100.0E+03 (N00405)-
100.0E+03

(N00627) 100.0E+03 (N00651)-100.0E+03 (N00891) 100.0E+03 (N00915)-
100.0E+03

(N01173) 100.0E+03 (N01197)-100.0E+03 (N01473) 100.0E+03 (N01497)-
100.0E+03

(N01791) 100.0E+03 (N01815)-100.0E+03 (N02127) 100.0E+03 (N02151)-
100.0E+03

(N02481) 100.0E+03 (N02505)-100.0E+03 (N02853) 100.0E+03 (N02877)-
100.0E+03

(N03243) 100.0E+03 (N03267)-100.0E+03 (N03651) 100.0E+03 (N03675)-
100.0E+03

(N04077) 100.0E+03 (N04101)-100.0E+03 (N04521) 100.0E+03 (N04545)-
100.0E+03

(N04983) 100.0E+03 (N05007)-100.0E+03 (N05463) 100.0E+03 (N05487)-
100.0E+03

(N05961) 100.0E+03 (N05985)-100.0E+03 (N06477) 100.0E+03 (N06501)-
100.0E+03

(N07011) 100.0E+03 (N07035)-100.0E+03 (N07563) 100.0E+03 (N07587)-
100.0E+03

(N08133) 100.0E+03 (N08157)-100.0E+03 (N08721) 100.0E+03 (N08745)-
100.0E+03

(N09327) 100.0E+03 (N09351)-100.0E+03 (N09951) 100.0E+03 (N09975)-
100.0E+03

(N10593) 100.0E+03 (N10617)-100.0E+03 (N11253) 100.0E+03 (N11277)-
100.0E+03
```

(N11931) 100.0E+03 (N11955)-100.0E+03 (N12627) 100.0E+03 (N12651)-
100.0E+03

(N13341) 100.0E+03 (N13365)-100.0E+03 (N14073) 100.0E+03 (N14097)-
100.0E+03

(N14823) 100.0E+03 (N14847)-100.0E+03 (N15591) 100.0E+03 (N15615)-
100.0E+03

(N16377) 100.0E+03 (N16401)-100.0E+03 (N17181) 100.0E+03 (N17205)-
100.0E+03

(N18003) 100.0E+03 (N18027)-100.0E+03 (N18843) 100.0E+03 (N18867)-
100.0E+03

(N19701) 100.0E+03 (N19725)-100.0E+03 (N20577) 100.0E+03 (N20601)-
100.0E+03

(N21471) 100.0E+03 (N21495)-100.0E+03 (N22383) 100.0E+03 (N22407)-
100.0E+03

(N23149) 0.0000 (N24280) 0.0000 (X_U1.3) 0.0000 (X_U2.3)
0.0000

(X_U3.3) 0.0000 (X_U4.3) 0.0000 (X_U5.3) 0.0000 (X_U6.3)
0.0000

(X_U7.3) 0.0000 (X_U8.3) 0.0000 (X_U9.3) 0.0000 (N140654)
0.0000

(N475113) 0.0000 (N674740) 0.0000

(N690612) 0.0000 (N691909) 0.0000

(X_U10.3) 0.0000 (X_U11.3) 0.0000

(X_U12.3) 0.0000 (X_U13.3) 0.0000

(X_U14.3) 0.0000 (X_U15.3) 0.0000

(X_U16.3) 0.0000 (X_U17.3) 0.0000

(X_U18.3) 0.0000 (X_U19.3) 0.0000

(X_U20.3) 0.0000 (X_U21.3) 0.0000

(X_U22.3) 0.0000 (X_U23.3) 0.0000

(X_U24.3) 0.0000 (X_U25.3) 0.0000

(X_U26.3) 0.0000 (X_U27.3) 0.0000

(X_U28.3) 0.0000 (X_U29.3) 0.0000

(X_U30.3) 0.0000 (X_U31.3) 0.0000

(X_U32.3) 0.0000 (X_U33.3) 0.0000

(X_U34.3)	0.0000	(X_U35.3)	0.0000
(X_U36.3)	0.0000	(X_U37.3)	0.0000
(X_U38.3)	0.0000	(X_U39.3)	0.0000
(X_U40.3)	0.0000		

VOLTAGE SOURCE CURRENTS

NAME	CURRENT
X_U24.V1	0.000E+00
X_U34.V1	0.000E+00
X_U9.V1	0.000E+00
X_U29.V1	0.000E+00
X_U1.V1	0.000E+00
X_U20.V1	0.000E+00
X_U38.V1	0.000E+00
X_U30.V1	0.000E+00
X_U28.V1	0.000E+00
X_U7.V1	0.000E+00
X_U11.V1	0.000E+00
X_U27.V1	0.000E+00
X_U31.V1	0.000E+00
X_U2.V1	0.000E+00
X_U3.V1	0.000E+00
X_U16.V1	0.000E+00
X_U15.V1	0.000E+00
X_U26.V1	0.000E+00
X_U32.V1	0.000E+00
X_U4.V1	0.000E+00
X_U23.V1	0.000E+00
X_U35.V1	0.000E+00
X_U17.V1	0.000E+00
X_U21.V1	0.000E+00
X_U37.V1	0.000E+00
X_U14.V1	0.000E+00
X_U8.V1	0.000E+00
X_U10.V1	0.000E+00
X_U5.V1	0.000E+00
X_U18.V1	0.000E+00
X_U40.V1	0.000E+00
X_U13.V1	0.000E+00
X_U33.V1	0.000E+00
X_U25.V1	0.000E+00
X_U19.V1	0.000E+00
X_U39.V1	0.000E+00
X_U6.V1	0.000E+00
X_U12.V1	0.000E+00
X_U22.V1	0.000E+00
X_U36.V1	0.000E+00

TOTAL POWER DISSIPATION 0.00E+00 WATTS

```
          JOB CONCLUDED

**** 05/27/09 18:18:27 ******* PSpice 10.0.0 (Jan 2003) ******* ID#
1111111111
 ** Profile: "SCHEMATIC1-LTD"  [ H:\Private\LTD-100kV\ltd-
pspicefiles\schematic1\ltd.sim ]


 ****     JOB STATISTICS SUMMARY


*******************************************************************************


  Total job time (using Solver 1)   =         .92
```

BIBLIOGRAPHY

[1] M. E. Cuneo, R. A. Vesey, G. R. Bennett, D. B. Sinars, W. A. Stygar, E. M. Waisman, J. L. Porter, P. K. Rambo, I. C. Smith, S. V. Lebedev, J. P. Chittenden, D. E. Bliss, T. J. Nash, G. A. Chandler, B. B. Afeyan, E. P. Yu, R. B. Campbell, R. G. Adams, D. L. Hanson, T. A. Mehlhorn, and M. K. Matzen, "Progress in Symmetric ICF Capsule Implosions and Wire-Array Z-Pinch Source Physics for Double-Pinch-Driven Hohlraums," *Plasma Physics and Controlled Fusion*, vol. 48, 2006, pp. R1-R35.

[2] M. G. Mazarakis, M. E. Cuneo, W. A. Stygar, H. C. Harjes, D. B. Sinars, B. Jones, C. Deeney, E. M. Waisman, T. J. Nash, K. W. Struve, and D. H. McDaniel, "X-Ray Emission Current Scaling Experiments for Compact Single-Tungsten-Wire Arrays at 80-Nanosecond Implosion Times," *Physical Review E*, vol. 79, 2009, pp. 1-15.

[3] C. A. Coverdale, B. Jones, D. J. Ampleford, J. Chittenden, C. Jennings, J. W. Thornhill, J. P. Apruzese, R. W. Clark, K. G. Whitney, A. Dasgupta, J. Davis, J. Guiliani, P. D. LePell, C. Deeney, D. B. Sinars, and M. E. Cuneo, "K-Shell X-Ray Sources at the Z Accelerator," *High Energy Density Physics*, vol. 6, 2010, pp. 143-152.

[4] M. C. Jones, D. J. Ampleford, M. E. Cuneo, C. A. Jennings, B. Jones, M. R. Lopez, G. A. Rochau, M. E. Savage, and J. L. Porter, "Total X-ray Power Improvement on Recent Wire Array Experiments on the Z-Machine," Chicago, Illinois: 2010.

[5] T. W. L. Sanford, R. C. Mock, J. F. Seamen, M. R. Lopez, R. G. Watt, G. C. Idzorek, and D. L. Peterson, "Wire fixturing in high wire-number z pinches critical for high radiation power and reproducibility," *Physics of Plasmas*, vol. 12, 2005, pp. 1-8.

[6] R. W. Lemke, M. D. Knudson, D. E. Bliss, K. Cochrane, J. P. Davis, A. A. Giunta, H. C. Harjes, and S. A. Slutz, "Magnetically Accelerated, Ultrahigh Velocity Flyer Plates for Shock Wave Experiments," *Journal of Applied Physics*, vol. 98, 2005, pp. 1-9.

[7] R. Cauble, D. B. Reisman, J. R. Asay, C. A. Hall, M. D. Knudson, W. F. Hemsing, J. H. Goforth, and D. G. Tasker, "Isentropic Compression Experiments to 1 Mbar using Magnetic Pressure," *Journal of Physics: Condensed Matter*, vol. 14, 2002.

[8] R. W. Lemke, M. D. Knudson, A. C. Robinson, T. A. Haill, K. W. Struve, J. R. Asay, and T. A. Mehlhorn, "Self-Consistent, Two-Dimensional, Magnetohydrodynamic simulations of Magnetically Drivern Flyer Plates," *Physics of Plasmas*, vol. 10, 2003, pp. 1867-1874.

[9] J. E. Bailey, P. Arnault, T. Blenski, G. Dejonghe, O. Peyrusse, J. J. MacFarlane, R.

C. Mancini, M. E. Cuneo, D. S. Nielsen, and G. A. Rochau, "Opacity Measurements of Tamped NaBr Samples Heated by Z-Pinch X-Rays," *Journal of Quantitative Spectroscopy & Radiative Transfer*, vol. 81, 2003, pp. 31-45.

[10] D. H. Cohen, J. J. MacFarlane, J. E. Bailey, and D. A. Liedahl, "X-Ray Spectral Diagnostics of Neon Photoionization Experiments on the Z-Machine," *Review of Scientific Instruments*, vol. 74, 2003, pp. 1962-1965.

[11] D. V. Rose, D. R. Welch, E. A. Madrid, C. L. Miller, R. E. Clark, W. A. Stygar, M. E. Savage, G. A. Rochau, J. E. Bailey, T. J. Nash, M. E. Sceiford, and K. W. Struve, "Three-Dimensional Electromagnetic Model of the Pulsed-Power Z-Pinch Accelerator," *Physical Review Special Topics - Accelerators and Beams*, vol. 13, 2010, pp. 1-12.

[12] W. A. Stygar, M. E. Cuneo, D. I. Headley, H. C. Ives, R. J. Leeper, M. G. Mazarakis, C. L. Olson, J. L. Porter, T. C. Wagoner, and J. R. Woodworth, "Architecture of Petawatt-Class Z-Pinch Accelerators," *Physical Review Special Topics - Accelerators and Beams*, vol. 10, 2007, pp. 1-24.

[13] R. M. Gilgenbach, M. R. Gomez, J. C. Zier, W. W. Tang, D. M. French, Y. Y. Lau, M. G. Mazarakis, M. E. Cuneo, M. D. Johnston, B. V. Oliver, T. A. Mehlhorn, A. A. Kim, and V. A. Sinebryukhov, "MAIZE: a 1 MA LTD-Driven Z-Pinch at the University of Michigan," *Dense Z-Pinch Conference Proceedings*, vol. 7th, 2008.

[14] A. A. Kim, M. G. Mazarakis, V. A. Sinebryukhov, B. M. Kovalchuk, V. A. Visir, S. N. Volkov, F. Bayol, A. N. Bastrikov, V. G. Durakov, S. V. Frolov, V. M. Alexeenko, D. H. McDaniel, W. E. Fowler, K. R. LeChien, C. L. Olson, W. A. Stygar, K. W. Struve, J. L. Porter, and R. M. Gilgenbach, "Development and Tests of Fast 1-MA Linear Transformer Driver Stages," *Physical Review Special Topics - Accelerators and Beams*, vol. 12, 2009, pp. 1-10.

[15] M. G. Mazarakis, W. E. Fowler, K. R. LeChien, F. W. Long, M. K. Matzen, D. H. McDaniel, R. G. McKee, C. L. Olson, J. L. Porter, S. T. Rogowski, K. W. Struve, W. A. Stygar, J. R. Woodworth, A. A. Kim, V. A. Sinebryukhov, R. M. Gilgenbach, M. R. Gomez, D. M. French, Y. Y. Lau, J. C. Zier, D. M. Van De Valde, R. A. Sharpe, and K. Ward, "High-Current Linear Transformer Driver Development at Sandia National Laboratories," *IEEE Transactions on Plasma Science*, vol. 38, 2010, pp. 704-713.

[16] M. G. Mazarakis, W. E. Fowler, A. A. Kim, V. A. Sinebryukhov, S. T. Rogowski, R. A. Sharpe, D. H. McDaniel, C. L. Olson, J. L. Porter, K. W. Struve, W. A. Stygar, and J. R. Woodworth, "High Current, 0.5-MA, fast, 100-ns, Linear Transformer Driver Experiments," *Physical Review Special Topics - Accelerators and Beams*, vol. 12, 2009, pp. 1-10.

[17] M. R. Gomez, R. M. Gilgenbach, Y. Y. Lau, W. W. Tang, J. C. Zier, M. G. Mazarakis, and W. A. Stygar, "Design of a MITL for a 1MA LTD Driving a Wire Array Z-Pinch Load," *Pulsed Power Conference Proceedings*, vol. 16th, 2007.

[18] D. V. Rose, C. L. Miller, D. R. Welch, R. E. Clark, E. A. Madrid, C. B. Mostrom, W. A. Stygar, K. R. LeChien, M. G. Mazarakis, W. L. Langston, J. L. Porter, and J. R. Woodworth, "Circuit models and three-dimensional electromagnetic simulations of

a 1-MA linear transformer driver stage," *Physical Review Special Topics - Accelerators and Beams,* vol. 13, 2010, pp. 1-11.

[19] M. G. Mazarakis and R. B. Spielman, "A Compact, High-Voltage E-Beam Pulser," Monterey, CA: IEEE, 1999, pp. 412-415.

[20] M. G. Mazarakis, R. B. Spielman, K. W. Struve, and F. W. Long, "A New Linear Inductive Voltage Adder Driver for the Saturn Accelerator," Monterey, CA: 2000, pp. 1-3.

[21] M. G. Mazarakis, R. B. Spielman, K. W. Struve, and F. W. Long, "Ultrafast LTD's for bremsstrahlung diodes and Z-pinches," Las Vegas, NV: IEEE, 2001, pp. 587-590.

[22] A. A. Kim, M. G. Mazarakis, V. I. Manylov, V. A. Visir, and W. A. Stygar, "Energy loss due to eddy current in linear transformer driver cores," *Physical Review Special Topics - Accelerators and Beams,* vol. 13, 2010, pp. 1-7.

[23] J. R. Woodworth, J. A. Alexander, F. R. Gruner, W. A. Stygar, M. J. Harden, J. R. Blickem, G. J. Dension, F. E. White, L. M. Lucero, H. D. Anderson, L. F. Bennett, S. F. Glover, D. M. Van De Valde, and M. G. Mazarakis, "Low-inductance gas switches for linear transformer drivers," *Physical Review Special Topics - Accelerators and Beams,* vol. 12, 2009, pp. 1-17.

[24] J. R. Woodworth, W. A. Stygar, L. F. Bennett, M. G. Mazarakis, H. D. Anderson, M. J. Harden, J. R. Blickem, F. R. Gruner, and R. White, "New low inductance gas switches for linear transformer drivers," *Physical Review Special Topics - Accelerators and Beams,* vol. 13, 2010, pp. 1-9.

[25] M. R. Lopez, R. M. Gilgenbach, D. W. Jordan, S. A. Anderson, M. D. Johnston, M. W. Keyser, H. Miyake, C. W. Peters, M. C. Jones, V. B. Neculaes, Y. Y. Lau, T. A. Spencer, J. W. Luginsland, M. D. Haworth, R. W. Lemke, and D. Price, "Cathode Effects on a Relativistic Magnetron Driven by a Microsecond E-Beam Accelerator," *IEEE Transactions on Plasma Science,* vol. 30, 2002, pp. 947-955.

[26] D. B. Sinars, S. A. Slutz, M. C. Herrmann, R. D. McBride, M. E. Cuneo, K. J. Peterson, R. A. Vesey, C. Nakhleh, B. E. Blue, K. Killebrew, D. Schroen, K. Tomlinson, A. D. Edens, M. R. Lopez, I. C. Smith, J. Shores, V. Bigman, G. R. Bennett, B. W. Atherton, M. E. Savage, W. A. Stygar, G. T. Leifeste, and J. L. Porter, "Measurements of Magneto-Rayleigh-Taylor Instability Growth during the Implosion of Initially Solid Al Tubes Driven by the 20-MA, 100-ns Z Facility," *Physical Review Letters,* vol. 105, 2010, pp. 1-4.

[27] K. R. LeChien, M. E. Savage, V. Anaya, D. E. Bliss, W. T. Clark, J. P. Corley, G. Feltz, J. E. Garrity, D. W. Guthrie, K. C. Hodge, J. E. Maenchen, R. Maier, K. R. Prestwich, K. W. Struve, W. A. Stygar, T. Thompson, J. Van Den Avyle, P. E. Wakeland, Z. R. Wallace, and J. R. Woodworth, "Development of a 5.4 MV Laser Triggered Gas Switch for Multimodule, Multimegampere Pulsed Power Drivers," *Physical Review Special Topics - Accelerators and Beams,* vol. 11, 2008, pp. 1-17.

[28] D. V. Rose, D. R. Welch, T. P. Hughes, R. E. Clark, and W. A. Stygar, "Plasma Evolution and Dynamics in High-Power Vacuum-Transmission-Line Post-Hole

Convolutes," *Physical Review Special Topics - Accelerators and Beams*, vol. 11, 2008, pp. 1-10.

[29] T. D. Pointon, W. A. Stygar, R. B. Spielman, H. C. Ives, and K. W. Struve, "Particle-In-Cell Simulations of Electron Flow in the Post-Hole Convolute of the Z Accelerator," *Physics of Plasmas*, vol. 8, 2001, pp. 4534-4544.

[30] D. V. Rose, D. R. Welch, T. P. Hughes, R. E. Clark, C. B. Mostrom, and W. A. Stygar, "Plasma Formation, Evolution, and Dynamics in 100 TW Vacuum-Transmission-Line Post-Hole Convolutes," *Pulsed Power Conference Proceedings*, vol. 16th, 2007, pp. 171-174.

[31] D. V. Rose, D. R. Welch, R. E. Clark, E. A. Madrid, C. L. Miller, C. Mostrom, W. A. Stygar, M. E. Cuneo, C. A. Jennings, B. Jones, D. J. Ampleford, and K. W. Struve, "ZR-Convolute Analysis and Modeling: Plasma Evolution and Dynamics Leading to Current Losses," *Pulsed Power Conference Proceedings*, vol. 17th, 2009, pp. 1153-1158.

[32] T. D. Pointon and D. B. Seidel, "Current Loss in the Vacuum Section of the Refurbished Z Accelerator," *Pulsed Power Conference Proceedings*, vol. 17th, 2009, pp. 1159-1164.

[33] T. D. Pointon, W. L. Langston, and M. E. Savage, "Computer Simulations of the Magnetically Insulated Transmission Lines and Post-Hole Convolute of ZR," *Pulsed Power Conference Proceedings*, vol. 16th, 2007, pp. 165-170.

[34] T. C. Wagoner, W. A. Stygar, H. C. Ives, T. L. Gilliland, R. B. Spielman, M. F. Johnson, P. G. Reynolds, J. K. Moore, R. L. Mourning, D. L. Fehl, K. E. Androlewicz, J. E. Bailey, R. S. Broyles, T. A. Dinwoodie, G. L. Donovan, M. E. Dudley, K. D. Hahn, A. A. Kim, J. R. Lee, R. J. Leeper, G. T. Leifeste, J. A. Melville, J. A. Mills, L. P. Mix, W. B. S. Moore, B. P. Peyton, J. L. Porter, G. A. Rochau, G. E. Rochau, M. E. Savage, J. F. Seamen, J. D. Serrano, A. W. Sharpe, R. W. Shoup, J. S. Slopek, C. S. Speas, K. W. Struve, D. M. Van De Valde, and R. M. Woodring, "Differential-Output B-Dot and D-Dot Monitors for Current and Voltage Measurements on a 20-MA, 3-MV Pulsed-Power Accelerator," *Physical Review Special Topics - Accelerators and Beams*, vol. 11, 2008, pp. 1-18.

[35] K. R. LeChien, W. A. Stygar, M. E. Savage, P. E. Wakeland, V. Anaya, D. S. Artery, M. J. Baremore, D. E. Bliss, R. Chavez, G. D. Coombs, J. P. Corley, P. A. Jones, A. K. Kipp, B. A. Lewis, J. A. Lott, J. J. Lynch, G. R. McKee, S. D. Ploor, K. R. Prestwich, S. A. Roznowski, D. C. Spencer, S. D. White, and J. R. Woodworth, "6.1-MV, 0.79-MA Laser-Triggered Gas Switch for Multimodule, Multiterawatt Pulsed-Power Accelerators," *Physical Review Special Topics - Accelerators and Beams*, vol. 13, 2010, pp. 1-11.

[36] D. V. Rose, D. R. Welch, C. L. Miller, R. E. Clark, E. A. Madrid, C. B. Mostrom, T. C. Wagoner, J. K. Moore, W. A. Stygar, J. E. Bailey, T. J. Nash, G. A. Rochau, and D. B. Sinars, "10^7-A Load-Current B-Dot Monitor: Simulations, Design, and Performance," *Physical Review Special Topics - Accelerators and Beams*, vol. 13, 2010, pp. 1-9.

[37] C. A. Jennings, J. P. Chittenden, M. E. Cuneo, W. A. Stygar, D. J. Ampleford, E. M.

Waisman, M. C. Jones, M. E. Savage, K. R. LeChien, and T. C. Wagoner, "Circuit Model for Driving Three-Dimensional Resistive MHD Wire Array Z-Pinch Calculations," *IEEE Transactions on Plasma Science,* vol. 38, 2010, pp. 529-539.

[38] R. B. Spielman, W. A. Stygar, K. W. Struve, and J. F. Seamen, "PBFA Z: A 55 TW/4.5 MJ Electrical Generator," Vancouver, B. C., Canada: IEEE, 1998, pp. 1235-1239.

[39] W. A. Stygar, R. B. Spielman, G. O. Allshouse, C. Deeney, D. R. Humphreys, H. C. Ives, F. W. Long, T. H. Martin, M. K. Matzen, D. H. McDaniel, C. W. Mendel, Jr, L. P. Mix, T. J. Nash, J. W. Poukey, J. J. Ramirez, T. W. L. Sanford, J. F. Seamen, D. B. Seidel, J. W. Smith, D. M. Van De Valde, R. W. Wavrik, P. A. Corcoran, J. W. Douglas, I. D. Smith, M. A. Mostrom, K. W. Struve, T. P. Hughes, R. E. Clark, R. W. Shoup, T. C. Wagoner, T. L. Gilliland, and B. P. Peyton, "Design and Performance of the Z Magnetically-Insulated Transmission Lines," *SAND Report*, vol. 97, 1997, pp. 1-8.

[40] S. A. Slutz, M. C. Herrmann, R. A. Vesey, A. B. Sefkow, D. B. Sinars, D. C. Rovang, K. J. Peterson, and M. E. Cuneo, "Pulsed-Power-Driven Cylindrical Liner Implosions of Laser Preheated Fuel Magnetized with an Axial Field," *Physics of Plasmas*, vol. 17, 2010, pp. 1-15.

[41] R. B. Spielman, P. Corcoran, J. Fockler, H. Kishi, and P.W. Spence, "A Double Post-Hole Vacuum Convolute Diode for Z-Pinch Experiments on Saturn," *Pulsed Power Conference Proceedings*, vol. 7th, 1989, pp. 445-448.

[42] M. G. Mazarakis, J. W. Poukey, S. L. Shope, C. A. Frost, B. N. Turman, J. J. Ramirez, K. R. Prestwich, and P. J. Pankuch, ""SMILE": A Self Magnetically Insulated Transmission Line Adder for the 8-Stage RADLAC II Accelerator," San Diego, CA: IEEE, 1991, pp. 86-89.

[43] J. M. Creedon, "Relativistic Brillouin flow in the high nu/gamma diode," *Journal of Applied Physics*, vol. 46, 1975, pp. 2946-2955.

[44] J. M. Creedon, "Magnetic cutoff in high-current diodes," *Journal of Applied Physics*, vol. 48, 1976, pp. 1070-1077.

[45] B. Goplen, L. Ludeking, D. Smith, and G. Warren, "User-Configurable MAGIC for Electromagnetic PIC Calculations," *Computer Physics Communications*, vol. 87, 1995, pp. 54-86.

[46] M. E. Cuneo, "The effect of electrode contamination, cleaning and conditioning on high-energy pulsed-power device performance," *IEEE Transactions on Dielectrics and Electrical Insulation*, vol. 6, 1999, pp. 469-485.

[47] D. R. Welch, D. V. Rose, N. Bruner, R. E. Clark, B. V. Oliver, K. D. Hahn, and M. D. Johnston, "Hybrid simulation of electrode plasmas in high-power diodes," *Physics of Plasmas*, vol. 16, 2009, pp. 1-9.

[48] C. D. Child, "Discharge from Hot CaO," *Physical Review (Series I)*, vol. 32, 1911, p. 492.

[49] F. W. Grover, *Inductance Calculations*, Dover Publications, 2009.

[50] O. A. Hurricane, "Optimized minimal inductance transmission line configuration for Z-pinch experiments," *Journal of Applied Physics,* vol. 95, 2004, pp. 4503-4505.

[51] J. E. Bailey, R. Adams, A. L. Carlson, C. H. Ching, and A. B. Filuk, "High-accuracy time- and space-resolved Stark shift measurements," *Review of Scientific Instruments,* vol. 68, 1997, pp. 1009-1014.

[52] J. E. Bailey, A. L. Carlson, R. L. Morrison, and Y. Maron, "Visible spectroscopy measurements in the PBFA II ion diode," *Review of Scientific Instruments,* vol. 61, 1990, pp. 3075-3080.

[53] G. Dunham, J. E. Bailey, A. L. Carlson, P. W. Lake, and M. D. Knudson, "Diagnostic methods for time-resolved optical spectroscopy of shocked liquid deuterium," *Review of Scientific Instruments,* vol. 75, 2004, pp. 928-935.

[54] K. Cochrane, J. E. Bailey, P. W. Lake, and A. L. Carlson, "Wavelength-dependent measurements of optical-fiber transit time, material dispersion, and attenuation," *Journal of Applied Optics,* vol. 40, 2001, pp. 150-156.

[55] M. D. Johnston, B. V. Oliver, D. W. Droemer, B. Frogget, M. D. Crain, and Y. Maron, "Absolute Calibration Method for Nanosecond-Resolved, Time-Streaked, Fiber Optic Light Collection, Spectroscopy Systems," *SAND Report,* vol. 2010, 2010, pp. 1-28.

[56] P. W. Lake, Private Communication, Apr. 2010.

[57] J. E. Bailey, A. B. Filuk, A. L. Carlson, D. J. Johnson, P. W. Lake, E. J. McGuire, T. A. Mehlhorn, T. D. Pointon, T. J. Renk, W. A. Stygar, and Y. Maron, "Measurement of Acceleration Gap Dynamics in a 20-TW Applied-Magnetic-Field Ion Diode," *Physical Review Letters,* vol. 74, 1995, pp. 1771-1774.

[58] G. A. Rochau, J. E. Bailey, and Y. Maron, "Applied Spectroscopy in Pulsed Power Plasmas," *Physics of Plasmas,* vol. 17, 2010, pp. 1-8.

[59] A. B. Filuk, J. E. Bailey, A. L. Carlson, D. J. Johnson, P. W. Lake, T. A. Mehlhorn, L. P. Mix, T. J. Renk, W. A. Stygar, and Y. Maron, "Charge-Exchange Atoms and Ion Source Divergence in a 20 TW Applied-B Ion Diode," *Physical Review Letters,* vol. 77, 1996, pp. 3557-3560.

[60] W. A. Stygar, S. E. Rosenthal, H. C. Ives, T. C. Wagoner, G. O. Allshouse, K. E. Androlewicz, G. L. Donovan, D. L. Fehl, M. H. Frese, T. L. Gilliland, M. F. Johnson, J. A. Mills, D. B. Reisman, P. G. Reynolds, C. S. Speas, R. B. Spielman, K. W. Struve, A. Toor, and E. M. Waisman, "Energy loss to conductors operated at lineal current densities <= 10 MA/cm: Semianalytic model, magnetohydrodynamic simulations, and experiment," *Physical Review Special Topics - Accelerators and Beams,* vol. 11, 2008, pp. 1-14.

[61] H. R. Griem, *Spectral Line Broadening by Plasmas,* New York: Academic Press, 1974.

[62] H. R. Griem, *Principles of Plasma Spectroscopy,* Cambridge Monographs on Plasma Physics, 1997.

[63] E. Stambulchik, S. Alexiou, H. R. Griem, and P. C. Kepple, "Stark broadening of

high principal quantum number hydrogen Balmer lines in low-density laboratory plasmas," *Physical Review E*, vol. 75, 2007, pp. 1-9.

[64] E. Stambulchik, D. V. Fisher, Y. Maron, H. R. Griem, and S. Alexiou, "Correlation effects and their influence on line broadening in plasmas: Application to H-alpha," *High Energy Density Physics*, vol. 3, 2007, pp. 272-277.

[65] E. Stambulchik and Y. Maron, "Plasma line broadening and computer simulations: A mini-review," *High Energy Density Physics*, vol. 6, 2010, pp. 9-14.

[66] E. Stambulchik, K. Tsigutkin, and Y. Maron, "Recent Advances in Stark Line Broadening Calculations and their Applications to Precise Spectroscopy of Pulsed Plasmas," St. Petersburg, FL: ECA, 2003, pp. 1.58:1-4.

[67] R. D. McBride, C. A. Jennings, R. A. Vesey, G. A. Rochau, M. E. Savage, W. A. Stygar, M. E. Cuneo, D. B. Sinars, M. C. Jones, K. R. LeChien, M. R. Lopez, J. K. Moore, K. W. Struve, T. C. Wagoner, and E. M. Waisman, "Displacement current phenomena in the magnetically insulated transmission lines of the refurbished Z accelerator," *Physical Review Special Topics - Accelerators and Beams*, vol. Accepted, 2010.

[68] F. F. Chen, *Introduction to Plasma Physics and Controlled Fusion*, New York: Springer, 2006.

[69] L. Spitzer, *Physics of Fully Ionized Gases*, New York: Interscience, 1956.

[70] I. Langmuir, "The Effect or Space Charge and Residual Gases on Thermionic Currents in High Vacuum," *Physical Review (Series II)*, vol. 2, 1913, pp. 450-486.

[71] S. V. Yadavalli and R. L. Bollen, "Child-Langmuir law in the relativistic regime," *Nuclear Instruments and Methods*, vol. 75, 1969, pp. 229-230.

[72] F. C. Jahoda, E. M. Little, W. E. Quinn, G. A. Sawyer, and T. F. Stratton, "Continuum Radiation in the X Ray and Visible Regions from a Magnetically Compressed Plasma," *Physical Review*, vol. 119, 1960, pp. 843-856.

[73] M. Lamoureux, C. Moller, and P. Jaegle, "Validity of Electron-Temperature Measurements using Continuum Plasma Emission," *Journal of Quantitative Spectroscopy & Radiative Transfer*, vol. 33, 1985, pp. 127-131.